AWARD NUMBER: W81XWH-10-2-0165

TITLE: "Biomechanics of Head, Neck, and Chest Injury Prevention for Soldiers: Phase 2 & 3"."

PRINCIPAL INVESTIGATOR: Stefan M. Duma, PhD

CONTRACTING ORGANIZTION: Virginia Polytechnic Institute and State University
Blacksburg, VA 24061

REPORT DATE: August 2016

TYPE OF REPORT: Final Report

PREPARED FOR: U.S. Army Medical Research and Materiel Command
Fort Detrick, Maryland 21702-5012

DISTRIBUTION STATEMENT: Approved for public release; distribution unlimited

The views, opinions and/or findings contained in this report are those of the author(s) and should not be construed as an official Department of the Army position, policy or decision unless so designated by other documentation.

REPORT DOCUMENTATION PAGE

Form Approved
OMB No. 0704-0188

1. REPORT DATE	2. REPORT TYPE	3. DATES COVERED
August 2016	Final Report	28Sep2010 - 27Sep2016

4. TITLE AND SUBTITLE

"Biomechanics of Head, Neck, and Chest Injury Prevention for Soldiers: Phase 2 & 3"."

5a. CONTRACT NUMBER
W81XWH-10-2-0165

5b. GRANT NUMBER
W81XWH-10-2-0165

5c. PROGRAM ELEMENT NUMBER

6. AUTHOR(S)

Stefan Duma, Andrew Kemper, Steve Rowson, Joel Stitzel,

Ashley Weaver, Philip Brown, and Vanessa Alphonse

email: Duma@vt.edu

5d. PROJECT NUMBER

5e. TASK NUMBER

5f. WORK UNIT NUMBER

7. PERFORMING ORGANIZATION NAME(S) AND ADDRESS(ES)

Virginia Polytechnic Institute and State University
Blacksburg, VA 24061

8. PERFORMING ORGANIZATION REPORT NUMBER

9. SPONSORING / MONITORING AGENCY NAME(S) AND ADDRESS(ES)

U.S. Army Medical Research and Materiel Command
Fort Detrick, Maryland 21702-5012

10. SPONSOR/MONITOR'S ACRONYM(S)

11. SPONSOR/MONITOR'S REPORT NUMBER(S)

12. DISTRIBUTION / AVAILABILITY STATEMENT
Approved for Public Release; Distribution Unlimited

13. SUPPLEMENTARY NOTES

14. ABSTRACT

This is the final report for the cooperative agreement between the Virginia Tech – Wake Forest University, Center for Injury Biomechanics and the U.S. Army entitled "Biomechanics of Head, Neck, and Chest Injury Prevention for Soldiers." This final report includes activities performed between October 27, 2015 and May 27, 2016. Task 1.2 details the development of a new biofidelic eye, with area sensing capabilities, for the Facial and Ocular CountermeasUre Safety (FOCUS) headform that can assess injury risk in both blunt and blast loading scenarios. Task 1.3 details the experimental blast overpressure testing performed on porcine eyes and the computational modeling efforts performed to assess eye injury risk due to blast overpressure loading. Task 1.3.1 details the research performed to improve the understanding of the biomechanics of the head and brain. Task 2.3 details the computational modeling efforts conducted to evaluate the response of the cervical spine and the effects of cervical arthrodesis and arthroplasty during simulated automobile collisions and rotary-wing aircraft impacts. This section also details the progress made on the development of a testing apparatus to evaluate cervical spine implants in survivable loading scenarios. Task 4.3 provides details on the National Research Symposium on Military Biomechanics that is hosted by the Virginia Tech – Wake Forest University, Center for Injury Biomechanics annually in accordance with this cooperative agreement. Finally, the Dissemination of Knowledge section provides a list of all of the papers that have been published as a result of the research that was performed under this cooperative agreement, as well as the publication plan for additional publications. To date, this research has yielded nine (n=9) refereed publications and six (n=6) conference publications. Three (n=3) additional manuscripts have been submitted to peer reviewed journals and are currently under review. Finally, five (n=5) more manuscripts will be submitted to peer reviewed journals within the next six months.

15. SUBJECT TERMS
blast biomechanics, eye injury risk from blast loading, biofidelic area sensing eye for the FOCUS headform, cervical spine implants, biomechanics of the head and brain, symposium on military biomechanics

16. SECURITY CLASSIFICATION OF:			17. LIMITATION OF ABSTRACT	18. NUMBER OF PAGES	19a. NAME OF RESPONSIBLE PERSON
a. REPORT	**b. ABSTRACT**	**c. THIS PAGE**			USAMRMC
U	U	U	UU	213	**19b. TELEPHONE NUMBER** *(include area code)*

Biomechanics of Head, Neck, and Chest Injury Prevention for Soldiers

Final Report

PREPARED FOR

Ray F. Santullo, OD FAAO
Congressionally Directed Medical Research Programs
1077 Pachtel St
Fort Detrick, MD 21702-5012

PREPARED BY

Stefan Duma, Andrew Kemper, Steve Rowson, Joel Stitzel,
Ashley Weaver, Philip Brown, and Vanessa Alphonse
Virginia Tech - Wake Forest, Center for Injury Biomechanics
325 Stanger Street, Kelly Hall 439
Blacksburg, VA 24061
(540) 231-1617
duma@vt.edu

August 5, 2016

Virginia Tech - Wake Forest
Center for Injury Biomechanics

www.cib.vt.edu

EXECUTIVE SUMMARY

This is the final report for the cooperative agreement between the Virginia Tech – Wake Forest University, Center for Injury Biomechanics and the U.S. Army entitled "Biomechanics of Head, Neck, and Chest Injury Prevention for Soldiers." This final report includes activities performed between October 27, 2015 and May 27, 2016. Task 1.2 details the development of a new biofidelic eye, with area sensing capabilities, for the Facial and Ocular CountermeasUre Safety (FOCUS) headform that can assess injury risk in both blunt and blast loading scenarios. Task 1.3 details the experimental blast overpressure testing performed on porcine eyes and the computational modeling efforts performed to assess eye injury risk due to blast overpressure loading. Task 1.3.1 details the research performed to improve the understanding of the biomechanics of the head and brain. Task 2.3 details the computational modeling efforts conducted to evaluate the response of the cervical spine and the effects of cervical arthrodesis and arthroplasty during simulated automobile collisions and rotary-wing aircraft impacts. This section also details the progress made on the development of a testing apparatus to evaluate cervical spine implants in survivable loading scenarios. Task 4.3 provides details on the National Research Symposium on Military Biomechanics that is hosted by the Virginia Tech – Wake Forest University, Center for Injury Biomechanics annually in accordance with this cooperative agreement. Finally, the Dissemination of Knowledge section provides a list of all of the papers that have been published as a result of the research that was performed under this cooperative agreement, as well as the publication plan for additional publications. Overall, the research conducted under this cooperative agreement has generated a considerable amount of novel data that will add to the literature. To date, this research has yielded nine (n=9) refereed publications and six (n=6) conference publications. Three (n=3) additional manuscripts have been submitted to peer reviewed journals and are currently under review. Finally, five (n=5) more manuscripts will be submitted to peer reviewed journals within the next six months.

TABLE OF CONTENTS

LIST OF FIGURES

4

5

6

LIST OF TABLES

EXPERIMENTAL TESTING

Area-Sensitive FOCUS Eye for Prediction of Injury Risk during Blunt and Blast Loading

Background

The current Facial and Ocular CountermeasUre Safety (FOCUS) eye and orbit assembly is limited in data collection to only the reaction force measured by the load cell behind the eye. The field of injury biomechanics currently implements eye injury risk curves based on normalized energy (i.e., the kinetic energy of a projectile divided by the projectile area) to predict eye injury risk (Kennedy et al., 2011). However, the size and normalized energy of a projectile are rarely known in many scenarios. The development of a synthetic eye with the ability to quantify the area of loading could be used to assess injury risk resulting from either projectile or blast loading events when loading characteristics are not known a priori.

Methods

The current FOCUS eye was modified to create an area-sensitive eye (Figure 1). This was done by bisecting the eye at 40% of the anterior-posterior depth of the eye. An array of nine miniature pressure sensors (Model 060, 100 psi, Precision Measurement Company, Ann Arbor, MI) was placed along the larger half of the cut surface. A thin layer of silicon adhesive was then used to secure the smaller half of the cut surface to the larger half.

FOCUS Eye	Bisected Eye	Pressure Sensor Array	Silicon Adhesive
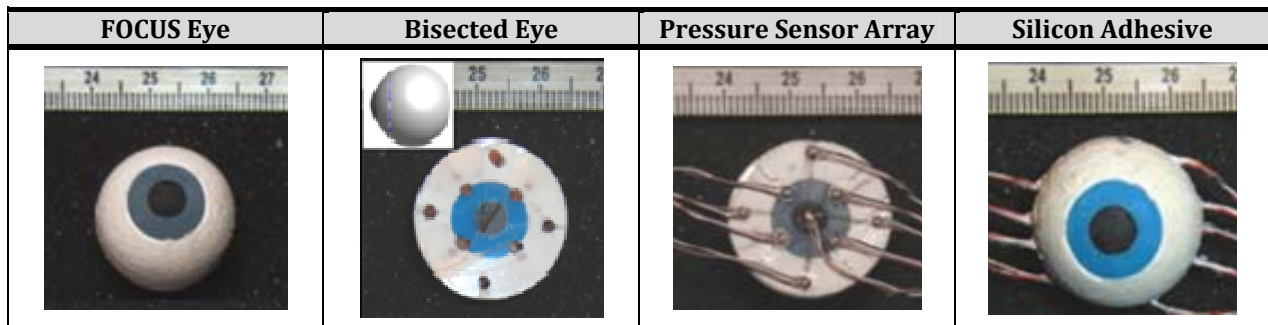
Figure 1: Area-sensitive FOCUS eye development.

The area-sensitive eye was tested in blunt and blast loading conditions in an isolated eye test setup. The area-sensitive eye was placed in a similar test setup as the one used for the isolated porcine eye experimental blast loading tests, which is described in detail in the next section. This consisted of a rigid concave cup that minimized boundary conditions around the eye. The eye was secured in place within this rigid concave cup using a small amount of silicon adhesive. The FOCUS eye load cell was attached to the back side of the rigid concave cup for both blunt and blast tests.

Blunt impact tests were conducted with a drop tower system using three different impactor tip diameters: 6.4 mm, 12.7 mm, and 17.5 mm (Figure 2, left). Tests were conducted in triplicate at two drop heights (12 in. and 24 in.) to simulate multiple impacting energies. The mass of the impactor (175 g) was consistent for all tests. Blunt tests were designed for a direct corneal impact for this test series.

Blast tests were conducted in triplicate at 10 psi, 20 psi, and 30 psi (static overpressure), which are survivable pressure levels, using the VT Advanced Blast Simulator (ABS) (Figure 3). The helium gas-driven ABS consists of equally shaped "driver" and "driven" sections separated by a frangible aluminum membrane, which was scored with an "X" pattern. The driver section is pressurized with helium gas until the membrane passively ruptures and sends a burst of gas down the driven section. As the gas compresses upon itself, a shock-front forms and the shock wave propagates through the tube. The small VT ABS is specifically designed for testing small specimens, and is able to produce peak overpressures up to approximately 30 psi (static overpressure) with a positive duration around 2.5 ms. Pressure was measured at a number of locations around the eye for these tests. Static overpressure in the fluid flow was measured using a "pencil" sensor mounted 2 inches from the temporal side of the eye (Model 137A24, PCB Piezotronics, Depew, NY, USA). The sensing element of the pencil sensor was aligned with the front of the cornea. Total overpressure was measured for the isolated eye condition using a sensor mounted above the eye (Model 113B21, PCB Piezotronics, Depew, NY, USA). Static overpressure was also measured along the wall using three high frequency response pressure sensors (Model 102B15, PCB Piezotronics, Depew, NY) mounted flush to the inside wall of the tube. These sensors are located 12 in apart from each other, with the middle sensor located at the test region. Shock wave velocity can be quantified using the time of arrival of the shock wave at these sensors.

Blunt Loading			Blast Loading
6.4 mm Dia. Impactor	12.7 mm Dia. Impactor	17.5 mm Dia. Impactor	
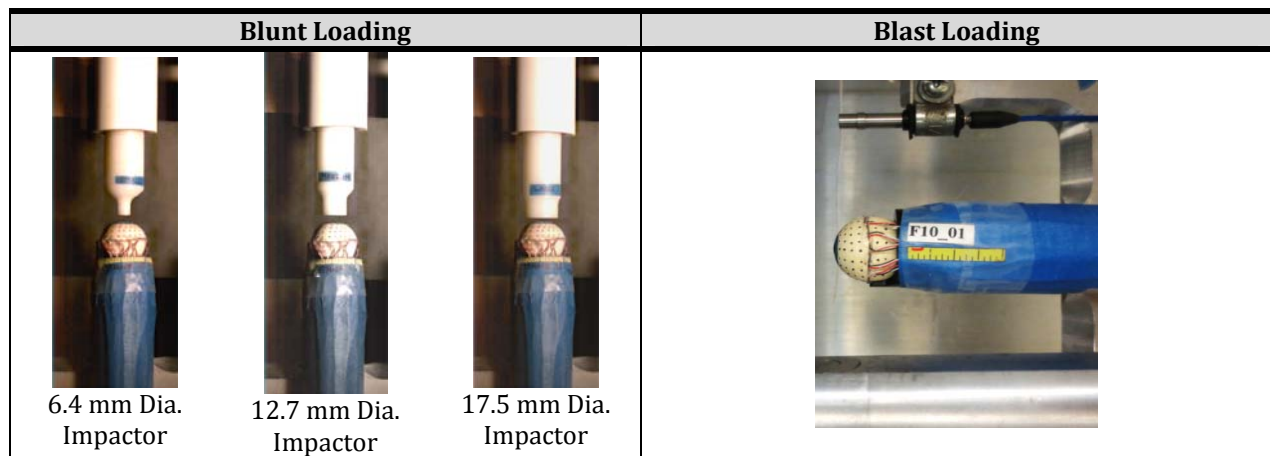
Figure 2: Blunt and blast loading experimental test setups for the area-sensitive eye.
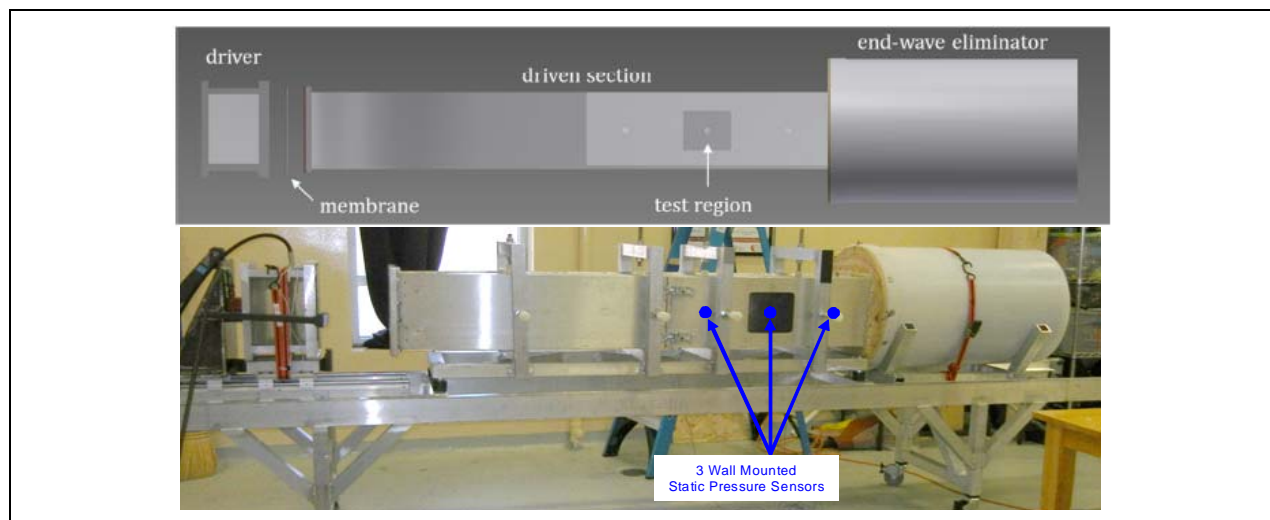
Figure 3: Schematic and photograph of gas-driven ABS.

Data Acquisition and Processing

All data were collected at 38 kHz for blunt tests and at 301.887 kHz for blast tests (TDAS PRO, Diversified Technical Systems, Inc., Seal Beach, CA). The standard TDAS PRO anti-aliasing filter was bypassed for the blast tests because the frequency content of the blast overpressure exceeded the 4,300 Hz cutoff frequency. However, the TDAS PRO sensor input modules (SIMs) bandwidth of 0-25 kHz acts as a low-pass filter with a frequency cutoff of 25 kHz. All pressure and load data were zeroed prior to the event. A custom MATLAB® script (version7.11.0.584 (R2010b), The MathWorks, Inc., Natick, MA) was used to quantify pulse parameters (peak pressure, positive duration, and positive impulse) for each sensor for all tests. High speed video of each test was captured at 1000 fps for blunt tests and 10 kfps for blast tests (v9.1, Vision Research, Wayne, NJ).

The array of pressure sensors was analyzed as a system; the simultaneous response of all nine pressure sensors was assessed for both peak pressure and positive duration in order to create characteristic response profiles for each loading condition. Normalized peak pressure was quantified by dividing the peak pressure from each channel by the maximum peak pressure value of all nine pressure sensors in the eye. Thresholds for positive duration and normalized peak pressure were quantified at values that were chosen to distinguish between blunt loading and blast loading.

Results

Figure 4 shows the response of the area-sensitive eye in both the blunt and blast test setups. Note the difference in peak pressure and duration for blunt and blast loading pulses. Figure 5 and Figure 6 show representative pressure traces for the nine sensor array during blunt and blast loading, respectively. These figures show characteristically different responses for blunt and blast loading. The notable differences in peak pressure and duration of the pulse indicate that these parameters can be used to distinguish between blunt and blast loading. Normalized peak pressure and positive duration for all tests are shown in Figure 7 and Figure 8, respectively. Thresholds for normalized peak pressure and positive duration are given in Table 1 and Table 2, respectively. Channel 7 of the nine-sensor array was excluded from the analyses presented herein, because it consistently responded differently from the three other sensors in the outer "ring". It is possible that this sensor was damaged during preparation of the area-sensitive eye.

Blunt and Blast Loading of the Area-Sensitive FOCUS Eye
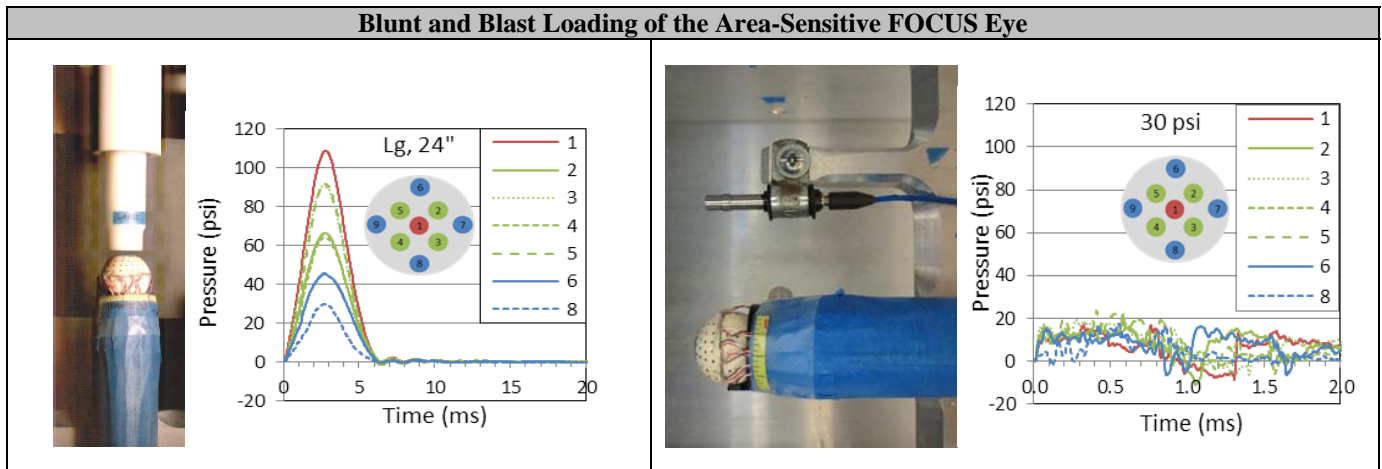
Figure 4: Area-sensitive FOCUS eye testing using the isolated eye test setup. Blunt tests were performed by directly impacting the cornea with three impactor sizes (Dia.= 6.4, 12.7, and 17.5mm) dropped at one of two heights to simulate a variety of energies. (Left) Blast tests were performed using an ABS and were conducted at 10 psi, 20 psi, and 30 psi.
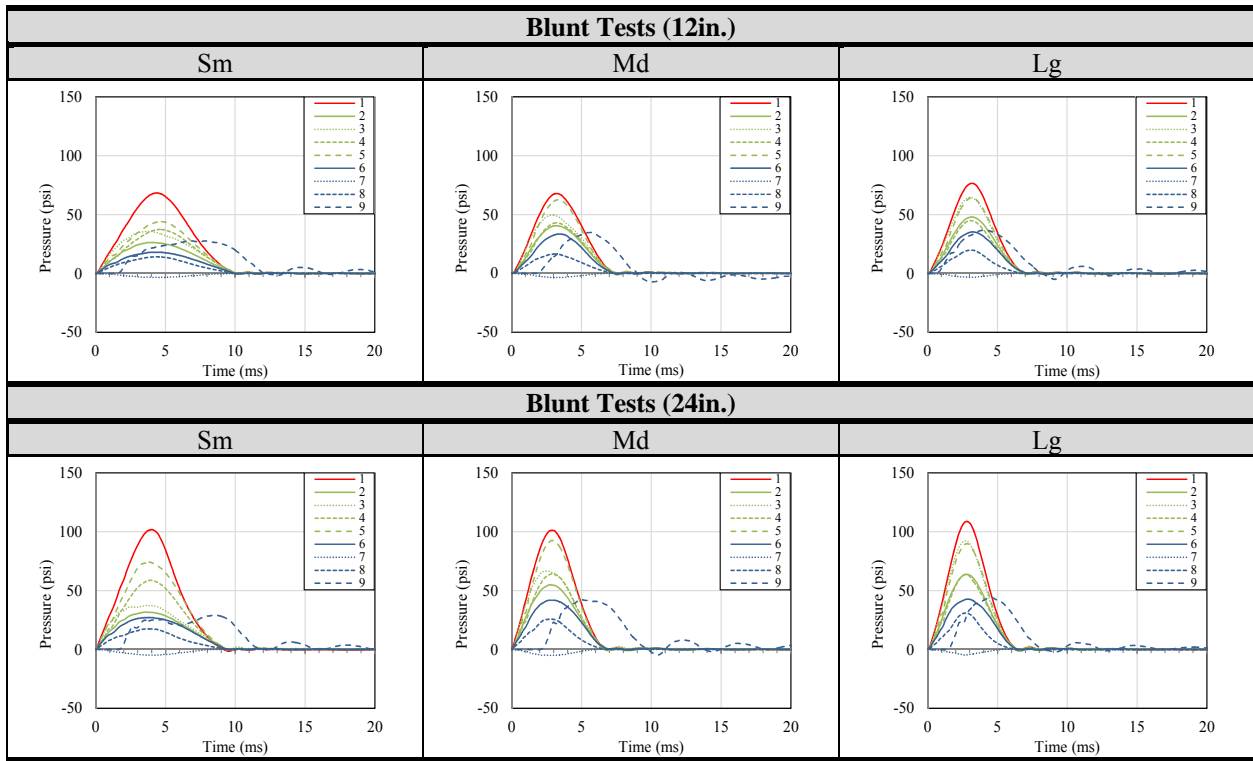
Figure 5: Characteristic responses of area-sensitive FOCUS eye sensors due to blunt loading.
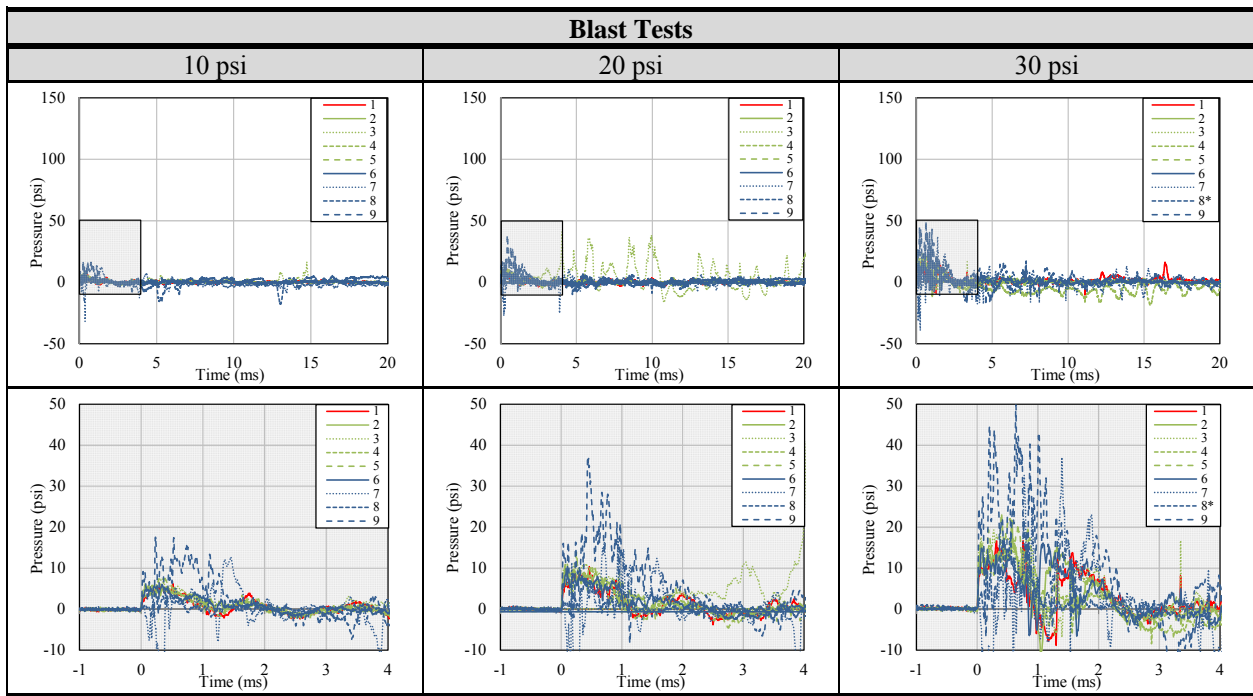
Figure 6: Characteristic responses of area-sensitive FOCUS eye sensors due to blast loading.
Note: Bottom graphs are zoomed in views of the blast event.
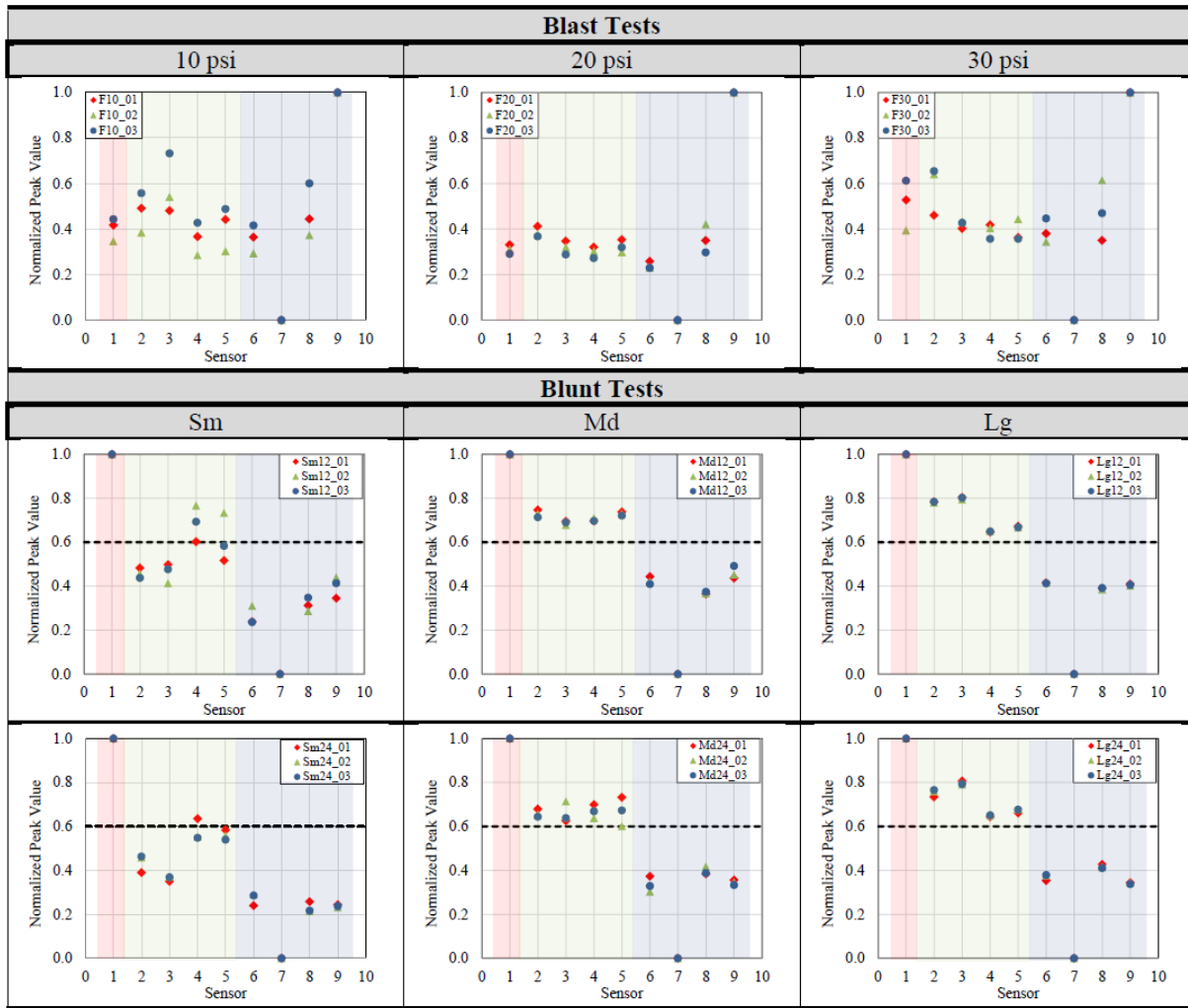
Figure 7: Normalized peak pressure for the area-sensitive FOCUS eye sensors.

Table 1: Normalized peak overpressure thresholds for area-sensitive FOCUS eye.

Blunt v. Blast Loading	
Blunt Loading	"Bullseye" loading with highest magnitude at center sensor.
Blast Loading	All sensors approximately same magnitude at same time.
Blunt Loading	
Small Projectile	Not all middle sensors above 60% maximum. All outer sensors below 60% maximum.
Medium Projectile	All middle sensors above 60% maximum. All outer sensors below 60% maximum.
Large Projectile	
Blast Loading	
10 psi	
20 psi	Cannot distinguish between chosen pressure levels.
30 psi	

Blast Tests

10 psi	20 psi	30 psi

Blunt Tests

Sm	Md	Lg

Figure 8: Positive duration for the area-sensitive FOCUS eye sensors.

Table 2: Normalized peak overpressure thresholds for area-sensitive FOCUS eye.

Blunt v. Blast Loading	
Blunt Loading	Duration >3 ms.
Blast Loading	Duration <3 ms.
Blunt Loading	
Small Projectile	Duration >9ms.
Medium Projectile	Duration <9ms.
Large Projectile	
Blast Loading	
10 psi	Cannot distinguish between chosen pressure levels.
20 psi	
30 psi	

Summary

Overall, the area-sensitive eye designed and assessed in this study serves as a proof of concept that a biofidelic, area-sensitive, eye for an advanced anthropomorphic test device can distinguish between blunt and blast loading as well as between various impactor sizes for blunt impacts. This is an improvement beyond the abilities of the current FOCUS eye, which relies solely on load measured during loading to predict injury risk. Based on blunt testing with direct impacts to the cornea and blast testing with a forward-facing orientation to the shock wave, the current area-sensitive eye can distinguish between blunt and blast loading based on the characteristic response of the nine-sensor array. Normalized peak overpressure of the nine sensor array can be used to further distinguish between impactor sizes less than and greater than 12.70 mm in diameter. It is possible that additional sensors may provide sensitivity to further distinguish between additional projectile sizes. Furthermore, testing the area-sensitive eye within the FOCUS headform will provide a more realistic response of the eye to various loading.

TASK 1.3: BLAST EYE MODELING/ BLAST EYE INJURY CRITERIA

EXPERIMENTAL TESTING USING AN ADVANCED BLAST SIMULATOR

Effect of Boundary Conditions on the Response of Unprotected Porcine Eyes during Blast Overpressure Exposure

Background

While it is suggested that blast overpressure can cause eye injuries, there is no data in the literature that confirms primary blast overpressure as an eye injury mechanism. Previous testing was performed on isolated human eyes to facilitate the direct quantification of the eye response to blast overpressure. These tests used fireworks to simulate low-level blasts with peak static overpressures up to 6.0 psi, peak total overpressures up to 8.3 psi, and positive durations of approximately 0.25 ms. It was concluded that at these energy levels, no observable eye injuries were caused by overpressure exposure. However, the blast energy levels were very low in this study and there were no reflective surfaces around the eye. Due to the paucity of studies in the literature that specifically examine the response of the eye to primary blast overpressure exposure, it is paramount to examine higher level blast overpressures and to assess the effect of both orbital and facial geometries surrounding the eye. Therefore, the objectives of this study are twofold: 1) quantify eye response and injuries caused by survivable primary blast overpressures, and 2) examine the effect of increasing biofidelity of the boundary conditions surrounding the eye during blast overpressure exposure. To fulfill these objectives, a series of experiments were developed to systematically evaluate the effects of orbital boundary conditions on the response and injury tolerance of the eye at increasing blast overpressure energy levels. Overall, data from these experiments will shed light on the likelihood of primary blast overpressure to cause eye injuries and will provide data that is critical to the validation of both physical and computational models of the eye specifically designed for blast loading scenarios.

Methods

Advanced Blast Simulator (ABS)
All blast overpressure tests were conducted using the small VT Advanced Blast Simulator (ABS) and aluminum membranes (Figure 9). The helium gas-driven ABS (aka shock tube) was used to create a blast overpressure waves that simulates free-field conditions. Briefly, the helium gas-driven ABS consists of equally shaped "driver" and "driven" sections separated by a frangible aluminum membrane. The driver section is pressurized with helium gas until the membrane passively ruptures and sends a burst of gas down the driven section. As the gas compresses upon itself, a shock-front forms and the shock wave propagates through the tube. The small VT

ABS is specifically designed for testing small specimens, and is able to produce peak overpressures up to approximately 30 psi (static overpressure) with a positive duration around 2.5 ms. The ABS eliminates the need for using high energy explosives and does not result in projected material, thereby allowing for the study of the isolated effect of overpressure on the eye. Static overpressure was measured along the wall using three high frequency response pressure sensors (Model 102B15, PCB Piezotronics, Depew, NY) mounted flush to the inside wall of the tube. These sensors are located 12 in apart from each other, with the middle sensor located at the test region. Shock wave velocity can be quantified using the time of arrival of the shock wave at these sensors.
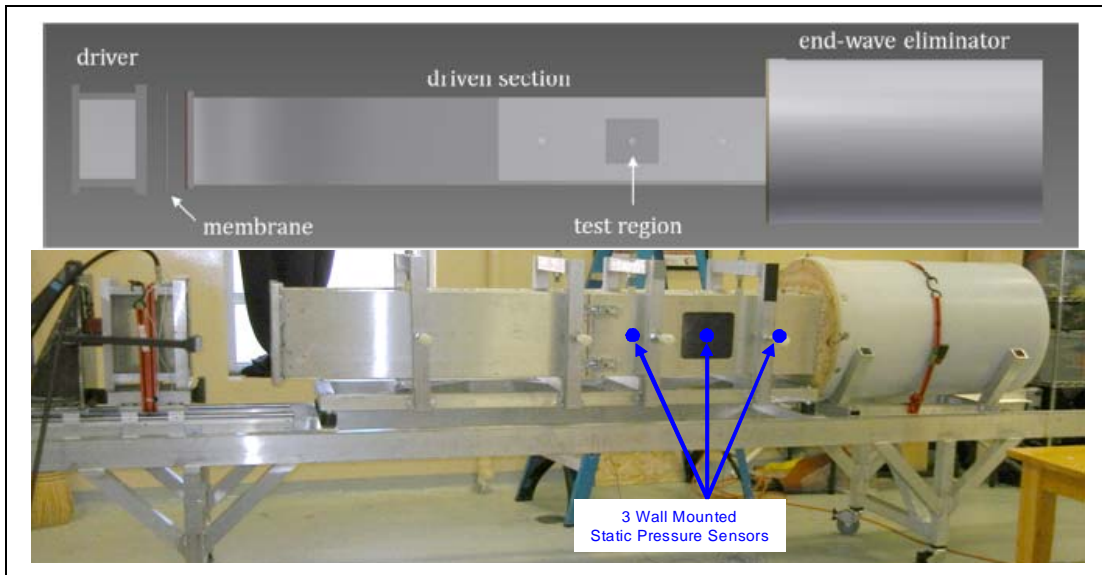
Figure 9: Schematic and photograph of gas-driven ABS.

Over 150 tests were conducted using three aluminum alloy membranes (3003, 2024, 7075) in order to determine the parameters required to obtain the desired peak static overpressures of 10 psi, 20 psi, and 30 psi at the test section. Membrane thickness, scoring depth, and helium tank regulator pressure were systematically modified to achieve the desired peak pressures at the test section. Two aluminum alloys were chosen for the membranes based on the resulting peak overpressure and pressure trace shape. A 25 mil thick aluminum 3003 plate with a 7 mil depth "X" pattern reliably produced a peak overpressure of 10 psi in the test section (Figure 10-Left). A 20 mil thick aluminum 2024 plate with an 8 mil depth "X" pattern reliably produced a peak overpressure of 20 psi in the test section (Figure 10-Middle). A 32 mil thick aluminum 2024 plate with a 14.5 mil depth "X" pattern reliably produced a peak overpressure of 30 psi in the test section (Figure 10-Right).

10 psi: Al 3003-25 mil**,** 7 mil depth "X" pattern, 300 psi pressure regulator

20 psi: Al 2024-20 mil**,** 8 mil depth "X" pattern, 400 psi pressure regulator

30 psi: Al 2024-32 mil**,** 14.5 mil depth "X" pattern**,** 500 psi pressure regulator
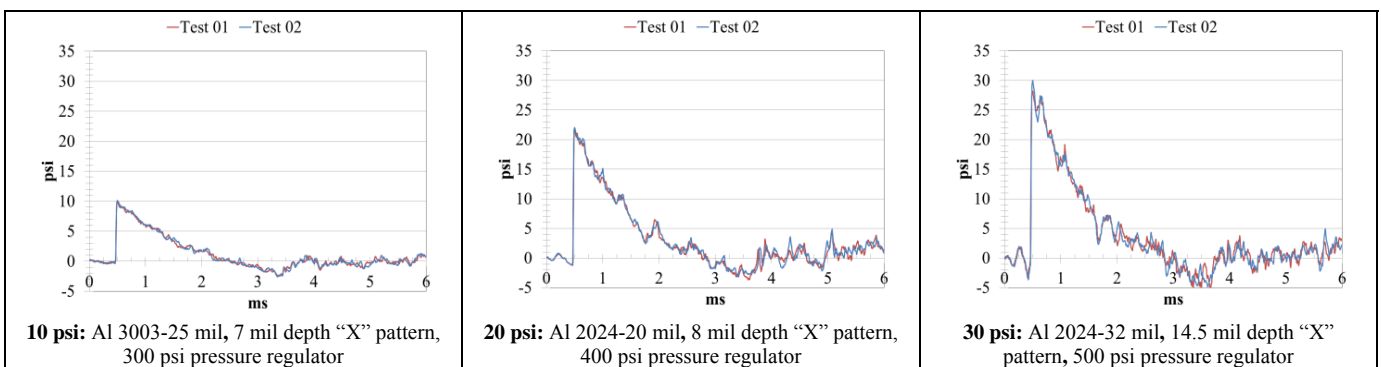
Figure 10: Representative pressure traces for 10 psi, 20 psi, and 30 psi peak static overpressures measured along the wall at the test region during empty tube tests. Membrane characteristics are noted below each plot.

Porcine Eye Procurement and Preparation

A total of 88 porcine eyes were used in this study (Table 3). Fresh porcine eyes were shipped overnight on wet ice, stored in a refrigerator, and tested within three days of slaughter (Animal Technologies, Tyler, TX, USA). Control eyes were used to assess postmortem effects and damage from tissue procurement. Sham eyes were used to quantify potential injuries from pre-test preparation techniques, including the insertion of a pressure sensor and pressurization tube into the eye through the optic nerve and setting the eye in a rigid concave cup or in gelatin. All eyes were prepared with the following technique. Skin and musculature was removed to expose only the globe and optic nerve. Cornea clarity was qualitatively assessed (clear, not clear), and visibility of the "Y" suture on the lens was noted. Fluorescein dye was applied to the cornea and a blue light was used to help visualize corneal abrasions. Any existing corneal abrasions were noted. Control eyes were dissected at this point to assess and quantify baseline damage to the eye caused by postmortem degradation and procurement from the abattoir. The remaining eyes were further prepared by applying a dot pattern on the surface of the sclera using permanent black ink. A miniature pressure sensor (Model 060S, 100 psi, Precision Measurement Company, Ann Arbor, MI) and a small tube were inserted through the optic nerve into the vitreous fluid and secured in place using a cable tie. A bag of Lactated Ringer's solution was connected to the small tube and suspended 8 in. above the eye to provide normal physiologic pressure to the eye during the duration of testing (0.29 psi or 14.95 mmHg). Intraocular pressure was measured before and after each test using a veterinary tonometer (Tono-Pen AVIA Vet® Veterinary Tonometer, Reichert Technologies, Depew, NY, USA). Due to minor variations, measurements were taken using the tonometer until three sequential measurements recorded the same IOP at a 95% confidence.

Unprotected Eye Test Conditions

Eyes were placed in one of three boundary conditions ("Isolated Eye", "Synthetic Orbit", "3D Orbit") and exposed to a single blast event at 10 psi, 20 psi, or 30 psi static overpressure (Figure 11). The synthetic orbit and the 3D Orbit represented the left orbit geometry. These pressure levels were chosen to examine the effects of increasingly severe, yet survivable blast events (Stuhmiller et al., 1991). The three boundary conditions surrounding the eye were tested to assess the effects of increasing biofidelity of the orbit and facial geometries. Each test condition is designed to provide critical information for the subsequent condition, thereby systematically fulfilling the objectives and answering questions posed by this research. Tests were conducted on isolated eyes to understand how the pressure wave propagates through the eye tissue with no surrounding structures. Tests were also conducted on eyes were potted in two orbits of varying complexity and biofidelity to simulate the *in situ* boundary conditions around the eye, i.e., a synthetic orbit with a simplified geometry and a 3D printed orbit modeled after a realistic human facial geometry.
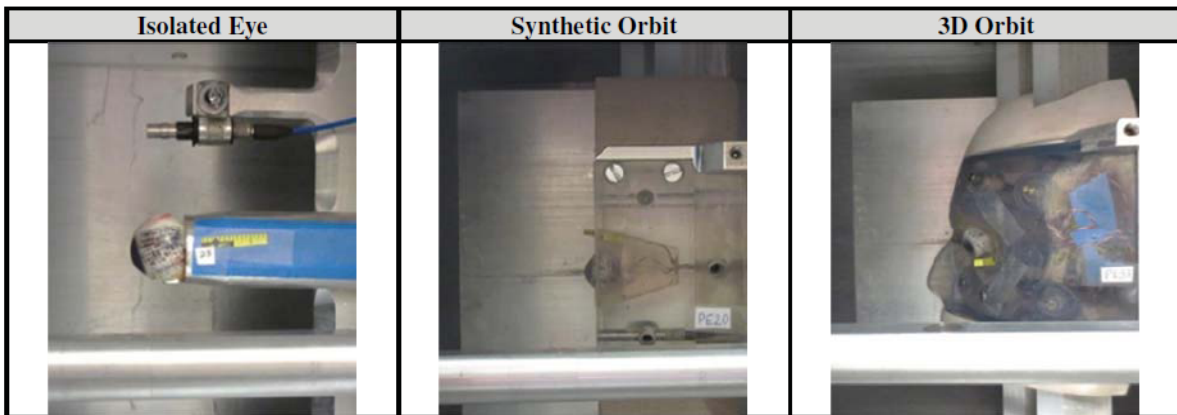
Figure 11: Unprotected eye experimental test setups: (left) isolated eye, (middle) synthetic orbit, and (right) 3D orbit.

Table 3: Unprotected Eye Test Matrix.

Control	Sham	Isolated Eye	Synthetic Orbit	3D Orbit
Quantify damage from postmortem degradation and procurement	Quantify damage from preparation methods	Quantify isolated eye response with no reflected surfaces	Quantify response with simplified orbit using flat reflective surfaces	Quantify response with human orbit using complex reflective surfaces
16 eyes	8 eyes in isolated 16 eyes in gelatin	5 eyes at 10 psi 6 eyes at 20 psi 4 eyes at 30 psi	5 eyes at 10 psi 6 eyes at 20 psi 5 eyes at 30 psi	6 eyes at 10 psi 5 eyes at 20 psi 6 eyes at 30 psi

The isolated eye test condition was designed to isolate the eye from the orbital bones, muscle, and fat. The isolated eye test experimental setup consisted of a rigid concave cup with a hole in the back through which the optic nerve, IOP sensor, and pressurization tube could pass (Figure 12). The rigid concave cup was designed to provide support for the eye during the test, and provided minimal reflective surfaces around the eye. Approximately one third of the posterior portion of the eye contacted the concave cup. Eyes were prepped with the experimental apparatus oriented vertically, such that the cornea faced the ceiling, so that only gravity affected the eye and no additional tension was placed on the optic nerve or the back of the eye. An alligator clip attached to the cable tie held the eye in place. When the experimental apparatus was rotated such that it was oriented horizontally for testing, the eye loosely rested on a small ledge to prevent drooping. A miniature pressure sensor was inserted into the eye through the optic nerve to quantify intraocular pressure (IOP). A sensor was placed in the flow field above the eye at a location that matches the reflected pressure sensor (face-on pressure sensor) in the synthetic orbit and close to the location of the top middle sensor in the 3D orbit. Static overpressures were measured at three locations on the wall of the ABS (Model 102B15-100psi, PCB Piezotronics, Depew, NY) (12 inches ahead of the test region, at the test region, and 12 inches behind the test region). Static overpressure was also measured in the flow field using a pencil sensor (Model 137A24-250psi, PCB Piezotronics, Depew, NY) approximately two inches away from the orbit.
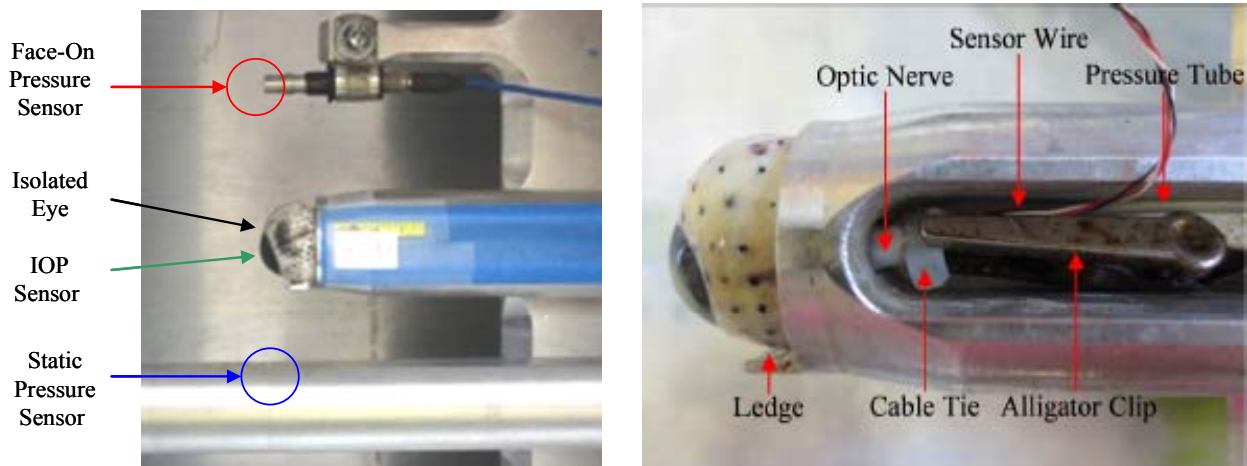
Figure 12: Isolated eye experimental setup.

The synthetic orbit experimental setup consisted of a clear orbit, plane of symmetry, and first-order approximations of the forehead and chin (Figure 13). The plane of symmetry (PoS) was added along the nasal side of the synthetic orbit to prevent unrealistic pressure relief around the nose. Each eye was potted in a synthetic orbit with 10% Knox gelatin to simulate the fat/musculature around the eye. This was done by first suspending the eye was within the orbit using fishing line, with approximately one third of the anterior portion of the eye exposed. A 10% Knox® gelatin solution was then poured around the eye within the orbit. The orbit was refrigerated for at least minutes to allow the gelatin to set. A miniature pressure sensor that inserted into the eye through the optic nerve was used to quantify intraocular pressure (IOP). Reflected pressure (i.e., face-on pressure) was measured at the forehead of the synthetic orbit using a pressure sensor orthogonal to the pressure wave (Model 113B21-200psi, PCB Piezotronics, Depew, NY). Static overpressures were measured at three locations on the wall of the ABS (Model 102B15-100psi, PCB Piezotronics, Depew, NY) (12 inches ahead of the test region, at the test region, and 12 inches behind the test region). Static overpressure was also measured in the flow field using a pencil sensor (Model 137A24-250psi, PCB Piezotronics, Depew, NY) approximately two inches away from the orbit. Four pressure sensors (Model 060S, 100 psi, Precision Measurement Company, Ann Arbor, MI) were also mounted to the walls inside the orbit (Figure 14). There was a small hole in the back of the orbit to allow the IOP sensor, orbit sensors, and pressurization tube to pass through.
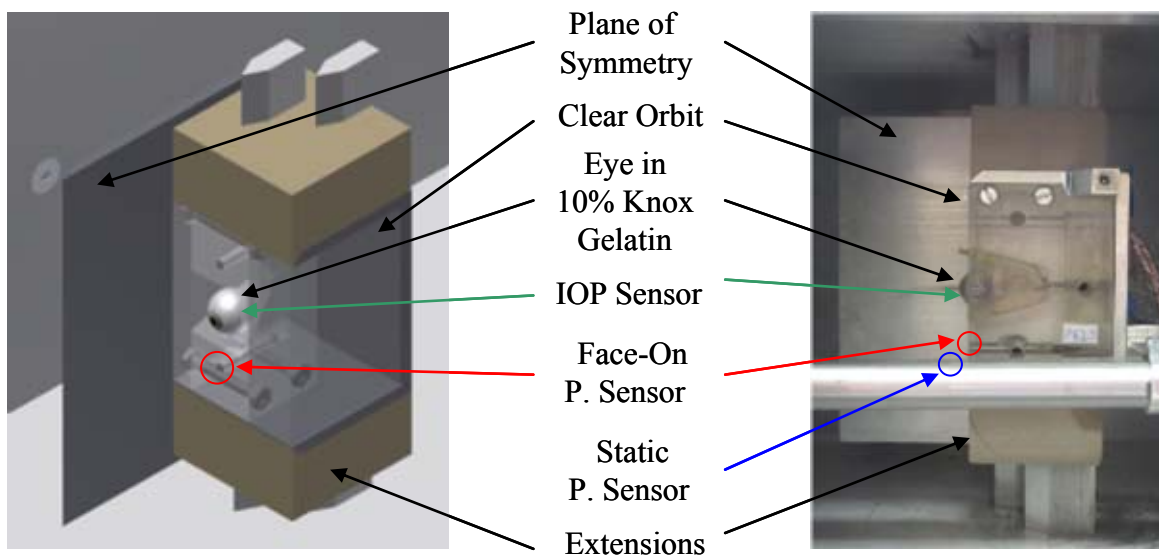
Figure 13: Synthetic orbit experimental setup.

Front View   Side View
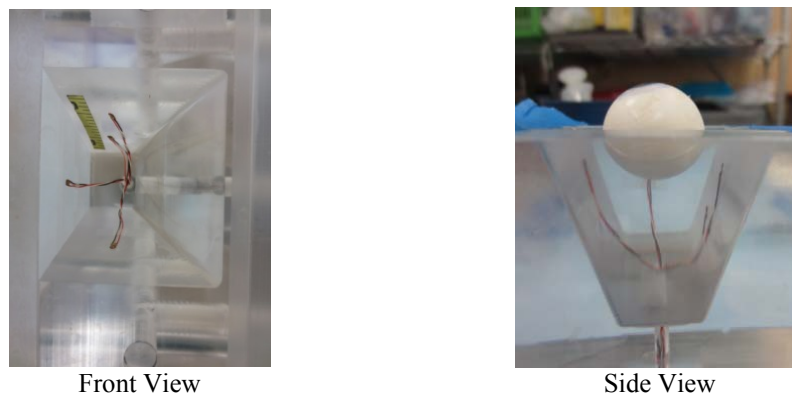
Figure 14: Miniature pressure sensors mounted to the synthetic orbital walls.

The 3D orbit was created from the 50th percentile male Global Human Body Models Consortium (GHBMC) Finite Element Model (FEM) skull and skin CAD geometry (Figure 15). Therefore, this model simulates physiologic facial anatomy around the eye, including the nose and skin thickness, of a 50th percentile male. To generate the printed orbit, a rectangle of the surface geometry of the skull and skin was centered about the left orbit to create a block with an accurate outer skin and inner orbit surface. The small area surrounding the eye was designed to be modeled separately using a clear material with properties similar to skin. The rest of the 3D orbit was manufactured via a high quality stereolithography (SLS, 0.005" layer thickness, +/- 0.015" tolerances). The fixture was made of a clear polymer similar to polycarbonate and then hand finished with a two part clear coat for optical clarity. The model contains seven mounting ports for PCB pressure sensors, which were designed to be normal to and flush with the outer surface. Three sensor ports were placed superior and inferior to the orbit with an additional port located on the bridge of the nose. In addition to the 3D printed orbit fixture, open and closed eyelid flesh geometries were created. The production of silicone flesh surrogate plugs was found to be difficult and expensive. Therefore, two negative eye skin molds were designed and manufactured to cast the eyelid skin from gelatin. The negative molds were designed to be mounted to the fixture using three of the sensor ports and several screws, thereby enclosing the eye and orbit. Each custom negative eye skin orbit mold contains an exhaust port and a filling cylinder. This allows for Knox gelatin to be injected in the orbit to fill the remaining space around the eye. Once the gelatin cures, the mold can be removed and the sprue cut off.

(a) Final CAD drawings (left) and printed (right) 3D orbit without eyelid molds

(b) Final CAD drawings of open eyelid (left) and closed eyelid (right)

(c) Final CAD drawing (left) and printed (right) negative eyelid molds

(e) Final CAD drawing (left) and printed (right) 3D orbit with open eyelid negative mold installed
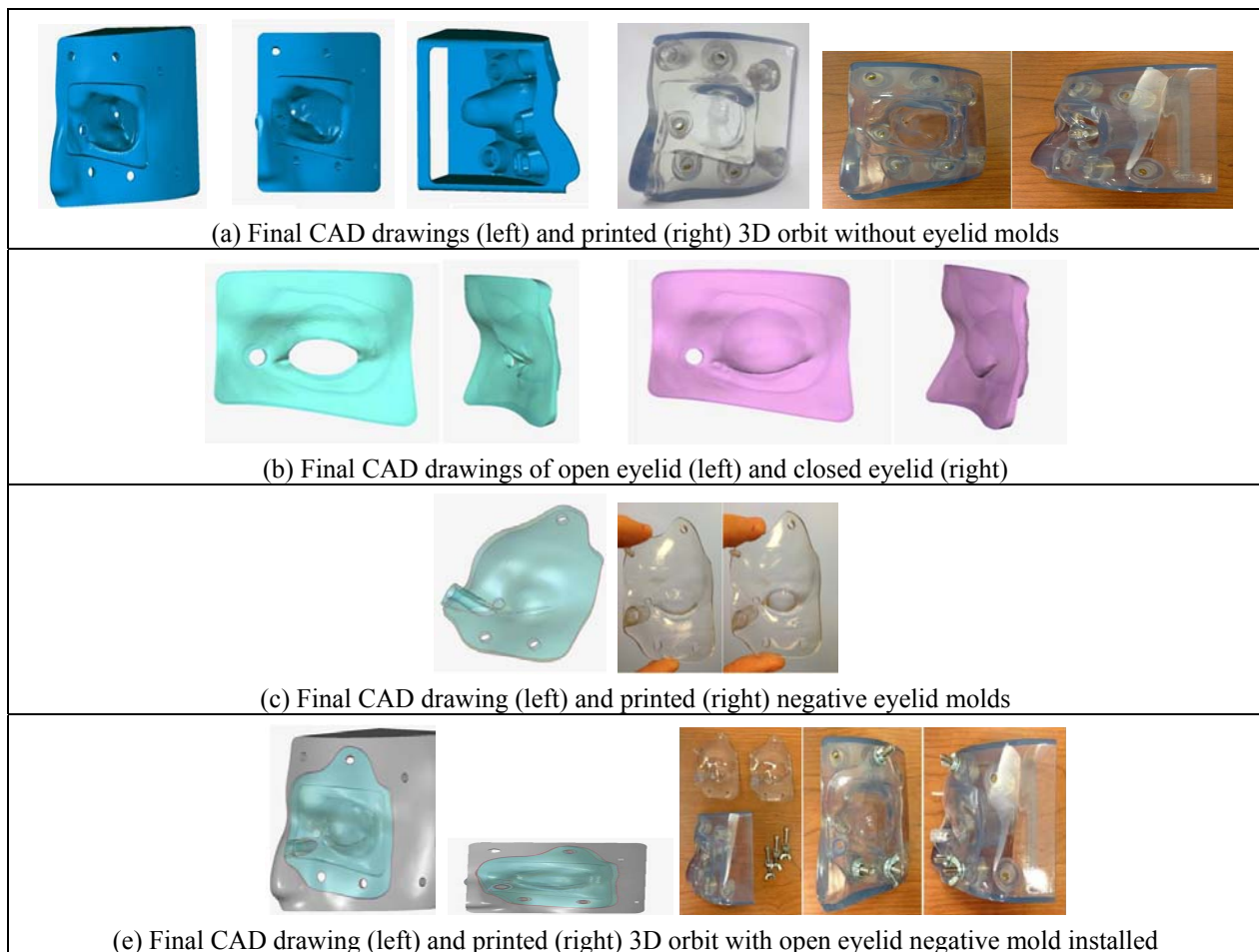
Figure 15: Design and fabrication of 3D printed orbit.

A technique was developed to consistently pot an eye in the 3D printed orbit. As the 3D printed orbit is an exact replica of the human facial anatomy around the eye, including the nose and skin thickness, it requires a mold over the eye to generate either an open or closed eyelid (Figure 15-Top Left). In order to pot the eye in the orbit, fishing line was suspended around the eye to hold it in place. Then the negative eyelid skin mold for an open eyelid was secured to the orbit using three screws placed through the pressure sensor ports (Figure 15-Bottom Left). A 10% solution of Knox gelatin was then poured around the eye, using a filling cylinder in the mold, and allowed to gel in a refrigerator. The 10% gelatin solution is used to simulate the skin, fat, and musculature around the eye (Figure 15- Middle and Right). Once the gelatin cured, the mold and the fishing line were removed. Finally, the sprue, *i.e.* the small cylinder of excess material attached to the poured surface along the input tunnel, was cut off.

Figure 15: (Left, top) Open eyelid mold. (Left, bottom) Open eyelid mold bolted to 3D orbit. (Middle, Right) 3D printed orbit with 10% gelatin solution to simulate skin, fat, and musculature

The final orbit and mounting bracket was modified by installing superior and inferior extensions to the clear orbit fixture to improve blast wave propagation (Figure 16). The extensions were created using the same facial geometry as the orbit fixture and modeled to fit over the aluminum mounting bracket and vertical mounting plates, which have a leading edge. The two blocks were created as solid models using our in house Z-Corp 350 rapid prototyping machine (Figure 17). To prepare them for testing, they were hand finished and sealed with a cyanoacrylate adhesive. They were then test fit with the existing system in preparation for testing (Figure 18).
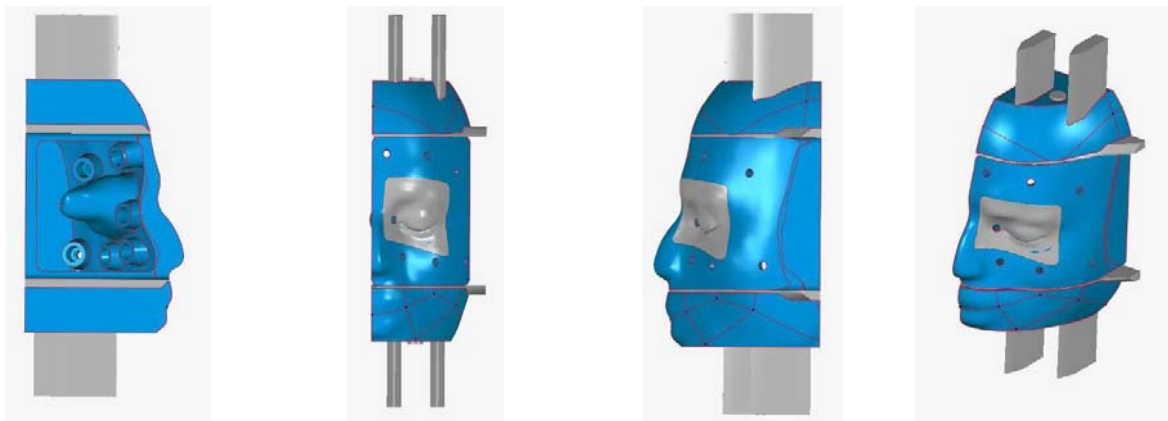
Figure 16: CAD model of 3D orbit, orbit mounting bracket, vertical mounting plates, and extensions.

Figure 17: Superior and inferior 3D fixture extension blocks after printing, hand finishing, and sealing. Superior and inferior surfaces (left), internal surfaces (center), anterior surfaces (right).
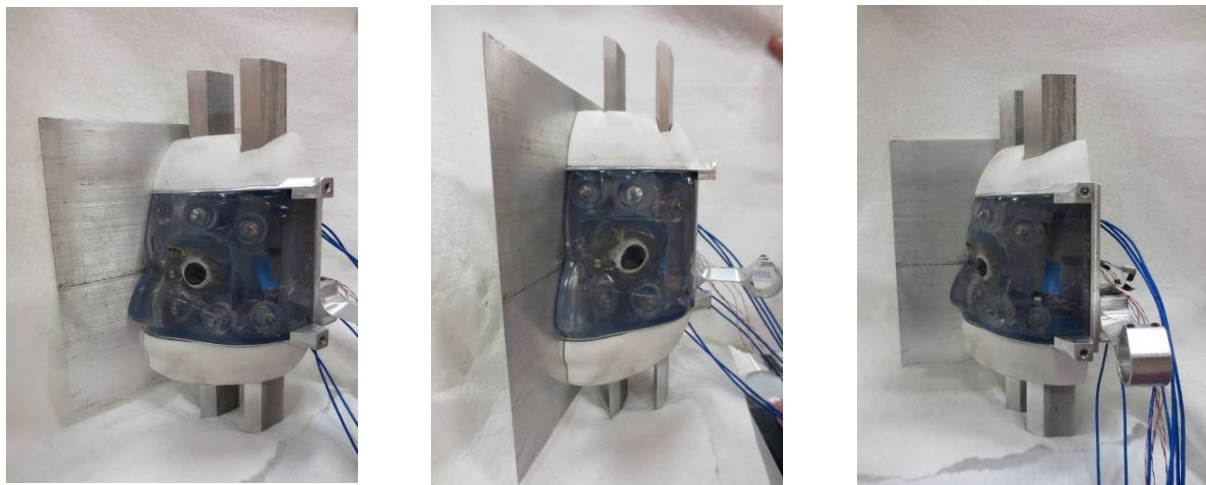
Figure 18: Extension blocks on full fixture set up. This includes the clear orbit fixture, plane of symmetry, orbit mounting bracket, vertical mounting plates, extension blocks, pressure sensors, porcine eye, and silicon orbit flesh surrogate.

The final design of the 3D orbit experimental setup consisted of a clear orbit, plane of symmetry, and extensions representing the forehead and chin (Figure 19). The plane of symmetry (PoS) was added along the nasal side of the 3D orbit to prevent unrealistic pressure relief around the nose. Reflected pressure (i.e., face-on pressure) was measured by seven pressure sensors (Model 113B21-200psi, PCB Piezotronics, Depew, NY) located on the surface of the skin of the 3D orbit geometry using pressure sensors, which are normal to and flush with the outer surface. These were labeled 'nasal', 'top medial', 'top middle', 'top temporal', 'bottom medial', 'bottom middle', and 'bottom temporal'. All sensing elements were flush with the external geometry of the 3D orbit. The nasal sensor was located adjacent to the eye. The top and bottom sensors are located on the forehead and chin, respectively. Static overpressures were measured at three locations on the wall of the ABS (Model 102B15-100psi, PCB Piezotronics, Depew, NY) (12 inches ahead of the test region, at the test region, and 12 inches behind the test region). Static overpressure was also measured in the flow field using a pencil sensor (Model 137A24-250psi, PCB Piezotronics, Depew, NY) approximately two inches away from the orbit. Four pressure sensors (Model 060S, 100 psi, Precision Measurement Company, Ann Arbor, MI) were also mounted to the walls inside the orbit (Figure 20). There was a small hole in the back of the orbit to allow the IOP sensor, orbit sensors, and pressurization tube to pass through.
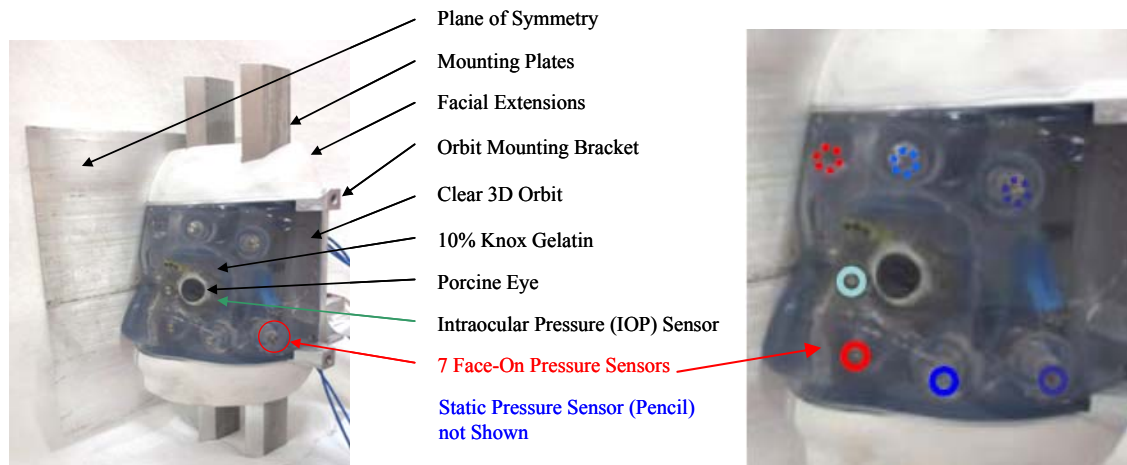
Figure 19: 3D printed orbit experimental setup.

| Front View | Side View |
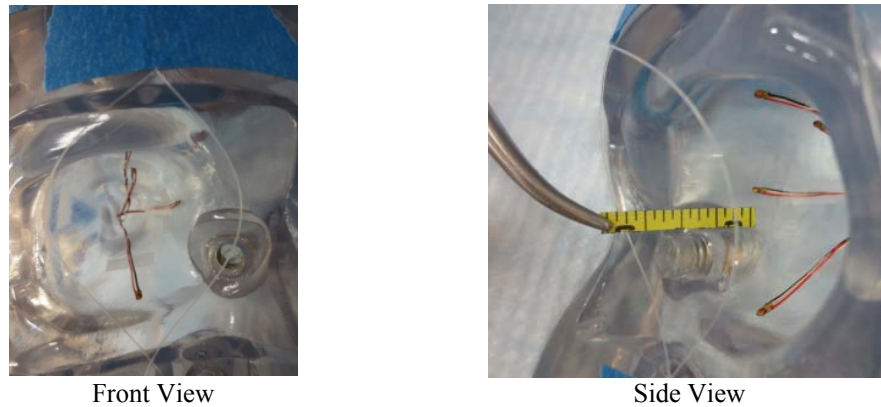
Figure 20: Miniature pressure sensors mounted to the 3D orbital walls.

Data Acquisition and Processing

All data were collected at 301.887 kHz (TDAS PRO, Diversified Technical Systems, Inc., Seal Beach, CA). The standard TDAS PRO anti-aliasing filter was bypassed because the frequency content of the blast overpressure wave exceeded the 4,300 Hz cutoff frequency. However, the TDAS PRO sensor input modules (SIMs) bandwidth of 0-25 kHz acts as a low-pass filter with a frequency cutoff of 25 kHz. All pressure data were zeroed prior to the event. High speed video of each test was captured at 20 kfps (v9.1, Vision Research, Wayne, NJ). Movement of a string hung from the top of the tube located near the eye was used to quantify the time of arrival of the shock wave using high speed video analysis.

A custom MATLAB® (version 7.11.0.584 (R2010b), The MathWorks, Inc., Natick, MA) script was used to quantify the shock wave characteristics of each pressure sensor location (time of arrival, peak overpressure, positive duration, and positive impulse). Pressure measured inside the driver was used to quantify the time at which the membrane burst, which was considered t=0. Time of arrival (ToA) for each sensor location was based on the time of membrane rupture. Peak overpressure was defined as the maximum pressure value recorded during the test. Positive duration was defined as the time interval between initiation of positive overpressure and the time at which overpressure returned to zero. Impulse was defined as the area under the positive portion of the pressure-

time history. A one-way ANOVA was conducted on the average peak IOP, positive duration, and positive impulse for each boundary condition with tukey-kramer multiple comparison test to determine significance between groups with a $p < 0.05$.

Peak intraocular pressure was correlated to peak static overpressure measured at the wall and within the flow field. Peak intraocular pressure was also correlated to peak total (isolated eye test condition only) or peak reflected overpressure (synthetic and 3D orbit conditions only). Further, peak static pressure measured at the wall was correlated to peak overpressure measured in the fluid flow.

Injury Assessment

Injuries were assessed in two ways. First, gross dissection of each eye following the test was used to quantify physical damage to the tissues and structures of the eye. Second, injury risk for physiologic injuries was calculated using the peak intraocular pressure measured for each test. Specific methods for each of these techniques are described below in further detail.

All eyes were dissected using the following technique (Figure 16). The cornea and sclera were examined for damage. Fluorescein dye was reapplied to the cornea and a blue light was used to help visualize any new corneal abrasions incurred during preparation and testing. The cornea was cut off to expose the iris and anterior portion of the lens. The iris was cut away to expose the anterior sides of the ciliary body, zonules, and lens. Damage to these structures was noted. Using a surgical microscope, damage to the zonules was further assessed by gently pushing on the lens with a Q-tip and tugging on iris flap contralateral to the zonules being examined. The eye was then bisected to expose the retina and the posterior sides of the ciliary body and lens. A dissection microscope was used to magnify and examine these structures in detail, as many were not visible to the naked eye. Photographs were taken of each step of the dissection. Any damage that may have been caused by dissection techniques was noted.
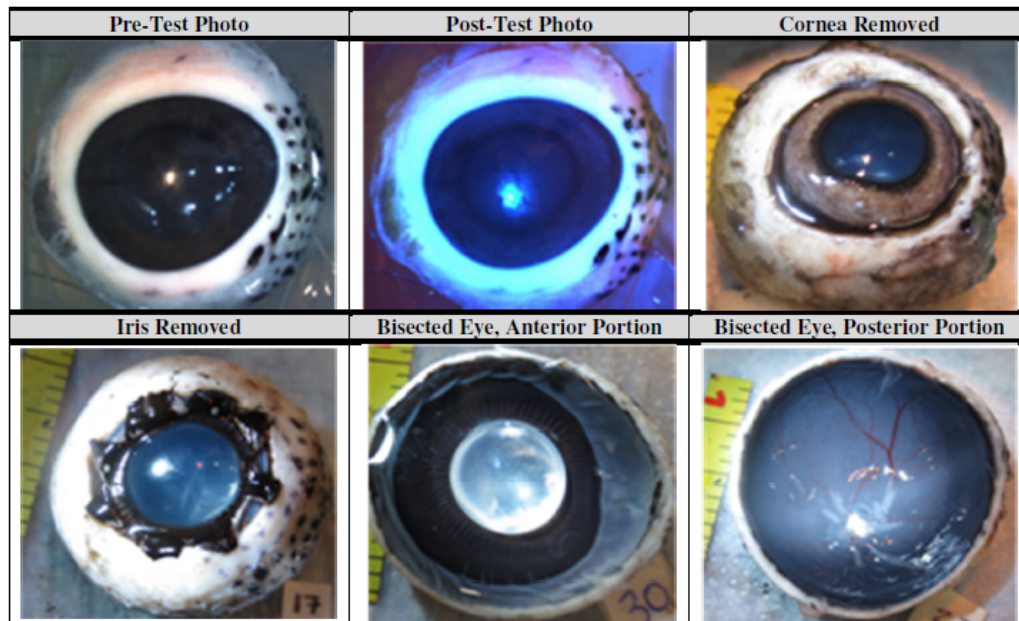
Figure 16: Photographs from gross dissection of porcine eyes.

It should be noted that the retina is especially sensitive to postmortem effects, most notably, detachment due to the lack of blood flow and constant physiologic intraocular pressure. As such, the retina was examined in the current study, but no retinal injuries were conclusively identified as being a result of exposure to blast overpressure to due to presence of retinal injuries in both control and sham eyes (Figure 17). Other structures such as the cornea, iris, zonules, ciliary body, and lens that are less prone to postmortem effects were assessed for potential blast-induced injury.
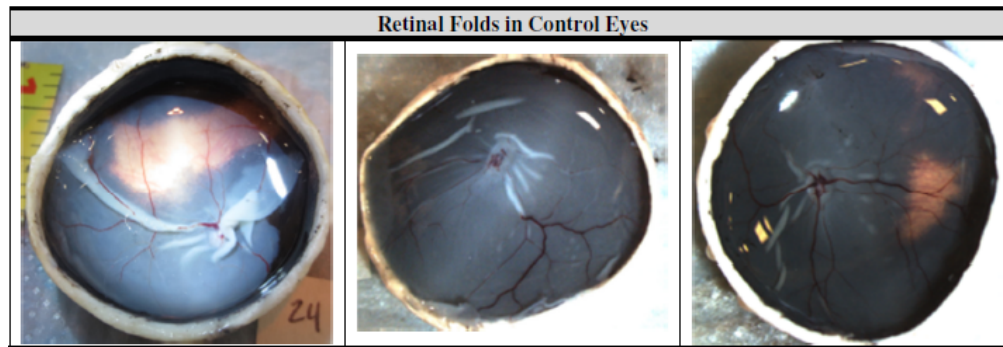
Figure 17: Retinal folds in control eyes.

Injury risk curves for projectile impacts exist for the prediction of hyphema, lens damage, retinal damage, and globe rupture using normalized energy (Kennedy et al., 2011). Normalized energy is defined as the kinetic energy of an impacting object divided by the projected area of the object. Neither kinetic energy nor projected area could be calculated for blast scenarios because blast loading is inherently different from projectile loading. Therefore, NE was quantified using three published correlations between IOP and NE that were developed based on projectile impacts to the eye (Duma et al., 2012). Normalized energy was quantified for each of the three correlations based on the projectile diameters: 6.35 mm, 9.25 mm, and 11.15 mm. As the current test series was designed to study the effect of blast on an unprotected eye, the 11.15 mm diameter projectile correlation was used for the final injury risk prediction. This was chosen because the area of an open eye affected by a blast, i.e., the area of the eye not covered by the eyelid, is most similar to the projected area of the 11.16 mm diameter rod. However, the two remaining correlations were also used to predict injury risk for comparison and to provide a more conservative injury risk prediction.

Results

Overall, peak overpressures increased as the test pressure level increased for all three boundary conditions. Average ± 1 standard deviation pressure-time histories for static (in flow), and total or reflected overpressure are shown for each boundary condition in Figure 18. A secondary peak at ~0.25 ms in the static overpressure trace was exacerbated with the addition of the PoS for the synthetic and 3D orbits. Average ± 1 standard deviation pressure-time histories for IOP are shown for each boundary condition in Figure 19. Correlations between peak overpressure (static, total, and reflected) and peak IOP are also shown for each test condition in Figure 19. Figure 20 shows the average peak shock wave parameters (peak IOP, positive duration, and positive impulse) for all three boundary conditions. Peak IOP was significantly higher for the synthetic orbit than for the isolated eye at the 20 psi level. Positive duration and positive impulse were not significantly different for any of the boundary conditions. Correlations between static overpressure measured at the wall and static overpressure measured in the fluid flow are shown in Figure 21.
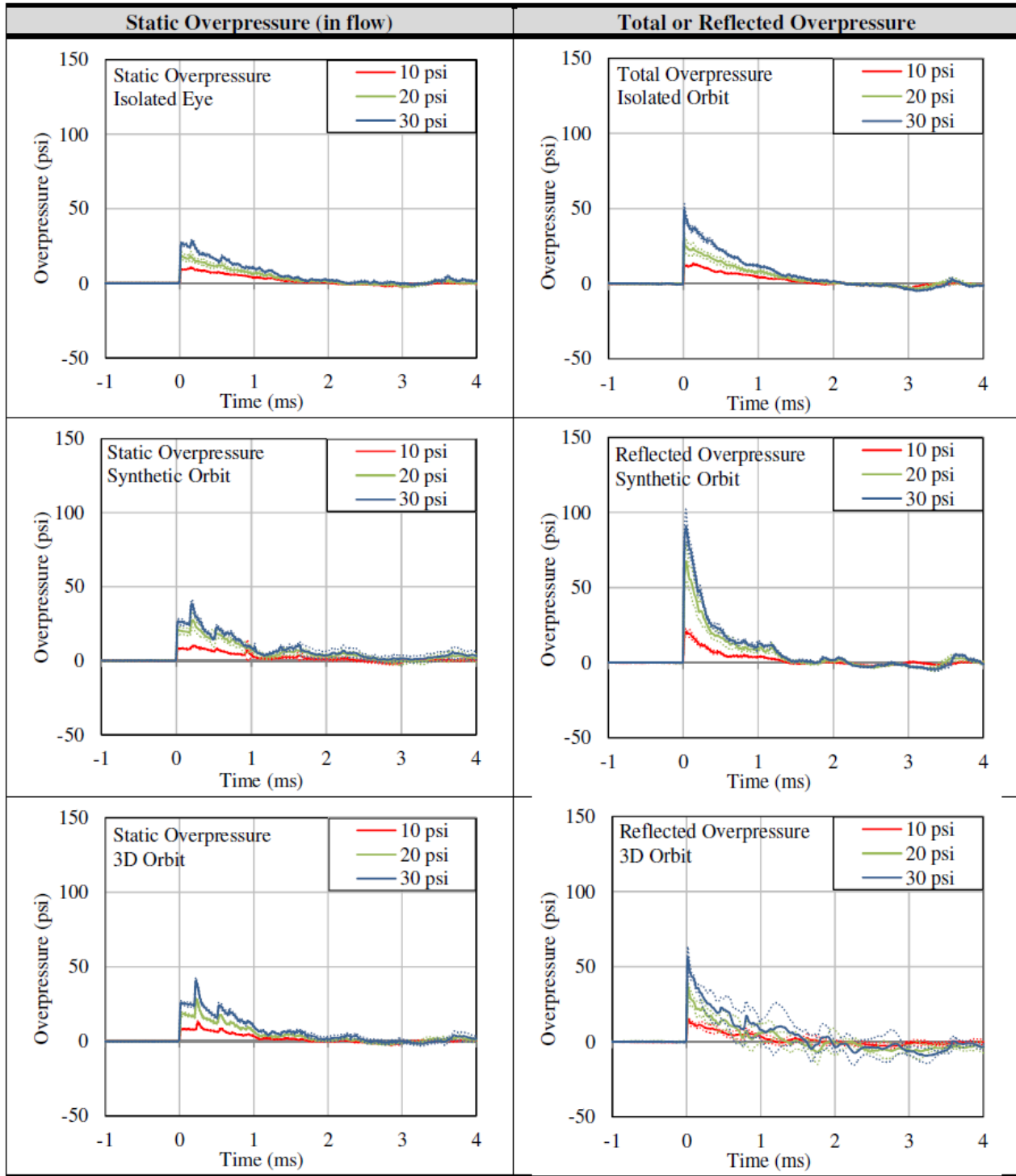
Figure 18: Average static (in-flow), total, and reflected overpressure time histories for unprotected porcine eye tests. Note: Solid lines indicate the average and dotted lines indicate ± 1 standard deviation (i.e., response corridor).
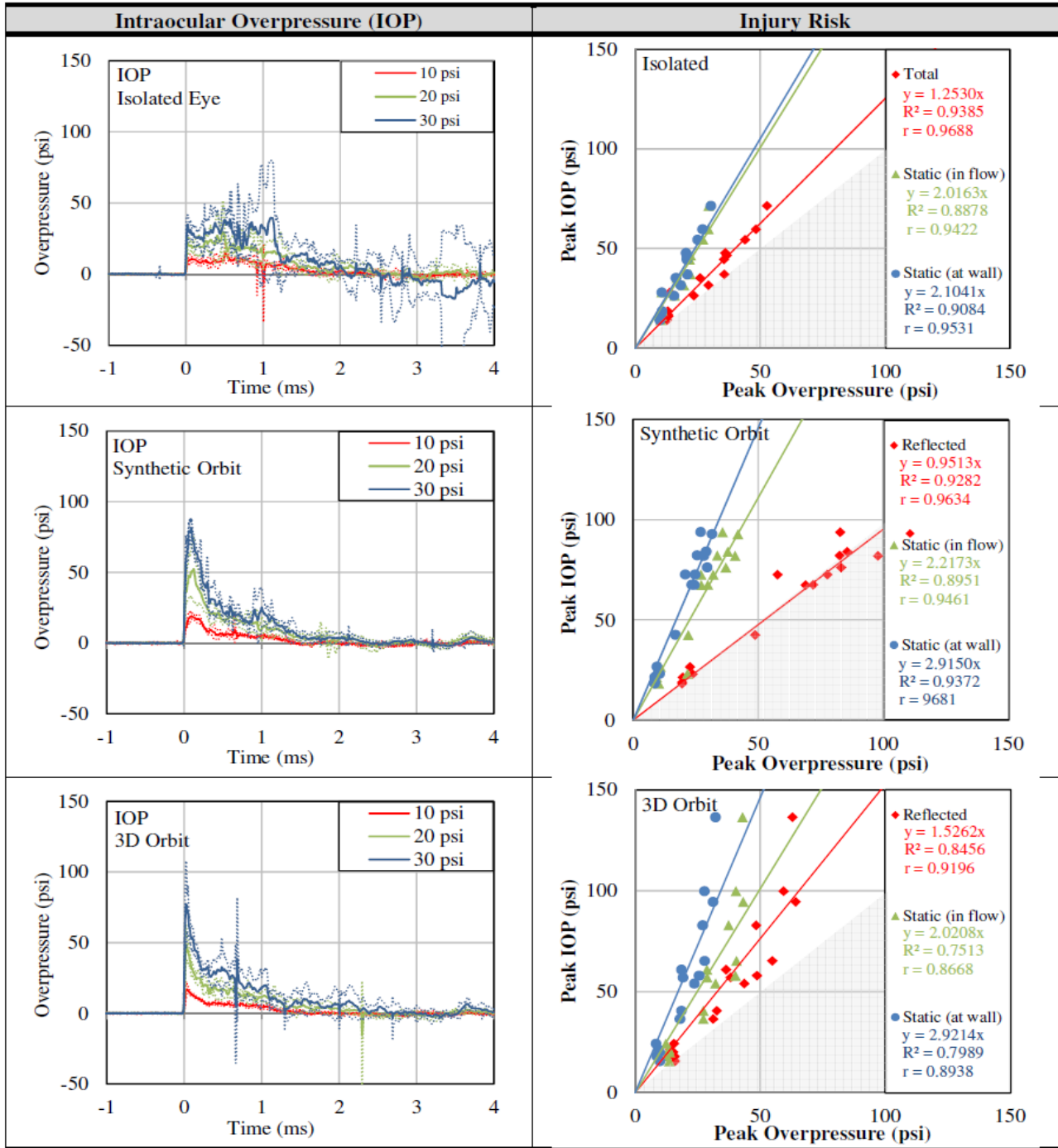
Figure 19: Average intraoccular overpressure time histories for unprotected porcine eye tests (left) and correlations between intraoccular pressure and static and total overpressure (right).
Note: Solid lines indicate the average and dotted lines indicate ± 1 standard deviation (i.e., response corridor).
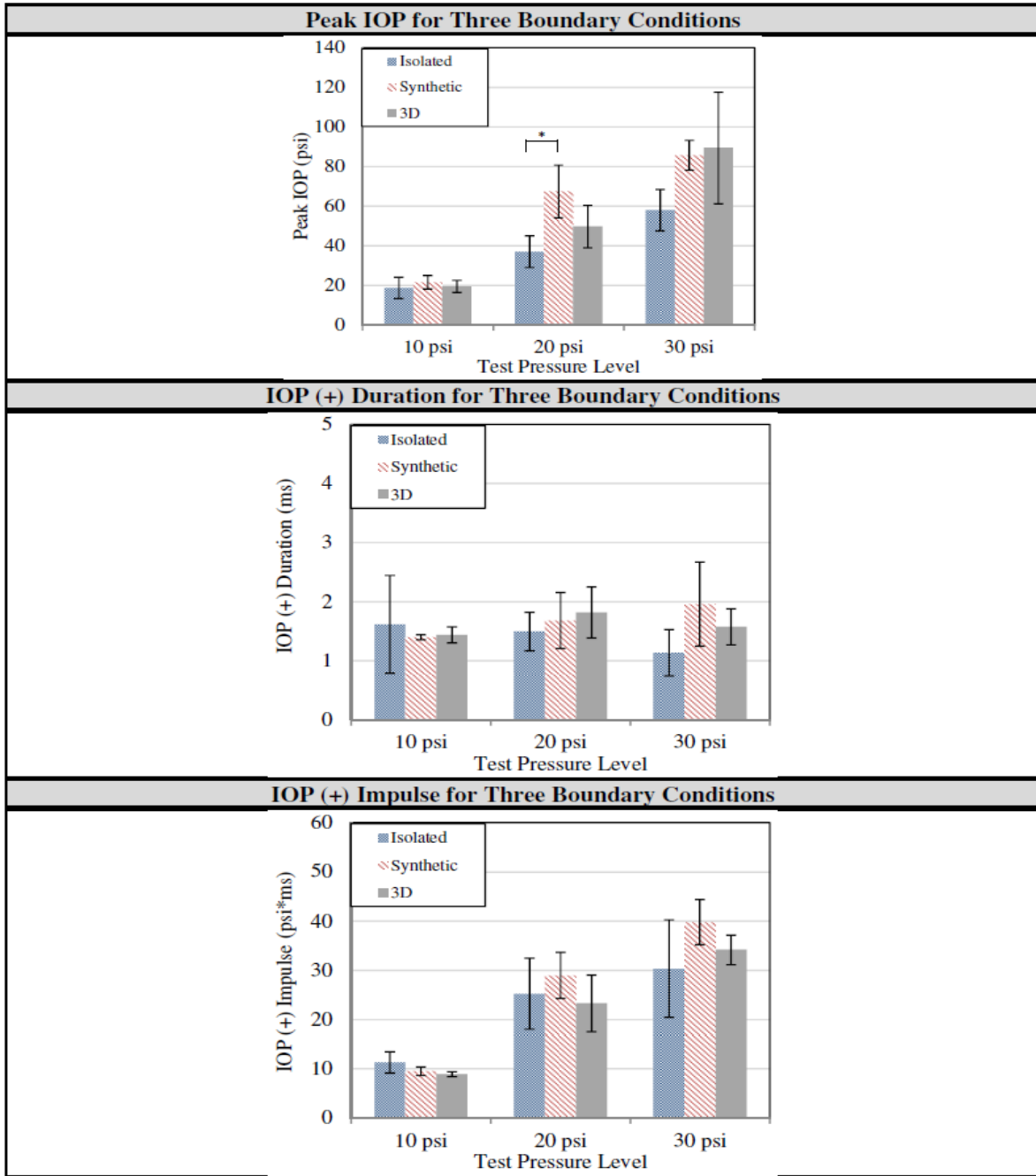
Figure 20: Average peak shock wave parameters for the three ocular boundary conditions.
Note: * indicates a significant difference.
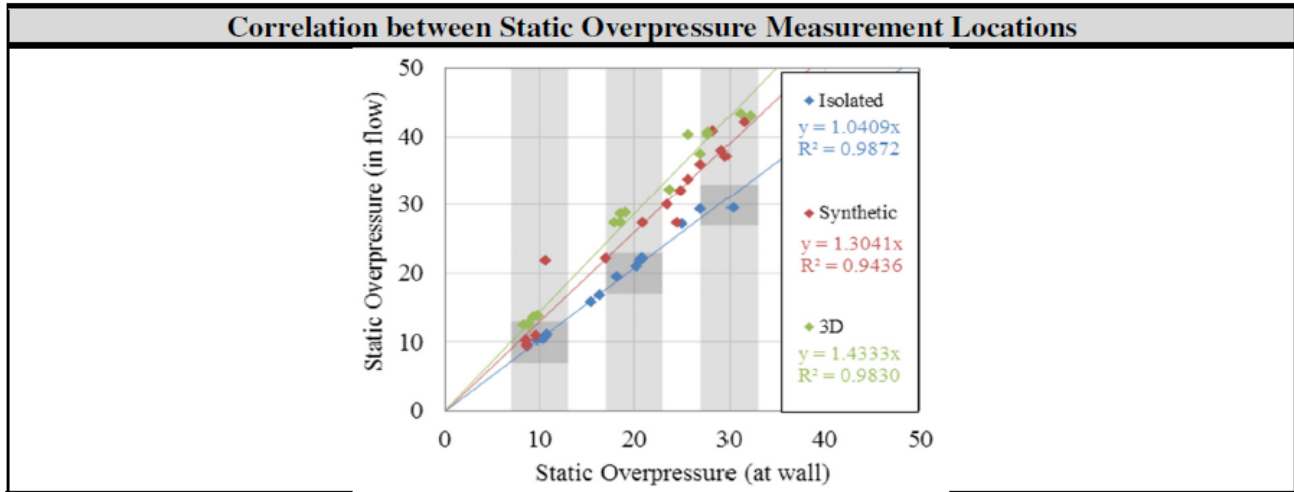
Figure 21: Correlations between static overpressure in-flow and static overpressure at the wall.

The general trends in facial pressure response were that the ToA was delayed and peak overpressure decreased as the pressure sensor location moved medially-laterally across the face (Figure 22). This was due to the expected reduction in pressure as the wave propagated to locations further away from the bursting membrane as well wave propagation around the curved surface of the face. As the pressure sensor location moved medially-laterally across the face, the sensing elements became less normal to the direction of shock wave propagation. As such, these sensors measured decreasing amounts of dynamic pressure, thereby decreasing the overall peak pressure at these locations. These trends are consistent with the physics of blast wave propagation as well as the type of pressure measured by sensors.
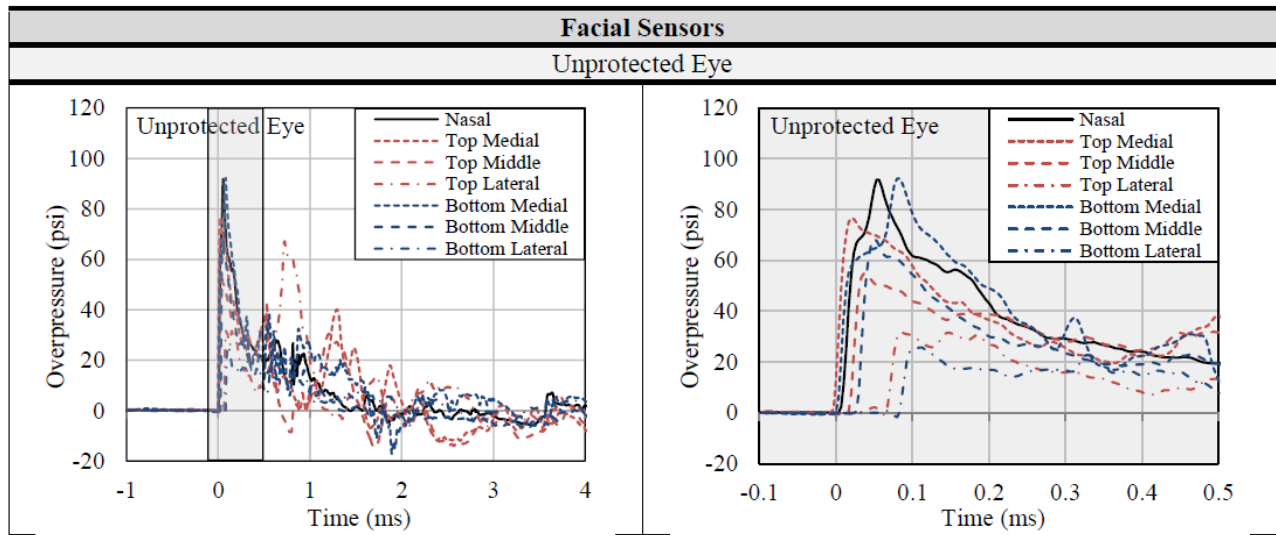
Figure 22: 3D orbit facial sensor time histories at the 30 psi test level.

Exemplar images for the synthetic orbit tests with point tracking are shown in Figure 23. Deflection of the cornea was less than 3 mm for all tests. Movement of the gelatin surrounding the eye in the 3D orbits made analysis of the high speed videos for the 3D orbit tests difficult. Notably, there was rippling on the surface gelatin which made it impossible to accurately locate the ink-printed dots on the sclera (Figure 24).
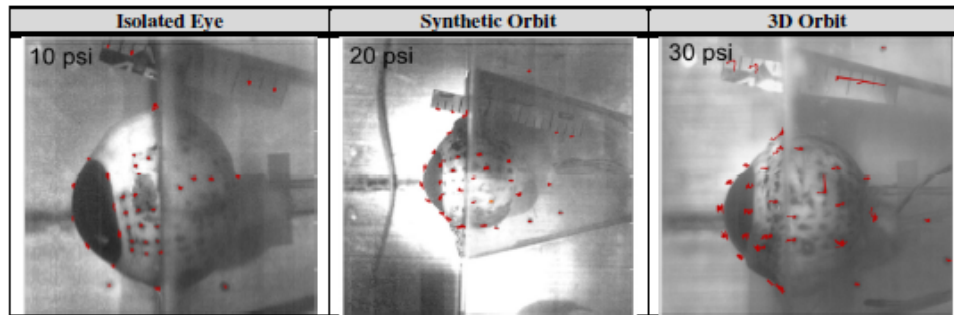
Figure 23: Typical photographs from high-speed video anaylsis for the synthetic orbit. Red lines obtained by tracking points.

Figure 24: Still images from high-speed video of the 30 psi 3D orbit test.

The dissections revealed zonula, lens, ciliary body, and retinal injuries in the sham and test eyes. A number of the injuries observed at the lens and ciliary body upon dissection were caused during dissection or by the tube used to pressurize the eye, which sometimes penetrated the posterior half of the lens and/or ciliary body. Due to the number of sham eyes with reported injuries, significant differences between the proportion of injured sham eyes and the proportion of injured test eyes could not be identified. Due to rapid postmortem degradation, retinal damage was present in all eyes and was therefore not correlated to exposure to blast overpressure. Figure 17 shows three photographs of the retinal folds and partial retinal detachments observed in control eyes. Overall, no major injuries could be attributed to primary blast overpressure exposure.

Predicted injury risk was <5% for all eye injuries in all test conditions at all overpressure levels tested, calculated using peak IOP and the 11.16mm correlation between IOP and NE. Table 4 shows the average ± standard deviation for injury risk calculated for hyphema, lens damage, retinal damage, and globe rupture using the largest correlation. Figure 25 shows the injury risk for hyphema for the three boundary conditions. Significant differences are noted with an asterisk. Table 5 and Table 6 show the average ± standard deviation for injury risk predicted for hyphema, lens damage, retinal damage, and globe rupture using the correlations developed with medium (9.25 mm) and small (6.35 mm) impactors for comparison, respectively. Only when using the 6.35mm correlation does injury risk increase above 5% (hyphema only), which is the most conservative prediction. Injury risk for lens damage, retinal damage, and globe rupture are virtually non-existent at these overpressure levels for even the most conservative prediction.

Table 4: Predicted injury risk calculated using 11.15mm diameter aluminum rod correlation (avg ±stdev).

	Hyphema % Injury Risk	Lens Damage % Injury Risk	Retinal Damage % Injury Risk	Globe Rupture % Injury Risk
Isolated				
10 psi	0.07 ± 0.04	0.00 ± 0.00	0.00 ± 0.00	0.00 ± 0.00
20 psi	0.26 ± 0.12	0.00 ± 0.00	0.00 ± 0.00	0.00 ± 0.00
30 psi	0.67 ± 0.26	0.00 ± 0.00	0.00 ± 0.00	0.00 ± 0.00
Synthetic				
10 psi	0.09 ± 0.03	0.00 ± 0.00	0.00 ± 0.00	0.00 ± 0.00
20 psi	0.94 ± 0.35	0.00 ± 0.00	0.00 ± 0.00	0.00 ± 0.00
30 psi	1.54 ± 0.30	0.01 ± 0.00	0.01 ± 0.00	0.00 ± 0.00
3D				
10 psi	0.07 ± 0.02	0.00 ± 0.00	0.00 ± 0.00	0.00 ± 0.00
20 psi	0.49 ± 0.21	0.00 ± 0.00	0.00 ± 0.00	0.00 ± 0.00
30 psi	1.89 ± 1.37	0.01 ± 0.02	0.02 ± 0.03	0.00 ± 0.00
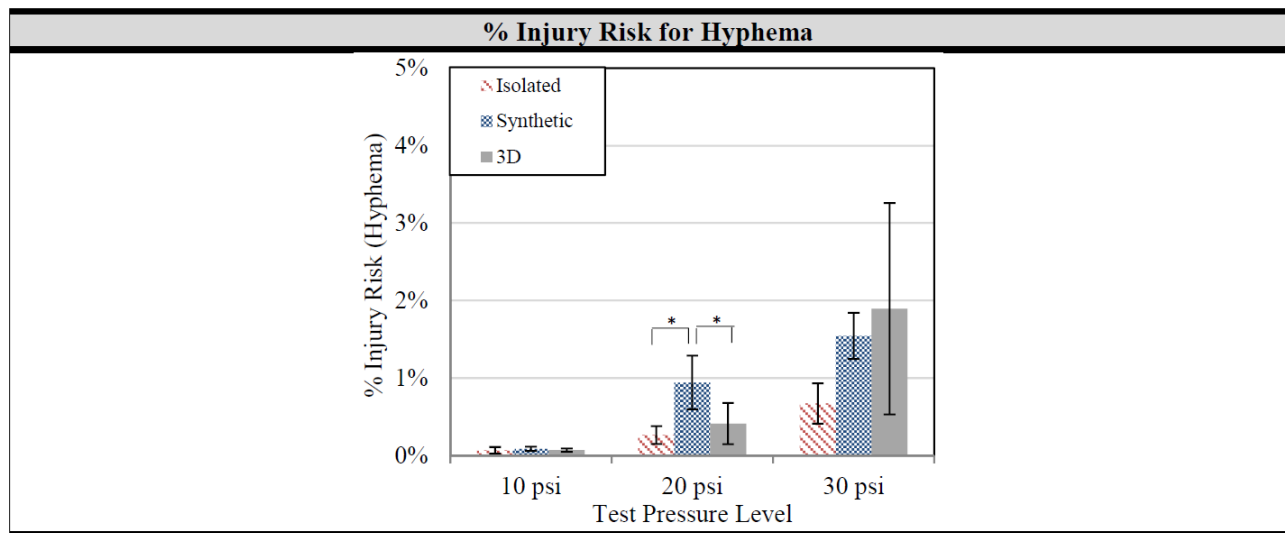
Figure 25: Average injury risk for hyphema for the three ocular boundary conditions.
Notes: Injury risk calculated using 11.15mm diameter aluminum rod correlation, * indicates a significant difference.
.

Table 5: Predicted injury risk calculated using 9.25mm diameter aluminum rod correlation (avg ±stdev).

	Hyphema % Injury Risk	Lens Damage % Injury Risk	Retinal Damage % Injury Risk	Globe Rupture % Injury Risk
Isolated				
10 psi	0.02 ± 0.01	0.00 ± 0.00	0.00 ± 0.00	0.00 ± 0.00
20 psi	0.10 ± 0.05	0.00 ± 0.00	0.00 ± 0.00	0.00 ± 0.00
30 psi	0.34 ± 0.18	0.00 ± 0.00	0.00 ± 0.00	0.00 ± 0.00
Synthetic				
10 psi	0.02 ± 0.01	0.00 ± 0.00	0.00 ± 0.00	0.00 ± 0.00
20 psi	0.54 ± 0.25	0.00 ± 0.00	0.00 ± 0.00	0.00 ± 0.00
30 psi	1.06 ± 0.29	0.00 ± 0.00	0.00 ± 0.00	0.00 ± 0.00
3D				
10 psi	0.02 ± 0.01	0.00 ± 0.00	0.00 ± 0.00	0.00 ± 0.00
20 psi	0.22 ± 0.12	0.00 ± 0.00	0.00 ± 0.00	0.00 ± 0.00
30 psi	1.57 ± 1.60	0.01 ± 0.02	0.02 ± 0.03	0.00 ± 0.00

Table 6: Predicted injury risk calculated using 6.35mm diameter aluminum rod correlation (avg ±stdev).

	Hyphema % Injury Risk	Lens Damage % Injury Risk	Retinal Damage % Injury Risk	Globe Rupture % Injury Risk
Isolated				
10 psi	0.36 ± 0.24	0.00 ± 0.00	0.00 ± 0.00	0.00 ± 0.00
20 psi	1.52 ± 0.70	0.01 ± 0.01	0.01 ± 0.01	0.00 ± 0.00
30 psi	4.11 ± 1.70	0.05 ± 0.04	0.07 ± 0.06	0.00 ± 0.00
Synthetic				
10 psi	0.46 ± 0.16	0.00 ± 0.00	0.00 ± 0.00	0.00 ± 0.00
20 psi	5.89 ± 2.27	0.11 ± 0.07	0.15 ± 0.09	0.00 ± 0.00
30 psi	9.93 ± 2.03	0.30 ± 0.13	0.39 ± 0.16	0.00 ± 0.00
3D				
10 psi	0.37 ± 0.12	0.00 ± 0.00	0.00 ± 0.00	0.00 ± 0.00
20 psi	2.94 ± 1.31	0.02 ± 0.02	0.04 ± 0.03	0.00 ± 0.00
30 psi	12.27 ± 9.10	0.78 ± 1.25	0.91 ± 1.36	0.00 ± 0.01

Summary

This study is the first of its kind to assess the response and injuries of a porcine eye model exposed to survivable primary blast overpressure levels with increasing biofidelity of the boundary conditions surrounding the eye. Three boundary conditions ("Isolated Eye", "Synthetic Orbit", "3D Orbit") were tested at 10 psi, 20 psi, and 30 psi (static overpressure) to examine the effects of both increasing test overpressure level and experimental test setup biofidelity on the response of the eye. Care was taken to ensure the experimental test setups maintained a realistic fluid flow. All test setups occluded <20% of the cross-sectional area of the tube. A plane of symmetry (PoS) was added along the nasal side of the synthetic and 3D orbits to prevent unrealistic pressure relief around the nose. Pressure relief around the eye was greatest for the isolated eye due to the lack of large reflective structures surrounding the eye in this condition. The synthetic orbit produced the highest pressures at each test level due to the reflective surfaces perpendicular to shock wave propagation. Despite this, all tests resulted in low predicted injury risk. Furthermore, no injuries could be attributed solely to primary blast overpressure. Therefore, it was concluded that at these test pressure levels, eye injury risk is extremely low. Ultimately, these results indicate that boundary condition fidelity is critical to evaluating, modeling, and predicting eye injuries caused by primary blast overpressure exposure. These results expand the field by providing realistic test conditions that can be repeated or modeled for future studies and by adding the prediction of eye injury risk using intraocular pressure.

Effect of Spectacles and Goggles on the Response of Protected Porcine Eyes during Exposure to Blast Overpressure

Background

Reduced fatality rates in military conflicts have been linked to the use of advanced personal protective equipment (PPE), which is often designed to minimize the effects of ballistics and shrapnel (Fisher, 2015). Despite the availability of protective eyewear, eye injuries occurred in 17% of cases where protective eyewear was used and jumped to 26% when protective eyewear was not used (Thomas et al., 2009). The incidence of eye injuries that occur even when protective eyewear is used motivates the need to more fully understand primary blast overpressure as an eye injury mechanism for protected eyes. While initial experimental and computational models suggest eye protection can reduce peak overpressure exposure to the eye, it is imperative to understand the actual ocular response during blast overpressure exposure (Bailor et al., 2015). However, there is a paucity of experimental data in the literature that can be used to validate computational models. Furthermore, the question remains whether spectacles and/or goggles reduce eye injury risk from primary blast. Therefore, the purpose of this study is to quantify the eye response and injuries when wearing eye PPE, specifically spectacles and goggles, during primary blast overpressure exposure and evaluate the effectiveness of these PPE by comparing the results to those obtained for the unprotected eye.

Methods

Advanced Blast Simulator (ABS)

All blast overpressure tests were conducted using the small VT ABS and aluminum membranes, as described in the previous section (Figure 9). Briefly, the helium gas-driven ABS consists of equally shaped "driver" and "driven" sections separated by a frangible aluminum membrane. The driver section is pressurized with helium gas until the membrane passively ruptures and sends a burst of gas down the driven section. As the gas compresses upon itself, a shock-front forms and the shock wave propagates through the tube. The small VT ABS is specifically designed for testing small specimens, and is able to produce peak overpressures up to approximately 30 psi (static overpressure) with a positive duration around 2.5 ms using aluminum membranes.

Porcine Eye Procurement and Preparation

A total of 33 porcine eyes were acquired for this study. Fresh porcine eyes were shipped overnight on wet ice, stored in a refrigerator, and tested within three days of slaughter (Animal Technologies, Tyler, TX, USA). Three eyes were tested at the 10 psi and 20 psi static overpressure levels and five eyes were tested at the 30 psi static overpressure level for each piece of eyewear. An additional eleven eyes were used as controls (n=8) and shams (n=3). Control eyes were used to assess postmortem effects and damage from tissue procurement. Sham eyes were used to quantify potential injuries from pre-test preparation techniques, including the insertion of a pressure sensor and pressurization into the eye and setting the eye in a rigid concave cup or in gelatin. All eyes were prepared with the following technique. Skin and musculature was removed to expose only the globe and optic nerve. Eyes were identified as left (OS) or right (OD). Cornea clarity was qualitatively assessed (clear, not clear), and visibility of the "Y" suture on the lens was noted. Fluorescein dye was applied to the cornea and a blue light was used to help visualize corneal abrasions. Any existing corneal abrasions were noted. Control eyes were dissected at this point to assess and quantify baseline damage to the eye caused by postmortem degradation and procurement from the abattoir. The remaining eyes were further prepared by applying a dot pattern on the surface of the sclera using permanent black ink. A miniature pressure sensor (Model 060S, 100 psi, Precision Measurement Company, Ann Arbor, MI) and a small tube were inserted through the optic nerve into the vitreous fluid and secured in place using a cable tie. Normal physiologic intraocular pressure (IOP) was provided throughout the duration of the test using a gravity-fed system. Specifically, a bag of Lactated Ringer's solution

was connected to the small tube and suspended 8 in. above the eye. Intraocular pressure was measured before and after each test using a veterinary tonometer (Tono-Pen AVIA Vet® Veterinary Tonometer, Reichert Technologies, Depew, NY, USA). Due to minor variations, measurements were taken using the tonometer until three sequential measurements recorded the same IOP at a 95% confidence.

Protected Eye Test Conditions: Ocular PPE

One pair of spectacles and one pair of goggles were selected from the Authorized Protective Eyewear List (APEL) provided by the Program Executive Office (PEO Soldier) (Authorized Protective Eyewear List (APEL), 2015). The Eye Safety Systems, Inc. (ESS2) Crossbow and Profile NVG were chosen because of their popularity as reported through multiple contacts with PEO Soldier (Figure 26).

Spectacle: ESS Crossbow	Goggle: ESS Profile NVG
APEL, UPLC Approved	APEL, UPLC Approved
Manufacturer Part Number: 740-0615	Manufacturer Part Number: 740-0127
Cost: $40.00	Cost: $100.00

Figure 26: Spectacles and goggles used for protected porcine eye blast tests.

The 3D orbit, described in detail in the previous section (i.e., unprotected porcine eye blast tests), was used for all protected porcine eye blast tests. Pressure measurement locations are the same as those described in the previous section (i.e., unprotected porcine eye blast tests). The spectacles and goggles were placed on the 3D printed orbit that was previously used for the unprotected porcine eye tests (Figure 27). A single pair of each the spectacles and goggles was used for all tests. The eyewear was cut in half in order to fit over the 3D orbit and against the plane of symmetry (PoS). As the lens for both the spectacles and goggles was separate from the rim and nosepiece, super glue was used to secure these pieces together. The spectacles and goggles were both rigidly held in place at the bridge of the nose using a screw to attach the lens to a small aluminum block, which was rigidly mounted to the PoS. The earpiece of the spectacles was held in place at the temple using a plastic cable fastener. The position of the cable fastener simulated the position above the ear where the spectacles would rest, without the addition of a head strap. The goggles were held in place at the temple by securing the strap to the back of the experimental test setup. Tension on the strap was strong enough for the goggle to remain in contact with the face, but not strong enough to compress the goggles. This preparation technique was developed after a number of users were instructed to adjust the goggles for comfort, as would be done *in theatre*. Additionally, the goggles were placed on the FOCUS headform to compare fit and contact between the goggle and the headforms. While both the ESS Crossbow and ESS Profile NVG are Universal Prescription Lens Carrier (UPLC) compatible, allowing soldiers who require prescription lenses to use this eyewear, all tests were conducted without the prescription lens attachment. The spectacles did not contact any of the seven facial pressure sensors. The goggles contacted five of the facial pressure sensors. The nasal and bottom nasal sensors remain exposed with the goggles in place.

ESS Crossbow Spectacles	ESS Profile NVG Goggles
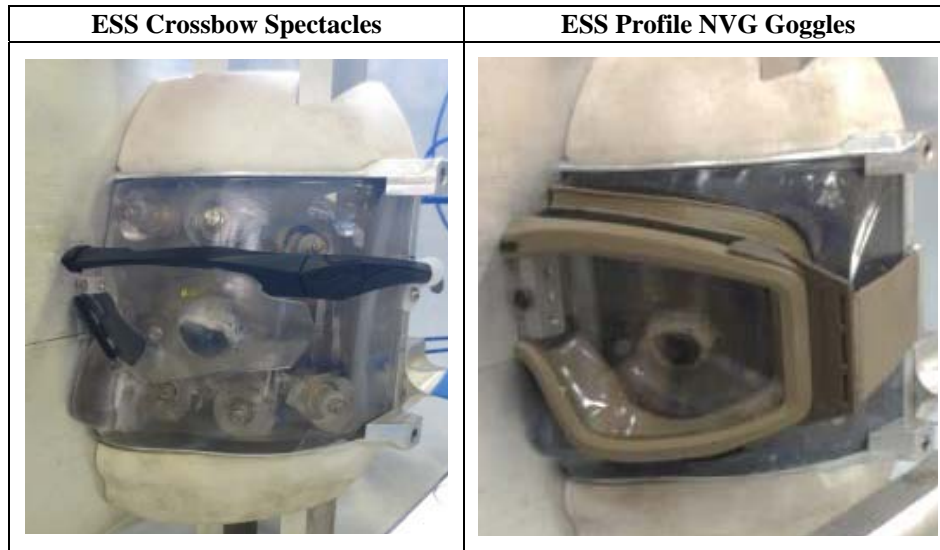
Figure 27: Spectacles and goggles attached to the 3D orbit.

Data Acquisition and Processing

All data were collected at 301.887 kHz (TDAS PRO, Diversified Technical Systems, Inc., Seal Beach, CA). The standard TDAS PRO anti-aliasing filter was bypassed because the frequency content of the blast overpressure wave exceeded the 4,300 Hz cutoff frequency. However, the TDAS PRO sensor input modules (SIMs) bandwidth of 0-25 kHz acts as a low-pass filter with a frequency cutoff of 25 kHz. All pressure data were zeroed prior to the event. High speed video of each test was captured at 20 kfps (v9.1, Vision Research, Wayne, NJ).

A custom MATLAB® (version 7.11.0.584 (R2010b), The MathWorks, Inc., Natick, MA) script was used to quantify the shock wave characteristics at each pressure sensor location (time of arrival, peak overpressure, positive duration, and positive impulse). Using MATLAB®, a one-way ANOVA was conducted on the average peak IOP, reflected overpressure, static overpressure (in the flow), and static overpressure (along the wall) for the spectacles, goggles, and unprotected 3D orbit tests with tukey-kramer multiple comparison test to determine significance between groups with a $p < 0.05$.

Injury Assessment

Injuries were assessed in two ways. First, gross dissection of each eye following the test was used to quantify physical damage to the tissues and structures of the eye. Second, injury risk for physiologic injuries was calculated using the peak intraocular pressure measured for each test. The gross dissection methods and injury risk calculations are described in detail in the previous section (i.e., unprotected porcine eye blast tests).

Results

Pressure-time histories for all tests with the spectacles and goggles are shown in Figure 28, Figure 29, and Figure 30. The unprotected eye IOP time histories from the previous section are included for comparison. Peak IOP increased with increasing test level. Compared to the unprotected eye, the recorded IOP pulses for both the spectacles and goggles had a delayed time to peak overpressure. This was observed to a greater extent for the goggles than for the spectacles. Peak IOP decreased with the addition of the spectacles at the 20 psi and 30 psi test levels. Peak IOP decreased with the addition of the goggles at all three test levels.
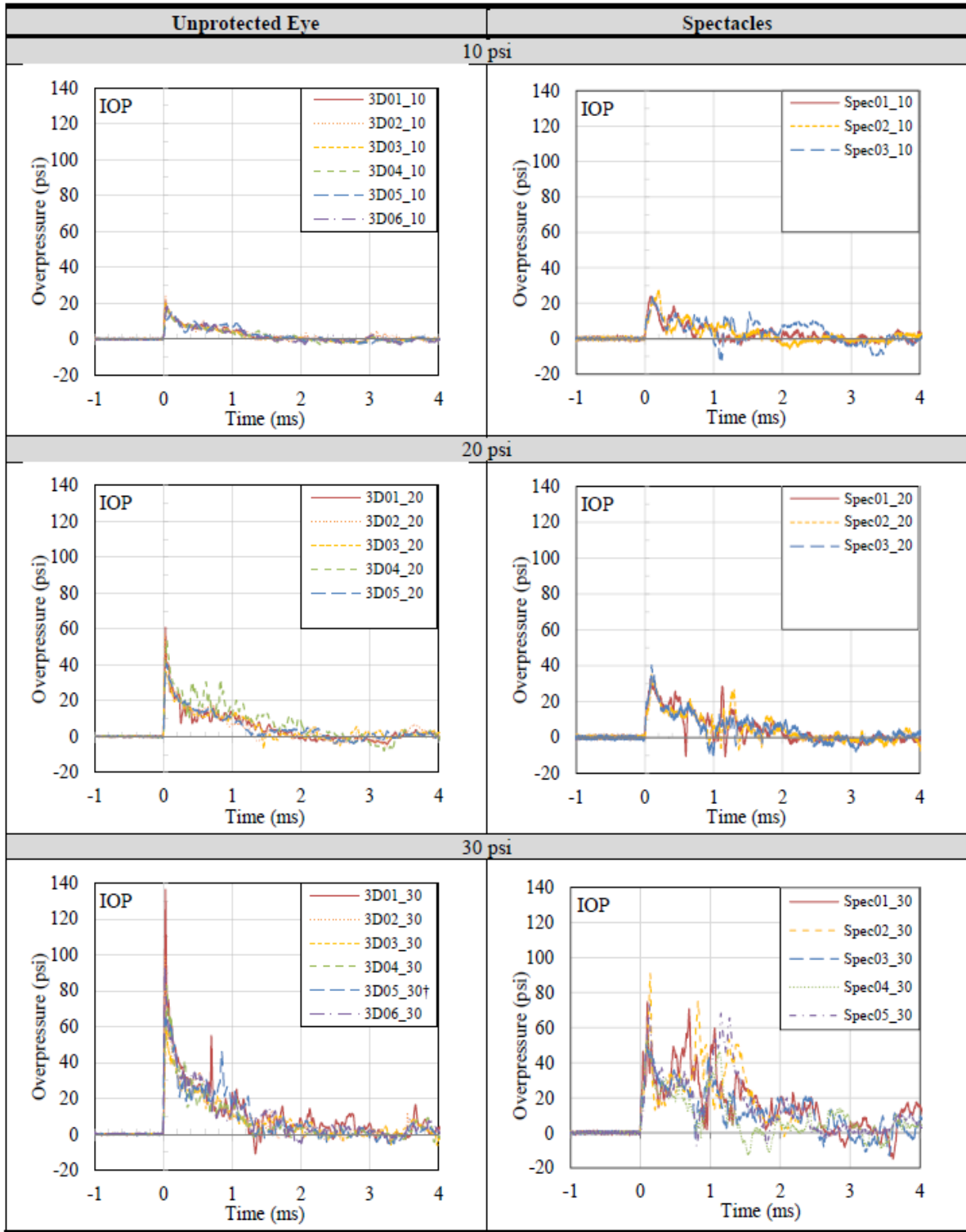
Figure 28: Intraocular overpressure time histories for porcine eye tests- unprotected and spectacles.
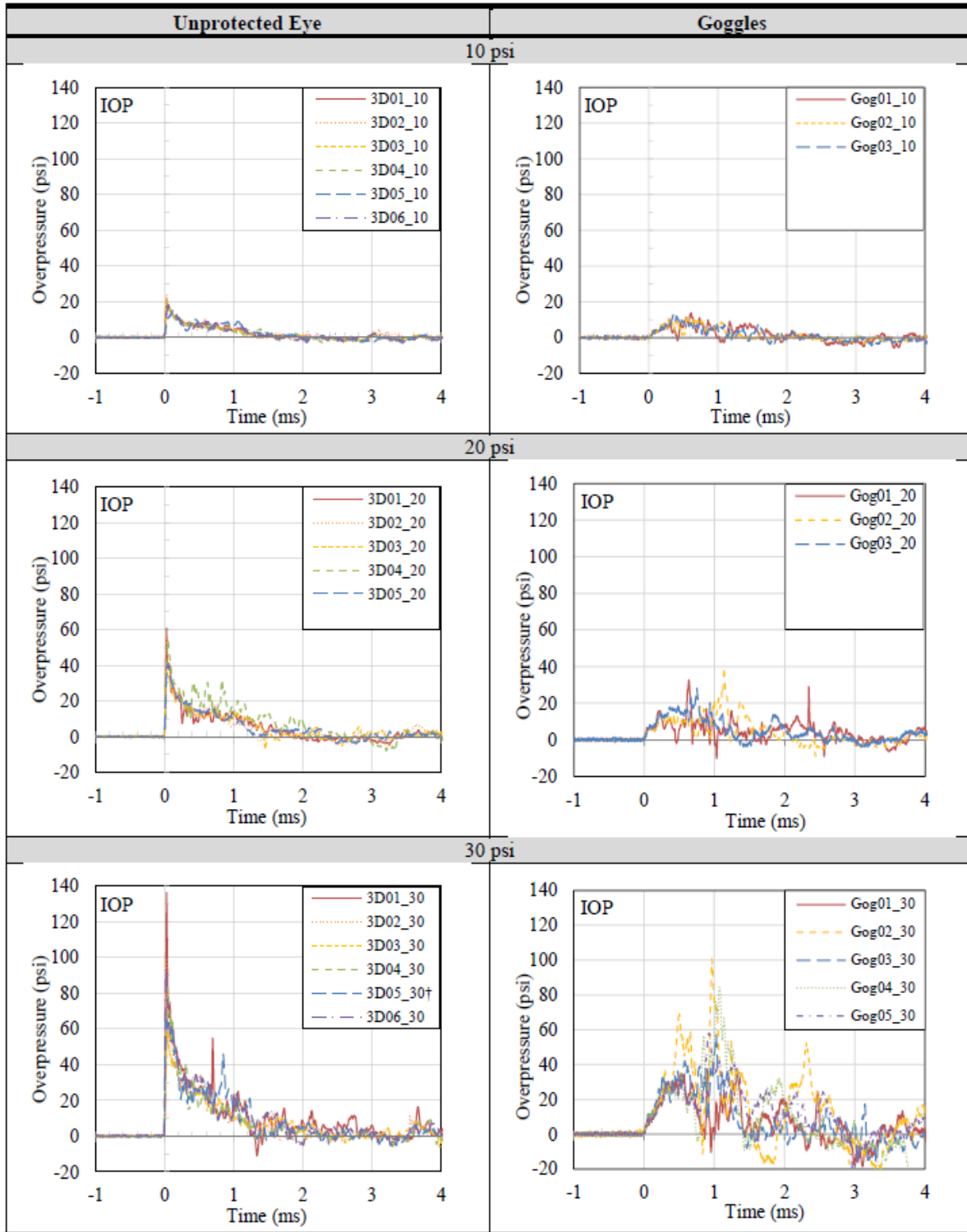
Figure 29: Intraocular overpressure time histories for porcine eye tests- unprotected and goggles.
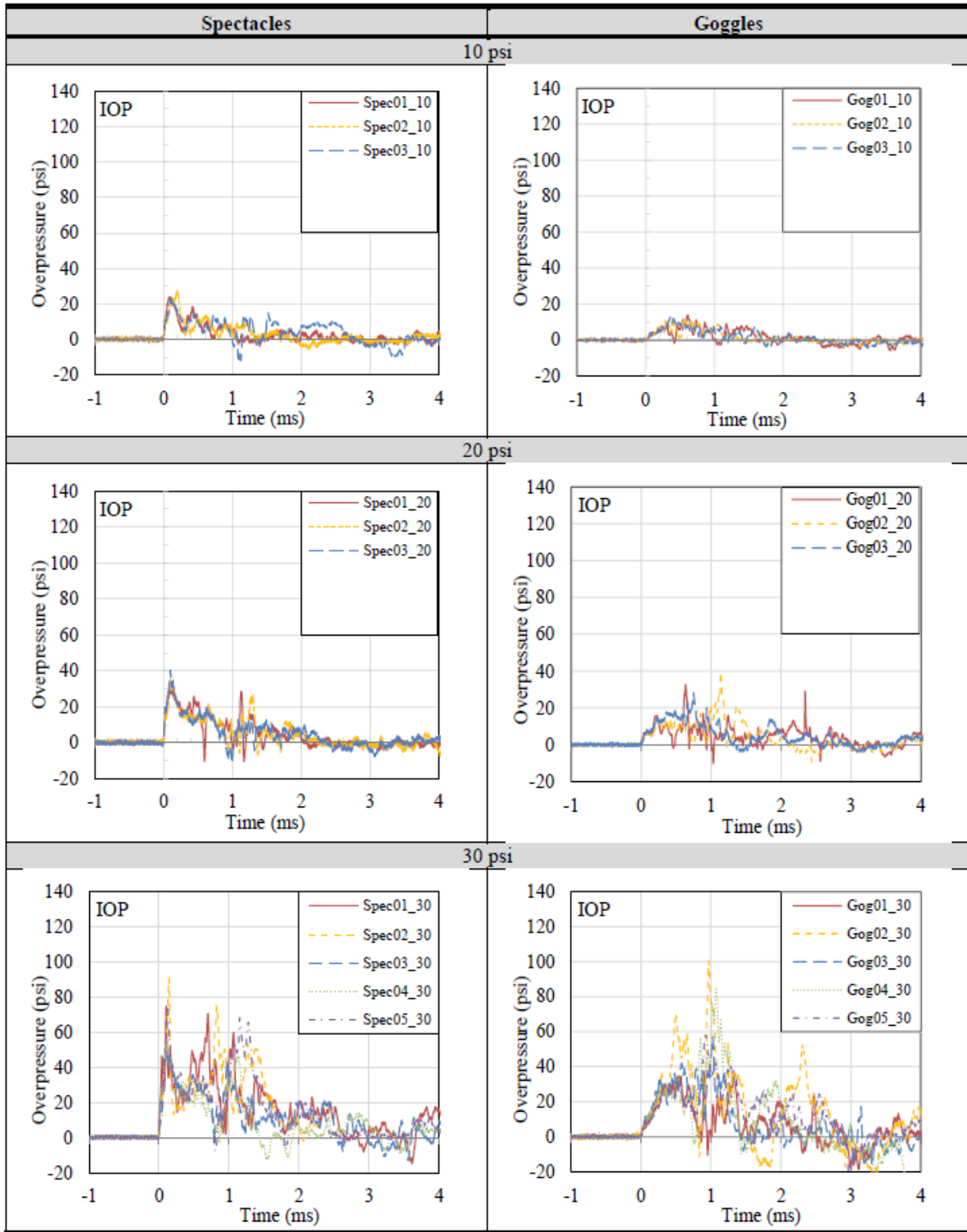
Figure 30: Intraocular overpressure time histories for porcine eye tests- spectacles and goggles.

Peak overpressure measured at all locations increased with increasing test pressure level for both the spectacles and goggles (Figure 31). The goggles resulted in a greater reduction in peak IOP than the spectacles at all three test levels. Both the spectacles and goggles showed a decrease in peak IOP at the 20 psi and 30 psi levels. However, the reduction in peak IOP at the 20 psi and 30 psi levels was not significantly different from the unprotected eye. The spectacles recorded a significant increase in peak IOP compared to the unprotected eye and the goggles at the 10 psi level. The goggles recorded a significant decrease in peak IOP compared to the unprotected eye and spectacles at the 10 psi level.
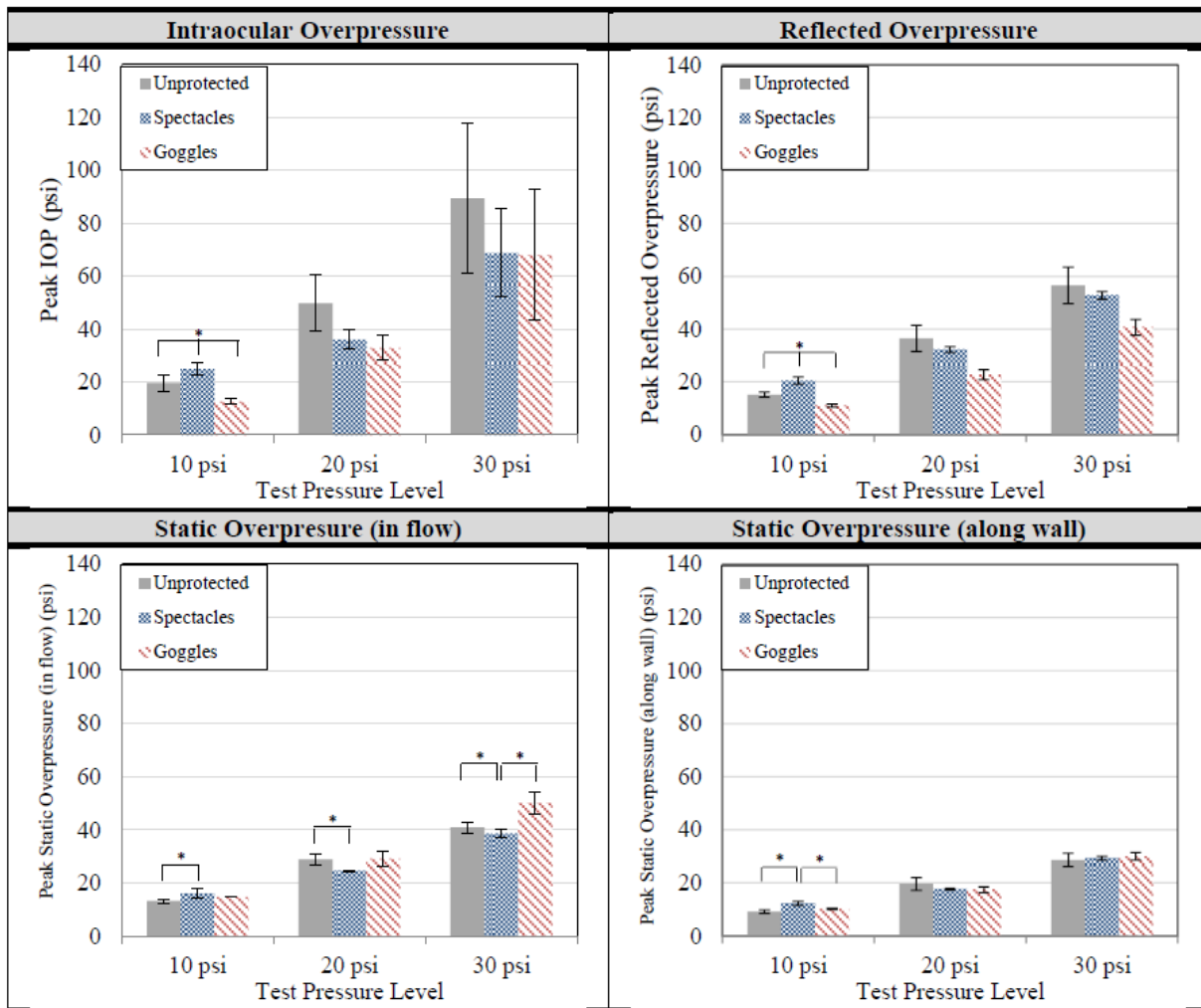
Figure 31: Average peak IOP for unprotected and protected eyes.
Note: * indicates a significant difference.

Similar to peak overpressure, positive impulse showed significant differences at the 10 psi level for all four pressure measurement locations (Figure 32). Positive impulse was higher for the spectacles than the unprotected eye at each pressure measurement location, and was significantly higher than the goggles at the IOP, reflected overpressure, and static overpressure (along the wall) locations. Generally, positive duration did not vary significantly at each sensor location. Positive duration for the spectacles was significantly lower than the unprotected eye at the 20 psi level for IOP, and significantly higher than the goggles at the 10 psi for reflected overpressure.
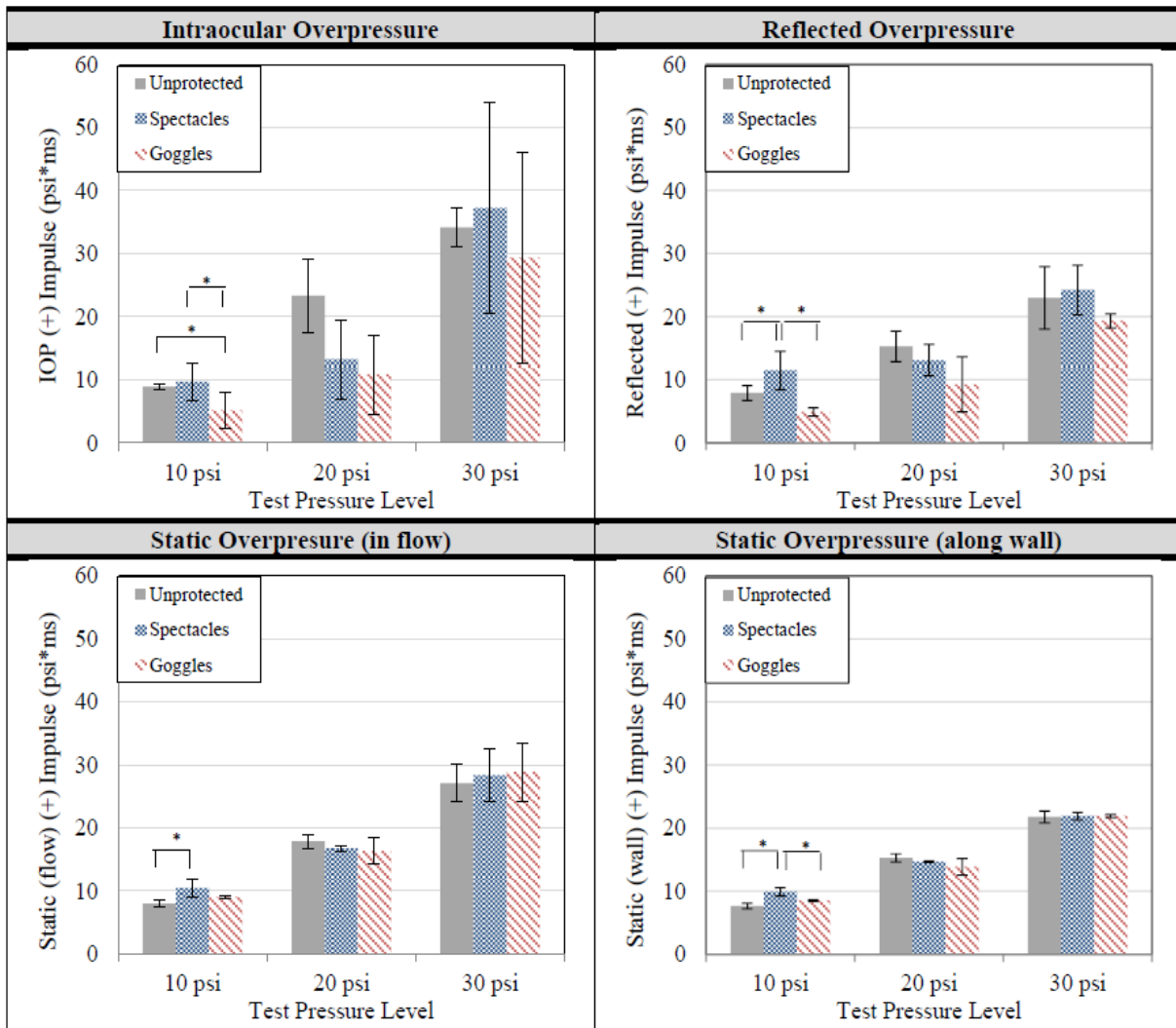
Figure 32: Average positive impulse for unprotected and protected eyes.
Note: * indicates a significant difference.

Still images of high speed video during the first 800 µs of the blast event show a rippling effect on the gelatin surrounding the eye and minor deflection of the lens for both the spectacles and goggles (Figure 33 and Figure 34). The rippling effect was previously observed with the unprotected eyes, and was more noticeable with the spectacles as compared to the goggles. Deflection of the lens could not be accurately quantified from this single side-on view video image due to the fact that deflections occurred in multiple axes. The nosepiece of the goggle that initially contacted the nose moved off the nose during the event, causing slapping against the nose and gelatin.
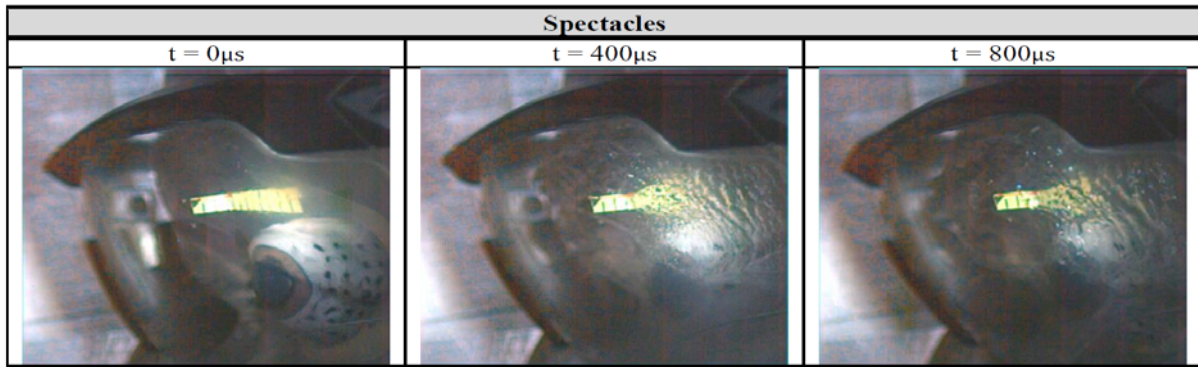
Figure 33: Still images from high-speed video of 30 psi blast test with spectacles.
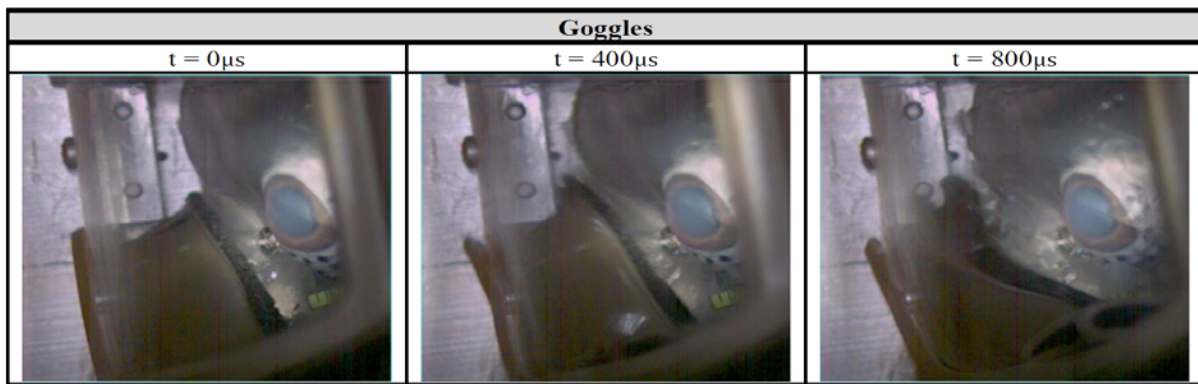
Figure 34: Still images from high-speed video of 30 psi blast test with goggles.

A number of the injuries observed at the lens and ciliary body upon dissection were incurred during dissection. Other than two cases of lens damage, only ciliary body injuries were reported as potentially being independent of preparation techniques. However, using chi-square tests, it was determined that there was no significant difference between the proportion of ciliary body injury observed between sham eyes and any of the unprotected eyes, eyes with spectacles, or eyes with goggles. Therefore, it was concluded that the reported injuries were not due to exposure to primary blast overpressure.

Predicted injury risk increased with increasing test pressure level (Table 7). Injury risk was <2% for all eye injuries for both spectacles and goggles. Predicted injury risk calculated for the spectacles and goggles was lower than the unprotected eye.

Table 7: Predicted injury risk for porcine eye tests with spectacles and goggles calculated using 11.15mm diameter aluminum rod correlation (avg ±stdev).

	Hyphema	Lens Damage	Retinal Damage	Globe Rupture
	% Injury Risk	% Injury Risk	% Injury Risk	% Injury Risk
Unprotected Eye				
10 psi	0.07 ± 0.02	0.00 ± 0.00	0.00 ± 0.00	0.00 ± 0.00
20 psi	0.49 ± 0.21	0.00 ± 0.00	0.00 ± 0.00	0.00 ± 0.00
30 psi	1.89 ± 1.37	0.01 ± 0.02	0.02 ± 0.03	0.00 ± 0.00
Spectacles				
10 psi	0.11 ± 0.02	0.00 ± 0.00	0.00 ± 0.00	0.00 ± 0.00
20 psi	0.24 ± 0.05	0.00 ± 0.00	0.00 ± 0.00	0.00 ± 0.00
30 psi	1.00 ± 0.51	0.00 ± 0.00	0.00 ± 0.00	0.00 ± 0.00
Goggles				
10 psi	0.03 ± 0.01	0.00 ± 0.00	0.00 ± 0.00	0.00 ± 0.00
20 psi	0.20 ± 0.06	0.00 ± 0.00	0.00 ± 0.00	0.00 ± 0.00
30 psi	1.11 ± 0.76	0.00 ± 0.01	0.01 ± 0.01	0.00 ± 0.00

Summary

This study quantified peak intraocular pressure for porcine eyes protected by spectacles and goggles to assess the ability of military protective eyewear to minimize eye injury risk from primary blast overpressure. The addition of the spectacles increased IOP at the 10 psi level, but decreased IOP at the 20 psi and 30 psi test levels. However, these changes were only significantly different for the 10 psi level. The addition of the goggles decreased IOP at all test levels. The reduction of peak IOP measured in this study correlates to a lower risk of eye injuries from primary blast overpressure for scenarios where eye protection is used. This further supports the need to increase military personnel compliance in regard to the proper use of protective eyewear during combat. Interestingly, the spectacles and goggles produced similar reduction in peak IOP at the 30 psi condition. It is possible that the 30 psi test level represents the threshold between spectacles and goggles where lens shape and/or contact with the face does not affect the resulting propagation of pressure toward the eye. Future work with higher pressure levels will elucidate further trends in the ability of spectacle and goggles to protect the eye from primary blast overpressure. Further, the combined effects of protective eyewear and helmets will increase the fidelity of the results for comparison to combat scenarios.

EYE BLAST FINITE ELEMENT MODELING

Parametric Eye Blast Study

A paper entitled "Injury Risk Prediction from Computational Simulations of Ocular Blast Loading" detailing blast eye modeling work that was performed in earlier phases of this project is in review with Biomechanics and Modeling in Mechanobiology and is provided below. This study used a predictive Lagrangian-Eulerian finite element eye model to analyze 2.27 kg and 0.45 kg trinitrotoluene (TNT) equivalent blasts detonated from different locations. Free air and ground level blasts were simulated directly in front of the eye and at lateral offset locations with box, average, less protective, and more protective orbital anthropometries, resulting in 96 simulations. Injury risk curves were developed for hyphema, lens dislocation, retinal damage, and globe rupture from experimental and computational data to compute risk from corneoscleral stress and intra-ocular pressure computational outputs. Corneoscleral stress, intra-ocular pressure, and risk of injuries increased with larger blast size and with the blast located nearer to the eye. Orbital geometry affected the observed stresses, pressures, and associated ocular injury risks for the blast conditions simulated. Results of this parametric computational study of ocular blast loading are valuable to the design of eye protection equipment and the mitigation of blast-related eye injuries.

TITLE: Injury Risk Prediction from Computational Simulations of Ocular Blast Loading
AUTHORS: Weaver AA, Stitzel SM, Stitzel JD
JOURNAL: Biomechanics and Modeling in Mechanobiology
STATUS: Under Review

Abstract

A predictive Lagrangian-Eulerian finite element eye model was used to analyze 2.27 kg and 0.45 kg trinitrotoluene (TNT) equivalent blasts detonated from 24 different locations. Free air and ground level blasts were simulated directly in front of the eye and at lateral offset locations with box, average, less protective, and more protective orbital anthropometries, resulting in 96 simulations. Injury risk curves were developed for hyphema, lens dislocation, retinal damage, and globe rupture from experimental and computational data to compute risk from corneoscleral stress and intra-ocular pressure computational outputs. Corneoscleral stress, intra-ocular pressure, and injury risks increased when the blast size was larger and located nearer to the eye. Risks ranged from 20-100% for hyphema, 1-100% for lens dislocation, 2-100% for retinal damage, and 0-98% for globe rupture depending on the blast condition. Orbital geometry affected the stresses, pressures, and associated ocular injury risks for the blast conditions simulated. Orbital geometries that more fully surrounded the eye such as the more protective orbit tended to produce higher corneoscleral stresses, and compression of the eye against the surrounding rigid orbit contributed to high stresses as the blast wave propagated. However, the more protective orbit tended to produce lower intra-ocular pressures in comparison to the other three orbital geometries which may indicate that the more protective orbit inhibits propagation of the blast wave and reduces ocular loading. Results of this parametric computational study of ocular blast loading are valuable to the design of eye protection equipment and the mitigation of blast-related eye injuries.

Introduction

Military combat has recently seen an increase in the use of improvised explosive devices (IEDs), with explosive events accounting for over 75% of combat-related fatalities in Operation Iraqi Freedom and Operation Enduring Freedom (Belmont et al. 2010). IEDs are responsible for up to 51% of ocular injuries in recent military studies (Mader et al. 2006), and ocular injury from blast loading is associated with severe ocular morbidity and visual impairment (Weichel et al. 2008). Blast injuries are classified into four categories: primary, secondary, tertiary, and quaternary. Primary ocular injuries caused directly by blast overpressure are the focus of this study.

Experiments with human and animal eyes have determined injury tolerance for agents of blunt trauma, predicting ocular injury risk from the kinetic energy, velocity, mass, or normalized energy of the projectile (Berger 1978; Duma and Crandall 2000; Duma et al. 2005a; Kennedy and Duma 2011; Kennedy et al. 2007; Kennedy et al. 2006; Scott et al. 2000). Instrumented surrogates such as the Facial and Ocular Countermeasure Safety (FOCUS) headform have also been used to predict ocular injury risk from projectile loading (Bisplinghoff and Duma 2009; Kennedy et al. 2007). Blast overpressure experiments with animal eyes have demonstrated globe rupture, retinal damage, hyphema, corneal edema, and optic nerve degeneration when the eye is exposed to higher pressure levels (Bricker-Anthony et al. 2014a; Bricker-Anthony et al. 2014b; Choi et al. 2015; Hines-Beard et al. 2012; Sherwood et al. 2014; Zou et al. 2013). However, other experiments with fireworks have concluded that isolated primary blast overpressure does not cause severe eye injury (Alphonse et al. 2012).

Finite element (FE) models of the eye have been used to simulate a variety of impacts and analyze injury potential (Bhardwaj et al. 2014; Esposito et al. 2015; Karimi et al. 2016; Kennedy et al. 2008; Kisielewicz et al. 1998; Liu et al. 2015; Power et al. 2002; Stitzel et al. 2002; Stitzel et al. 2005; Uchio et al. 2004; Uchio et al. 1999; Uchio et al. 2001; Weaver et al. 2011a; Weaver et al. 2011b). The Virginia Tech – Wake Forest University (VT-WFU) eye model is a FE model validated to predict globe rupture for dynamic blunt eye impacts (Stitzel et al. 2002; Weaver et al. 2011a). The model has been validated with 79 matched experimental tests and computational simulations of ocular impacts with eight different projectiles at varying velocities. Additional studies with the VT-WFU eye model have investigated the effect on eye injury as age, orbital anthropometry, projectile type, and loading characteristics are varied (Kennedy et al. 2008; Stitzel et al. 2005; Weaver et al. 2011a; Weaver et al. 2011b; Weaver et al. 2010).

The objective of the study was to use the VT-WFU eye model to simulate different blast scenarios by varying blast location and size, as well as orbital anthropometry. A secondary goal was to develop injury risk curves and to predict risk for hyphema, lens dislocation, retinal damage, and globe rupture from the blast simulations.

Methods

Computational Modeling of Ocular Blast Loading
Ocular blast loading was simulated in LS-Dyna (Livermore Software Technology Corporation, Livermore, CA) using the VT-WFU eye model which was updated previously from a quarter cylinder geometry to represent the entire eye (Weaver et al. 2011b). This model is based on two spherical geometries forming chambers anterior and posterior to the lens, and includes Lagrangian and Eulerian meshes to accurately represent the mechanics of both solid and fluid interactions. The model was developed with Hypermesh (Hyperworks v.9.0, Altair, Troy, MI) in conjunction with LS-Prepost (Livermore Software Technology Corporation, Livermore, CA). Material properties (Uchio et al. 1999), definitions, and cross sectional dimensions have been reported previously (Stitzel et al. 2002; Weaver et al. 2011b). The Lagrangian mesh includes a corneoscleral shell with variable thickness (consisting of the cornea, sclera, and limbus), as well as the ciliary body, zonules, and lens. The Lagrangian mesh is embedded in an Eulerian fluid mesh to model large deformations of the fluid-filled anterior and posterior chambers of the eye. The Eulerian mesh encompasses the volume of the corneoscleral shell as well as a region surrounding the eye to account for possible equatorial expansion and posterior translation during loading.

Ocular blast loading was simulated with four different orbital geometries used in previous FE studies: a box orbit (Weaver et al. 2011a) and average, less protective, and more protective orbits (Weaver et al. 2011b) (Figure 35). A rigid box orbit was modeled with deformable gelatin material that surrounded the eye, approximating experimental test setups which used a polycarbonate and polypropylene eye mount to represent the orbit and surrounding soft tissue (Stitzel et al. 2002; Weaver et al. 2011a). Average, less protective, and more protective orbits were modeled based on orbital height and width, brow protrusion angle, and lateral eye protrusion measurements previously collected from Caucasian subjects (Weaver et al. 2010). The average orbit had an average orbital aperture (orbital width and height: 36.26 and 31.61 mm), brow protrusion (27.05 degrees), and eye

protrusion (12.06 mm). The less protective orbit had a larger orbital aperture (orbital width and height: 40.04 and 36.40 mm), less brow protrusion (19.75 degrees) and more eye protrusion (18.23 mm). The more protective orbit had a smaller orbital aperture (orbital width and height: 32.48 and 26.82 mm), more brow protrusion (34.35 degrees), and less eye protrusion (5.89 mm). These three orbits were modeled as rigid parts in the blast simulations.

Twenty-four different blast scenarios (Table 8) were simulated for each of the four orbit geometries, resulting in a total of 96 simulations. Each of the 24 blast scenarios is described by four parameters: blast size (trinitrotoluene, or TNT equivalence), standoff distance (distance from the eye), lateral distance (right or left of the eye) and height (vertical distance). Two blast sizes were modeled to represent 0.45 kg (1 lb) and 2.27 kg (5 lb) TNT equivalent blasts. These are relatively small blasts that are similar in explosive capacity to what would be expected from a small IED. A firebomb, molotov cocktail, or postal explosive device may be on the order of 0.45 kg, while a typical pipe bomb is on the order of 2.27 kg (Sullivan 2002). Each of these blast sizes was simulated in 12 different locations (Figure 35). Standoff distance was varied between two locations at 1.52 m (5 ft) and 3.05 m (10 ft) anterior to the cornea. Lateral distance was varied between three locations: directly in front of the eye with no lateral offset at 0.00 m, or offset by 1.83 m (6 ft) to the left or right of the eye. The height of the blast was modeled as either a "free air" blast located at eye level (defined as 0.00 m) or a "ground" blast located 1.68 m (5.5 ft) inferior to the eye at ground-level.

Table 8: Test matrix of blast scenarios simulated for each orbit geometry.

ID#	Blast Size: TNT Equivalence (kg)	X-offset: standoff distance (m)	Y-offset: lateral distance (m)	Z-offset: vertical distance (m)	Location Description
1	2.27	1.52	0.00	0.00	Eye Level, No Offset
2	2.27	1.52	1.83	0.00	Eye Level, Right Offset
3	2.27	1.52	-1.83	0.00	Eye Level, Left Offset
4	2.27	1.52	0.00	-1.68	Ground Level, No Offset
5	2.27	1.52	1.83	-1.68	Ground Level, Right Offset
6	2.27	1.52	-1.83	-1.68	Ground Level, Left Offset
7	2.27	3.05	0.00	0.00	Eye Level, No Offset
8	2.27	3.05	1.83	0.00	Eye Level, Right Offset
9	2.27	3.05	-1.83	0.00	Eye Level, Left Offset
10	2.27	3.05	0.00	-1.68	Ground Level, No Offset
11	2.27	3.05	1.83	-1.68	Ground Level, Right Offset
12	2.27	3.05	-1.83	-1.68	Ground Level, Left Offset
13	0.45	1.52	0.00	0.00	Eye Level, No Offset
14	0.45	1.52	1.83	0.00	Eye Level, Right Offset
15	0.45	1.52	-1.83	0.00	Eye Level, Left Offset
16	0.45	1.52	0.00	-1.68	Ground Level, No Offset
17	0.45	1.52	1.83	-1.68	Ground Level, Right Offset
18	0.45	1.52	-1.83	-1.68	Ground Level, Left Offset
19	0.45	3.05	0.00	0.00	Eye Level, No Offset
20	0.45	3.05	1.83	0.00	Eye Level, Right Offset
21	0.45	3.05	-1.83	0.00	Eye Level, Left Offset
22	0.45	3.05	0.00	-1.68	Ground Level, No Offset
23	0.45	3.05	1.83	-1.68	Ground Level, Right Offset
24	0.45	3.05	-1.83	-1.68	Ground Level, Left Offset
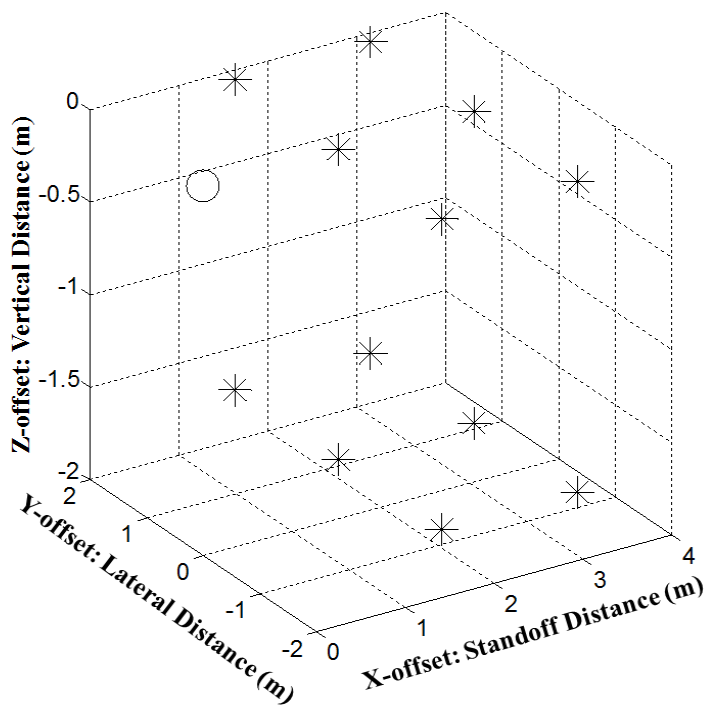
Figure 35: The 12 blast locations simulated are designated with asterisks in relation to the eye (circle located at the origin).
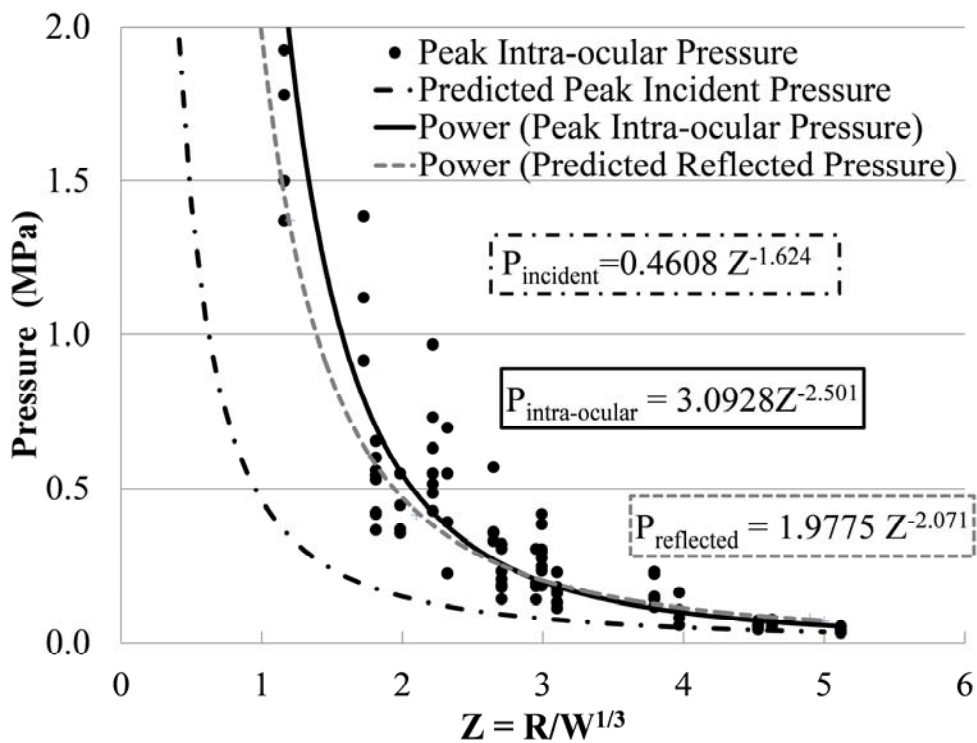
Figure 36: Peak intra-ocular pressure versus normalized blast parameter, Z, for the 96 blast scenarios, plotted with predicted peak incident and reflected pressures.
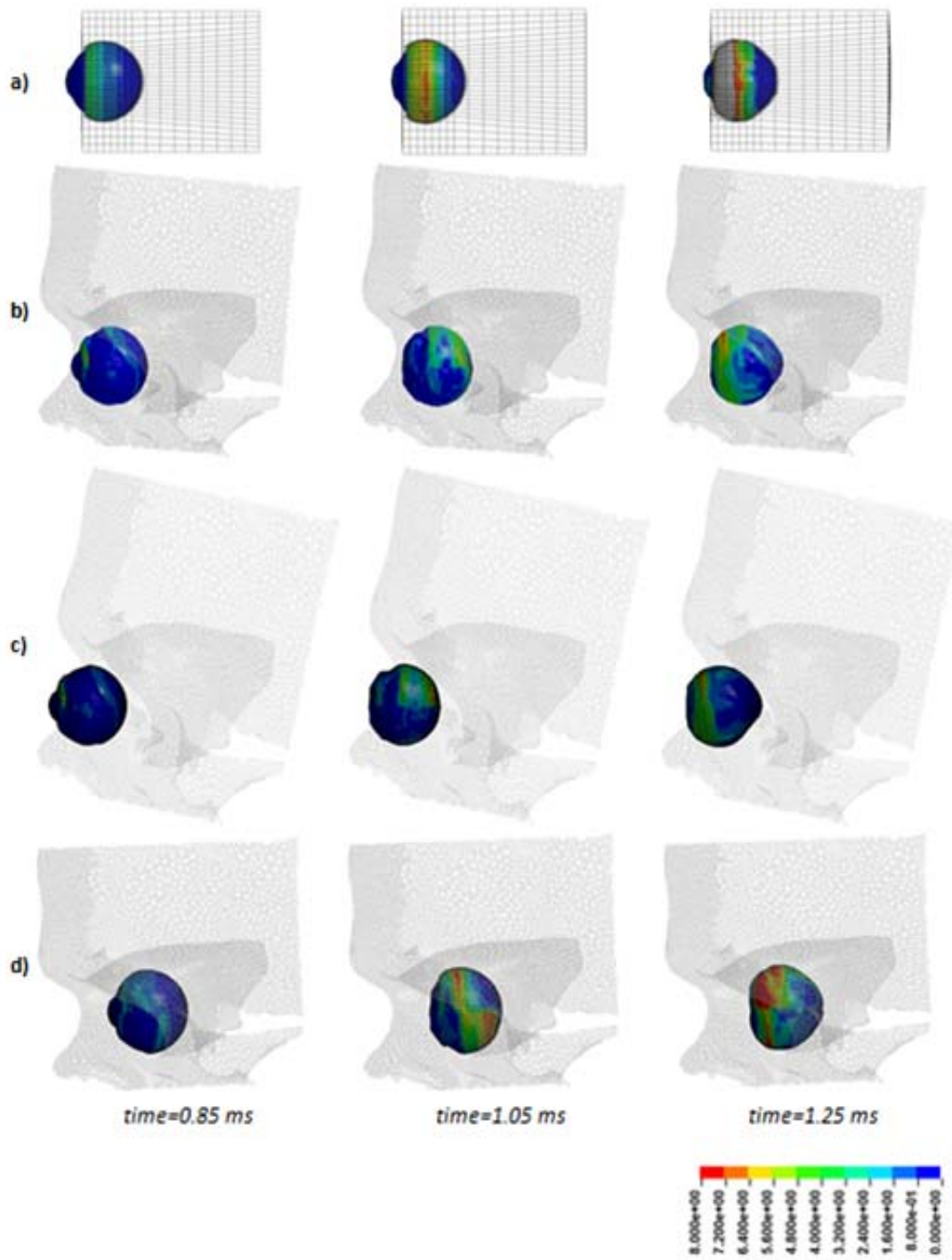
Figure 37: Maximum principal stress (MPa) in the corneoscleral shell of the eye model during a 0.45 kg TNT equivalent 1.52 m standoff blast with no offset (Blast ID# 13) with the a) box orbit, b) average orbit, c) less protective orbit, d) more protective orbit. The maximum principal stress reached 10.22 MPa for the box orbit (a), 10.80 MPa for the average orbit (b), 9.45 MPa for the less protective orbit (c), and 11.55 MPa for the more protective orbit (d).

The blast wave loading was based on an implementation of the CONWEP (CONventional WEApons) software into LS-Dyna (Livermore Software Technology Corporation, Livermore, CA) as outlined by Schwer (Schwer March 2009). In this model, the pressure wave characteristics for a specific charge mass and range combination are calculated utilizing the cube-root scaled distance, Z (a function of TNT equivalent charge mass and charge location), and a set of parameterized power fit equations representing the pressure wave characteristics of the blast wave as a function of the scaled distance.

The cube-root scaling law says that explosive charges of similar geometry will produce self-similar blast waves at identical scaled distances. Using Equation 1, the scaled distance, Z, is computed using the distance of the eye from the blast, R, and the charge mass, W. This scaled distance was used to parameterize an extensive collection of experimental data into forms used by CONWEP, and implemented in LS-Dyna using the *Load_Blast keyword. The *Load_Blast implementation requires inputs of the explosive equivalent TNT mass, the location of the center of the charge, the blast type (free air or ground) and the segments to which the calculated pressure history should be applied. Peak incident pressures (*Pmax*), impulses (*Imax*), and time of arrival (*TOA*) can be calculated using a power fit series as a function of Z for any charge weight and range combination (Kingery April 1984).

$$Z = \frac{R}{W^{\frac{1}{3}}} \qquad \text{(Eqn. 1)}$$

This calculated blast wave was used to define the surface loading and was applied to the corneoscleral shell elements that are unprotected by the orbit. It is important to note two simplifications made in the blast modeling. The blast wave was modeled with the simplifying assumption that surfaces normal to the blast see a reflected pressure, while surfaces with an angle of incidence greater than 90 degrees see the incident pressure. For the blast scenarios considered in free air, the reflected pressure seen by the surface normal to the blast is on the order of 2-8.5 times the calculated maximum incident overpressure (Stuhmiller 1991). Additionally, reflections of the blast pressure off the surface geometry are not calculated, meaning any effects of the facial contours of the orbit on the blast wave itself were not considered.

Ocular Injury Risk Prediction
Injury risk curves were developed for eye injuries including hyphema (HY), lens dislocation (LD), retinal damage (RD), and globe rupture (GR). The curves compute ocular injury risk from 1) maximum principal stress in the corneoscleral shell (filtered with SAE 3000 Hz) and 2) peak intra-ocular pressure averaged from four elements in the center of the vitreous of the eye model (filtered with SAE 10000 Hz). The risk curves were developed from published curves in the literature and the results of matched experimental and computational tests (Kennedy and Duma 2011; Weaver et al. 2011a).

Globe Rupture Risk Prediction
Stress and pressure-based GR risk curves were developed using data from a 79 projectile matched experimental and computational study (Weaver et al. 2011a). A survival analysis for arbitrarily censored data was performed in Minitab (v 15.1.30.0, Minitab Inc, State College, PA) to generate the GR risk curves (Figure 38). The survival analysis was evaluated using a Weibull distribution with maximum likelihood estimation. The equation for injury risk based on survival analysis is provided in Equation 2, where x is the measure used to calculate risk (either stress or pressure), and a and b are values provided in Table 9.

$$InjuryRisk,\% = \left[1 - e^{-\left(\frac{x}{a}\right)^b} \right] * 100 \qquad \text{(Eqn. 2)}$$
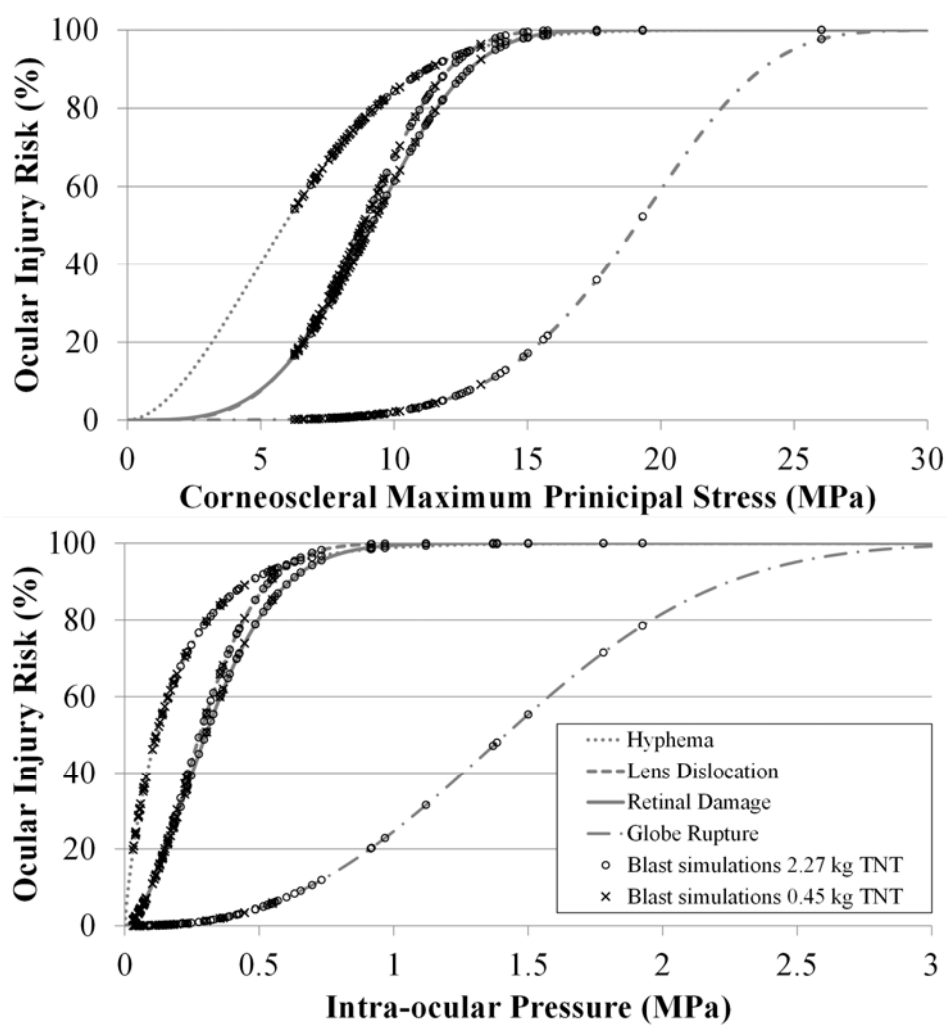
Figure 38: Risk curves for hyphema, lens dislocation, retinal damage, and globe rupture calculated from maximum principal stress in the corneoscleral shell elements (top) or intra-ocular pressure in the center of the vitreous (bottom). The calculated risks from the blast simulations are plotted on the curves, and are stratified by 2.27 kg versus 0.45 kg TNT equivalent blast size.

Table 9: Parameter values for risk curves for different ocular injuries calculated using different measures. Values highlighted in gray were obtained from Kennedy et al (3).

Eye Injury	Measure, *x*	*a*	*b*	Source
Globe Rupture (GR)	Stress (MPa)	20.41040 (MPa)	5.44749	Developed in this study
Globe Rupture (GR)	Pressure (MPa)	1.63013 (MPa)	2.58763	
Hyphema (HY)	Normalized Energy (kJ/m^2)	14.23320 (kJ/m^2)	1.94012	Kennedy and Duma 2011
Lens Dislocation (LD)	Normalized Energy (kJ/m^2)	19.01200 (kJ/m^2)	4.03800	
Retinal Damage (RD)	Normalized Energy (kJ/m^2)	19.82630 (kJ/m^2)	3.73625	
Globe Rupture (GR)	Normalized Energy (kJ/m^2)	38.52490 (kJ/m^2)	5.73194	

Hyphema, Lens Dislocation, and Retinal Damage Risk Prediction

For each simulation, the stress- or pressured-based GR injury risk was correlated to risk for HY, LD, and RD using risk curves based on normalized energy (Kennedy and Duma 2011). Kennedy and Duma developed the normalized energy-based risk curves defined by Equation 2 and parameters in Table 9 using survival analysis with a Weibull distribution and maximum likelihood estimation. In the current study, Equation 3 was solved to calculate normalized energy from the GR risk calculated in the blast simulation, *Injury Risk, %$_{GR}$*. Note that Equation 3 is the equivalent of solving Equation 2 for *x* using the GR parameter values reported by Kennedy et al. (*a*=38.52490 kJ/m^2, *b*=5.73194).

$$Normalized\_Energy = \left[-38.52490^{5.73194} In\left(-InjuryRisk,\%_{GR}+1\right)\right]^{\frac{1}{5.73194}} \quad \text{(Eqn. 3)}$$

Once normalized energy was determined for a given blast simulation, it was input into Equation 2 as *x*, along with the parameter values for HY, LD, and RD (from Table 9), to calculate risk of HY, LD, and RD injury. The resulting HY, LD, RD, and GR injury risk curves are reported in Figure 38.

Results

The peak intra-ocular pressure data was validated by examining the predicted peak incident pressure calculated from the parameterized power fit series used by CONWEP and the reflected pressure coefficient. Figure 36 shows the peak intra-ocular pressure data fit with a power trend line for all 96 blast scenarios (R^2=0.88). The parameterized power series equation used in CONWEP for peak incident pressure is also plotted. The pressure seen by a surface normal to the blast in free air is on the order of 2-5 times the calculated peak incident overpressure (Stuhmiller 1991), and using a calculated reflection coefficient (a function of Z, which varies from 2-8.5 for the blast scenarios considered here), the predicted reflected pressure seen by the eye reasonably matches the intra-ocular pressure. The corneoscleral maximum principal stress data also fit a power series equation well (R^2=0.61).

For a given blast scenario, the magnitude, timing, and distribution of maximum principal stress in the corneoscleral shell varied between the four orbital geometries simulated (Figure 37). In this example of a 0.45 kg TNT equivalent 1.52 m standoff blast (Blast ID# 13), corneoscleral stress was lowest with the less protective orbit (9.45 MPa) compared to the box (10.22 MPa), average (10.80 MPa), and more protective (11.55 MPa) orbits. Blast-induced compression of the eye against the more confined geometry of the average and more protective orbits is likely the cause of the higher corneoscleral stresses.

The peak corneoscleral maximum principal stress and intra-ocular pressure is provided in the Table 10 for each of the 96 blast scenarios, along with the calculated risk for HY, LD, RD, and GR using the developed stress-based or pressure-based risk curves. The stress-based and pressure-based risk for HY, LD, RD, and GR is plotted on the risk curves in Figure 38 for each of the 96 blast scenarios, stratifying for blast size. Peak corneoscleral stress ranged from 6.27 MPa (Blast ID# 9, less protective orbit) to 26.03 MPa (Blast ID# 1, less protective orbit). Peak intra-ocular pressure ranged from 0.03 MPa (Blast ID# 23-24, box orbit and Blast ID# 24, less protective orbit) to 1.93 MPa (Blast ID# 1, box orbit). Overall, higher stresses and pressures were observed with the larger blast size (2.27 kg TNT equivalent) and in blast scenarios where the distance between the blast and the eye was reduced.

Table 10: Peak corneoscleral maximum principal stress and intra-ocular pressure measured in the 96 blast scenarios. The risk of hyphema, lens dislocation, retinal damage, and globe rupture is reported based on the stress-based or pressure-based risk curves. See Table 1 for blast conditions specified for each ID#.

Orbit	ID#	Stress (MPa)	Pressure (MPa)	Hyphema Risk (%)		Lens Dislocation Risk (%)		Retinal Damage Risk (%)		Globe Rupture Risk (%)	
				Stress	*Pressure*	*Stress*	*Pressure*	*Stress*	*Pressure*	*Stress*	*Pressure*
Box	1	19.32	1.93	99.80	99.97	100.00	100.00	99.99	100.00	52.36	78.51
	2	12.44	0.56	93.73	93.33	92.50	91.54	87.28	86.10	6.52	6.10
	3	12.31	0.43	93.39	88.07	91.69	77.54	86.29	71.04	6.17	3.04
	4	11.84	1.12	92.02	99.30	88.26	99.98	82.28	99.83	5.02	31.52
	5	14.85	0.73	97.85	96.74	99.40	98.21	97.91	95.50	16.21	11.84
	6	12.85	0.97	94.72	98.74	94.68	99.88	90.11	99.30	7.73	22.86
	7	10.01	0.70	84.36	96.24	67.53	97.48	61.45	94.24	2.04	10.50
	8	9.73	0.31	82.81	79.65	63.53	55.86	57.76	50.82	1.75	1.30
	9	11.33	0.23	90.29	71.52	83.62	39.31	77.23	36.21	3.97	0.65
	10	11.47	0.57	90.79	93.61	84.99	92.20	78.69	86.91	4.24	6.38
	11	10.60	0.24	87.28	71.79	75.37	39.78	68.91	36.63	2.78	0.66
	12	9.53	0.30	81.64	79.52	60.60	55.55	55.10	50.55	1.57	1.29
	13	10.22	0.45	85.46	89.12	70.42	80.42	64.16	73.93	2.28	3.43
	14	7.85	0.17	69.43	61.63	35.76	24.73	33.11	23.42	0.55	0.29
	15	9.11	0.13	78.98	53.26	54.32	16.12	49.45	15.73	1.23	0.15
	16	13.26	0.20	95.57	65.86	96.34	30.30	92.48	28.32	9.10	0.41
	17	8.70	0.12	76.13	49.69	48.14	13.26	43.97	13.12	0.96	0.11
	18	9.18	0.14	79.47	55.69	55.44	18.33	50.45	17.72	1.28	0.18
	19	7.31	0.10	64.63	46.19	28.58	10.84	26.82	10.89	0.37	0.08
	20	6.57	0.07	57.41	35.83	20.03	5.56	19.24	5.88	0.21	0.03
	21	6.42	0.06	55.87	30.26	18.50	3.64	17.87	3.98	0.18	0.02
	22	7.09	0.07	62.56	36.18	25.87	5.70	24.43	6.01	0.31	0.03
	23	7.03	0.03	61.98	20.77	25.16	1.48	23.80	1.73	0.30	0.00
	24	8.45	0.03	74.27	19.81	44.41	1.33	40.69	1.57	0.82	0.00
Average Orbit	1	15.76	1.78	98.62	99.94	99.84	100.00	99.16	100.00	21.69	71.51
	2	11.27	0.66	90.06	95.52	83.02	96.26	76.60	92.35	3.86	9.02
	3	11.18	0.53	89.72	92.45	82.08	89.37	75.62	83.54	3.70	5.34
	4	15.02	1.38	98.02	99.75	99.52	100.00	98.22	99.99	17.15	48.04
	5	11.32	0.52	90.25	91.96	83.52	88.08	77.13	82.08	3.95	4.97
	6	12.74	0.55	94.47	93.04	94.15	90.83	89.40	85.26	7.39	5.83
	7	8.20	0.39	72.32	86.15	40.73	72.28	37.46	65.93	0.69	2.46
	8	7.78	0.19	68.83	64.85	34.79	28.89	32.26	27.09	0.52	0.38
	9	9.26	0.32	79.93	80.96	56.52	58.95	51.41	53.60	1.34	1.47
	10	8.54	0.36	74.95	84.03	45.75	66.65	41.86	60.63	0.86	1.97
	11	9.62	0.42	82.17	87.68	61.93	76.48	56.30	69.99	1.65	2.91
	12	8.65	0.30	75.77	78.66	47.39	53.59	43.31	48.80	0.93	1.19
	13	10.80	0.55	88.17	93.04	77.81	90.83	71.30	85.26	3.07	5.83
	14	6.63	0.23	58.02	71.12	20.66	38.59	19.81	35.59	0.22	0.63
	15	8.89	0.18	77.48	63.64	51.00	27.26	46.50	25.65	1.07	0.34
	16	7.95	0.31	70.28	79.61	37.16	55.77	34.34	50.74	0.59	1.30
	17	8.93	0.15	77.76	57.43	51.61	20.05	47.04	19.26	1.10	0.21
	18	9.38	0.23	80.72	71.12	58.38	38.59	53.08	35.59	1.44	0.63
	19	8.83	0.08	77.06	38.89	50.10	6.87	45.70	7.14	1.04	0.04
	20	7.67	0.07	67.88	35.12	33.29	5.29	30.95	5.61	0.48	0.03
	21	7.68	0.08	67.97	37.21	33.43	6.13	31.07	6.43	0.49	0.03
	22	8.14	0.05	71.84	28.66	39.87	3.19	36.71	3.52	0.67	0.01
	23	8.65	0.04	75.77	24.43	47.39	2.17	43.31	2.47	0.93	0.01
	24	7.88	0.04	69.69	24.43	36.18	2.17	33.48	2.47	0.56	0.01

Orbit	ID#	Stress (MPa)	Pressure (MPa)	Hyphema Risk (%)		Lens Dislocation Risk (%)		Retinal Damage Risk (%)		Globe Rupture Risk (%)	
				Stress	Pressure	Stress	Pressure	Stress	Pressure	Stress	Pressure
Less Protective Orbit	1	26.03	1.37	100.00	99.73	100.00	100.00	100.00	99.99	97.68	47.15
	2	10.68	0.54	87.62	92.86	76.30	90.39	69.82	84.73	2.89	5.68
	3	11.80	0.60	91.89	94.41	87.92	94.02	81.89	89.24	4.92	7.31
	4	14.18	0.92	97.06	98.46	98.62	99.77	96.25	98.94	12.85	20.25
	5	10.95	0.49	88.81	90.85	79.56	85.15	73.06	78.86	3.31	4.27
	6	10.80	0.43	88.17	88.18	77.81	77.83	71.30	71.32	3.07	3.07
	7	9.10	0.55	78.88	93.04	54.10	90.83	49.25	85.26	1.22	5.83
	8	7.94	0.18	70.19	63.28	37.02	26.80	34.21	25.25	0.58	0.33
	9	6.27	0.21	54.30	67.93	17.04	33.37	16.56	31.02	0.16	0.48
	10	8.80	0.33	76.85	81.80	49.64	61.01	45.30	55.46	1.02	1.59
	11	7.60	0.28	67.26	76.70	32.35	49.34	30.13	45.03	0.46	1.00
	12	6.87	0.38	60.42	85.71	23.30	71.10	22.16	64.81	0.27	2.34
	13	9.45	0.36	81.15	83.74	59.42	65.90	54.02	59.94	1.50	1.92
	14	6.91	0.13	60.82	52.20	23.76	15.23	22.56	14.92	0.27	0.14
	15	6.28	0.11	54.41	48.11	17.14	12.12	16.65	12.08	0.16	0.10
	16	7.76	0.18	68.66	63.82	34.52	27.49	32.02	25.86	0.51	0.35
	17	8.05	0.12	71.11	49.17	38.58	12.88	35.58	12.77	0.63	0.10
	18	9.63	0.23	82.23	71.25	62.08	38.83	56.43	35.80	1.66	0.63
	19	7.71	0.16	68.23	59.89	33.84	22.70	31.43	21.62	0.50	0.25
	20	8.24	0.06	72.64	30.65	41.32	3.76	37.98	4.10	0.71	0.02
	21	7.66	0.07	67.79	36.18	33.16	5.70	30.83	6.01	0.48	0.03
	22	6.40	0.04	55.66	24.43	18.30	2.17	17.70	2.47	0.18	0.01
	23	7.11	0.04	62.75	23.98	26.11	2.08	24.64	2.37	0.32	0.01
	24	8.47	0.03	74.43	20.77	44.70	1.48	40.95	1.73	0.83	0.00
More Protective Orbit	1	17.60	1.50	99.48	99.84	99.99	100.00	99.92	100.00	35.99	55.35
	2	13.99	0.42	96.79	87.62	98.28	76.30	95.63	69.81	11.99	2.89
	3	12.56	0.37	94.04	84.45	93.19	67.75	88.16	61.66	6.85	2.06
	4	15.60	0.92	98.51	98.44	99.79	99.76	99.00	98.91	20.65	20.10
	5	11.23	0.49	89.91	90.85	82.60	85.15	76.17	78.86	3.79	4.27
	6	13.80	0.63	96.51	95.07	97.89	95.40	94.93	91.11	11.18	8.25
	7	8.70	0.23	76.13	70.56	48.14	37.64	43.97	34.76	0.96	0.60
	8	8.12	0.19	71.68	64.34	39.58	28.19	36.46	26.47	0.66	0.36
	9	7.83	0.14	69.26	55.47	35.48	18.12	32.87	17.53	0.54	0.18
	10	7.07	0.36	62.37	83.74	25.63	65.90	24.22	59.94	0.31	1.92
	11	8.63	0.19	75.62	64.17	47.09	27.96	43.05	26.27	0.92	0.36
	12	9.42	0.25	80.97	73.46	58.97	42.85	53.62	39.32	1.47	0.76
	13	11.55	0.37	91.05	84.59	85.70	68.12	79.45	62.00	4.39	2.09
	14	7.55	0.18	66.82	63.53	31.69	27.12	29.54	25.53	0.44	0.34
	15	8.32	0.16	73.27	59.49	42.49	22.25	39.00	21.22	0.75	0.25
	16	10.07	0.14	84.68	55.25	68.37	17.90	62.23	17.34	2.11	0.17
	17	8.15	0.14	71.92	55.69	40.01	18.33	36.84	17.72	0.67	0.18
	18	9.58	0.22	81.94	70.28	61.34	37.17	55.77	34.34	1.61	0.59
	19	8.77	0.06	76.62	30.26	49.15	3.64	44.86	3.98	1.00	0.02
	20	8.37	0.05	73.66	28.25	43.22	3.08	39.65	3.41	0.78	0.01
	21	7.00	0.06	61.69	31.80	24.80	4.12	23.49	4.46	0.29	0.02
	22	7.19	0.06	63.51	30.49	27.09	3.71	25.50	4.05	0.34	0.02
	23	7.07	0.05	62.37	28.82	25.63	3.24	24.22	3.56	0.31	0.01
	24	8.77	0.04	76.64	23.54	49.19	1.99	44.90	2.28	1.00	0.01

The stress-based and pressure-based risks for each ocular injury were well correlated with each other with R^2 values of 0.51, 0.63, 0.65, and 0.57 for HY, LD, RD, and GR, respectively. Risk of HY ranged from 54-100% using the stress criteria and 20-100% using the pressure criteria. For 75% of the cases, the stress-based and

pressure-based risk of HY is above 69% and 49%, respectively. Risk of LD ranged from 17-100% using the stress criteria and 1.3-100% using the pressure criteria. For 50% of the cases, the stress-based and pressure-based risk of LD is above 50% and 38%, respectively. Risk of RD ranged from 17-100% using the stress criteria and 1.6-100% using the pressure criteria. For 50% of the cases, the stress-based and pressure-based risk of RD is above 45% and 35%, respectively. Risk of GR ranged from 0.2-98% using the stress criteria and 0-79% using the pressure criteria. For 75% of the cases, the stress-based and pressure-based risk of GR is below 4%. For 90% of the cases, the GR risk based on stress and pressure is below 10% and 11%, respectively. Only 2.27 kg TNT equivalent blasts at a 1.52 m standoff distance resulted in a risk of GR above 10%.

When averaging the peak corneoscleral stresses from the 24 simulations of each orbital geometry, the highest stresses were observed for the box orbit (10.31 MPa), followed by the more protective (9.87 MPa), average (9.62 MPa), and less protective (9.36 MPa) orbits. The influence of orbital geometry on corneoscleral stress varied depending on the blast conditions (Figure 39). The box orbit resulted in the highest corneoscleral stress in 10 blast scenarios (ID#: 5, 7-12, 14-16), with the majority of these being 2.27 kg TNT equivalent blasts at 1.52 m standoff distance. The box orbit surrounds the eye with gelatin which is not present in the other three orbits, and this gelatin may play a role in the higher corneoscleral stresses observed with the box orbit. The more protective orbit resulted in the highest corneoscleral stress in seven blast scenarios (ID#: 2-4, 6, 13, 20, 24), with five of these being offset blasts. It is possible that offset blasts cause higher stresses through blast-induced compression of the eye against the rigid, more protective orbit which surrounds the eye more considerably. The average orbit produced the highest corneoscleral stress in five 0.45 kg TNT equivalent blast scenarios located at further distances from the eye (ID#: 17, 19, 21-23). The less protective orbit produced the highest corneoscleral stress in only two blast scenarios (ID#: 1, 18), with all orbital geometries producing nearly equivalent stresses in Blast ID#18. Overall, Figure 39 illustrates lower corneoscleral stresses for smaller blast sizes (0.45 kg TNT equivalent) and decreasing stresses with increasing distance from the blast. A left or right offset for any given geometry results in decreased stresses relative to a centered blast, and ground level blasts also result in decreased stresses (as total distance from the blast increases).
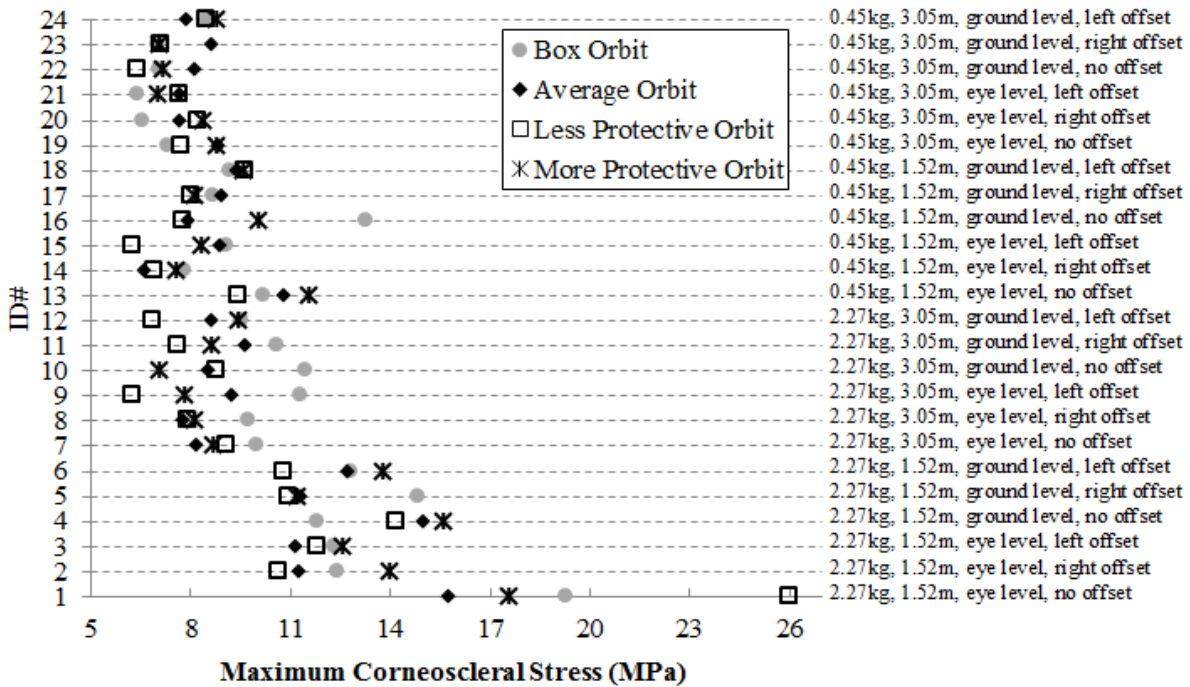
Figure 39: For each of the 24 blast scenarios, the maximum corneoscleral stress is plotted for each orbital geometry.

When averaging the peak intra-ocular pressures from the 24 simulations of each orbital geometry, the highest pressures were observed for the box orbit (0.40 MPa), followed by the average (0.39 MPa), less protective (0.33 MPa), and more protective (0.30 MPa) orbits. The box orbit resulted in the highest intra-ocular pressure in seven blast scenarios (ID#: 1, 5-8, 10, 22), with six of these scenarios being 2.27 TNT equivalent blasts. The average orbit produced the highest intra-ocular pressure in 12 blast scenarios located at ground level and/or offset distances from the eye (ID#: 2, 4, 9, 11, 13-17, 20, 21, 24). The less protective orbit produced the highest intra-ocular pressure in four blast scenarios (ID#: 3, 12, 18, 19), with three of these being offset blast scenarios. The more protective orbit resulted in the highest intra-ocular pressure in only one blast scenario (ID# 23). For 11 blast scenarios, the more protective orbit produced the lowest intra-ocular pressure which may suggest the rigid orbital geometry which closely surrounds the eye prevents some propagation of the blast loading to the eye. Similar to the stress trends observed, Figure 40 illustrates lower intra-ocular pressures for smaller blast sizes (0.45 kg TNT equivalent) and decreasing pressure in scenarios with larger standoff distances, left or right offset, or ground level blasts since the distance of the blast from the eye increases.
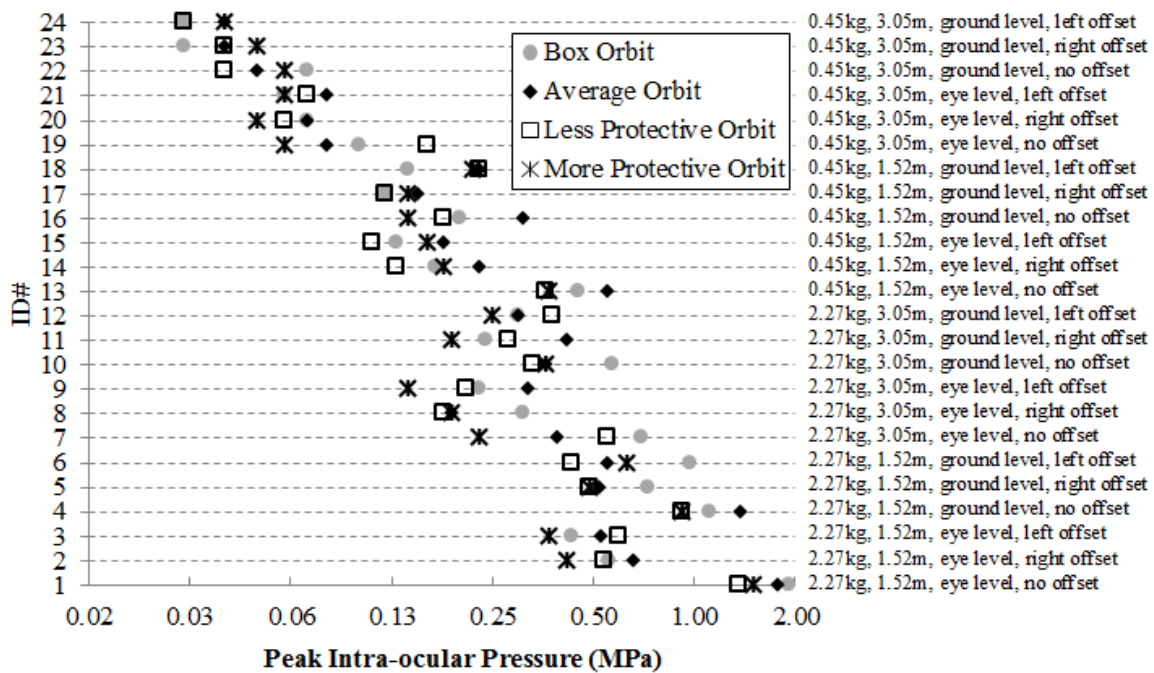
Figure 40: For each of the 24 blast scenarios, the peak intra-ocular pressure on a logarithmic scale is plotted for each orbital geometry.

Discussion

As expected, corneoscleral stress, intra-ocular pressure, and risk of HY, LD, RD, and GR increased when the blast size was larger and when the blast was located nearer to the eye. Orbital geometry affected the observed stresses, pressures, and associated ocular injury risks for the blast conditions simulated.

Orbital geometries that more fully surrounded the eye such as the more protective orbit tended to produce higher corneoscleral stresses, particularly in offset blast scenarios. Inspection of these simulations reveals compression of the eye against the surrounding rigid orbit as the blast wave propagates, contributing to high stresses in the area of the eye in contact with the orbit. As further support, the less protective orbit generally resulted in lower stresses with minimal contact of the eye against the surrounding orbit. Similar trends have been observed in baseball impact simulations with this eye model and these orbital geometries, where greater brow protrusion, less eye

protrusion, and smaller orbital apertures are more protective only if the orbital aperture is large enough to deter contact between the orbit and eye (Weaver et al. 2011b). While the box orbit also produced higher corneoscleral stresses in some simulations, the surrounding gelatin appears to play a more pertinent role rather than compression of the eye against the orbit. The inclusion of a medium such as gelatin to simulate the fat and musculature surrounding the eye within the average, more protective, and less protective orbits may be an important factor to consider in future investigations.

While the more protective orbit produced higher corneoscleral stresses in some blast scenarios, it tended to produce lower intra-ocular pressures in comparison to the other three orbital geometries for a given blast scenario. The more protective orbit produced the lowest intra-ocular pressure in 45% of the simulations and the second lowest intra-ocular pressure in 25% of the simulations. This may indicate that the more protective orbit which more fully surrounds the eye inhibits propagation of the blast wave and reduces the blast loading that is applied to the eye, thus reducing intra-ocular pressure measured at the center of the vitreous.

In a previous study, Bhardwaj et al. (2014) simulated a 2 kg TNT equivalent blast located in front of the eye at a distance of 2.5 m with an eye and orbit scaled to match the average orbital anthropometry used in the current study (Bhardwaj et al. 2014; Weaver et al. 2010). This produced asymmetric loading on the eye that resulted in globe distortion and large deviatoric stresses in the sclera which was suggested to be an indicator for the risk of interfacial failure between the scleral tissue and the orbit. Bhardwaj et al.'s blast conditions were similar to the conditions of Blast ID# 7 with the average orbit (2.27 kg, 3.05 m standoff distance) in this study, and these simulations resulted in similar peak intra-ocular pressures (0.40 MPa versus 0.39 MPa, respectively). However, <0.01% risk for HY, LD, RD, and GR was predicted by Bhardwaj et al., which contrasts the 86%, 72%, 66%, and 3% risks predicted for these injuries in the Blast ID# 7 average orbit simulation. While both studies utilized risk curves published by Kennedy and Duma (2011), the method to calculate risk from pressure measured in the simulations varied, which likely explains the discrepancies (Kennedy and Duma 2011). Bhardwaj et al. correlated the maximum intra-ocular pressure measured in their simulations with the normalized energy of a 11.16 mm aluminum projectile, whereas our approach does not require assumption of a particular projectile size.

Esposito et al. (2013) simulated blasts of varying magnitudes located at various distances in front of the eye in a parametric FE modeling study with a computational eye and orbit model (Esposito et al. 2015). A blast condition representing 50% lethality (1.5 kg TNT equivalent at 1 m) produced peak pressures of 5, 4, 9, and 15 MPa at the corneal apex, vitreous base, equator area, and macula, respectively. Direct comparison to simulations in our study is limited as the nearest location simulated was 1.52 m from the eye. Blast ID# 1 (2.27 kg, 1.5 m) with the average orbit is the most similar blast condition, yet the increased distance of the blast from the eye is likely responsible for the much lower intra-ocular pressure observed (1.78 MPa). Esposito et al.'s blast condition representing lung injury (0.25 kg TNT equivalent at 1 m) produced peak pressures at the corneal apex, vitreous base, equator area, and macula of 0.8, 0.8, 1.3, and 2.3 MPa, which are in the range of the 0.55 MPa intra-ocular pressure observed in Blast ID# 13 (0.45 kg, 1.52 m). Esposito et al.'s blast condition representing tympanic damage (0.02 kg TNT equivalent at 1 m) produced peak pressures at the corneal apex, vitreous base, equator area, and macula of 0.09, 0.08, 0.15, and 0.23 MPa. These pressures are also approaching the 0.55 MPa intra-ocular pressure observed in Blast ID# 13 (0.45 kg, 1.52 m), yet are understandably lower because of the smaller 0.02 kg blast size. Macula pressure was 2.1 MPa for a 0.032 kg TNT equivalent blast at 0.5 m; however, our most similar point of comparison is Blast ID# 13 (0.45 kg, 1.52 m) with 0.55 MPa intra-ocular pressure which varies substantially from the blast size and location simulated by Esposito et al. Macula pressure was 0.75 MPa for a 2 kg TNT equivalent blast at 3 m which is the same order of magnitude as the 0.39 MPa intra-ocular measured in Blast ID# 7 (2.27 kg, 3.05 m). Macula pressure is also expected to be higher than intra-ocular pressure at the center of the vitreous based on the four pressures from the corneal apex to macula reported by Esposito et al. for the three blast conditions described earlier.

Liu et. al (2015) simulated 1 kg TNT equivalent blasts located at 0.75, 1, and 1.25 m standoff distances from the front of the eye with a partial facial orbit. Peak corneoscleral stresses were observed at the limbus with a peak

stress of 6.4 MPa for the blast located at 1.25 m. This blast is larger and closer than Blast ID# 13 (0.45 kg, 1.52 m) which resulted in 10.22 MPa peak stress, and it is smaller and closer than Blast ID# 1 (2.27 kg, 1.52 m) which resulted in 19.32 MPa peak stress. Although direct comparison with our data is limited since the blast conditions vary substantially, results suggest slightly underestimated stresses in the Liu et al. simulations compared to the results of the current study.

Higher risks for lesser severity eye injuries (HY, LD, and RD) were observed in this study compared to GR risk. GR risk was elevated above 20% for only three blasts (ID#: 1, 4, and 6) of the largest size (2.27 kg) and shortest standoff distance (1.52 m), and was less than 12% for all other blast scenarios. Experimentally, the dynamic intra-ocular pressure threshold for human GR has been determined to be 0.97 +/- 0.29 MPa (Bisplinghoff et al. 2009), which correlates well with the elevated GR risk predicted since some or all of the orbital geometries simulated in Blast ID# 1, 4, and 6 produced intra-ocular pressures greater than 0.97 MPa. In the simulations that exceeded the 0.97 MPa dynamic rupture threshold, GR risk ranged from 47-79% (Blast ID# 1, all orbital geometries), 32-48% (Blast ID# 4, box and average orbit), and 23% (Blast ID# 6, box orbit).

Limitations
Blast wave reflections off rigid surfaces such as the orbit models were not accounted for by the modeling approach which presents a limitation. Other studies have demonstrated reflections off facial features around the eye to have an influence on ocular pressure loading and this will be important to account for in future simulations with the VT-WFU eye model (Bhardwaj et al. 2014; Esposito et al. 2015). The extraocular muscles and orbital fat were approximated with gelatin in the box orbit, but were not accounted for in the average, less protective, and more protective orbits. The inclusion of more representative extraocular muscles and orbital fat into the orbital models may affect the results and is a topic of future investigation.

Future Work and Applications
Future work will include validation of the VT-WFU eye model and orbital geometries using experimental data from porcine or human eye specimens subjected to blast loading using a shock tube. Future FE simulations with the VT-WFU eye model will replicate the blast sizes and locations of other studies to directly compare corneoscleral stress, intra-ocular pressure, and injury risk (Bhardwaj et al. 2014; Esposito et al. 2015; Karimi et al. 2016; Liu et al. 2015). The modeling and injury risk prediction approach detailed in this study can be broadly applied to simulate blast loading to the eye with different blast sizes, blast locations, facial anthropometries, and eye protection equipment. The eye model and the injury metrics and risks output from the blast simulations are valuable to the design of eye protection equipment and the mitigation of blast-related eye injuries.

Acknowledgements

CFD and LS-Dyna Parametric Study of Blast Loading on the Eye and Validation with Virginia Tech Experimental Data

In collaboration with Virginia Tech, a test matrix of 9 simulations was structured and formulated to duplicate the experimental tests at Virginia Tech. The blast size (TNT equivalent) and blast location in the test matrix are estimated for CONWEP to produce the appropriate blast pressure in the experiment, but these are tunable parameters for validating the LS-Dyna simulations with the experimental data (Table 11). An additional 45 simulations were included in the test matrix in Table 11 that vary the blast size and blast location to represent scenarios reported in the literature (Bhardwaj et al., 2014; Esposito et al., 2015; Stitzel and Weaver, 2012).

A subcontract with Corvid was signed on 1/27/15 for them to conduct CFD simulations according to the test matrix of 54 blast impact simulations as seen in Table 11. The overall test matrix proposed for this study consisted of simulations that utilize both a finite element model of the eye in LS Dyna using CONWEP as well as external blast loads to the eye using CFD based approaches to validate the CONWEP approach (Table 11). Full CFD efforts to validate the blast boundary conditions for LS Dyna were conducted and the CFD effort was supported as it was previously with simulations in LS Dyna. A CFD based modeling approach was used by Corvid to simulate the tunnel geometry and blast load produced in the experimental tests and determine the boundary conditions that best matched the experiments. The 9 validation simulations were run first and compared to the experimental test data. For these simulations, Wake Forest and Corvid worked together to develop models of the geometries tested in the experiments, devise the modeling approach, formalize boundary conditions, select virtual instrumentation for the tests, define mechanics of materials, and develop the simulations carefully using that information. Models of the isolated eye, box orbit (i.e., synthetic orbit), 3D orbit geometry, and blast tube geometry based on the Virginia Tech experimental tests and the driver pressure data from the experimental tests were provided to Corvid for use in the CFD simulations (Figure 41- Figure 45, Table 12). Corvid used these geometries to conduct CFD simulations of the VT experiments. Corvid Technologies completed the 54 CFD simulations and reported good agreement between the pressure histories achieved in their CFD simulations and the VT blast experiments.

Corvid visited Wake Forest on 5/6/15 to present their simulation results and discuss any additional work that needed to be done to complete the CFD portion of this project. Figure 46 presents a sampling of results from the 9 validation simulations. These results showed strong agreement with peak pressures and wave speed. The 10 psi isolated eye test seen in Figure 46 shows that the pressures remained higher for a longer duration in the experimental tests compared to the computational model, although the pressure magnitudes were very similar. The synthetic orbit 20 psi test showed strong agreement for both sensors. The 3D orbit 30 psi test showed excellent agreement between the nasal sensors, but the agreement between the bottom lateral sensors in the experimental setup and the model was not as strong; this possibly could be due to the CAD construction.

Figure 47, Figure 48, and Figure 49 present a sampling of the 45 simulations of scenarios from literature. These results show the isolated eye provides the most pressure relief. The isolated and box orbit pressure measurements are nearly identical up until the time point where the box orbit geometry shows distinct re-pressurization from reflection off the flat surface. The box orbit re-pressurization is higher than the original blast wave. Also, the face geometry focuses blast around the eye and increases the duration of initial over-pressurization.

During the meeting with Corvid on 5/6/15 it was decided that simulations of the entire face would be beneficial to better understand the effect of facial geometry on pressure wave response. Corvid completed the five additional simulations with full face geometry on 6/15/15. These five simulations were created by using the same setup and parameters as five half-face tests (42, 43, 46, 47, and 48). After completing the additional simulations, Corvid sent the results to Wake Forest. Figure 50 presents a sample from one of the five full-face tests.

Table 11: Test matrix of eye blast simulations matched to VT experiments (#1-9) and for literature comparisons (#10-54).

#	Geometry	Blast pressure (psi)	*Blast size TNT equivalent, kg (estimated)*	Blast location, x: right+, m	*Blast location, y: anterior+, m (estimated)*	Blast location, z: superior+, m
Validation of VT Experiments						
1	Isolated eye	10	*0.36*	0.0	*2.0*	0.0
2		20	*2.1*	0.0	*2.5*	0.0
3		30	*3.0*	0.0	*2.45*	0.0
4	Eye with 'box' orbit (i.e., synthetic orbit)	10	*0.36*	0.0	*2.0*	0.0
5		20	*2.1*	0.0	*2.5*	0.0
6		30	*3.0*	0.0	*2.45*	0.0
7	Eye with 3D orbit (half face)	10	*0.36*	0.0	*2.0*	0.0
8		20	*2.1*	0.0	*2.5*	0.0
9		30	*3.0*	0.0	*2.45*	0.0
Additional Simulations for Comparison.						
10	Isolated eye	Stitzel (2012), ASME	0.5	0.0	1.5	0.0
11		Stitzel (2012), ASME	0.5	0.0	3.0	0.0
12		Stitzel (2012), ASME	0.5	1.5	1.5	0.0
13		Stitzel (2012), ASME	0.5	1.5	3.0	0.0
14		Stitzel (2012), ASME	0.5	0.0	1.5	-1.7
15		Stitzel (2012), ASME	0.5	0.0	3.0	-1.7
16		Stitzel (2012), ASME	0.5	1.5	1.5	-1.7
17		Stitzel (2012), ASME	0.5	1.5	3.0	-1.7
18		Bhardwaj (2014)	2.0	0.0	2.5	0.0
19		Bhardwaj (2014)	2.0	0.0	2.0	-1.5
20		Esposito (2013), 50% lethality	1.5	0.0	1.0	0.0
21		Esposito (2013), lung injury	0.25	0.0	1.0	0.0
22		Esposito (2013), tympanic damage threshold	0.02	0.0	1.0	0.0
23		Esposito (2013), isolethality	2.0	0.0	3.0	0.0
24		Esposito(2013), isopeak pressure	0.032	0.0	0.5	0.0
25	Eye with 'box' orbit (i.e., synthetic orbit)	Stitzel (2012), ASME	0.5	0.0	1.5	0.0
26		Stitzel (2012), ASME	0.5	0.0	3.0	0.0
27		Stitzel (2012), ASME	0.5	1.5	1.5	0.0
28		Stitzel (2012), ASME	0.5	1.5	3.0	0.0
29		Stitzel (2012), ASME	0.5	0.0	1.5	-1.7
30		Stitzel (2012), ASME	0.5	0.0	3.0	-1.7
31		Stitzel (2012), ASME	0.5	1.5	1.5	-1.7
32		Stitzel (2012), ASME	0.5	1.5	3.0	-1.7
33		Bhardwaj (2014)	2.0	0.0	2.5	0.0
34		Bhardwaj (2014)	2.0	0.0	2.0	-1.5
35		Esposito (2013), 50% lethality	1.5	0.0	1.0	0.0
36		Esposito (2013), lung injury	0.25	0.0	1.0	0.0
37		Esposito (2013), tympanic damage threshold	0.02	0.0	1.0	0.0
38		Esposito (2013), isolethality	2.0	0.0	3.0	0.0
39		Esposito(2013), isopeak pressure	0.032	0.0	0.5	0.0
40	Eye with 3D orbit (half face)	Stitzel (2012), ASME	0.5	0.0	1.5	0.0
41		Stitzel (2012), ASME	0.5	0.0	3.0	0.0
42		Stitzel (2012), ASME	0.5	1.5	1.5	0.0
43		Stitzel (2012), ASME	0.5	1.5	3.0	0.0
44		Stitzel (2012), ASME	0.5	0.0	1.5	-1.7
45		Stitzel (2012), ASME	0.5	0.0	3.0	-1.7
46		Stitzel (2012), ASME	0.5	1.5	1.5	-1.7
47		Stitzel (2012), ASME	0.5	1.5	3.0	-1.7
48		Bhardwaj (2014)	2.0	0.0	2.5	0.0
49		Bhardwaj (2014)	2.0	0.0	2.0	-1.5
50		Esposito (2013), 50% lethality	1.5	0.0	1.0	0.0
51		Esposito (2013), lung injury	0.25	0.0	1.0	0.0
52		Esposito (2013), tympanic damage threshold	0.02	0.0	1.0	0.0
53		Esposito (2013), isolethality	2.0	0.0	3.0	0.0
54		Esposito(2013), isopeak pressure	0.032	0.0	0.5	0.0

Table 12: Driver pressures for VT experimental tests.

Test Data			Pk. Driver (psi)	Avg. Pk. Driver (psi)	Stdev Pk. Driver (psi)
Isolated Eye	**10 psi**	27Aug14_Test01	65.15	**67.17**	**1.69**
		20Aug14_Test01	67.32		
		20Aug14_Test02	69.37		
		21Aug14_Test01	68.10		
		21Aug14_Test02	65.90		
	20 psi	11Nov14_Test01	148.89	**162.67**	**21.53**
		12Nov14_Test01	173.76		
		12Nov14_Test02	177.63		
		19Nov14_Test01	126.43		
		19Nov14_Test02	149.00		
		13Nov14_Test02	177.07		
		13Nov14_Test03	185.87		
	30 psi	28Aug14_Tes01_2	261.65	**238.37**	**46.17**
		28Aug14_Test02_2	197.47		
		10Sep14_Test01	276.01		
		10Sep14_Test02	286.46		
		17Sep14_Test01	248.17		
		11Sep14_Test01	242.52		
		18Sep14_Test02	156.30		
Eye in Box/ Synthetic	**10 psi**	15Apr14_Test01	48.39	**53.56**	**5.08**
		07May14_Test02	50.32		
		29Aug13_Test01	55.50		
		16Apr14_Test01	49.66		
		30Aug13_Test02	61.83		
		30Aug13_Test03	55.67		
	20 psi	11Sep13_Test01	209.35	**185.37**	**35.74**
		11Sep13_Test02	199.44		
		12Sep13_Test01	227.19		
		08May14_Test01	147.09		
		11Jun14_Test02	176.73		
		17Apr14_Test01	129.79		
		20Mar14_Test05	208.03		
	30 psi	18Jun14_Test01	278.41	**269.18**	**16.95**
		05Sep13_Test01	292.92		
		11Jun14_Test01	257.89		
		19Jun14_Test01	273.40		
		06Sep13_Test01	243.83		
		06Sep13_Test02	268.64		
Eye in 3D Orbit	**10 psi**	28Aug13_Test01	53.73	**53.00**	**3.33**
		07May14_Test01	49.78		
		29Aug13_Test02	55.59		
		18Mar14_Test02	53.85		
		16Apr14_Test02	49.55		
		30Aug13_Test01	58.33		
		17Apr14_Test02	50.18		
	20 psi	07May14_Test03	150.23	**164.46**	**24.25**
		20May14_Test01	144.29		
		18Sep13_Test02	156.30		
		19Mar14_Test03	205.70		
		25Mar14_Test01	190.36		
		19Sep13_Test01	143.55		
		19Sep13_Test02	144.97		
		13Nov14_Test01	180.30		
	30 psi	04Sep13_Test01	286.39	**263.50**	**15.29**

60
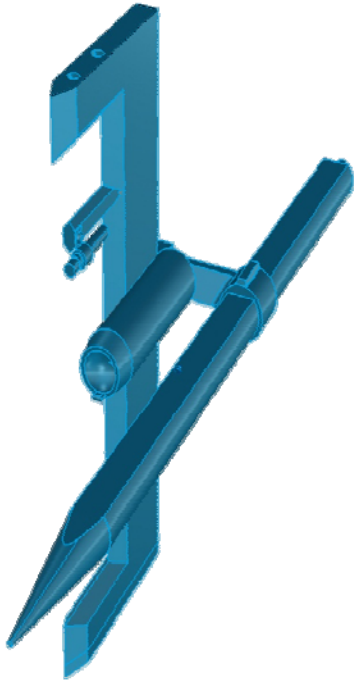
Figure 41: Geometry of base blast tube eye test.
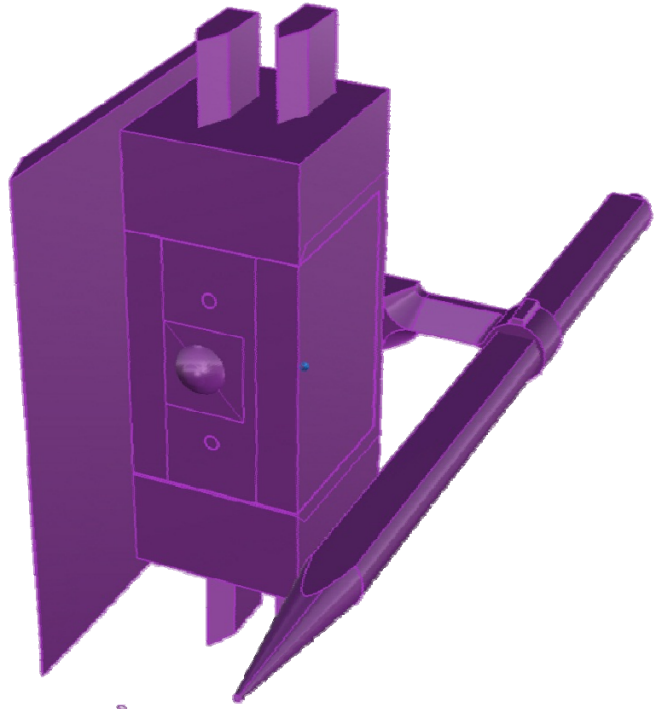
Figure 42: Geometry of box orbit blast tube eye test.

Figure 43: Geometry of anatomical orbit blast tube eye test.
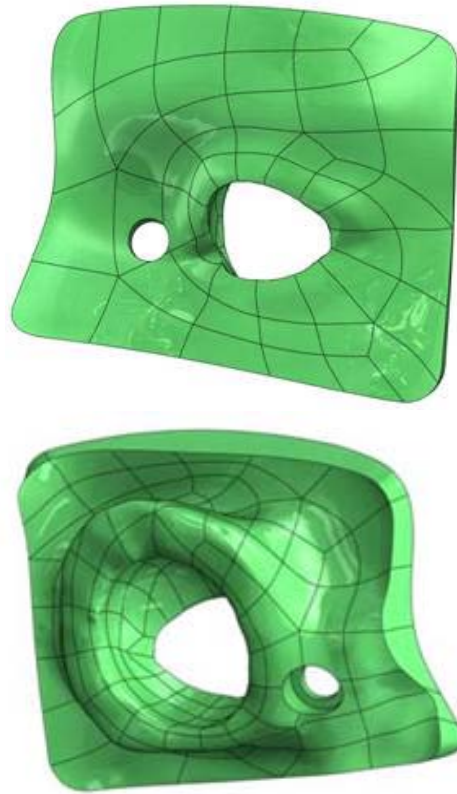
Figure 44: CAD geometry for eye plug used in the anatomical orbit geometry shown in Figure 43.

Figure 45: Full-face geometry used in blast tube eye test.
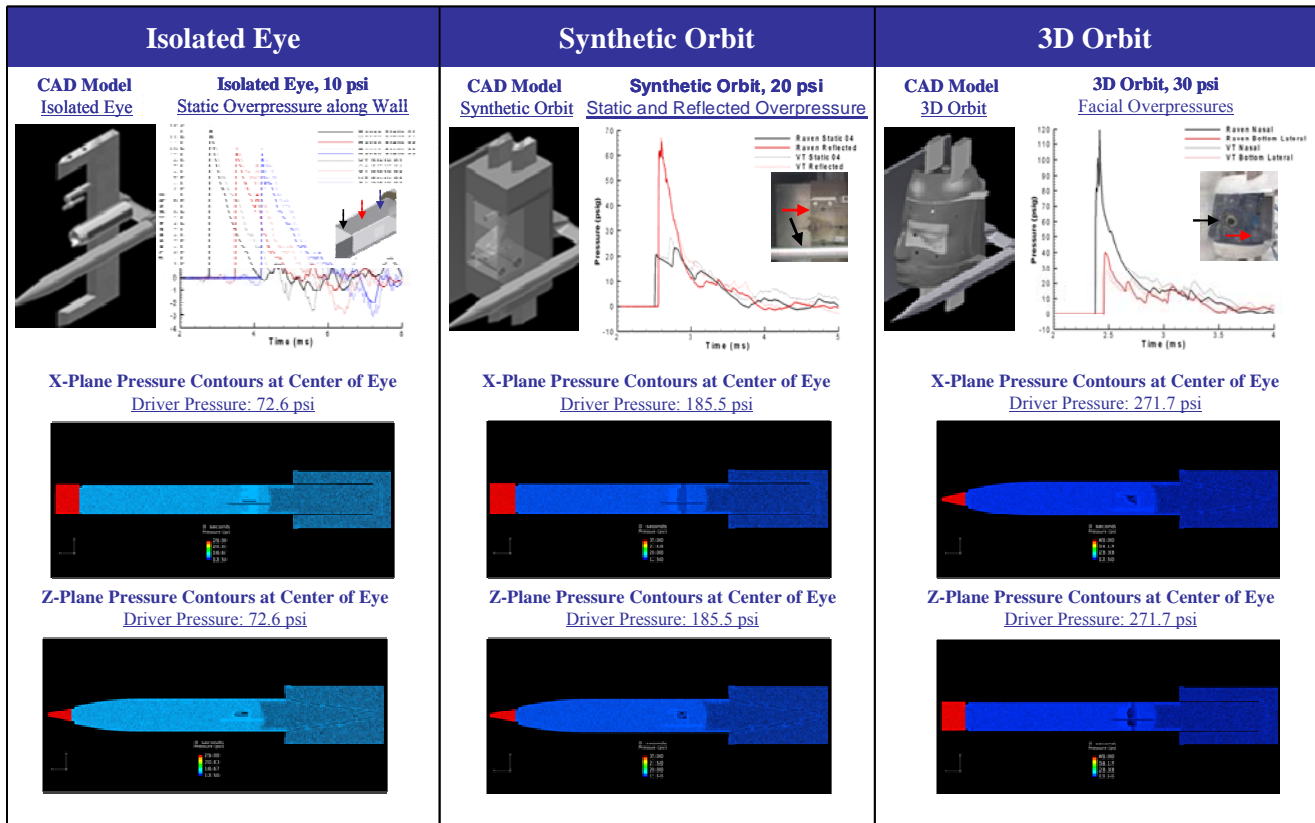
Figure 46: Sample of CFD results from the 9 validation simulations in comparison to experimental data.
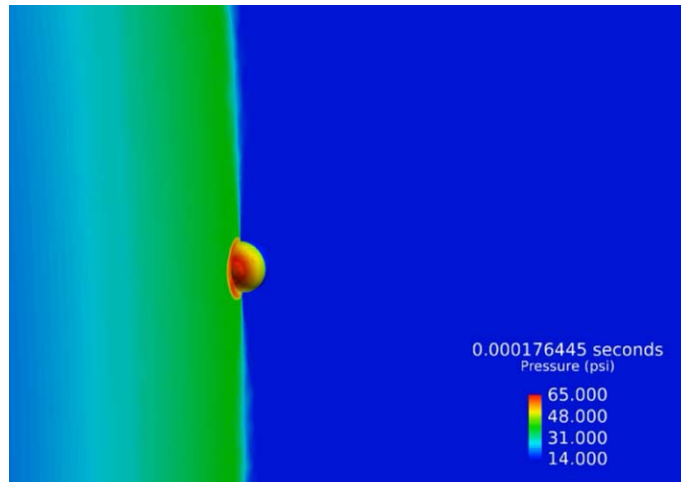
Figure 47: Pressure on isolated eye in case #10 CFD simulation.
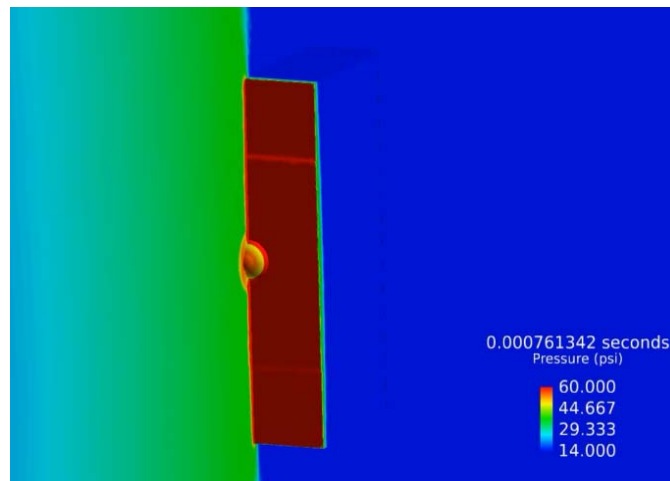
Figure 48: Pressure wave on box orbit in case #33 CFD simulation.
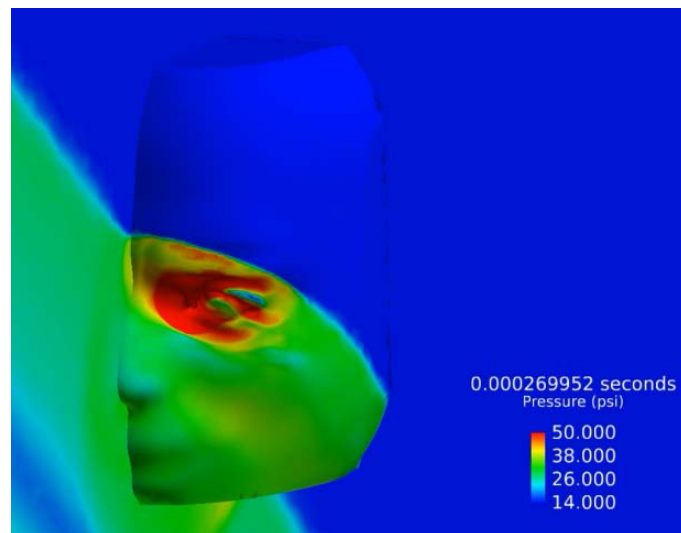
Figure 49: Pressure wave on half face geometry in case #44 CFD simulation.
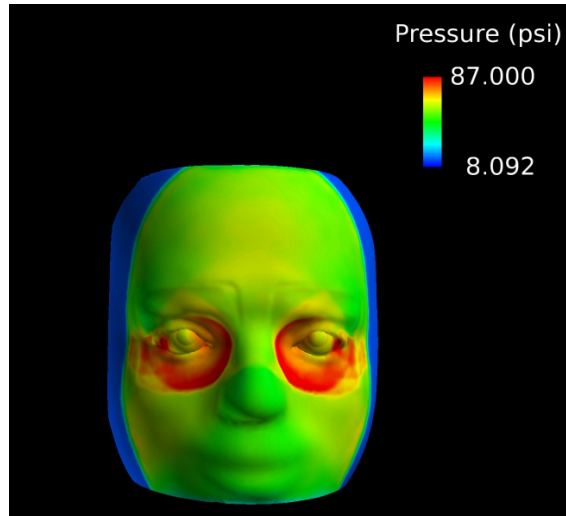
Figure 50: Pressure wave on full face geometry in case #48 CFD simulation.

Wake Forest created videos for a sample of the Corvid's simulations and began processing and plotting the pressure history data for a variety of pressure tap locations (sample shown in Figure 51). The pressure history is used to compare the CFD simulations performed by Corvid with the simulations performed in LS Dyna by Wake Forest. Once the CFD simulations were deemed acceptable to represent the blast boundary conditions, Wake Forest started setting up simulations with a finite element model of the eye in LS Dyna using CONWEP (Table 11). Using HyperMesh, Wake Forest meshed the geometries of the box orbit and isolated eye set up that were used by Virginia Tech for their experimental blast testing (Figure 52).
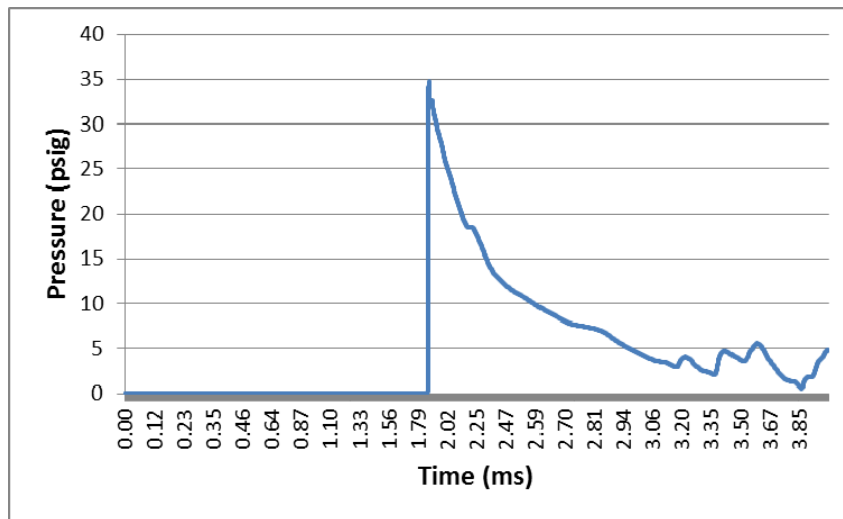
Figure 51: Example of Corvid pressure history data from case 9.
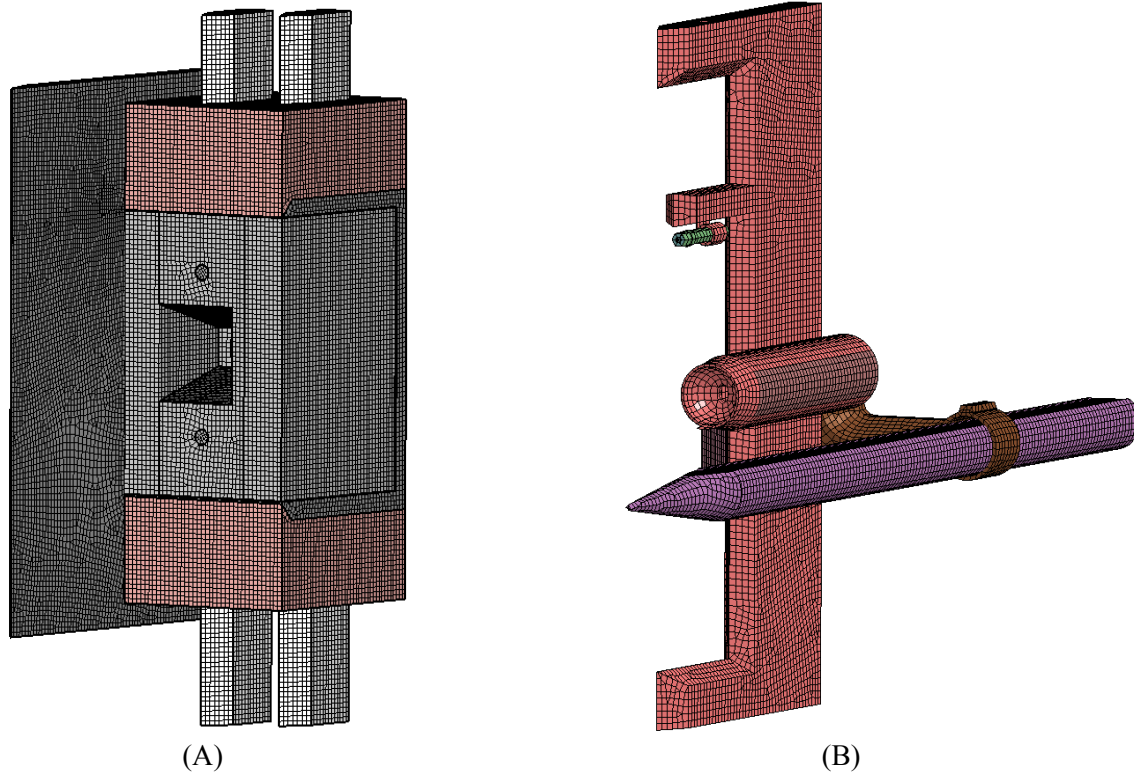
Figure 52: (A) box orbit and (B) isolated eye set up, which were used in blast testing, after being meshed in HyperMesh.

Wake Forest is currently running simulations with a finite element model of the eye in LS Dyna using CONWEP (Table 11). Wake Forest has set up and run the isolated eye validation simulations. The isolated eye orbit was meshed and the eye model (Figure 53) was placed into the isolated eye orbit model as seen in Figure 54. Several initial isolated eye simulations were completed for the first three blast levels (10 psi, 20 psi, and 30 psi) to check initial boundary conditions. Intraocular pressure was measured in the simulations by averaging the peak pressure of four elements located at the center of the Eulerian portion of the eye model, which are depicted in black in Figure 53. The intraocular pressure measurements from the LS-Dyna model for the three blast sizes are shown in Figure 55. The peak pressure measurements for the 10 psi, 20 psi, and 30 psi blasts from the LS Dyna model were 32.9 psi, 53.7 psi, and 143.3 psi, respectively. The average peak pressure measurements from Virginia Tech isolated eye experimental tests were 18.7 psi, 37.0 psi, and 58.0 psi. Although the measurements from these initial LS Dyna simulations were high in comparison to the Virginia Tech tests, the simulations were a first step in verifying boundary conditions between the eye model and the isolated eye geometry provided from Virginia Tech. The results from these initial simulations demonstrated that the isolated eye holder geometry, specifically the holder that supports the eye, may need to be updated to better fit with the LS Dyna eye model. Specifically, the holder may need to be widened so that the eye can be placed more fully into the holder. Previous work evaluating the effect of orbit geometries on eye response to impact demonstrated the sensitivity of the eye to surrounding geometry, so optimizing the holder to better accommodate the eye model is an important next step (Weaver et al., 2011b). Additionally, sensors need to be added to the LS-Dyna model to measure the static, total, and reflected pressure in the same manner as the Virginia Tech experiments. The additional sensors will help to fine tune the blast size and adjust the parameters in CONWEP.

The goal of future work will be to complete all validation simulations of the first three blast tests with the isolated eye set up shown in Table 11 and compare the responses measured in the Wake Forest model with the responses from the Virginia Tech blast experiments and the responses computed by Corvid. Once the CONWEP approach is

validated we can process the remaining 50 simulations. Simulations will be post-processed to look at the injury metrics and injury risk probabilities from the model. In previous work, we have established injury risk curves to predict hyphema, lens dislocation, retinal damage, and globe rupture from vitreous pressure and cornea-sclera stress measured in the eye model (Stitzel et al., 2012) Post-processing of the simulations will involve using the pressure and stress injury metrics and these established risk curves to predict eye injuries.
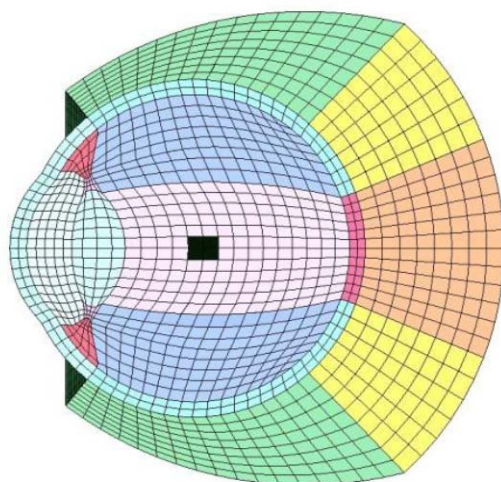
Figure 53: Four elements in black chosen for peak intraocular pressure measurement.
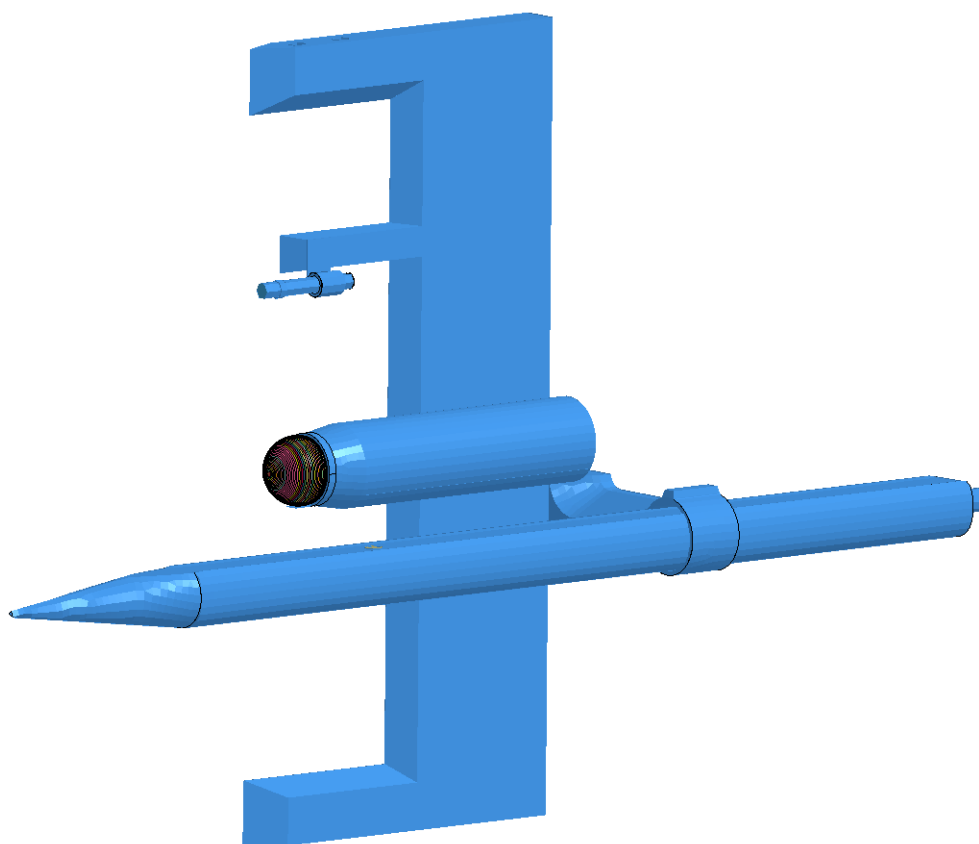
Figure 54: Isolated eye set up with eye model positioned into holder.

66

Blast Pressure (psi)	Intraocular Pressure (psi)
10	
20	
30	
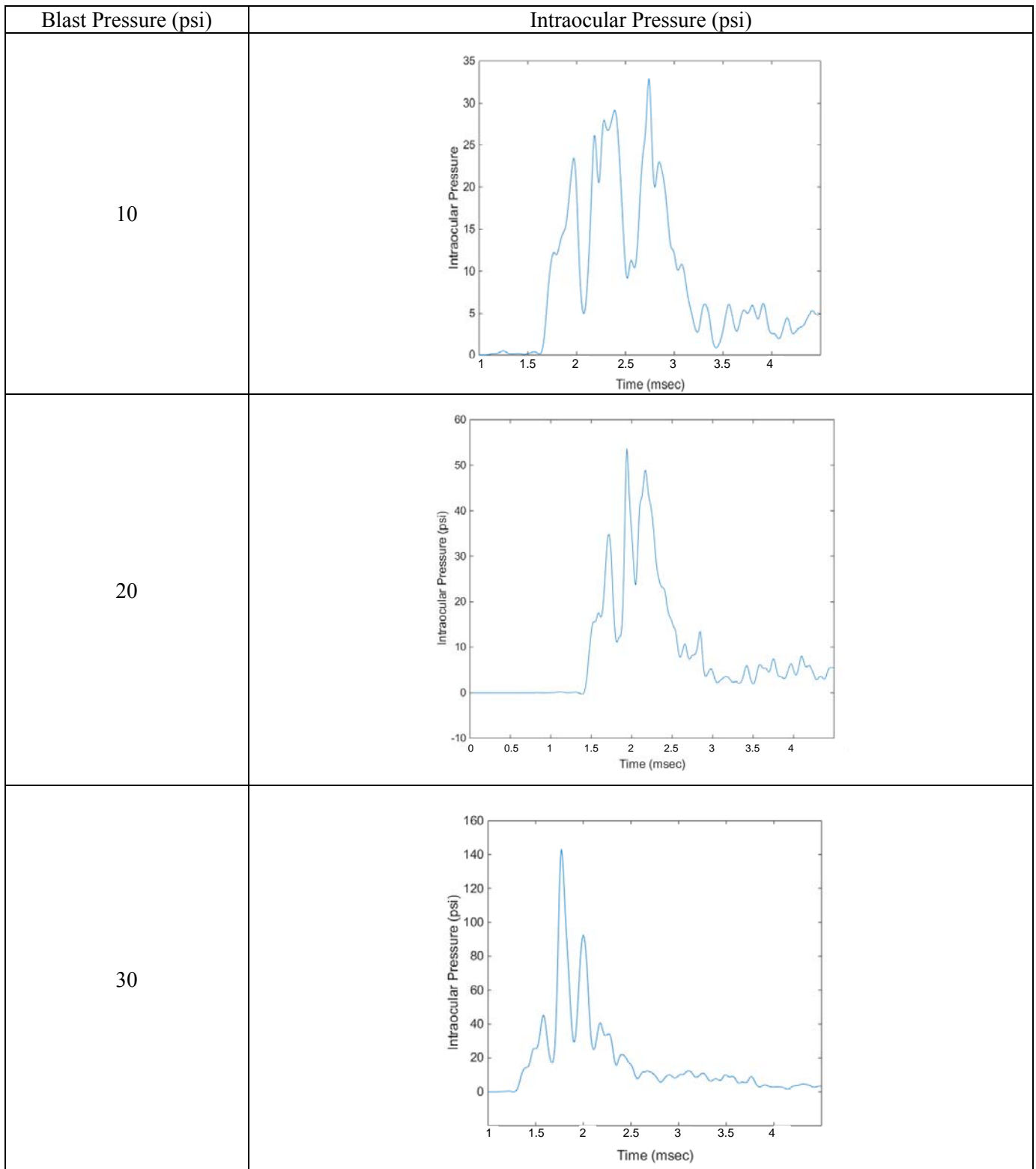
Figure 55: Initial isolated eye simulations of 10, 20, and 30 psi equivalent blasts.

TASK 1.3.1: BRAIN INJURY: BIOMECHANICS OF THE HEAD /BRAIN

MILD TRAUMATIC BRAIN INJURY RESEARCH

Headform Shape Analysis

Methods

We aimed to quantify shape differences between the Hybrid III 50th percentile male dummy headform and the medium NOCSAE headform (Figure 56). The 50th percentile male Hybrid III and medium NOCSAE headforms, were scanned using a coordinate measuring machine equipped with a Laser ScanArm (FARO, Lake Mary, FL), capable of a measurement accuracy of ± 35 μm. Position data for points on the surfaces of the two headforms were collected and used to generate 3D point-cloud representations. For scanning, the headforms were mounted to a 50th percentile male Hybrid III neck which was rigidly mounted to a table. Post processing of the 3D data to remove excess points and smooth surfaces was conducted using Geomagic Studio 2012 software (3D Systems, Rock Hill, SC). The resulting point-cloud data were imported into MATLAB (MathWorks, Natick, MA) for dimensional analyses.

Figure 56: The Hybrid III (left) and NOCSAE (right) headforms are the most commonly used headforms in helmet impact performance testing.

MATLAB script files were written to import the point-cloud data using the Wavefront OBJ toolbox and to align the headforms to a common global coordinate system. The mid-sagittal plane of each headform was found by comparing symmetry across the mid-lines of three coronal plane cross-sections: one 38.1 mm (1.5 in) anterior to the center of gravity (CG) of the headform, a second at the CG, and a third 63.5 mm (2.5 in) posterior to the CG. Each coronal cross-section was divided into 1˚ increments from -90˚ to 90˚ with the 0˚ line at the top of the

headform, separating the left and right sides. The root-sum-square (*RSS*) of differences between corresponding radius values on the left and right sides (Eqn. 4) were determined for each coronal plane as roll (lateral neck flexion) and yaw (head rotation about the long axis of the body) of the head were varied.

$$RSS_{L-R} = \sqrt{\sum_i (r_R(\theta_i) - r_L(-\theta_i))^2}$$ (Eqn. 4)

The first term in Eq. 1 corresponds to the radii on right (*R*) side and the second term to those on the left (*L*) side of the head with the angle (θ_i) ranging from 1˚ to 90˚. The head orientation where the sum of the *RSS* values from the three coronal planes was minimized was selected as the mid-sagittal plane of the headform. After defining the mid-sagittal plane for each headform, the headforms were aligned to a common coordinate system about the CG of the Hybrid III. The RSS of the differences between the Hybrid III and NOCSAE headforms in the mid-sagittal plane (Eqn. 5) were minimized by varying pitch angle (neck flexion/extension) of the NOCSAE and translating it in the sagittal plane.

$$RSS_{HIII-NOCSAE} = \sqrt{\sum_i (r_{HIII}(\theta_i) - r_{NOCSAE}(\theta_i))^2}$$ (Eqn. 5)

The first term in Eq. 2 represents the radii of the Hybrid III for each angle, θ, in the plane of interest and the second term represents those of the NOCSAE for θ_i values ranging from -15˚ to 145˚. In the mid-sagittal plane, the polar coordinate system ranged from -180˚ to 180˚ with 0˚ at the back of the headform and ±180˚ at the front with positive angles measured counterclockwise.

Once the headforms were aligned, comparisons were made between headforms in four planes of interest and in 3D. Cross-sectional comparisons were made in the mid-sagittal, anterior-coronal (38.1 mm from the CG), mid-coronal (through Hybrid III CG), and posterior-coronal (63.5 mm from the CG) planes to highlight key differences between the headforms in regions that are likely to be in contact with helmet padding. The 3D comparison excluded regions that were unlikely to affect helmet fit, such as the face, ears, and areas below the bottom edge of a helmet.

For the cross-sectional comparisons, the data were transformed from Cartesian to a polar coordinate system in the planes of interest. Two metrics were used to quantify differences in the cross-sectional planes: root-mean-square radial deviation (*RMSD*) and maximum radial deviation (*MRD*). The *RMSD* was defined by Eqn. 6, where *N* is the number of points compared. The MRD was defined by Eqn. 7.

$$RSS = \sqrt{\frac{1}{N}\sum_i (r_{HIII}(\theta_i) - r_{NOCSAE}(\theta_i))^2}$$ (Eqn. 6)

$$MRD = (r_{HIII}(\theta_i) - r_{NOCSAE}(\theta_i))_{max}$$ (Eqn. 7)

The ranges over which the two headforms were compared in each plane were selected to represent regions where a football helmet is likely to contact the head (Table 13). Ranges where the headforms deviated substantially from one another were excluded from *RMSD* and *MRD* calculations, but were highlighted and discussed separately. The included ranges were selected such that the *MRD* was not at the edge of the range. For the mid-sagittal contour, the polar coordinate system ranged from -180˚ to 180˚ with 0˚ at the right side of the figures (along the positive x-axis). For all three coronal contours, the coordinate system ranged from -180˚ to 180˚ with 0˚ at the top of the figures.

Table 13: Ranges over which planar comparisons were made among headforms. The ranges were selected to make comparisons between headforms in regions relevant to football helmet fit.

Plane	Headform Comparison Regions		
Mid-Sagittal	Upper skull	Base of skull	Chin
	-15˚ to 155˚	-15˚ to -35˚	-120˚ to -135˚
Mid-Coronal	Upper skull	Left Jaw	Right Jaw
	-100˚ to 100˚	-100˚ to -145˚	100˚ to 145˚
Anterior-Coronal	Upper Skull	Left Jaw	Right Jaw
	-115˚ to 115˚	-115˚ to -155˚	115˚ to 155˚
Posterior-Coronal	Upper skull	Lower Left	Lower Right
	-115˚ to 115˚	-115˚ to -145˚	115˚ to 145˚

The same metrics, *RMSD* and *MRD*, were used for 3D comparisons. A spherical coordinate system was defined, with the origin located at the CG of the Hybrid III. Azimuth ranged from ‑180˚ to 180˚ with 0˚ at the front of the headform and positive values on the left side. Elevation ranged from -90˚ to 90˚ with negative at the bottom, positive at the top, and 0˚ passing through the origin. Comparisons between the headforms were made at 1˚ increments of azimuth and elevation for all azimuth values and elevation values greater than -30˚ (Figure 57). Regions which were unlikely to affect helmet fit were excluded. In the face region, where azimuth values range from -45˚ to 45˚, elevation values below 20˚ were excluded. Likewise, the ear regions, -90˚ to -130˚ and 90˚ to 130˚, were excluded below an elevation of 15˚. On the back of the heads, where azimuth values ranged from 130˚ to ‑180˚ and 130˚ to 180˚, elevation values below ‑15˚ were excluded. The ear and face regions are not expected to substantially impact helmet fit or performance. The differences at the base of the headforms, which are likely to have an effect on helmet fit, will be discussed separately.

(a)   **(b)**
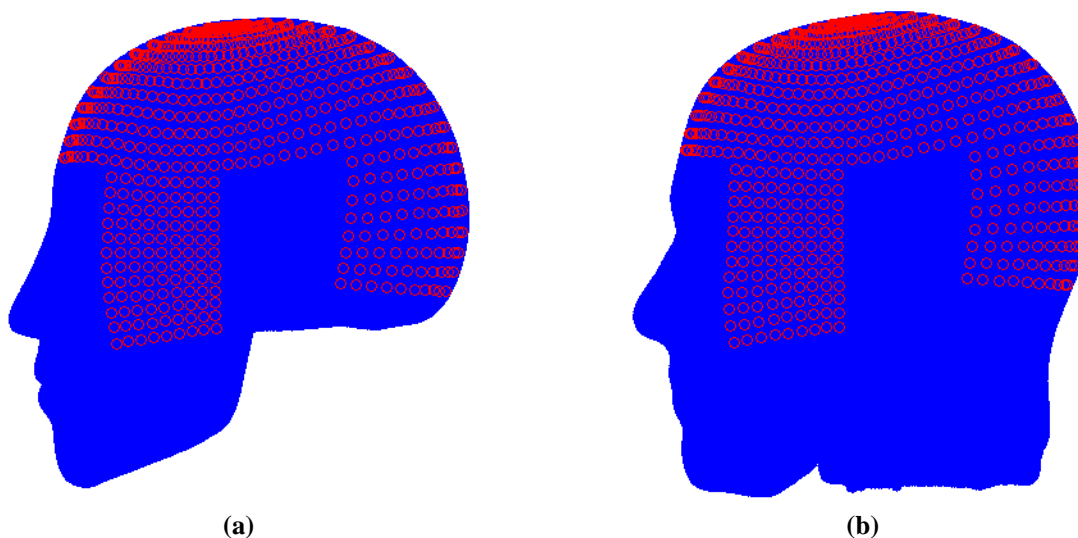
Figure 57: Profile view of the (a) Hybrid III and (b) NOCSAE headforms with markers indicating the locations of 3D comparative radial measurements between the two headforms. Circle locations were defined in spherical coordinates by azimuth and elevation at 1˚ increments.

Results

In the mid-sagittal contour, the upper skull regions, which go from the base of the skull to the brow (-15° to 155°), were nearly identical (Figure 58). The *MRD* between the two headform in this region was found to be 2.1 mm, located on the forehead. The *RMSD* over this range was 1.1 mm. More substantial differences were evident around the base of the skull (-15° to -35°) where the contours of the two headforms diverge. The Hybrid III contour follows the shape of the occipital bone while the NOCSAE contour continues down, following the shape of the neck. One more notable difference between headforms that was evident in this plane was the difference in chin shape (-120° to -135°). Comparing the chins between the two headforms, a *MRD* of 7.6 mm and *RMSD* of 3.4 mm were found.
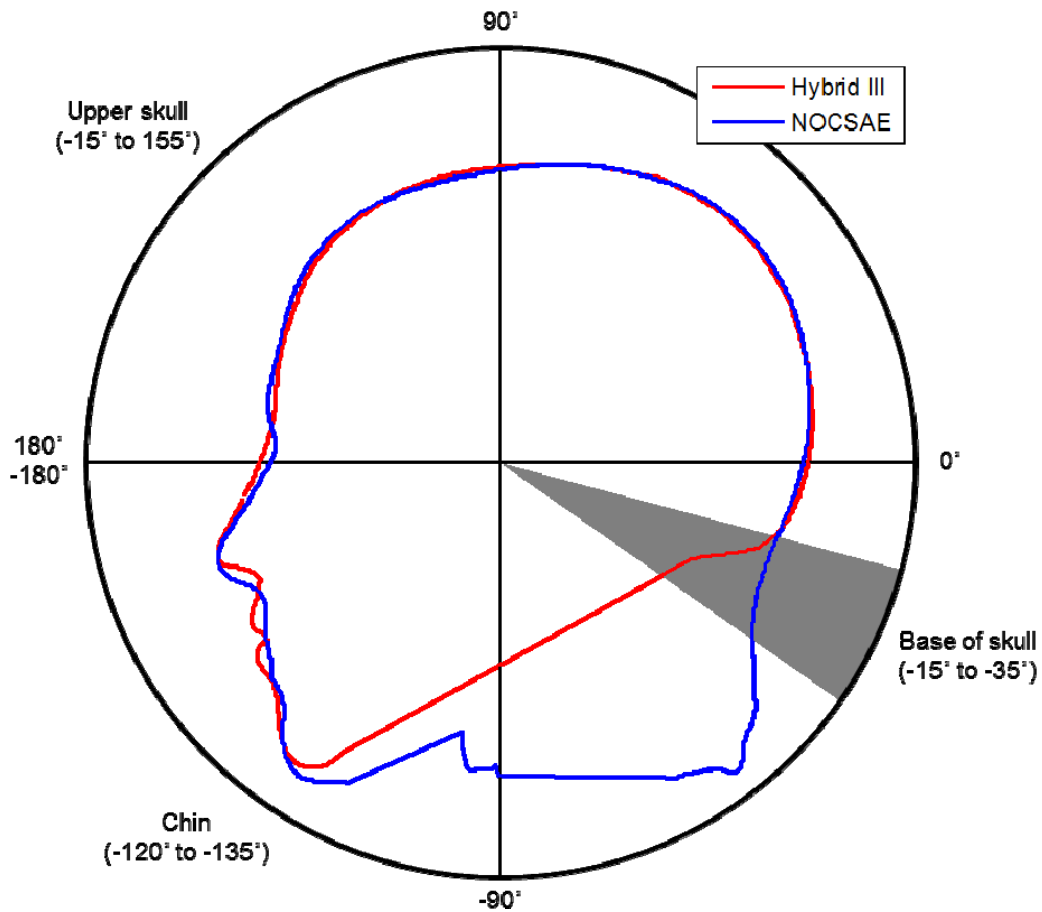
Figure 58: Shape comparisons between the Hybrid III 50th percentile male and NOCSAE medium headforms for the mid-sagittal plane.

At an offset of 38.1 mm (1.5 in) anterior to the CG of the Hybrid III (Figure 59), the differences between the two headforms in the jaw region which were noted in the mid-coronal plane become more pronounced. The *MRD* in the lower portion of this cross-section (-115° to -155° and 115° to 155° on the left and right respectively) was 6.5 mm and the *RMSD* was 4.6 mm. The upper portion has a *MRD* of 3.5 mm and *RMSD* of 1.7 mm.
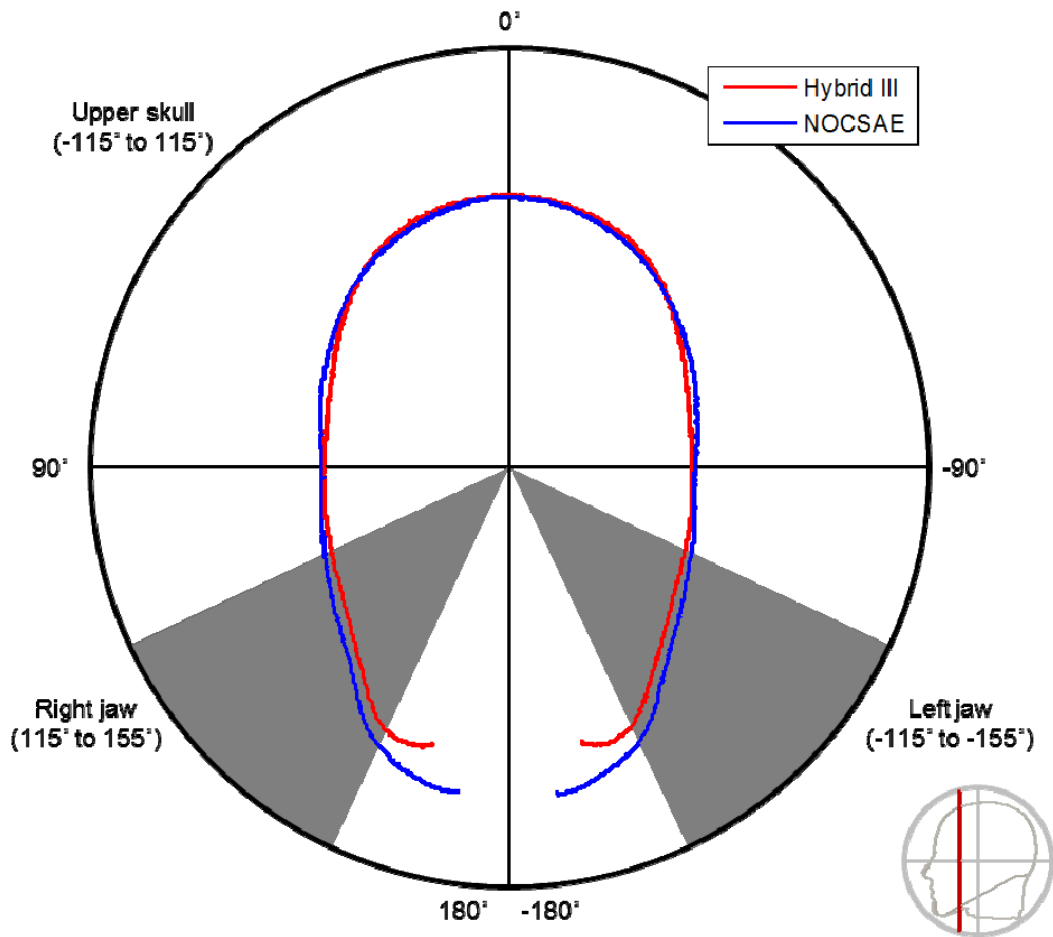
Figure 59: Coronal plane cross-section of a Hybrid III (blue) and NOCSAE headform through a point 38.1 mm (1.5 in) anterior to the CG of the Hybrid III. Along the upper portion, the *MRD* was 3.5 mm and the *RMS*D was 1.7 mm. At the jaw, the values were 6.5 mm and 4.6 mm respectively.

The two headforms were also nearly identical in the upper skull region (-100˚ to 100˚) of the coronal plan passing through the CG of the Hybrid III (Figure 60). The *MRD* between the two headforms was found to be 2.1 mm while the *RMSD* was 1.2 mm. In the lower portions of the headforms (-100˚ to -145˚ and 100˚ to 145˚ on the left and right respectively), where the contour cuts through the jaw, the Hybrid III is noticeably narrower than the NOCSAE. The *MRD* between the two headforms in this region was 7.6 mm and the *RMSD* was 4.2 mm. In addition to being narrower, the Hybrid III headform does not extend as far down as the NOCSAE.
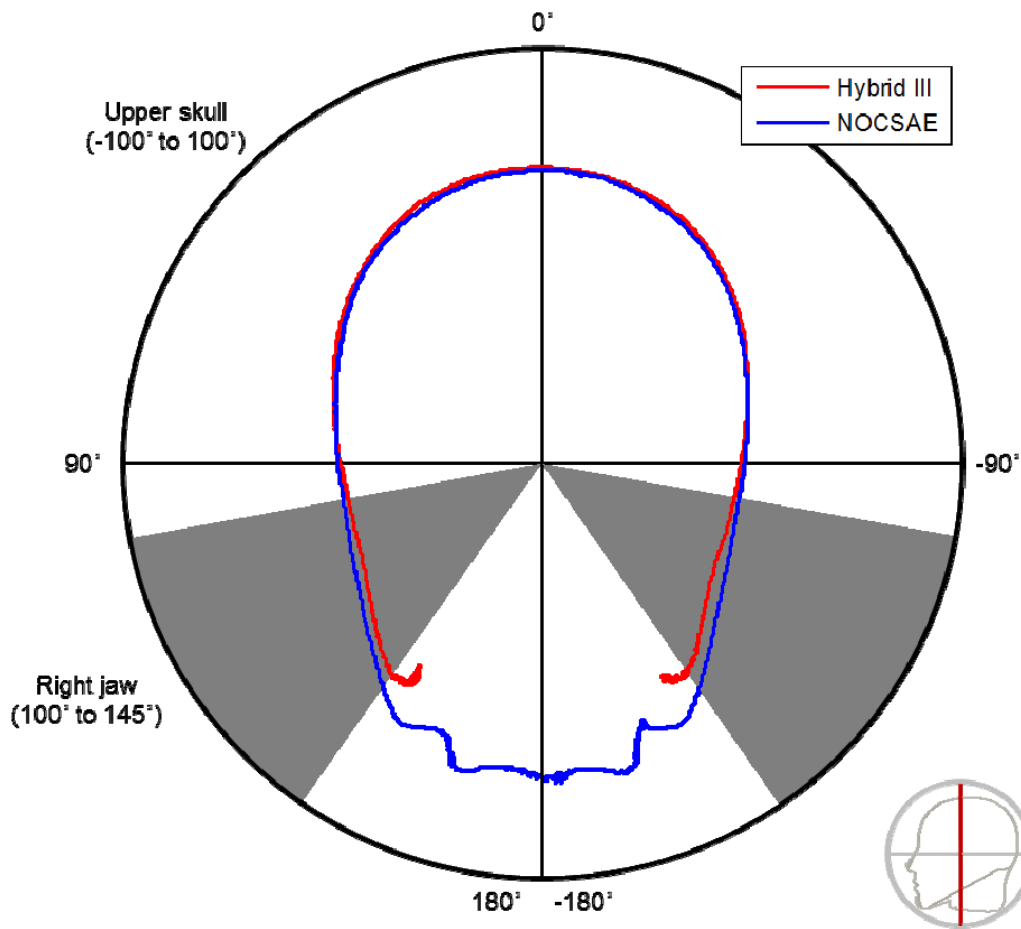
Figure 60: Coronal plane cross-section of the Hybrid III (red) and NOCSAE (blue) headform through the CG of the Hybrid III. The MRD along the upper skull was 2.1 mm and the *RMSD* was 1.2 mm. At the jaw, the values were 7.6 mm and 4.2 mm respectively.

Differences between the two headforms were more apparent 63.5 mm (2.5 in) posterior to the CG (Figure 61). The upper portions of the headforms (-115° to 115°) still matched well, with a *MRD* of 2.6 mm and *RMSD* of 1.4 mm. A more substantial difference was evident in the lower portion of the headforms, where the two contours diverge. Similar to the mid-sagittal plane, the contour of the Hybrid III resembles the shape of the skull only, but the NOCSAE contour includes the upper part of the neck. The regions of divergence are highlighted from -115° to -145° and 115° to 145°.
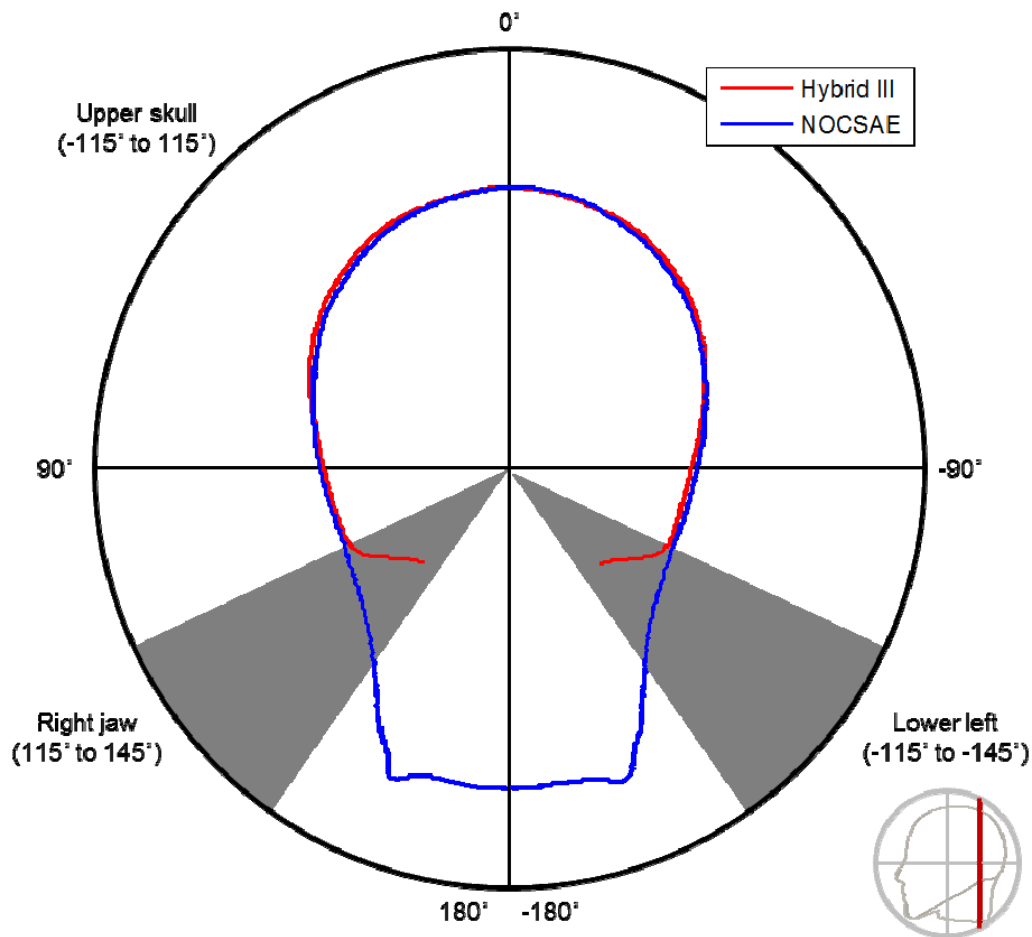
Figure 61: Coronal plane cross-section of the Hybrid III (red) and NOCSAE (blue) headform through a point 63.5 mm (2.5 in) posterior to the CG of the Hybrid III. Along the upper skull, the *MRD* was 2.6 mm and was *RMSD* 1.4 mm. For the lower portions of the contour, the headforms deviate substantially.

For the 3D comparisons, the differences between the headforms were minor in most regions (Figure 62). The *MRD* was 5.6 mm and the *RMSD* was 1.4 mm. The largest deviations between the headforms occurred in the cheek and jaw regions.
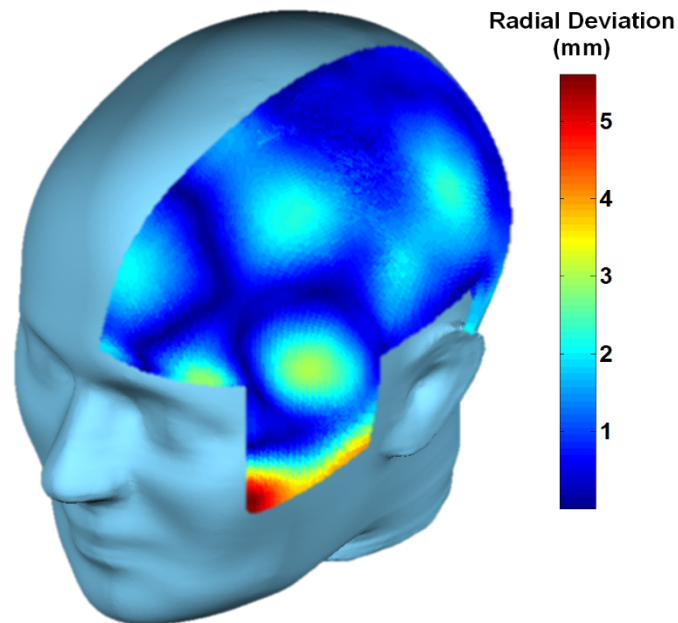
Figure 62: Heat map showing the 3D comparisons between the Hybrid II and NOCSAE headforms displayed on a NOCSAE headform. The differences on the left and right sides were averaged and displayed on the left side of the headform. The largest radial deviations, those greater than 3.5mm, occurred in the cheek region of the headforms and are indicated by orange and red coloration.

Discussion

The results of this study are directly applicable to head impact and helmet testing in the laboratory. In the upper portion of the headforms, only minor differences were found. The differences are unlikely to substantially affect helmet fit as padding will deform to accommodate the minor variations in head shape. Differences in the base of the skull, the jaw, and the cheeks explain the issue of fitting a helmet to the Hybrid III. The padding should be in contact with the head in these three regions making them important for quality of helmet fit and performance. Differences between the chins of the two headforms may affect chinstrap fit and performance.

Several important limitations should be noted regarding this study. Only one headform of each type was measured in this study. Other Hybrid III and NOCSAE headforms which meet the respective manufacturing tolerances may yield slightly different measurements, though the differences are not expected to substantially affect the results or conclusions of this study. The analysis addressed only headform shape characteristics. Other factors such as inertial properties, attachment to a biofidelic neck, and instrumentation installation should also be considered in future studies. Measurements were taken of headforms that were intended to represent an average man, limiting the applicability of these results for large or small men, women, and children.

Proper helmet fit and sizing on dummy headforms for laboratory testing is dependent on headform shape. The head circumference measured above the brow alone is not adequate to characterize headform size for helmet testing. In this study, the differences in shape between the Hybrid III and NOCSAE headforms were quantified. While only minor differences were noted in the upper portions of the headforms, substantial differences were found in other areas.

Headform Impact Analysis

Background

Beyond comparison of headform shape, we aimed to quantify differences in impact response between the Hybrid III and NOCSAE headforms. The Hybrid III headform is a part of the full-body anthropomorphic test device (ATD) by the same name. The dummy was designed for automotive safety testing by researchers working for General Motors. In addition to automotive safety, the Hybrid III headform has also been used extensively for sports helmet testing (Hubbard and McLeod, 1974; Viano et al., 2012a; Viano et al., 2012b; Pellman et al., 2003; Pellman et al., 2006; Gwin et al. 2010).

The full body ATD includes a neck to which the headform can be attached, allowing for angular accelerations (Gwin et al. 2010). A hollow cavity in the headform also makes it well suited for the instrumentation used to measure linear and angular head acceleration (Padgaonkar et al., 1975). The biomechanical response of the head has been validated for direct loading to the forehead using a drop test method and loading through the neck attachment (Hubbard and McLeod, 1974). In both cases, the headform was compared with cadaver response corridors. While the dimensions and shape of the upper part of headform were based on measurements from human subjects and cadavers, the headform was not designed to evaluate helmets. Some portions of the headform are not representative of a human head, most notably the nape of the neck, making proper helmet fit difficult (Cobb et al., 2014).

Contrary to the Hybrid III, the NOCSAE headform was developed specifically for helmet testing (Hodgson, 1975). The headform was built to replicate linear acceleration characteristics in drop tower tests; as such, the headform attaches rigidly to a drop carriage and has limited space for instrumentation. A shaft from the underside of the chin to an area near the center of gravity (CG) of the headform was designed to allow for placement of a triaxial accelerometer package for linear acceleration measurement only (Kendall et al., 2012). While previous studies have implemented other six degree of freedom (DOF) instrumentation arrangements, recent advances in instrumentation technology have also allowed researchers to accurately measure 6DOF kinematics using an accelerometer and angular rate sensor package that fits inside the NOCSAE instrumentation shaft (Kendall et al., 2012l; Bartsch et al., 2012). Size and shape specifications for the headform were based on a cadaver determined to be representative of the average American football player and the model includes all parts of the head that are important for helmet fit (Hodgson, 1975).

To date, no studies have compared impact response characteristics for Hybrid III and NOCSAE headforms where both heads were mounted on a Hybrid III neck. Differences between the two headforms in mass, inertia, instrumentation, and other properties are likely to have implications on impact test results. This study tested the hypothesis that there would be no difference in impact responses between the Hybrid III and NOCSAE headforms over a range of acceleration magnitudes.

Methods

Impact tests were conducted on two helmeted dummy headforms, a 50th percentile male Hybrid III and a medium NOCSAE headform (Figure 63). Both headforms were mounted on a 50th percentile male Hybrid III neck attached to a five degree of freedom (DOF) adjustable linear slide table with a mass of 16 kg, similar to previous pendulum and linear impactor studies (Viano et al., 2012b; Pellman et al., 2006; Gwin et al. 2010; Beckwith et al., 2012). All tests were conducted using a custom pendulum impactor consisting of a 15.5 kg anvil with a flat impactor face at the end of a 1.90 m arm. The total moment of inertia of the pendulum arm and anvil was 72 kg-m^2. The impactor face was a 127 mm (5 in) diameter, 25 mm thick piece of nylon mounted directly to a steel anvil. The two headforms were fitted with a large Riddell Speed Revolution helmet (Riddell, Rosemont, IL), and struck five times at each test condition using six locations and three impactor velocities for a total of one hundred

eighty tests. Impact locations were to the front, facemask, jaw, side, rear boss, and rear of the helmet (Figure 64). For each impact location, the headforms were rotated into the same positions and then translated to align markers on the helmet with the impactor face. The slide table allows for rotations to lean the head and neck toward or away from the impactor (elevation) and twist the head and neck about the long axis of the body (azimuth). Impactor velocities of 3.1 m/s, 4.9 m/s, and 6.4 m/s were selected to reproduce a range of linear accelerations. High magnitude impact conditions were selected for this study because they are the most likely to cause injury and therefore most relevant for evaluating brain injury risk in the laboratory. More detailed specifications of shape and inertial properties are provided in studies by Cobb et al. (2014) and Kendall et al (2012).

Figure 63: The most commonly used headforms in helmet impact testing, (a) a 50th percentile male Hybrid III headform and (b) a medium NOCSAE headform, both mounted on a 50th percentile male Hybrid III neck.

Front – Azimuth: 0˚, Elevation: 30˚

Facemask – Azimuth: 0˚, Elevation: -10˚

Jaw – Azimuth: -90˚, Elevation: -5˚

Side – Azimuth: -90˚, Elevation: 15˚

Rear-Boss – Azimuth: -135˚, Elevation: 15˚

Rear – Azimuth: 180˚, Elevation: 0˚
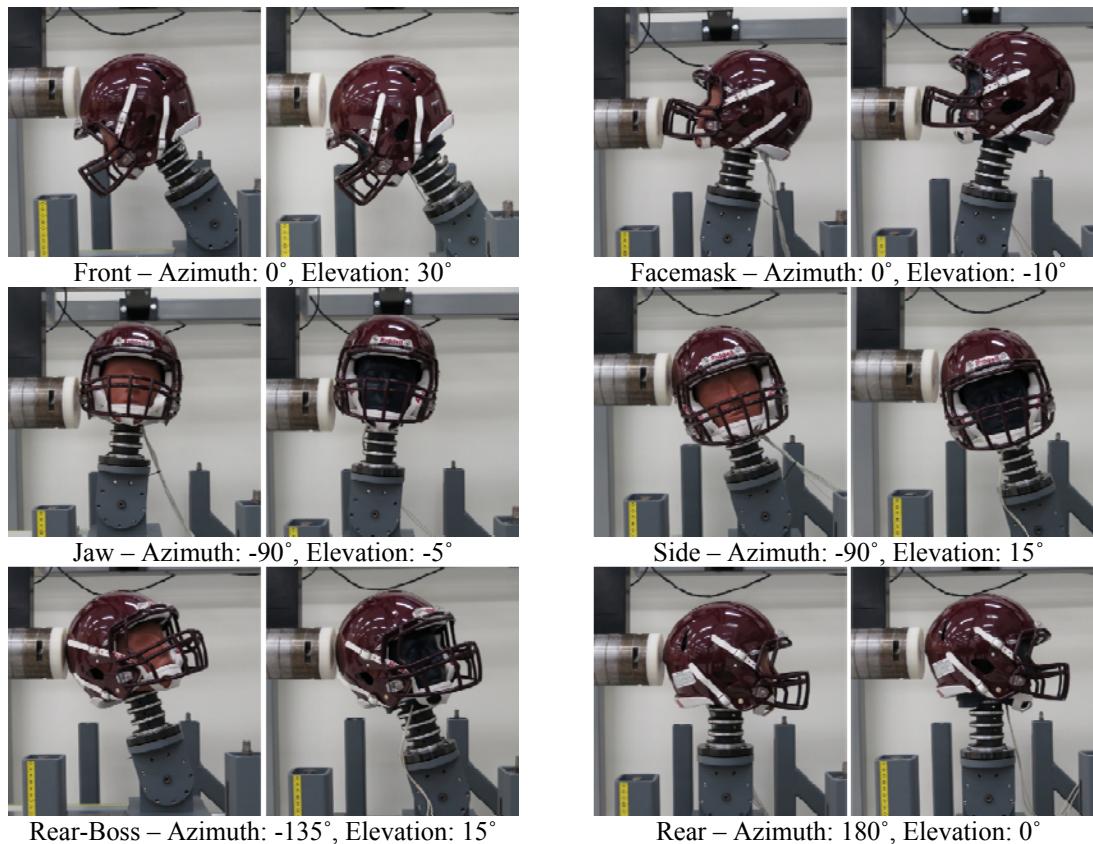
Figure 64: Helmeted Hybrid III and NOCSAE headforms showing the six impact locations: front, facemask, jaw, side, rear-boss, and rear.

Kinematic data of the Hybrid III headform were collected at 20 kHz using nine accelerometers (7264-2000B, Endevco, San Juan Capistrano, CA) in a 3-2-2-2 arrangement. The accelerometer arrangement allowed for calculation of linear and angular acceleration about the center of gravity of the headform. Linear acceleration data were filtered in accordance with SAE J211 standards using a Channel Frequency Class (CFC) 1000 low-pass anti-aliasing filter. Angular acceleration data were filtered with a CFC 180 filter for angular acceleration calculations in accordance with published best-practices to reduce the effect of spurious noise (Beckwith et al., 2012; Newman et al., 2005).

While the Hybrid III headform was mounted on the Hybrid III neck as designed, the NOCSAE headform required a custom adapter plate and modifications to the headform (Figure 65) to allow for neck attachment. The adapter plate mounted on the base of the headform via three screws that fit into existing threaded holes. A 12.7 mm (0.5 in) diameter shaft through the adapter plate allowed for attachment to a Hybrid III neck via the occipital condyle (OC) joint similar to how the Hybrid III headform attaches. The adapter plate was 22.2 mm (0.875 in) thick and the bottom face sat directly on top of the neck, without rubber nodding blocks (a standard feature on the Hybrid III neck). Minor modifications were made to the NOCSAE headform to accommodate the adapter plate and move the OC joint forward to more closely resemble relative position of the OC joint to the CG of the Hybrid III headform. The plate was placed such that the distance in the anterior-posterior and medial-lateral directions between the OC joint and the CG would be the same for the Hybrid III and NOCSAE headforms. With the adapter plate, the OC joint was 22 mm more inferior to the CG than the OC joint on the Hybrid III headform. The OC joint shaft was centered 18.8 mm (0.74 in) forward of center threaded hole in the headform and 12.7 mm (0.50 in) inferior to the base of the headform. Some material was removed from the headform around the original neck mount and instrumentation channel (Figure 65) to make room for the adapter plate and Hybrid III neck. The mass of the adapter plate and mounting screws matched that of the removed material.
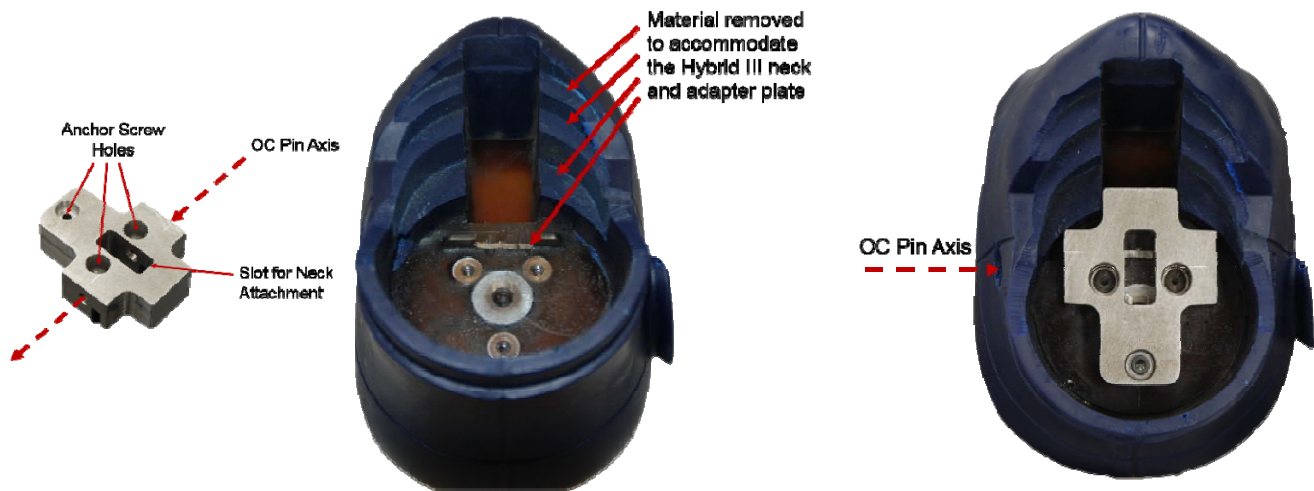
Figure 65: Adapter plate (left) and headform modifications (center) required to fit a NOCSAE headform to a Hybrid III neck and move the occipital condyle joint forward. Headform material was removed around the underside of the chin to accommodate the adapter plate and neck. The far right picture shows the adapter plate installed on the underside of the headform with the location of the occipital condyle (OC) pin labeled.

Kinematic data of the NOCSAE headform were collected at 20 kHz using a 6DX Pro 2k-18k six-degree of freedom (6DOF) sensor package (DTS, Seal Beach, CA). The sensor package was mounted on a custom-built aluminum block placed inside the instrumentation shaft of the NOCSAE headform placing the measurement axis 5.74 mm (0.226 in) anterior (x-axis) and 0.89 mm (0.035 in) inferior (z-axis) to the CG of the headform and rotated -20˚ about the y axis (J211 coordinate system). Accelerometer data were filtered using a CFC 1000 low-pass anti-aliasing filter in accordance with SAE J211 standard and angular rate data were filtered using a CFC 155 filter. The filter specification for angular rate data was based on a previous test series in which the peak acceleration values of the 6DOF sensor package were optimized to match those of the 3-2-2-2 arrangement. Kinematic data measured at the sensor package were rotated to match the orientation of the SAE J211 head coordinate system. Angular acceleration values were calculated in the rotated coordinate system and then linear accelerations were calculated for the CG of the headform.

Impact response was assessed using a series of parameters based on the acceleration and angular rate measurements. Resultant linear and angular accelerations were determined for the CG of the headforms as functions of time. Peak acceleration and peak angular rate values, which are associated with the pressures and strains in the brain that have been correlated with concussion risk, were recorded (Hardy et al., 2007). The linear acceleration traces were also used to ascertain measures of impact event duration that are associated with concussion risk (Ommaya, 1985). Time to peak linear acceleration was defined as the time from the start of the impact event to the peak linear acceleration, while event duration was the time from the start of the impact event to the time of peak resultant linear velocity. The start of the impact event was defined using a 0.5 g threshold for resultant linear acceleration. The ratio of the resultant linear acceleration to the resultant angular acceleration was used to approximate the radius of rotation of the headform as a function of time.

Two other commonly used head injury metrics, Gadd Severity Index (SI) and Head Injury Criterion (HIC) were also calculated for each impact (Gadd, 1966; Versace, 1971). Both SI and HIC combine weighted accelerations with duration to calculate a single number that is associated with head injury (Viano et al., 2012a; Pellman et al., 2003; Pellman et al., 2006; Duma et al., 2005b). These metrics serve as correlates to energy transferred to the head during impact.

Differences between the two headforms in biomechanical magnitudes and variances among matched test conditions were assessed for all parameters. Statistical comparisons were made using a three-way analysis of variance (ANOVA) test to compare the affects impactor velocity and impact location had on the kinematic parameters of the two headforms. Post-hoc 2-way ANOVAs and Fisher's LSD tests were conducted to compare differences in parameters between the two headforms for each velocity-location combination. Repeatability among matched tests was assessed using coefficient of variation (COV), which is the ratio of the standard deviation of matched test responses to the mean, expressed as a percentage. COV values for each parameter of the two headforms were compared across all test conditions using two-sample Student's t-test. Significance was set at $\alpha = 0.05$ for all statistical analyses.

Results

Throughout the 180 tests conducted, the headforms demonstrated similar response patterns to one another for corresponding test conditions (Figure 66 and Figure 67). The response corridors in Figure 66 and Figure 67 show the upper and lower bounds of all repeated tests by test condition and headform. Statistical analyses using three-way ANOVAs revealed significant differences among test conditions ($p < 0.001$) for all parameters. Post-hoc analyses revealed significant differences between headform by impact velocity-location combinations for all parameters ($p < 0.001$), including linear and angular acceleration.

Linear and angular acceleration comparisons by matched location and magnitude conditions (Table 14) showed significant differences between headforms for several test conditions. For linear acceleration, eight out of eighteen (8/18) test conditions had significant differences. The NOCSAE headform peak linear acceleration was as much as 10.1% lower than that of the Hybrid III headform for the medium velocity jaw impacts and as much as 19.9% higher for the medium velocity facemask impacts. The angular acceleration comparisons revealed significant differences in eleven out of eighteen (11/18) test conditions. As with linear acceleration, the largest differences between headforms occurred at the facemask location. No significant differences were found in COV values between the two headforms for linear ($p = 0.335$) or angular acceleration ($p = 0.841$). Relatively large variances were found for several test conditions, including the facemask, where the acceleration plots show wide corridors.

Differences between the headforms varied by impact location. At the front location, a significant difference in peak linear acceleration was found for the high velocity condition, where the NOCSAE headform was 9.0% higher than the Hybrid III. The Hybrid III and NOCSAE headforms had COV values of 1.7% and 3.4%, respectively, for this test condition. Larger significant differences were found at the facemask location, where the NOCSAE headform had 19.9% and 17.7% higher peak linear accelerations for the medium and high velocity conditions. Large differences were also found in the angular acceleration values at the facemask location, where the NOCSAE headform was 65.3% higher, 28.5% higher, and 22.5% lower than the Hybrid III for the low, medium, and high velocities. Impacts to the jaw resulted in significant differences in peak linear and angular acceleration for both the medium and high velocities. For linear acceleration, the NOCSAE headform had 10.1% lower and 4.0% lower values than the Hybrid III. The angular accelerations of the NOCSAE headform were 26.9% higher and 25.3% higher than the Hybrid III for the medium and high velocity conditions. For side impacts, no significant differences were found in peak linear acceleration. The NOCSAE headform did have 9.1% higher angular acceleration for the medium velocity. At the rear-boss location, the only significant difference was for peak linear acceleration at the high velocity condition, where the NOCSAE headform acceleration was 8.0% higher than that of the Hybrid III. Several significant differences were found at the rear impact location, where differences in peak linear acceleration were found for the medium and high velocities, and differences in peak angular acceleration were found at all three velocities. The differences at the rear location ranged from 7.2% for linear acceleration at the high velocity condition to 29.4% for angular acceleration at the medium velocity.

Condition-specific significant differences between the headforms for matched magnitudes and locations were also found in all the other parameters ($p < 0.001$). No significant differences were found between the headforms in COV values. COV and mean percent differences are summarized in Table 15 for all parameters.
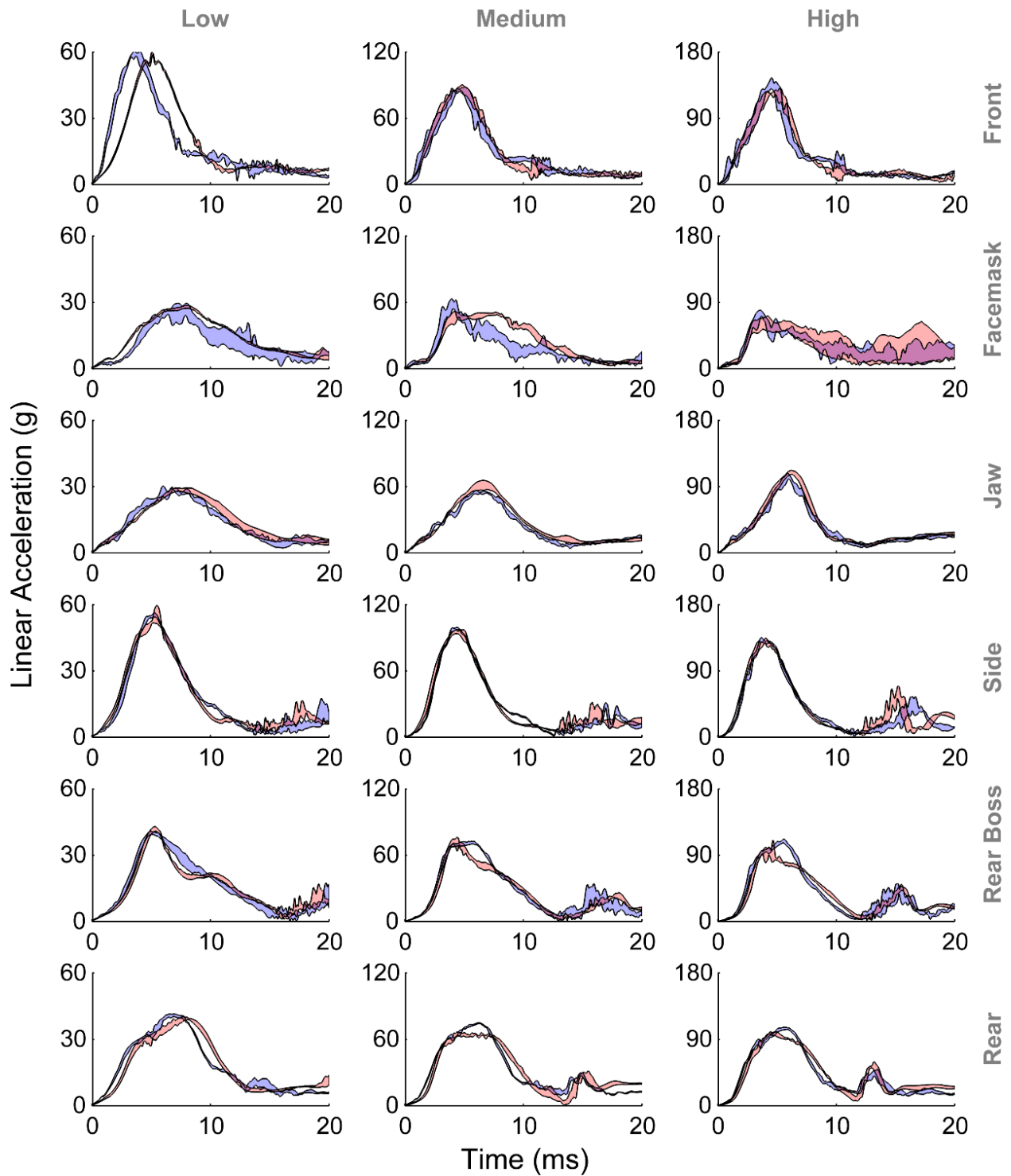
Figure 66: Linear acceleration time traces for each velocity (columns) and location (rows) for the Hybrid III (red) and NOCSAE (blue) headforms. Shaded regions correspond to corridors bounded by the highest and lowest headform acceleration responses at each instant in time (relative to the start of the events) for the respective headform. The acceleration traces show good agreement between repeated tests and headforms for all test conditions except those at the facemask location.
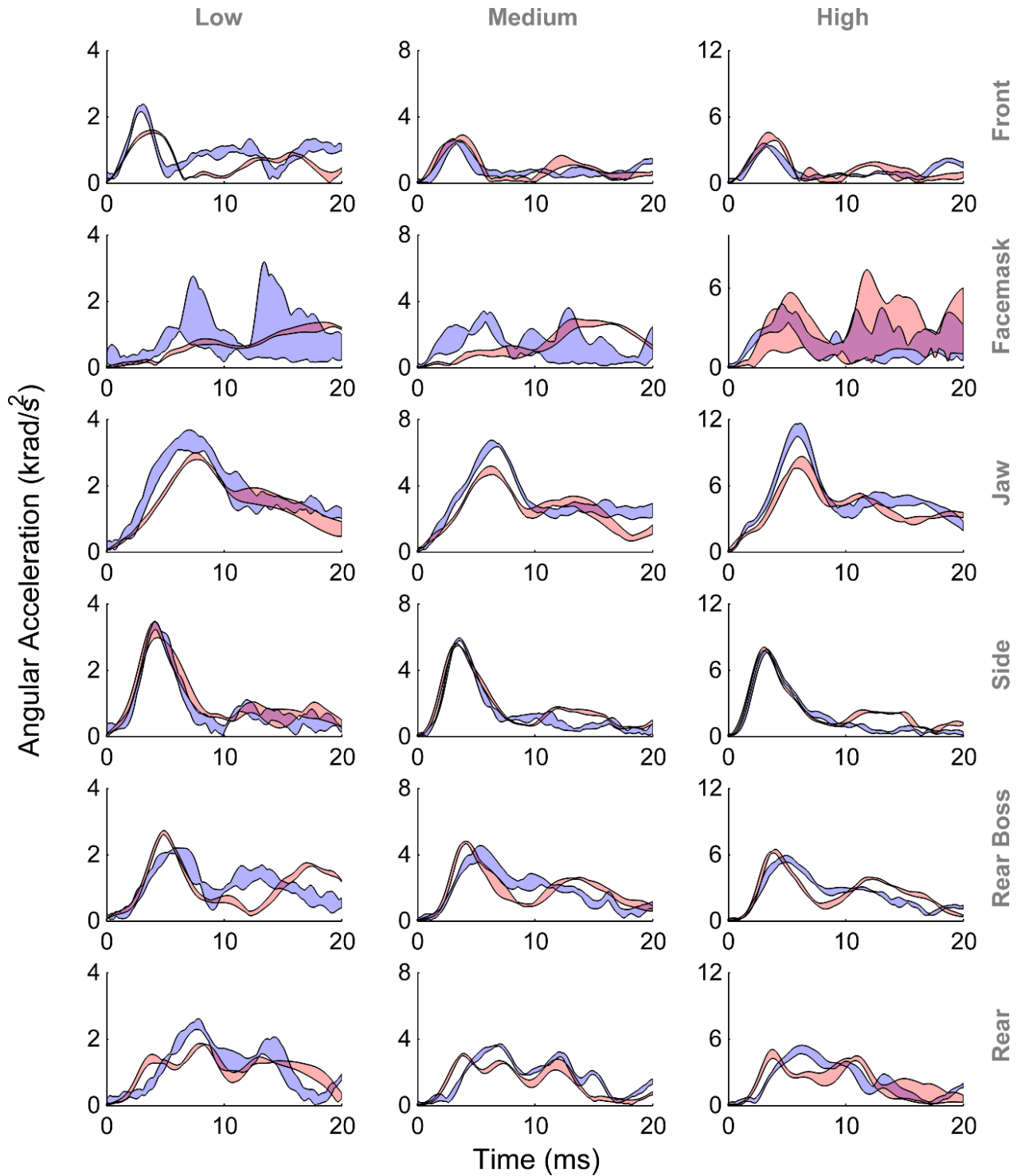
Figure 67: Angular acceleration time traces for each velocity (columns) and location (rows) for the Hybrid III (red) and NOCSAE (blue) headforms. Shaded regions correspond to corridors bounded by the highest and lowest headform acceleration responses at each instant in time (relative to the start of the events) for the respective headform. The acceleration traces show good agreement between repeated tests and headform for most test conditions.

Table 14: Summary of peak linear and angular acceleration comparisons between the Hybrid III and NOCSAE headforms for each test condition. The coefficient of variance (COV) for peak acceleration values of matched tests were similar for the two headforms. Differences between headforms were quantified as mean difference in peak acceleration (Δ). Positive values of Δ indicate larger NOCSAE headform values. Condition-specific significant differences were identified between headforms (denoted by *).

	Peak Linear Acceleration (g)					Peak Angular Acceleration (krad/s^2)				
	Hybrid III	COV (%)	NOCSAE	COV (%)	Δ	Hybrid III	COV (%)	NOCSAE	COV (%)	Δ
Front										
Low	59.5 ± 0.4	0.6	59.6 ± 0.7	1.2	0.0	1.70 ± 0.11	6.5	2.29 ± 0.08	3.4	0.59 *
Medium	88.8 ± 1.1	1.2	87.1 ± 1.5	1.7	-1.7	2.65 ± 0.12	4.5	2.55 ± 0.08	3.2	-0.10
High	128.1 ± 2.2	1.7	139.6 ± 4.7	3.4	11.5 *	4.09 ± 0.29	7.1	3.47 ± 0.09	2.5	-0.62 *
Facemask										
Low	28.1 ± 0.4	1.5	28.5 ± 1.2	4.0	0.4	1.50 ± 0.07	4.8	2.48 ± 0.66	26.6	0.98 *
Medium	50.3 ± 1.0	1.9	60.4 ± 3.2	5.3	10.0 *	2.82 ± 0.15	5.4	3.62 ± 0.28	7.8	0.80 *
High	63.2 ± 6.2	9.8	74.3 ± 3.0	4.1	11.2 *	5.62 ± 1.09	19.3	4.36 ± 0.34	7.7	-1.27 *
Jaw										
Low	29.1 ± 0.6	2.0	29.5 ± 0.5	1.7	0.4	3.09 ± 0.07	2.1	3.43 ± 0.18	5.4	0.33
Medium	62.1 ± 3.0	4.9	55.8 ± 0.5	0.9	-6.2 *	5.18 ± 0.13	2.6	6.57 ± 0.14	2.1	1.39 *
High	109.4 ± 1.8	1.6	105.1 ± 3.0	2.9	-4.3 *	8.88 ± 0.38	4.3	11.13 ± 0.46	4.2	2.25 *
Side										
Low	53.6 ± 3.0	5.6	55.5 ± 0.6	1.0	1.8	3.04 ± 0.09	3.0	3.34 ± 0.09	2.6	0.30
Medium	95.6 ± 1.4	1.4	98.1 ± 0.6	0.6	2.5	5.41 ± 0.11	2.0	5.91 ± 0.06	1.0	0.50 *
High	129.8 ± 2.4	1.9	132.1 ± 2.1	1.6	2.3	7.92 ± 0.13	1.6	7.71 ± 0.11	1.5	-0.20
Rear Boss										
Low	41.8 ± 0.7	1.6	40.4 ± 0.5	1.3	-1.4	2.43 ± 0.08	3.4	2.14 ± 0.06	2.7	-0.29
Medium	74.5 ± 1.6	2.1	71.6 ± 1.1	1.5	-3.0	4.25 ± 0.24	5.7	4.02 ± 0.30	7.5	-0.23
High	100.9 ± 5.0	5.0	109.0 ± 1.6	1.5	8.1 *	5.67 ± 0.16	2.7	5.67 ± 0.23	4.0	0.00
Rear										
Low	39.7 ± 0.4	1.0	41.1 ± 0.4	1.0	1.4	1.88 ± 0.10	5.2	2.43 ± 0.11	4.7	0.55 *
Medium	66.0 ± 0.7	1.1	74.6 ± 0.3	0.4	8.6 *	2.92 ± 0.06	1.9	3.65 ± 0.05	1.2	0.73 *
High	98.2 ± 1.3	1.3	105.2 ± 0.9	0.9	7.0 *	4.46 ± 0.26	5.8	4.99 ± 0.29	5.7	0.53 *

Table 15: Averaged percent difference in magnitude between headforms for various parameters, and corresponding COV values for each headform. No significant differences were identified between headforms in COV values.

	Percent difference in magnitude (%)	COV (%)	
		Hybrid III	NOCSAE
Peak Linear Acceleration	3.7 ± 7.8	2.6 ± 2.3	2.0 ± 1.4
Peak Angular Acceleration	12.0 ± 21.6	4.9 ± 4.0	5.2 ± 5.8
Time to Peak	-1.5 ± 18.3	6.4 ± 6.7	3.6 ± 2.2
Event Duration	14.2 ± 33.8	2.2 ± 2.7	2.0 ± 2.3
Peak Angular Rate	-7.9 ± 12.6	2.9 ± 3.5	2.1 ± 2.5
HIC	-5.6 ± 19.5	3.2 ± 3.8	4.1 ± 5.7
SI	-12.2 ± 12.8	2.7 ± 2.4	3.1 ± 4.6
Radius of Rotation	-4.1 ± 33.9	11.6 ± 11.9	9.7 ± 9.6

Discussion

This test series offers a comprehensive comparison of helmeted head impact response for the Hybrid III and NOCSAE headforms. The results show test condition-specific differences in kinematic data between the two headforms that should be considered when selecting a headform for helmet testing and evaluation. In terms of repeatability, the Hybrid III and NOCSAE headforms had similar coefficient of variation (COV) values for peak linear (μ_{HIII} = 2.6%; μ_{NOCSAE} = 2.0%) and peak angular acceleration (μ_{HIII} = 4.9%; μ_{NOCSAE} = 5.2%), which are consistent with past studies of headform response (Kendall et al., 2012; Walsh et al., 2011 ; Cobb et al., 2015). Both impact location and velocity affected the differences between headforms. A greater number of significant differences were identified at higher impact velocities, likely because the higher energy impacts exaggerated response differences due to inertial properties and headform-helmet interactions.

Impact location had a more complicated effect on differences in impact response between the two headforms. Impacts that were lower on the helmet (facemask, jaw, and rear) all resulted in significant differences in peak linear acceleration for the medium and high velocities. For angular acceleration, the facemask and rear impacts resulted in significant differences at all impact velocities. Shape differences between the Hybrid III and NOCSAE headforms may have contributed to differences in these impact locations by affecting the interaction between the headforms and helmet pads (Cobb et al., 2015). The Hybrid III has narrower cheeks than the NOCSAE headform and the back of the headform does not extend all the way to the bottom of the helmet pads. Impacts higher on the helmet (front, side, and rear-boss) tended to show better agreement between headforms, with significant differences in linear acceleration only for high velocity impacts and fewer significant differences in angular acceleration.

The facemask impacts resulted in some of the largest differences between headforms and COV values. In addition to headform shape, facemask deformation also substantially affected these results. As stated previously, the Hybrid III has narrower cheeks than the NOCSAE headform, allowing for more space between the helmet cheek pads and the face and helmet movement relative to the headform. Interestingly, impacts to the facemask resulted in lower peak linear acceleration values compared to other locations. The difference is likely due to the energy absorption and modulation associated with facemask deformation. At the highest impact magnitude, the facemask peak linear accelerations were nearly 30% lower than all other locations and resulted in permanent facemask deformation. Without the facemask impacts, the average percent difference between the headforms for linear acceleration would be 1.8 ± 6.0% and angular acceleration would be 9.6 ± 15.9%. The COV values would also decrease: linear acceleration COV values would be 2.2 ± 1.6% and 1.4 ± 0.8% for the Hybrid III and NOCSAE headforms while angular acceleration COV values would be 3.9 ± 1.8% and 3.4 ± 1.8%.

Linear acceleration results showed small differences between the headforms in terms of peak values and variation between matched tests. While significant differences were found between the two headforms for peak linear acceleration values in eight out of eighteen impact conditions, the average difference across all conditions was just 3.7%. The largest differences between the headforms occurred at the facemask location, where facemask deformation affected helmet fit and energy transfer to the headform. A second interesting finding was observed in the low magnitude impacts to the front location, where the Hybrid III time traces ramp up slowly for the first few milliseconds. The difference in response at this test condition may be due to energy absorption early in the impact by the rubber nodding blocks, which are small rubber blocks located anterior and posterior to the OC joint on the Hybrid III headform and allow limited sagittal plane rotation about the OC joint. While the headform had nodding blocks, the NOCSAE headform was mounted flush to the top of the neck with a metal to metal contact. At the medium and high magnitudes, the effect due to nodding blocks may not be substantial enough to be observed in the plots (Figure 66 and Figure 67). No significant differences were found between the two headforms in average coefficient of variance (COV) values of peak linear acceleration. These linear acceleration results show that helmeted impact tests conducted using a NOCSAE headform mounted on a Hybrid III neck differ from those conducted using a Hybrid III headform for some impact conditions; though, on average, the differences are small and the two test set ups are similarly repeatable. Given that only small differences were

found, these results suggest that both headforms provide reasonable impact responses in terms of linear acceleration.

Differences between the two headforms for angular acceleration were larger than those observed for linear acceleration, likely due to differences in inertial properties, helmet fit, and the larger variances associated with angular acceleration measurements. In general, the same angular acceleration patterns were observed in the time traces of the two headforms, particularly during the first 10 ms of the events. As with the linear acceleration results, the largest differences were observed at the facemask location and can likely be attributed to the facemask deformation noted in the discussion of linear acceleration data. Averaged across all test conditions, the NOCSAE headform had $12.0 \pm 21.6\%$ higher peak angular acceleration than the Hybrid III and significant differences were found at eleven out of eighteen conditions. Average COV values were significantly higher for angular acceleration for both headforms compared to the linear acceleration conditions ($p = 0.043$; $p = 0.031$), though no significant differences were observed between the two headforms (Linear: $p = 0.335$; Angular: $p = 0.841$).

For the other parameters, average differences tended to be small relative to standard deviations, and the differences were similar in magnitude to those observed for peak linear and angular accelerations. COV values were also in line with those observed for peak acceleration values for most parameters. Time to peak linear acceleration for the Hybrid III headform had a large average and standard deviation of COV values that can be attributed primarily to impacts to the facemask, where some COV values topped 20%. Radius of rotation had the highest average COV for both headforms. The high variance of the radius of rotation term is due to the contributions of variance from both peak linear and angular acceleration at the time of peak linear acceleration.

While some differences in impact response were identified between the Hybrid III and NOCSAE headforms, these differences do not indicate that one headform is superior to the other for impact testing. Rather, the results demonstrate two important findings: (1) the two headforms have similar levels of repeatability, (2) the two headforms produce similar, though not identical results. These two findings suggest that either headform is likely to consistently produce reasonable head impact response results for helmeted impacts, albeit they may not produce the same results. Given that both headforms offer acceptable accuracy and repeatability, other factors such as shape and helmet fit should be considered when selecting a headform for testing. The NOCSAE headform more closely resembles the shape of a human head, likely leading to a more realistic head-helmet interaction compared to the Hybrid III (Cobb et al., 2015).

This study has limitations that affect how these data can be interpreted. The Hybrid III neck utilized in this study is not a perfect representation of a human neck though it does produce head kinematics similar to those observed in field studies and is currently the best available option for these types of impact tests (Duma and Rowson, 2009; Cobb et al., 2013; Rowson et al., 2009). There were some challenges in setting the same impact locations for the two headforms. While the impactor face was aligned to a common marker on the helmets, differences in helmet fit could have affected the alignment. Furthermore, differences between the relative locations of CG and OC joint for the headforms likely had an effect on the directions of the impacts. Only one helmet type and one of each headform type was used for testing and non-helmeted impacts were not conducted. This study did not investigate the effects other factors such as temperature, humidity, impactor face, or helmet age may have on headform response (Rowson and Duma, 2013; Rowson et al., 2013).

State-of-the-Science Meeting on Environmental Sensors for MTBI

We participated in the International State-of-the-Science Meeting on the Biomedical Basis for mTBI Environmental Sensor Threshold Values in McLean VA. The purpose of this meeting was 4 fold: 1) to assess the current state-of-the-science for the biomedical basis of environmental sensor threshold values and their relationships with the risk of mTBI, 2) to identify gaps in the development and utilization of current environmental sensor injury threshold values, 3) to guide future research to gain understanding between varying blast forces and the development of mTBI, and 4) to improve protection, treatment, mitigation for both civilian and warfighter communities. At this meeting, we gave a presentation entitled "Biomechanically Characterizing Mild Traumatic Brain Injury using Helmet Instrumentation" which discussed our experiences with using helmet instrumentation, relating biomechanical measurements to risk of mTBI, and the challenges associated with defining threshold values. In short, we have used helmet-mounted accelerometer arrays to instrument hundreds of human subjects. Head acceleration data collected from these sensors have been paired with clinical data from the medical staff. We have used these data to characterize human tolerance to blunt head impact by relating the biomechanical data to the clinical data. The average brain injury was associated with a linear acceleration of 105 g, rotational acceleration of 5022 rad/s/s, and rotational velocity of 22 rad/s. From this work, we have also developed uni-variate and multi-variate brain injury risk functions for linear and rotational acceleration. We then went on to discuss the challenges associated with setting a threshold. Specifically, we explained how any threshold represents some specific risk. For example, if you set a threshold at 150 g, only 10% of impacts at 150 g result in mTBI, however, 85% of concussions occur at values less the 150 g. This meeting highlighted the importance of work evaluating head impact sensors to capture head kinematics during loading events. This work can help inform future decisions on sensors, how to interpret these data, and appropriately analyze risk.

We have previously reported on preliminary testing of environmental sensors that measure head kinematics. Since then, we have developed and implemented methods to comprehensively evaluated impact sensors. The methods and results are reported below.

Development and Implementation of Laboratory Test Methods for the Evaluation of Environmental Head Impact Sensors

Introduction

Head impact sensors have the potential to aid consumers in the injury diagnostic process by alerting to a severe impact. Researchers have also been using head impact sensors to investigate the biomechanics of concussive and sub-concussive impacts for years (Guskiewicz and Mihalik, 2011). Current efforts rely on volunteer athletes instrumented with wearable head impact sensors during practices and games in an effort to quantify variables associated with head impacts. One such widely-used sensor is the Head Impact Telemetry (HIT) System which has been used to develop risk curves for concussion in adult males (Funk et al., 2006; Funk et al., 2012; Rowson et al., 2012; Rowson and Duma, 2011). Higher concussion rates among women have led researchers to believe different factors play a role in concussions in women compared to men. These may include a woman's smaller mass, lower neck strength, or hormonal influences (Agel et al., 2007; Covassin et al., 2007). Alternative sensors provide new opportunities to study these populations; however, current accuracy in these sensors is limited (Wu et al., 2015; Press and Rowson, 2016). Current available wearable sensors vary in their applications and capabilities. Some simply alert the wearer of a severe impact via light or vibration while others output full head kinematics for each impact. The placement of each sensor also varies. The most common include those mounted on a helmet shell, in a headband, or skull cap. Others are adhered to the skin as a patch or worn as a mouth guard (Wu et al., 2015; Campbell et al., 2015; Higgins et al., 2007; Nevins et al., 2015; Wong et al., 2014). Unfortunately, the accuracy and reliability of these sensors are not regulated to ensure data are representative of true head kinematics. The objective of this study was to define and implement laboratory methods as an initial phase in evaluating wearable head impact sensors. A sample of currently available sensors were tested and analyzed according to the proposed protocol.

Methods

Test Setup

Impact tests were conducted using a custom pendulum impactor with a 15.5 kg anvil and 1.90 m pendulum arm. The total moment of inertia of the pendulum arm and anvil was 72 kg-m^2 (Rowson B et al., 2015). A medium NOCSAE headform custom fit with a Hybrid III neck was mounted on a linear slide table with five degrees of freedom (DOF) (Cobb et al., 2014; Cobb et al., 2016). Three linear accelerometers (7264b-2000, Endevco, Irvine, CA) and a triaxial angular rate sensor (ARS3 Pro 18k, DTS, Seal Beach, CA) located in the headform center of mass measured reference kinematics. Tests were performed in both unhelmeted and helmeted conditions. For the unhelmeted condition, a 127 mm diameter and 40 mm thick vinyl-nitrile impactor face was mounted at the end of the anvil. For the helmeted condition, a flat, rigid, nylon impactor face measuring 127 mm in diameter and 25 mm thick was used. A large Riddell Speed (Elyria, OH) football helmet without the facemask was worn by the headform throughout helmeted tests.

Impacts were performed to the front, front boss, rear boss, and rear locations of the headform (Figure 68, Table 16), at targeted head accelerations of 25, 50, 75, and 100 g. The four impact locations were equally spaced around the head and had variable directions of force. Facemask impacts were not included due to their high inherent variability and permanent deformation upon impact (Cobb et al., 2016). The four targeted head accelerations were chosen to represent a range of subconcussive and concussive impacts (Rowson and Duma, 2011; Daniel et al., 2012; Pellman et al., 2003). Since constant pendulum angles produced variation in head acceleration from one location to the next, angles were varied by location to maintain consistent head accelerations. This allowed for more accurate location comparisons since preliminary tests showed that many sensors experienced increased error with increasing head acceleration. To remain consistent between tests, reference values were verified to remain

within an average of ±5 g of the target acceleration for each test condition. Each test configuration was repeated four times, totaling 64 tests per sensor.
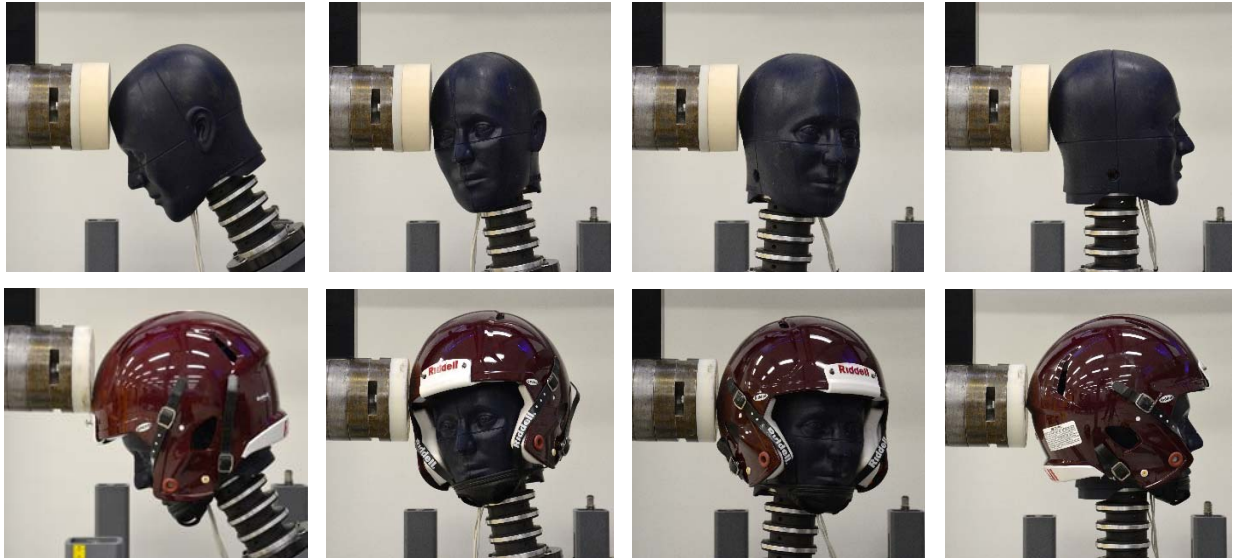
Figure 68: Impact locations from left to right: front, front boss, rear boss, rear. Unhelmeted tests (top) were conducted with a 40 mm-thick padded impactor. Helmeted tests (bottom) were conducted with a rigid impactor while the headform wore a large Riddell Speed helmet.

Table 16: NOCSAE headform translations and rotations on the linear slide table for each test condition.

Condition	Location	Y (cm)	Z (cm)	Ry (deg)	Rz (deg)
Unhelmeted	Front	0	-1.2	-30°	0°
	Front Boss	+3.5	+3.8	-10°	-60°
	Rear Boss	-2	+4.8	+5°	-120°
	Rear	0	+4.3	0°	-180°
Helmeted	Front	0	+4.3	-30°	0°
	Front Boss	+2	+3.8	-10°	-60°
	Rear Boss	-2	+5.3	+5°	-120°
	Rear	0	+4.3	0°	-180°

Notes: Y and Z-axis translation measurements were made with respect to the headform in a position where the median (midsagittal) and basic (transverse) plane intersection was aligned with the center of the impactor with 0° Y and Z-axis rotation, using the SAE J211 coordinate system. The position on the X-axis was defined as +1.25 cm before the helmeted headform contacted the pendulum in a neutral vertical position for all locations.

A sample of commercially-available wearable head impact sensors were assessed under this protocol (Figure 69, Table 17). The xPatch was developed by X2 Biosystems (Seattle, WA) and is adhered to the skin with an adhesive patch placed behind the ear over the mastoid process. Equivalent placement was found on the headform behind the right ear, and the sensor was tested under both unhelmeted and helmeted conditions. The SIM-G was developed by Triax Technologies (Norwalk, CT) and is worn in a headband with the sensor located at the back of the head along the nuchal line. It was tested under both unhelmeted and helmeted conditions. The Gforce Tracker (GFT) was developed by the company of the same name (Markam, ON) and has two possible sensor placements: fixed to a headband and adhered to the helmet shell. In the unhelmeted condition, GFT was fixed to a holder in the headband and worn with the sensor located at the back of the head along the nuchal line. In the helmeted condition, the sensor was adhered to the inside, back right side of the helmet shell oriented in the anterior-posterior direction. Shockbox was developed by Impakt Protective but is now owned by i1 Biometrics (Kirkland, WA) and is adhered to the helmet shell. It was only tested in the helmeted condition with the sensor located on the inside, right side of the helmet shell, oriented in the anterior-posterior direction. Hereafter, the sensors will be referred to as X2, Triax, GFT, and Shockbox. Sensor acceleration and velocity measurements were compared to reference measurements from the headform.

Figure 69: Sensors evaluated in this study. From left to right: X2, Triax, GFT, Shockbox.

Table 17: Wearable sensor details. Assessments were performed according to the ability of each sensor.

Sensor	Hardware Last Updated[a]	Components	Peak Headform Outputs[b]	Time Series Outputs	Output Sampling Rate	Location
X2	Oct 2014	3-axis accelerometer, gyroscope	LA, RV, RA	LA, RV	1000 Hz (RV: 850 Hz)	skin patch
Triax	June 2014	3-axis accelerometer, gyroscope	LA, RV, RA	LA, RV, RA	1000 Hz	headband
GFT	Oct 2015	3-axis accelerometer, gyroscope	LA, RV, RA	LA, RV	3000 Hz (RV: 760 Hz)	helmet, headband
Shockbox	Aug 2014[c]	3-axis accelerometer	LA	n/a	n/a	helmet

[a] All software and firmware were updated in Oct 2015
[b] LA = linear acceleration, RV = rotational velocity, RA = rotational acceleration
[c] An older model for Shockbox was tested to be consistent with the model used in Wong et al., 2014 [13]

Data Analysis

Linear acceleration and rotational velocity from the headform reference instrumentation were processed using MATLAB R2014a. The reference data were filtered at CFC 1000 for linear acceleration and CFC 155 for rotational velocity. Peak resultant linear acceleration, rotational velocity, and rotational acceleration values were computed for each impact. Sensor error was calculated by finding differences in peak values between the reference and wearable sensors. Negative error corresponds to underpredictions by the wearable sensors, whereas positive error corresponds to overpredictions. Average and standard deviations in sensor error were found for each wearable sensor at each location and impact energy. Because the sign of the error was retained, average error is representative of systematic error while the standard deviation is representative of random error.

Linear regressions constrained through the origin were used to define peak reference kinematics as a function of peak sensor kinematic measurements. Slope and R^2 were used as metrics of comparison between sensors. The slope is a measure of systematic error with values above and below 1.0 indicating under and overprediction, respectively. R^2 is a measure of random error, or the dispersion of test results. An R^2 value of one corresponds to an absence of random error, while error increases as R^2 approaches zero. Since the linear regression is constrained through the origin, negative R^2 values can also exist which indicate that the regression fits the data worse than a horizontal line.

For the sensors that also output time-series data, comparisons were made at each time point in addition to peak values. Since triggering thresholds for the start of the impact varied for each sensor compared to reference, the curves required systematic alignment. Sensor curves were iteratively time-shifted along references curves, and root mean square (RMS) error between the sensor and reference was found at each iteration (Eqn. 8):

$$RMS = \sqrt{\frac{\sum \left(x_{ref} - x_s\right)^2}{n}}$$ (Eqn. 8)

where x_{ref} is the kinematic value for the reference, x_s is the kinematic value for the wearable sensor, and n is the number of points in the time series. The minimum RMS error of all iterations was reported as RMS error for that impact. To compare between test conditions, the RMS error at a given test condition was normalized with respect to the reference peak. Average and standard deviations of normalized RMS error were calculated for each sensor at each location and impact energy.

Results

Overall, X2, Triax, and GFT performed best in rotational velocity as exhibited by slope and R^2 values closer to 1.00 (Table 18). X2 also performed well in linear acceleration with slopes near 1.0 and R^2 above 0.8. In rotational acceleration, however, X2 underpredicted the reference (m > 1.0) and exhibited large random error ($R^2 < 0.7$) for both conditions. Triax also performed worse in rotational acceleration with overpredictions of the reference (m < 1.0) and large random error ($R^2 < 0.2$) in both conditions. Unhelmeted GFT performed poorly for both linear acceleration and rotational velocity ($R^2 < 0.5$), although helmeted GFT only exhibited large random error in linear acceleration ($R^2 < 0.4$). Shockbox underpredicted in linear acceleration (m > 1.0) and exhibited such large random error that the data could not be modeled by the linear regression ($R^2 < 0$).

Table 18: Slope and R^2 values of linear regressions constrained through the origin based on peak reference kinematics as a function of peak sensor kinematic measurements.

Sensors and Conditions[a]		LA[b]		RV[b]		RA[b]	
		m	R^2	m	R^2	m	R^2
X2	U	1.05	0.98	1.01	1.00	1.65	0.61
	H	1.02	0.86	0.99	0.95	1.41	0.13
Triax	U	1.06	0.25	1.12	0.93	0.46	-0.56
	H	0.94	0.15	1.15	0.79	0.72	0.19
GFT	U	0.73	-0.24	0.65	0.42	n/a	
	H	0.38	0.39	1.06	0.89	n/a	
Shockbox	H	1.60	-1.19	n/a		n/a	

[a] U and H denote unhelmeted and helmeted test conditions, respectively.
[b] Values are given for linear acceleration (LA), rotational velocity (RV) and rotational acceleration (RA).

Normalized RMS error trends were similar to those observed with peak sensor error (Table 19). Lowest normalized RMS error for X2 and Triax was exhibited in rotational velocity. X2 exhibited the lowest error compared to the other sensors for both linear acceleration ($8 \pm 3\%$) and rotational velocity ($3 \pm 2\%$). Largest error for Triax was found in rotational acceleration for both unhelmeted ($43 \pm 36\%$) and helmeted ($30 \pm 15\%$) conditions. Helmeted GFT exhibited the largest error in linear acceleration ($46 \pm 27\%$) and unhelmeted GFT had the largest error in rotational velocity ($31 \pm 22\%$). Unhelmeted tests exhibited lower error than helmeted tests for X2, Triax, and GFT in linear acceleration and only X2 in rotational velocity. Shockbox did not output time-varying responses.

Table 19: Overall average (SD) normalized RMS error for the time-varying response of each sensor.

Sensors and Conditions[a]		LA (%)[b]		RV (%)[b]		RA (%)[b]	
X2	U	7.4	(0.8)	1.9	(1.3)	n/a	
	H	8.1	(2.5)	2.6	(1.7)	n/a	
Triax	U	18.4	(7.1)	15.1	(4.7)	42.8	(36.0)
	H	23.9	(11.1)	14.6	(5.6)	30.4	(14.9)
GFT	U	23.9	(15.8)	30.8	(22.4)	n/a	
	H	45.9	(26.6)	13.5	(4.4)	n/a	
Shockbox	H	n/a		n/a		n/a	

[a] U and H denote unhelmeted and helmeted test conditions, respectively.
[b] Values are given for linear acceleration (LA), rotational velocity (RV) and rotational acceleration (RA).

xPatch, X2 Biosystems

X2 successfully recorded all impacts for both unhelmeted and helmeted test conditions. Error in unhelmeted tests remained low for linear acceleration, with three test conditions exhibiting 12-17% systematic error while the remaining conditions were within 9% error (Figure 70, Table 20). Standard deviations, representing random error, remained within 3%. Rotational velocity demonstrated less than 4% systematic error. Standard deviations also remained below 6% with most test conditions remaining below 1%. Rotational acceleration displayed higher error than the other two kinematic variables: the front location systematically underpredicted the reference by 6 to 18% while the remaining locations

underpredicted by over 28%. However, standard deviations for all locations remained within 7%. X2 performed worse overall in helmeted tests. For linear acceleration, systematic error varied from 0 to 21% while standard deviations varied from 1 to 16%. Errors in rotational velocity mostly remained within 5% $\pm$ 2% except for the high-energy front condition which overpredicted by 9% $\pm$ 22%. The lowest error in rotational acceleration was found in the rear location, with sensor values underpredicting the reference by 4 to 18% with a standard deviation less than 4%. However, the remaining locations underpredicted up to 74% although standard deviations remained within 10%.

A two-way analysis of variance for unhelmeted tests yielded a significant main effect for location and energy in linear acceleration, and a significant interaction between location and energy ($p<0.001$). In rotational velocity, only significant differences were found in impact locations ($p<0.001$), not impact energy ($p=0.65$) or the interaction between location and energy ($p=0.06$). Rotational acceleration exhibited significant differences in location, energy, and the interaction between location and energy ($p<0.001$).

A two-way analysis of variance for helmeted tests yielded fewer significant effects in linear acceleration and rotational velocity. In linear acceleration, there was only significant differences in location and the interaction between location and energy ($p<0.001$). No significant differences were found in impact energy ($p=0.09$). There were also no significant differences in rotational velocity for either location ($p=0.25$), energy ($p=0.44$), or their interaction ($p=0.23$). Rotational acceleration exhibited significance in both the effects of location and energy as well as their interaction ($p<0.001$).
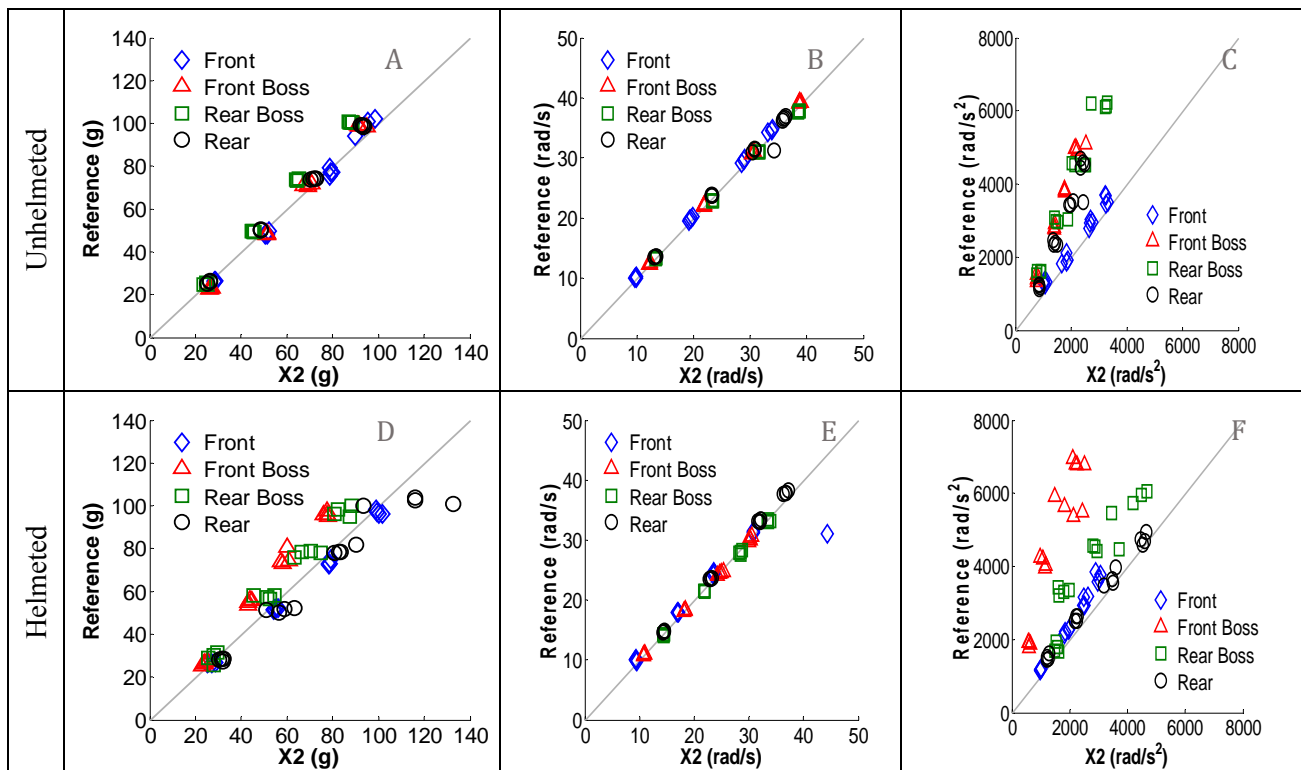
Figure 70: Peak reference values versus peak unhelmeted X2 (A,B,C) and helmeted X2 (D,E,F) values in linear acceleration (A,D), rotational velocity (B,E), and rotational acceleration (C,F). A 1:1 diagonal is drawn on each graph to visually show the amount of overprediction (points below line) and underprediction (points above line) of the reference.

Table 20: Average (SD) sensor error for unhelmeted and helmeted X2 tests. Column headings in peak linear acceleration represent the targeted values, while column headings for the other variables are peak reference averages for each impact energy.

		Error in Peak Linear Acceleration (g)							
		25		**50**		**75**		**100**	
Unhelmeted	Front	2.1	(0.1)	2.6	(0.4)	1.8	(1.7)	-4.6	(1.0)
	Front Boss	3.8	(0.2)	3.1	(0.1)	-2.0	(1.3)	-6.3	(2.1)
	Rear Boss	-0.5	(0.6)	-4.3	(0.7)	-9.3	(0.5)	-12.9	(0.9)
	Rear	0.1	(0.2)	-1.6	(0.1)	-2.2	(0.9)	-5.7	(1.0)
Helmeted	Front	-0.1	(1.5)	3.1	(0.6)	5.1	(0.8)	3.2	(2.1)
	Front Boss	-2.3	(0.1)	-11.4	(1.0)	-16.2	(3.1)	-18.9	(1.3)
	Rear Boss	-1.4	(2.4)	-6.4	(4.1)	-9.1	(4.4)	-12.7	(3.9)
	Rear	3.4	(0.9)	6.2	(4.7)	5.1	(2.7)	12.7	(15.7)

		Error in Peak Rotational Velocity (rad/s)							
		12		**21**		**30**		**35**	
Unhelmeted	Front	-0.3	(0.1)	-0.4	(0.1)	-0.7	(0.0)	-0.9	(0.1)
	Front Boss	-0.1	(0.1)	-0.2	(0.1)	-0.3	(0.1)	-0.4	(0.2)
	Rear Boss	0.1	(0.1)	0.4	(0.1)	0.5	(0.1)	0.9	(0.1)
	Rear	-0.3	(0.1)	-0.6	(0.1)	0.2	(1.8)	-0.6	(0.1)
Helmeted	Front	-0.6	(0.2)	-0.9	(0.1)	-0.9	(0.2)	2.9	(6.9)
	Front Boss	0.0	(0.1)	0.0	(0.1)	0.3	(0.1)	0.1	(0.2)
	Rear Boss	0.2	(0.2)	0.4	(0.1)	0.6	(0.3)	0.4	(0.3)
	Rear	-0.2	(0.0)	-0.5	(0.2)	-1.2	(0.2)	-1.2	(0.2)

		Error in Peak Rotational Acceleration (rad/s/s)							
		1482		**2799**		**3946**		**5048**	
Unhelmeted	Front	-240.2	(48.5)	-130.5	(120.1)	-227.0	(90.1)	-322.5	(160.0)
	Front Boss	-658.9	(73.6)	-1425.9	(70.7)	-2047.4	(25.3)	-2738.5	(134.0)
	Rear Boss	-747.3	(69.6)	-1451.5	(219.0)	-2235.7	(273.5)	-3036.8	(311.9)
	Rear	-337.6	(54.6)	-975.1	(111.0)	-1376.9	(191.7)	-2168.3	(134.0)
Helmeted	Front	-191.3	(10.5)	-336.6	(22.8)	-536.1	(101.5)	-730.5	(144.7)
	Front Boss	-1276.8	(83.3)	-3015.7	(217.1)	-3631.3	(627.2)	-4564.8	(244.3)
	Rear Boss	-223.5	(147.0)	-1577.2	(184.3)	-1420.6	(453.3)	-1608.1	(274.9)
	Rear	-279.7	(45.8)	-358.8	(54.7)	-233.1	(137.7)	-187.4	(121.9)

For unhelmeted X2 tests, average normalized RMS error for the entire time-varying response never exceeded 9% in linear acceleration and 4% in rotational velocity (Table 21). Standard deviations also remained below 5% with most test conditions remaining below 1%. Helmeted X2 tests exhibited slightly higher average normalized RMS error, but still did not exceed 12.6% in linear acceleration and 5.0% in rotational velocity. Standard deviations also remained below 6%. The largest differences in linear acceleration occurred in the rear boss and rear locations which exhibited spikes in acceleration 2 ms before the peak. Rotational velocity curves were very similar between helmeted X2 and reference, except for an occasional erroneous first data point in some test conditions.

Table 21: Average (SD) normalized RMS error for unhelmeted and helmeted X2 tests. Column headings for linear acceleration are targeted peak linear accelerations for each impact energy, while column headings for rotational velocity are peak reference averages.

		Normalized RMS Error in Linear Acceleration (%)							
		25 g		50 g		75 g		100 g	
Unhelmeted	Front	6.5	(0.2)	6.7	(0.2)	6.7	(0.6)	6.4	(0.6)
	Front Boss	7.9	(0.6)	7.4	(0.1)	7.1	(0.2)	7.5	(0.2)
	Rear Boss	7.5	(0.2)	7.1	(0.2)	7.4	(0.2)	6.7	(0.1)
	Rear	8.2	(0.2)	8.6	(0.3)	8.7	(0.2)	7.9	(0.3)
Helmeted	Front	6.3	(0.3)	6.5	(0.3)	5.3	(0.9)	6.6	(0.2)
	Front Boss	7.6	(0.3)	6.5	(0.2)	6.9	(0.7)	6.6	(0.4)
	Rear Boss	12.5	(5.9)	9.6	(0.8)	9.8	(2.9)	8.2	(0.9)
	Rear	9.5	(1.0)	9.5	(1.0)	9.3	(1.9)	9.5	(1.8)

		Normalized RMS Error in Rotational Velocity (%)							
		12 rad/s		21 rad/s		30 rad/s		35 rad/s	
Unhelmeted	Front	1.5	(0.4)	1.3	(0.5)	1.2	(0.5)	1.6	(0.2)
	Front Boss	1.9	(0.5)	1.9	(0.2)	2.0	(0.1)	3.2	(1.9)
	Rear Boss	1.4	(0.2)	1.9	(0.1)	2.3	(0.1)	2.6	(0.1)
	Rear	1.4	(0.3)	1.2	(0.4)	3.6	(4.4)	1.5	(0.2)
Helmeted	Front	1.6	(0.5)	1.9	(0.2)	2.0	(0.4)	4.9	(5.9)
	Front Boss	1.4	(0.2)	1.6	(0.1)	2.1	(0.4)	2.7	(0.5)
	Rear Boss	3.2	(0.3)	4.4	(0.5)	3.3	(0.6)	3.5	(0.9)
	Rear	1.6	(0.5)	3.1	(0.8)	2.3	(0.3)	1.7	(0.6)

A two-way analysis of variance for unhelmeted tests yielded a significant main effect for location ($p<0.001$) and energy ($p=0.005$) in linear acceleration, and a significant interaction between location and energy ($p=0.004$). In rotational velocity no significant differences were found in impact locations ($p=0.23$), impact energy ($p=0.18$) or the interaction between location and energy ($p=0.06$).

A two-way analysis of variance for helmeted tests yielded fewer significant effects in linear acceleration, yet more in rotational velocity. In linear acceleration, there were only significant differences in location ($p<0.001$). No significant differences were found in impact energy ($p=0.21$) or the interaction between location and energy ($p=0.48$). Similarly in rotational velocity, there were only significant differences in location ($p=0.02$). No significant differences were found in impact energy ($p=0.13$) or the interaction between location and energy ($p=0.23$).

SIM-G, Triax Technologies

Triax successfully recorded all helmeted impacts, although it failed to record two low-magnitude unhelmeted impacts. Unhelmeted tests exhibited widely variable error in linear acceleration: up to 130% at 25g and 2 to 48% in the remaining conditions with standard deviations between 1 and 35% (Figure 71, Table 22). Error was more consistent across test conditions in rotational velocity with the sensor systematically underpredicting 7 to 17%. Standard deviations also remained within 5%. The lowest error in rotational acceleration was found in the front boss location: 17 to 23% with standard deviations below 6%. The highest error was in the rear location with all systematic values over 170% and standard deviations between 12 and 60%. Helmeted tests performed similarly to unhelmeted, with up to 226% error in linear acceleration at 25 g, and 3 to 46% in the remaining conditions with standard deviations within 22%. Rotational velocity exhibited 3 to 37% systematic error. Standard deviations remained within 12% except for the rear location which displayed 26%. Rotational acceleration displayed up to 234% error at 25g, and 2 to 96% error in the remaining conditions with standard deviations between 3 and 58%.
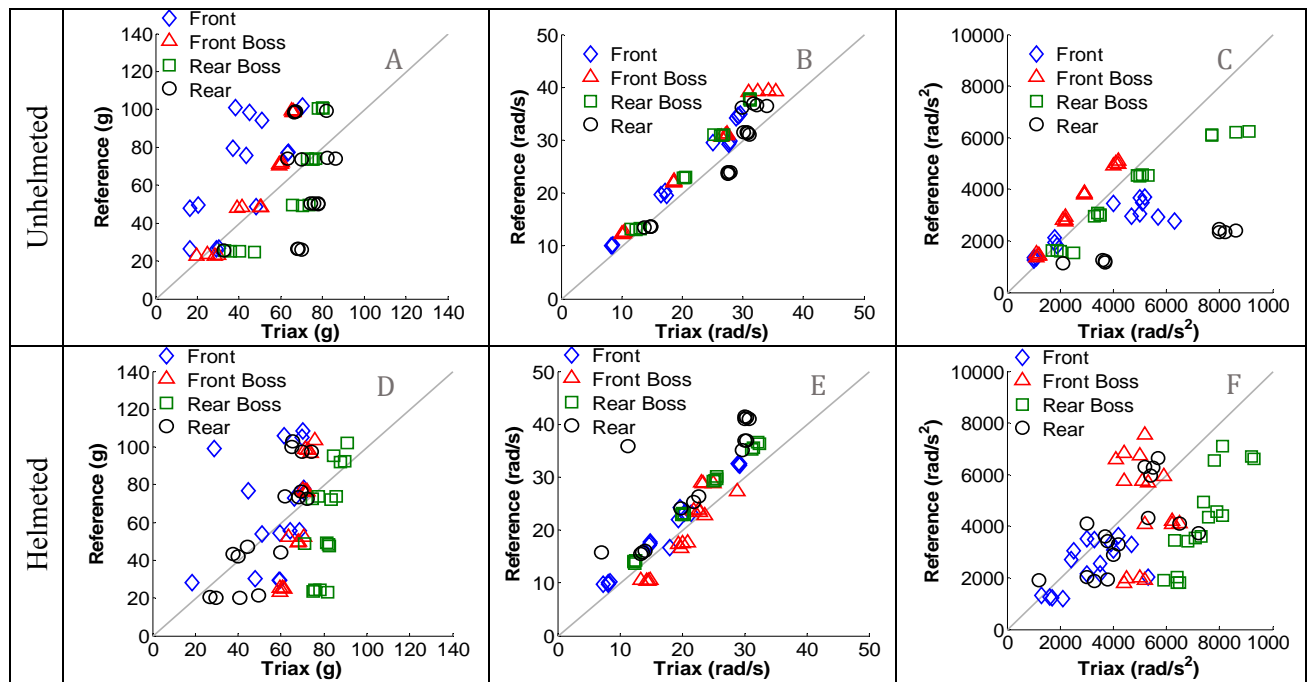
Figure 71: Peak reference values versus peak unhelmeted Triax (A,B,C) and helmeted Triax (D,E,F) values in linear acceleration (A,D), rotational velocity (B,E), and rotational acceleration (C,F). A 1:1 diagonal is drawn on each graph to visually show the amount of overprediction (points below line) and underprediction (points above line) of the reference.

A two-way analysis of variance for unhelmeted tests yielded significant main effects in all three kinematic variables for location and energy ($p<0.001$) as well as their interaction (LA: $p=0.02$; RV, RA: $p<0.001$).

A two-way analysis of variance for helmeted tests only yielded significant differences in all three kinematic variables for the main effects of location and energy ($p<0.001$). Linear acceleration did not exhibit significance in the interaction between location and energy ($p=0.09$), nor did rotational velocity ($p=0.14$). Rotational acceleration did exhibit significance on the interaction between the main effects ($p<0.001$).

For unhelmeted tests, average normalized RMS error ranged from 11% to 35% in linear acceleration, 9% to 27% in rotational velocity, and 10% to 131% in rotational acceleration (Table 23). Standard deviations were lowest in rotational velocity, remaining below 4%. Rotational acceleration exhibited standard deviations of up to 15%. Helmeted Triax tests exhibited similar error ranges: 12% to 54% in linear acceleration, 11% to 22% in rotational velocity, and 14% to 70% in rotational acceleration. Standard deviations were mostly lower than in the unhelmeted tests, except for the rear location in rotational velocity which displayed up to 18%.

A two-way analysis of variance for unhelmeted tests yielded significant main effects in all three kinematic variables for location and energy ($p<0.001$) as well as their interaction (LA: $p=0.003$; RV, RA: $p<0.001$).

A two-way analysis of variance for helmeted tests yielded fewer significant effects in rotational velocity and acceleration. In linear acceleration, significant differences were found in location, impact energy, and their interaction ($p<0.001$). Conversely for rotational velocity, there were no significant differences in location ($p=0.10$). No significant differences were found in impact energy ($p=0.33$) or the interaction between location and energy ($p=0.30$). Rotational acceleration only exhibit significance on the main effects of location ($p=0.05$) and energy ($p<0.001$), not their interaction ($p=0.32$).

Table 22: Average (SD) sensor error for unhelmeted and helmeted Triax tests. Column headings in peak linear acceleration represent the targeted values, while column headings for the other variables are peak reference averages for each impact energy.

		Error in Peak Linear Acceleration (g)							
		25		**50**		**75**		**100**	
Unhelmeted	**Front**	-1.0	(7.4)	-20.5	(17.2)	-25.5	(14.1)	-47.9	(13.4)
	Front Boss	2.9	(4.4)	-2.8	(5.7)	-11.2	(0.3)	-33.0	(0.6)
	Rear Boss	14.1	(6.3)	21.3	(3.6)	1.2	(1.6)	-21.0	(1.0)
	Rear	33.8	(17.6)	26.3	(1.8)	1.4	(10.6)	-28.2	(7.3)
Helmeted	**Front**	17.0	(18.7)	5.9	(6.8)	-12.7	(12.8)	-47.3	(15.9)
	Front Boss	35.8	(1.1)	16.8	(3.7)	-5.1	(1.3)	-25.8	(2.4)
	Rear Boss	53.8	(3.3)	30.7	(6.0)	7.1	(5.3)	-7.4	(4.4)
	Rear	16.3	(10.0)	1.3	(9.8)	-6.1	(4.7)	-30.9	(6.5)

		Error in Peak Rotational Velocity (rad/s)							
		12		**22**		**30**		**36**	
Unhelmeted	**Front**	-1.8	(0.1)	-2.8	(0.6)	-2.4	(1.4)	-5.4	(0.1)
	Front Boss	-2.1	(0.1)	-3.5	(0.2)	-3.8	(0.3)	-5.9	(1.9)
	Rear Boss	-0.7	(0.6)	-2.6	(0.2)	-4.7	(0.7)	-6.6	(0.1)
	Rear	0.9	(0.4)	3.8	(0.2)	-0.6	(0.6)	-4.6	(1.6)
Helmeted	**Front**	-2.0	(0.4)	-1.7	(2.0)	-2.9	(1.2)	-3.4	(0.2)
	Front Boss	3.9	(0.7)	2.8	(0.6)	-0.7	(1.2)	-3.4	(3.3)
	Rear Boss	-1.7	(0.3)	-2.9	(0.2)	-4.3	(0.2)	-4.2	(0.3)
	Rear	-3.8	(3.3)	-3.9	(0.5)	-10.9	(9.2)	-10.9	(0.5)

		Error in Peak Rotational Acceleration (rad/s/s)							
		1562		**2913**		**4029**		**5339**	
Unhelmeted	**Front**	-526.8	(499.3)	-557.3	(885.3)	2501.5	(813.6)	1244.6	(473.9)
	Front Boss	-271.7	(98.3)	-642.6	(76.2)	-913.0	(26.6)	-864.5	(63.6)
	Rear Boss	437.6	(380.8)	409.4	(101.8)	540.3	(168.8)	2112.3	(630.0)
	Rear	2076.6	(745.9)	5814.6	(299.6)	9502.2	(729.2)	9260.9	(503.9)
Helmeted	**Front**	434.8	(384.4)	1602.4	(1127.5)	-38.3	(658.1)	510.1	(785.0)
	Front Boss	2858.3	(354.3)	1909.4	(556.2)	-593.7	(565.9)	-2254.9	(343.6)
	Rear Boss	4410.8	(300.6)	3374.1	(363.8)	3187.7	(519.9)	1852.3	(850.4)
	Rear	885.7	(1129.0)	610.7	(466.3)	1430.7	(1966.5)	-843.4	(223.2)

Table 23: Average (SD) normalized RMS error for unhelmeted and helmeted Triax tests. Column headings for linear acceleration are targeted peak linear accelerations for each impact energy, while column headings for the remaining variables are peak reference averages.

		Normalized RMS Error in Linear Acceleration (%)							
		25 g		**50 g**		**75 g**		**100 g**	
Unhelmeted	**Front**	19.4	(5.3)	22.5	(4.9)	21.5	(5.5)	20.7	(4.5)
	Front Boss	15.5	(0.9)	13.3	(1.0)	11.8	(0.4)	11.8	(0.5)
	Rear Boss	24.4	(3.4)	18.3	(1.5)	11.0	(0.3)	11.7	(1.4)
	Rear	34.6	(10.2)	21.8	(4.6)	19.0	(5.5)	18.2	(2.9)
Helmeted	**Front**	30.7	(8.0)	24.4	(4.5)	22.6	(1.9)	18.9	(5.0)
	Front Boss	35.2	(2.7)	20.1	(1.7)	12.6	(1.6)	12.4	(4.5)
	Rear Boss	53.8	(3.9)	22.9	(4.0)	18.3	(2.2)	15.1	(2.2)
	Rear	36.6	(9.6)	22.1	(1.1)	15.0	(4.6)	21.5	(1.6)

		Normalized RMS Error in Rotational Velocity (%)							
		12 rad/s		**22 rad/s**		**30 rad/s**		**36 rad/s**	
Unhelmeted	**Front**	10.2	(0.3)	9.2	(0.8)	19.7	(2.6)	17.7	(0.8)
	Front Boss	11.1	(0.2)	11.3	(0.0)	11.4	(0.1)	12.9	(0.4)
	Rear Boss	15.7	(3.8)	14.4	(0.3)	15.8	(2.9)	12.8	(0.3)
	Rear	16.0	(1.2)	12.8	(0.4)	20.4	(2.0)	27.2	(0.7)
Helmeted	**Front**	14.8	(2.3)	17.8	(0.6)	13.8	(3.8)	11.2	(1.2)
	Front Boss	15.1	(0.9)	11.1	(0.6)	11.1	(0.9)	15.2	(2.0)
	Rear Boss	16.5	(1.0)	12.1	(0.9)	11.9	(0.6)	13.1	(1.6)
	Rear	20.0	(10.2)	13.3	(1.3)	21.9	(17.9)	14.4	(0.2)

		Normalized RMS Error in Rotational Acceleration (%)							
		1562 rad/s^2		**2913 rad/s^2**		**4029 rad/s^2**		**5339 rad/s^2**	
Unhelmeted	**Front**	10.6	(0.8)	13.1	(4.9)	51.9	(8.6)	40.8	(4.0)
	Front Boss	10.1	(0.5)	11.9	(0.5)	15.2	(0.8)	16.7	(2.0)
	Rear Boss	35.3	(13.6)	21.4	(1.4)	27.1	(2.6)	34.2	(1.5)
	Rear	64.3	(15.3)	84.4	(6.1)	130.7	(12.5)	101.6	(7.7)
Helmeted	**Front**	28.5	(11.6)	38.3	(17.5)	22.3	(3.3)	19.5	(2.9)
	Front Boss	48.7	(2.2)	28.0	(2.5)	16.8	(1.2)	16.3	(4.6)
	Rear Boss	69.6	(9.9)	38.5	(3.1)	30.0	(2.2)	23.5	(1.5)
	Rear	35.7	(5.3)	25.8	(4.6)	30.3	(10.3)	13.9	(0.5)

GFT successfully recorded all impacts for both unhelmeted and helmeted test conditions. In linear acceleration, the lowest error was found in the front location: 2 to 20% with standard deviations within 5% (Figure 72, Table 24). The rear boss and rear locations overpredicted the reference by over 200% at 25g and by 15 to 120% for the remaining impact energies. Standard deviations for these locations varied between 8 and 70%. Rotational velocity displayed lower error than linear acceleration. The lowest error was found in front boss: 5-12% with standard deviations between 6 and 20%. Rear boss and rear overpredicted by over 140% at 25g and 44 to 84% for the remaining conditions with standard deviations between 4 and 44%. Linear acceleration values for the helmeted tests exhibited higher systematic error, yet lower random error than unhelmeted tests. Front and front boss locations displayed 40 to 85% while rear and rear boss locations were over 140%. However, all standard deviations were less than 22%. Rotational velocity exhibited lower error overall compared to unhelmeted tests, with systematic error remaining within 22% and standard deviations within 16%.

A two-way analysis of variance for unhelmeted tests yielded significant main effects in both kinematic variables for location ($p<0.001$) and energy (LA: $p<0.001$; RV: $p=0.004$). There was no significant interaction between location and energy in linear acceleration ($p=0.05$), although there was a significant interaction in rotational velocity ($p<0.001$). A two-way analysis of variance for helmeted tests yielded significant main effects in both kinematic variables for location and energy as well as their interaction ($p<0.001$).
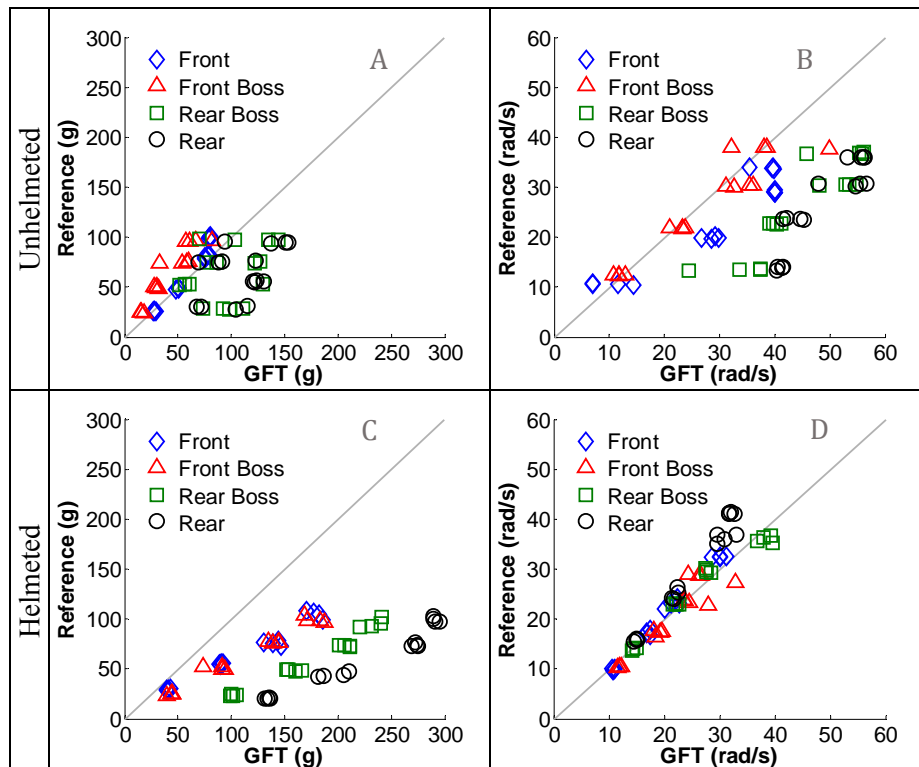
Figure 72: Peak reference values versus peak unhelmeted GFT (A,B) and helmeted GFT (C,D) values in linear acceleration (A,C) and rotational velocity (B,D). A 1:1 diagonal is drawn on each graph to visually show the amount of overprediction (points below line) and underprediction (points above line) of the reference.

Table 24: Average (SD) sensor error for unhelmeted and helmeted GFT tests. Column headings in peak linear acceleration represent the targeted values, while column headings for rotational velocity are peak reference averages for each impact energy.

		Error in Peak Linear Acceleration (g)							
		25		**50**		**75**		**100**	
Unhelmeted	**Front**	1.5	(1.2)	1.1	(1.0)	-3.9	(1.0)	-20.1	(0.8)
	Front Boss	-9.0	(2.1)	-19.9	(2.4)	-23.6	(12.0)	-29.2	(10.5)
	Rear Boss	65.8	(15.9)	21.7	(36.6)	28.1	(25.1)	15.3	(33.9)
	Rear	59.8	(23.9)	68.5	(4.2)	17.4	(21.8)	39.2	(28.1)
Helmeted	**Front**	11.4	(1.0)	35.2	(1.3)	64.2	(8.5)	74.1	(10.3)
	Front Boss	18.7	(1.6)	36.7	(10.5)	64.1	(5.2)	78.3	(11.8)
	Rear Boss	77.5	(2.4)	109.1	(7.4)	134.2	(5.7)	137.8	(6.5)
	Rear	113.7	(2.5)	151.6	(11.9)	198.9	(2.8)	191.7	(5.0)

		Error in Peak Rotational Velocity (rad/s)							
		13		**22**		**29**		**36**	
Unhelmeted	**Front**	-0.6	(3.8)	8.7	(1.3)	10.9	(0.3)	4.8	(2.2)
	Front Boss	-0.6	(0.9)	1.0	(1.2)	3.6	(2.2)	1.8	(7.5)
	Rear Boss	19.7	(6.0)	17.3	(0.9)	21.8	(2.8)	16.4	(5.0)
	Rear	27.1	(0.4)	19.7	(1.9)	23.0	(4.0)	19.4	(1.4)
Helmeted	**Front**	0.9	(0.3)	-0.1	(0.6)	-1.5	(0.8)	-2.5	(1.0)
	Front Boss	1.6	(0.3)	1.6	(0.7)	1.5	(2.5)	-0.9	(4.4)
	Rear Boss	0.4	(0.2)	-0.9	(0.5)	-1.8	(0.8)	2.4	(1.3)
	Rear	-0.9	(0.2)	-3.0	(0.7)	-5.4	(1.5)	-9.2	(0.6)

For unhelmeted tests, average normalized RMS error ranged from 6% to 59% in linear acceleration and 7% to 99% in rotational velocity (Table 25). The only standard deviations over 10% were found in low-magnitude rear boss impacts. For helmeted tests, higher average normalized RMS error was found in linear acceleration with values ranging from 21% to 118%. However, rotational velocity values exhibit less error than the unhelmeted tests with values ranging from 5% to 21%. Standard deviations also mainly remained below 5% for the helmeted impacts.

A two-way analysis of variance for both unhelmeted and helmeted tests yielded significant main effects in both kinematic variables for location and energy as well as their interaction ($p<0.0001$).

Table 25: Average (SD) normalized RMS error for unhelmeted and helmeted GFT tests. Column headings for linear acceleration are targeted peak linear accelerations for each impact energy, while column headings for rotational velocity are peak reference averages.

		Normalized RMS Error in Linear Acceleration (%)							
		25 g		**50 g**		**75 g**		**100 g**	
Unhelmeted	**Front**	8.5	(1.6)	6.4	(0.5)	5.5	(0.3)	8.5	(0.8)
	Front Boss	21.0	(1.1)	20.9	(0.2)	24.1	(2.4)	20.6	(1.8)
	Rear Boss	58.8	(9.9)	21.8	(14.0)	15.6	(2.7)	18.5	(2.6)
	Rear	56.7	(6.1)	45.1	(1.1)	28.3	(2.9)	23.0	(2.8)
Helmeted	**Front**	31.2	(2.0)	34.7	(1.1)	31.7	(1.1)	24.1	(2.6)
	Front Boss	33.8	(1.2)	26.0	(6.1)	23.9	(1.2)	20.9	(2.1)
	Rear Boss	78.0	(1.4)	48.7	(3.1)	37.6	(2.4)	29.0	(0.3)
	Rear	118.2	(5.3)	82.1	(3.9)	66.3	(1.6)	48.2	(3.0)

		Normalized RMS Error in Rotational Velocity (%)							
		13 rad/s		**22 rad/s**		**29 rad/s**		**36 rad/s**	
Unhelmeted	**Front**	31.6	(9.6)	30.1	(1.4)	23.4	(0.1)	6.6	(1.5)
	Front Boss	13.4	(4.5)	16.3	(1.4)	17.2	(2.6)	13.8	(2.4)
	Rear Boss	52.9	(13.6)	28.0	(12.6)	37.2	(12.8)	35.1	(3.8)
	Rear	99.0	(4.6)	47.0	(6.4)	25.1	(5.1)	15.4	(1.4)
Helmeted	**Front**	5.4	(0.3)	21.4	(1.1)	19.5	(3.4)	6.8	(1.3)
	Front Boss	12.9	(1.0)	11.9	(1.3)	13.5	(0.4)	18.5	(1.4)
	Rear Boss	9.1	(0.4)	11.0	(0.3)	13.0	(1.2)	15.0	(1.9)
	Rear	15.6	(2.0)	13.8	(2.7)	13.1	(1.4)	15.4	(0.3)

Shockbox failed to record nine low-magnitude helmeted impacts, including all those to the front and rear boss locations. Front, front boss, and rear boss locations systematically underpredicted the reference by 50 to 80% with standard deviations ranging from 3 to 24% (Figure 73, Table 26). The rear locations exhibited the lowest systematic errors of 4 to 42%. However, standard deviations ranged from 6 to 28%. Shockbox was excluded from statistical analyses due to the low number of data points.
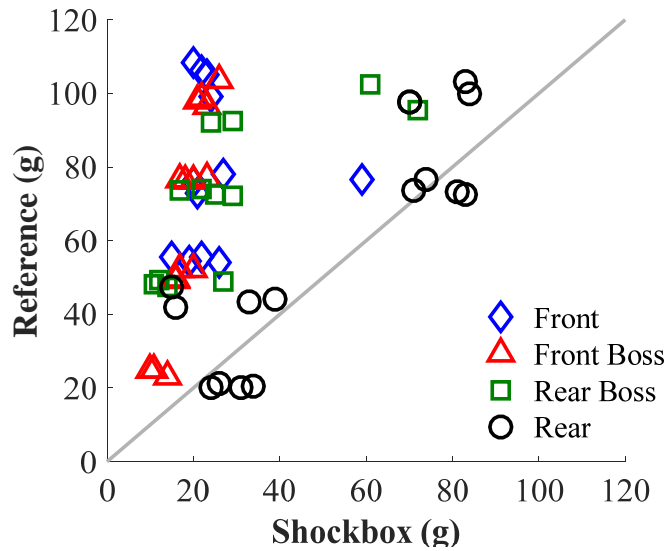
Figure 73: Peak reference values versus peak helmeted Shockbox values in linear acceleration. A 1:1 diagonal is drawn on each graph to visually show the amount of overprediction (points below line) and underprediction (points above line) of the reference.

Table 26: Average (SD) sensor error for helmeted Shockbox tests. Column headings in peak linear acceleration represent the targeted values. Empty cells indicate the absence of sensor data for those test conditions.

| | | **Error in Peak Linear Acceleration (g)** | | | | | | |
	25		**50**		**75**		**100**	
Front			-34.5	(5.1)	-44.1	(17.8)	-82.5	(5.5)
Front Boss	-12.6	(3.2)	-33.6	(1.3)	-57.0	(2.4)	-76.2	(1.8)
Rear Boss			-32.6	(7.3)	-49.9	(5.8)	-49.1	(20.7)
Rear	8.3	(4.7)	-18.5	(12.7)	3.2	(6.8)	-22.8	(5.8)

Shockbox does not output time series data for each impact, so normalized RMS error could not be calculated.

Discussion

Wearable head impact sensors have many promising benefits for both consumers and researchers such as objectively identifying severe impacts and investigating head impact biomechanics. However, the challenges of accurately measuring head kinematics in the real world are displayed by large errors and low reliability even in ideal laboratory tests. By creating an objective evaluation system for these sensors, consumers and researchers can be informed of their accuracy and manufacturers can use these methods as design criteria for further development. The commonly-used HIT System has previously been extensively tested in the laboratory under various conditions (Beckwith et al., 2012; Crisco et al., 2004; Jadischke et al. 2013). Beckwith et al. and Jadischke et al. both found minimal average error in helmet shell impacts of less than 2% in linear acceleration and 6% in rotational acceleration according to the slope of linear regressions constrained through the origin, although individual measurement error was found to be higher (Beckwith et al., 2012; Jadischke et al. 2013). Corresponding R^2 values remained above 0.9 in linear acceleration and 0.8 in rotational acceleration. These values indicate higher accuracy in rotational acceleration compared to the helmeted sensors evaluated in this study, and similar accuracy to X2 in linear acceleration. While the HIT System performed well in ideal conditions, Beckwith and Jadischke demonstrated decreased accuracy for facemask impacts with error in the slope greater than 60% and R^2 less than 0.6 (Beckwith et al., 2012; Jadischke et al. 2013). Jadischke also reported decreased accuracy in cases of poor helmet fit ($R^2 < 0$) (Jadischke et al. 2013).

It is important to note that there are factors inherent in the calculations of linear and rotational acceleration by the sensor that attribute to the higher error in those two kinematic variables compared to rotational velocity. Linear acceleration and rotational velocity of the sensor, which are directly measured, both have low sampling rates (850-1000 Hz) compared to that of the reference sensor (20000 Hz). Rotational acceleration is obtained by differentiating rotational velocity, which amplifies any noise present in rotational velocity. Linear acceleration at the center of gravity of the headform is then computed using both rotational velocity and rotational acceleration, introducing additional error.

Helmeted X2 exhibited spikes in the linear acceleration trace 2 ms before the expected peak in rear boss and rear locations. They may have been caused by helmet interactions with the sensor, since the rear boss and rear locations are in close proximity to the sensor placement behind the ear. Although these spikes were not large enough to decrease overall error in the sensor, they did affect the random error since they were not observed in every test of the same condition. In rotational velocity, one front helmeted X2 test had an erroneous first data point that was classified as the peak. If the correct peak was identified, the R^2 value would be 0.99 rather than 0.95. By identifying the true peak with the time-series data rather than relying on the peak value automatically output by the sensor, this problem can be eliminated. Overall, X2 performed well under ideal laboratory conditions.

Unhelmeted Triax tests produced significant differences in location and wide variability in systematic and random error among test conditions. In linear acceleration, Triax peak values did not exceed 86 g; therefore all 100 g tests exhibited large systematic error. Many test conditions also included up to 17 g in random error which indicates that accuracy will not be greatly increased with simple correction factors.

For helmeted Triax tests, errors were significantly higher than those seen in the unhelmeted condition, indicating a possible physical effect of the helmet on the sensor. With a helmeted headform, the sensor stays in constant contact with the helmet. Consequently, the helmet may cause extra movement of the sensor at all impact locations.

Unhelmeted GFT tests exhibited a second large, shorter-duration peak in linear acceleration occurring around 20 ms in the rear boss and rear locations that was often classified as the true peak. If the impact occurred before 20 ms, the R^2 value would increase from -0.24 to 0.62. The erroneous peaks may have occurred due to poor coupling between the headband and headform. In the rear boss and rear locations, the resultant headform motion at impact

is directed away from the sensor which is located at the back of the head. This positioning could result in an inertial effect of the sensor resulting in decoupling from the headform. Similar movement has been observed with an unhelmeted skull cap during head impacts (Wu et al., 2015).

Largest systematic errors for helmeted GFT occurred in the rear boss and rear locations. These large errors may be partly due to the fact that those two locations are closest to the sensor position on the inside shell of the helmet. The error trends for helmeted GFT in this study are similar to those found by Campbell et al. and Allison et al. including large overpredictions in linear acceleration but higher accuracy in rotational velocity (Campbell et al., 2015; Allison et al., 2014).

Shockbox was unreliable in recording many low-severity head impacts. The unreliability and large errors inherent in this sensor should be considered in on-field studies (Wong et al., 2014).

Limitations

Through laboratory testing, sensors were evaluated in an ideal scenario that does not take into account additional factors such as variations in sensor placement, sweat, hair, skin movement, and false hits. We propose a multi-phased approach to defining sensor accuracy in order to take into account various factors that could attribute to sensor error. Once sensors have demonstrated repeatability in the laboratory, they should additionally undergo field and cadaver tests.

Field tests include all possible factors that could cause the sensors to collect erroneous data, although there is currently no available on-field reference sensor to confirm the accuracy of kinematic output of the wearable sensors. Instead, field tests can provide information on the number of false positives (false impacts still recorded by the sensor) and false negatives (true impacts not recorded by the sensor) that occur during player use in practices and games. The X2 sensor which exhibited high repeatability in the lab was further evaluated on the field where it displayed inaccurate exposure counts and overpredictions of expected peak head kinematics possibly due to poor coupling with the skull (Press and Rowson, 2016). Kinematic overpredictions have also been found in cadaver tests as a result of relative motion between the skin and skull (Wu et al., 2015). Cadaver tests provide further detailed analysis of sensors that perform well both under ideal conditions and on the field. These tests give quantitative results of the effects of factors observed on the field that cannot be replicate on a dummy headform, such as skin movement. The framework of this multi-phased approach forms the basis of an overall sensor evaluation.

Lateral Facial Fracture Research

The following journal article was written and submitted to the Journal of the Mechanical Behavior of Biomedical Materials describing fracture tolerance of the facial bones to lateral impact.

TITLE: The tolerance and biomechanical response of facial bones to lateral impact
AUTHORS: Cormier JM, Rowson S, McNally C, Bolte J, and Duma SM
JOURNAL: Journal of the Mechanical Behavior of Biomedical Materials
STATUS: Under Review

Abstract

Previous studies on the tolerance of the facial bones have focused on its tolerance to anterior-posterior loading. This paper presents the results of 60 lateral facial bone impacts performed on male specimens. Acoustic emission sensors were used to identify the force at which fracture initiated. Parametric and non-parametric techniques were used to create a relationship between impactor force and risk of fracture. For the frontal bone, the non-parametric risk estimates indicate that a 50% risk of frontal bone fracture occurs at a force between 1700 and 2400 N. The nasal bone and zygoma reached a 50% risk at 90 to 130 N and 650 to 700 N respectively. Age was found to be a statistically significant factor in the risk of frontal bone fracture only. A Weibull model is also presented with age as a covariate to account for its influence on fracture risk. The fracture patterns resulting from the lateral impacts are also described. The data gathered during this study provides a model for predicting facial fracture due to lateral impact as well as a measure of its force-displacement response which can be useful in assessing the biofidelity of physical and computational models.

Introduction

The facial bones play an important role in protecting the head and brain from external forces. Understanding their tolerance and response to impact is crucial in developing countermeasures to prevent injuries to the head and brain. The majority of frontal bone fractures occur as a result of motor vehicle collisions, assaults, sports and falls (Gassner et al., 2003; Jayamanne and Gillie, 1996; Lim et al., 1993; Muraoka et al., 1995b; Shaprio et al., 2001). Fractures to the orbital bones have been observed in automobile accidents, sport impacts, and in military operations (Cormier and Duma, 2009; Cormier et al., 2006; Duma et al., 2002; Duma and Jernigan, 2003; Manoogian et al., 2006; Power et al., 2002; Shain et al., 2010; Vinger et al., 1999). The response of the frontal bone to impact has been studied by several previous groups which have focused on Anterior–Posterior directed impacts (Cormier et al., 2011a; Cormier et al., 2010b; Hodgson et al., 1970; Nahum, 1975b; Schneider and Nahum, 1972). These studies have provided information related to the tolerance and stiffness of the frontal bone to various shapes of impactors including cylindrical and flat. Cylindrical impactors were used to simulate impact with a steering wheel and were used to strike the face in an Anterior-Posterior direction or obliquely. When estimating the tolerance of the frontal bone, previous studies have used peak force or the onset of fracture identified using Acoustic Emission (AE) sensors. Previous studies have demonstrated that when fracture force is identified using AE, it often precedes the peak force achieved during impact (Allsop and Kennett, 2002; Allsop et al., 1988; Cormier et al., 2011a, b; Cormier et al., 2008; Funk et al., 2002; Kent et al., 2008). This suggests that previous studies on facial tolerance will overestimate fracture tolerance when using peak force.

The nasal bone is a weak and prominent facial structure and is the most frequently fractured facial structure. An analysis of motor vehicle collisions using NASS-CDS data demonstrated that in frontal impact, the nasal bone was the most commonly fracture facial structure (Cormier and Duma, 2009). The nasal bone is also among most commonly fractured structure for other types of trauma including violence, sports and falls (Alvi et al., 2003; Hackle et al., 2001; Muraoka et al., 1995a). With respect to violence, alcohol consumption is commonly

associated with facial trauma (Carvalho et al., 2010). A study of 322 facial fractures from sports found that nasal fractures were present in 56% which accounted for 55% of the patients requiring treatment under anesthesia (Carroll et al., 1995). Earlier studies evaluating the cause of facial fracture in automotive collisions found that the steering wheel and windshield were among the most common sources (Huelke and Compton, 1983; Karlson, 1982). Similar findings were reached in a recent study using NASS-CDS data that also demonstrated the protective benefits of airbags, especially for a belted occupant (Cormier and Duma, 2009).

Understanding the tolerance of the nasal bone will help design and evaluate facial protective measures. With respect to lateral impacts there has been no previous work using this impact direction. With respect to anterior-posterior impact, there is a limited amount of work that has been done which focused specifically on the nasal bone. Studies have evaluated the tolerance of the facial structures using cylindrical impactors meant to replicate a steering wheel (Allsop and Kennett, 2002; Cesari et al., 1989; Nyquist et al., 1986). Due to a relatively large impact surface, those impacts involve other areas of the face besides the nasal bone, limited there application to the nasal bone. A study by Nahum et al. determined a minimal tolerance of the nasal bone of 111 to 334 N using a round, flat impactor with an area of 6.45 cm^2 (Nahum, 1975b). The number of impacts performed was not documented and, therefore, the statistical significance is unknown. A more recent study, performed by the current authors determined a statistical relationship between impact force and fracture risk. The risk curve was based on 24 tests using a round flat impactor (6.45 cm^2) in which acoustic emission data were used to determine the force at the onset of fracture (Cormier et al., 2010a).

The majority of lateral impacts to the skull have been performed on the zygoma (zygomatic arch), temporoparietal bones (Bermond et al., 1999; Schneider and Nahum, 1972; Yoganandan et al., 1988). Among these areas, the zygoma has been found to be the weakest with a minimal force tolerance of 890 N compared to the temporoparietal bone with a tolerance of 2000 N (Schneider and Nahum, 1972). Bermond *et al.* (1999) performed oblique impacts to the frontal bone using a cylindrical impactor and measured an average peak force of 4050 N during tests not resulting in fracture (Bermond et al., 1999). Fracture tests had an average peak force of 5500 N. Similar impacts were performed by Allsop *et al.* (1988) using a cylindrical impactor in the A-P direction with the addition of AE sensors to detect the onset of fracture. During their study the average force at fracture onset was 4800 N. The differences between these cylindrical impactor studies are likely related to the A-P direction used by Allsop *et al.* which allows for the impactor force to be distributed across the frontal bone.

The tolerance and biomechanical response of the facial bones to lateral impacts can be applied toward future safety systems using the Facial and Ocular CountermeasUre for Safety (FOCUS) headform, which can measure forces in the area of the frontal bone (Cormier et al., 2010b). This headform has been used by the U.S. Army to evaluate the effectiveness of safety countermeasures for facial protection (Bisplnghoff et al., 2008). This is in partial response to the proportionally higher incidence of head and neck injuries caused by blast exposure in recent conflicts (Owens et al., 2008). Data obtained during a previous study by the current authors has been used to evaluate and improve Finite Element Models (FEM) of the face for fracture prediction due to impact (Laituri and El-jawahri, 2012). Therefore, the data gathered during the current study has the potential to provide valuable information regarding the biomechanical response and tolerance of the frontal bone to blunt impact. The purpose of this study is to expand on the current understanding of the biomechanical response of the facial bones by investigating their response to lateral impacts.

Methods

The data for this study were obtained by performing 60 lateral impact tests on 20 male cadaver specimens (Table 27). The unembalmed fresh-frozen subjects ranged in age from 53 to 90 with an average of 74. Each specimen was prepared by removing the soft tissue and partially inserting screws on the side of the skull to be mounted for testing. The soft tissues on the contralateral side were left intact for testing. The specimen was mounted horizontally in a polycarbonate fixture using Bondo. The impacting device was a free-falling rigid mass (3.2 kg)

with a cylindrical steel tip (Figure 74). The flat impacting surface had an area of 6.45 cm^2 (1 in^2) and was machined with a slight bevel to reduce edge effects.

For frontal bone impacts, the impactor was aligned by measuring 1 cm posteriorly from the anterior surface of the maxilla at a vertical level even with the bottom of the orbit. The impact location was then marked 6 cm superiorly from this point. For the nasal bone impacts, the impactor was aligned by palpating the nasal bone to determine its inferior margin. This location was then centered under the impactor and the anterior-posterior position was set to limit the interaction with the frontal process of the maxilla. For the zygoma impacts, the center of the impactor was aligned with a point 1 cm posterior to the inferior rim of the adjacent orbit.

Table 27: Specimen information.

Specimen Number	Age	Height (cm)	Weight (kg)
39	83	173	38
40	82	175	37
41	87	165	39
42	79	NA	NA
43	62	173	28
44	54	168	24
45	53	183	24
46	82	163	37
47	76	170	34
48	71	183	32
49	79	183	36
50	63	183	29
51	76	188	34
52	90	183	41
53	89	168	40
54	74	175	34
55	76	180	34
56	70	183	32
57	59	175	27
58	83	178	38

The rigid impactor was instrumented with a single-axis accelerometer (Endevco 7264B-2000, Endevco Corp., San Juan Capistrano CA). A load cell (Denton, 8617JTF, Rochester Hills, MI) was attached to the tip of the impactor which was also instrumented with a single axis accelerometer (Endevco 7264B-2000, Endevco Corp., San Juan Capistrano CA). Impact force was obtained using the impactor load cell while inertially compensating for the tip mass. The secondary accelerometer mounted at the top of the impactor was redundant. All data were sampled at 20 kHz and filtered to CFC 300 which has been utilized in previous studies (Cormier et al., 2010a; Cormier et al., 2011a, b). A spectral analysis was also performed to ensure the use of CFC 300 provided adequate noise reduction and did not remove any meaningful content of the data. Impactor displacement was calculated by double-integrating the acceleration data. High-speed video was also recorded at a frame rate of 4,000 fps (Phantom Brea, CA). The video data were used to determine impact velocity as well as identify tests that would be useful for assessing the force-displacement response. Impactor displacement was calculated by double integrating the accelerometer data. To describe the average stiffness of the frontal bone a corridor was created using the characteristic average (Lessley et al., 2004). The characteristic average was created up to peak force

unless the data contained a smaller peak prior to peak force, then the first peak was used as the cut-off for the corridor.
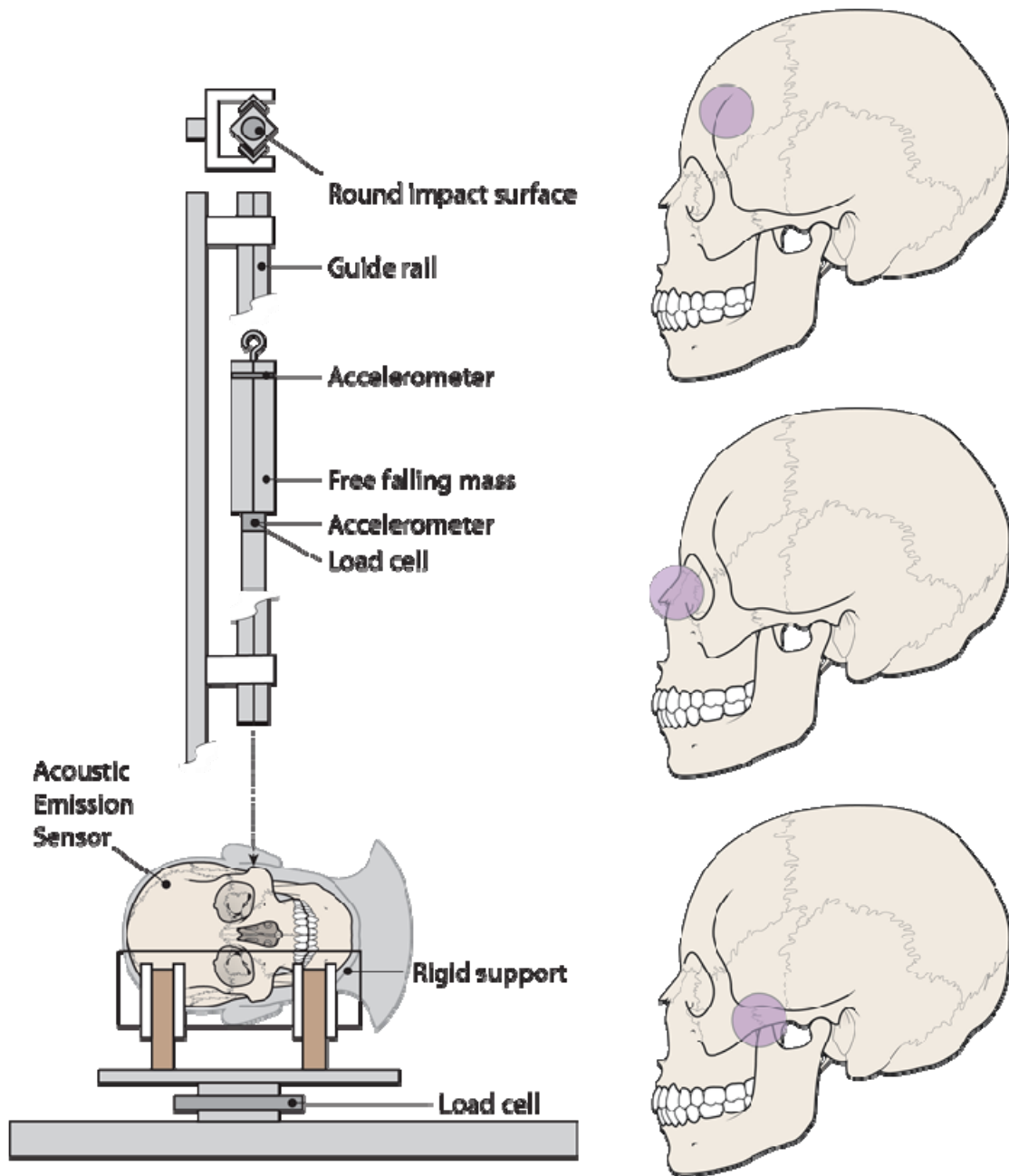
Figure 74: Schematic of test apparatus and impact location for lateral frontal (top), nasal (middle) and zygoma impacts.

In order to obtain acoustic emission data without fracture the first four specimens (39-42) were impacted twice, once at a low energy level and again at a higher fracture producing level. This provided the data necessary to differentiate the magnitude of AE that may be associated with non-fracture impacts and the level expected during a fracture producing impact. Similar to previous studies, a threshold was established by comparing the AE amplitude between fracture and non-fracture tests (Cormier et al., 2008; Funk et al., 2002; Kent et al., 2008; Rudd et al., 2004; Wells and Rawlings, 1985). The details of which are described in a previously published paper (Cormier et al., 2008). In all cases an AE sensor (Micro30S, Physical Instruments, New Jersey) was mounted to the skull just posterior to the apex of the frontal bone. The acoustic emission data were acquired at 5 MHz using an oscilloscope (TDS3000B Tektronix, Oregon). The AE sensor was mounted directly to the frontal bone by removing the soft tissue and periosteum and gluing the sensor in place with cyanoacrylate adhesive. AE data were used to determine the force at which fracture initiated which is often below peak force (Cormier et al., 2010a; Cormier et al., 2011a, b; Cormier et al., 2008; Duma et al., 1999; Kemper et al., 2009).

Survival analyses were then performed to determine the relationship between fracture force and the risk of fracture for the sample of specimens tested. A parametric approach was used using a Weibull model and was implemented using SAS (SAS Institute, Cary N.C). The Weibull model will account for the non-censored nature of the data used in the analysis to determine the model parameters (Allison, 1995; Cantor, 2003). Subject age was also included as covariates to assess their potential for predicting the risk of fracture. The Weibull CDF is given by (Eqn. 6),

$$CDF = 1 - \exp{-(\lambda \cdot F)^{\gamma}}$$

(6)

Where, λ and γ are the scale and shape parameters, respectively, and F is the applied force. This function will provide an estimate of risk of injury using the maximum likelihood estimates of the scale and shape parameters. A non-parametric model was also created using the Kaplan-Meier method. The Kaplan-Meier method assumes the data are only right or non-censored and determines the risk of fracture based on the number of subjects at risk which sustain a fracture for a given force (Kleinbaum and Klein, 2005).

Results

Frontal Bone

A total of 24 lateral frontal bone impacts were performed using male cadaver specimens (Table 28). Fracture did not occur during the four low energy impacts (1.5 J) used to characterize the AE signal as well as two of the high energy (>50 J) impacts. The average fracture force was 1994 N (Standard Deviation: 909 N) and the average peak force was 4056 N (SD: 2126) (Figure 75). A threshold for the Acoustic Emission (AE) data associated with fracture was set to 5 volts. This threshold was higher than the maximum value of AE recorded during the non-fracture tests (0.6 v) and was higher than the AE which occurred briefly before the maximum AE was reached. The fracture tests had an average peak AE of 8.7 volts. On average, fracture force was equal to 46% of the peak force achieved during a fracture test (Figure 76). Tests with an average impactor energy of 50 J produced fracture in 17 of 19 subjects. The two subjects that did not sustain a fracture were exposed to peak forces of 8886 and 7506 N.

Table 28: Results of lateral frontal bone impact tests.

Specimen Number	Impact Velocity (m/s)	Impact Energy (J)	Peak Force (N)	Fracture Force (N)
39	0.9	1.2	1112	
39	4.1	26.4	5632	2392
40	0.9	1.4	901	
40	5.7	50.6	3452	1382
41	1.0	1.7	352	
41	5.5	48.1	2710	664
42	0.8	1.1	720	
42	5.5	47.0	5068	2709
43	5.6	49.6	1753	1073
44	5.5	48.2	4413	1783
45	6.2	60.5	7506	
46	5.6	49.6	5409	2206
47	6.4	64.3	4483	710
48	6.3	62.8	3733	1703
49	5.5	48.0	6937	3870
50	5.7	51.4	4169	1502
51	5.9	54.3	4569	3461
52	5.6	49.6	3028	1464
53	5.5	48.6	3753	1172
54	5.7	50.9	5039	2872
55	5.7	51.4	4819	1719
56	5.8	53.4	8886	
57	6.4	63.7	4935	2830
58	5.6	50.2	3963	2380
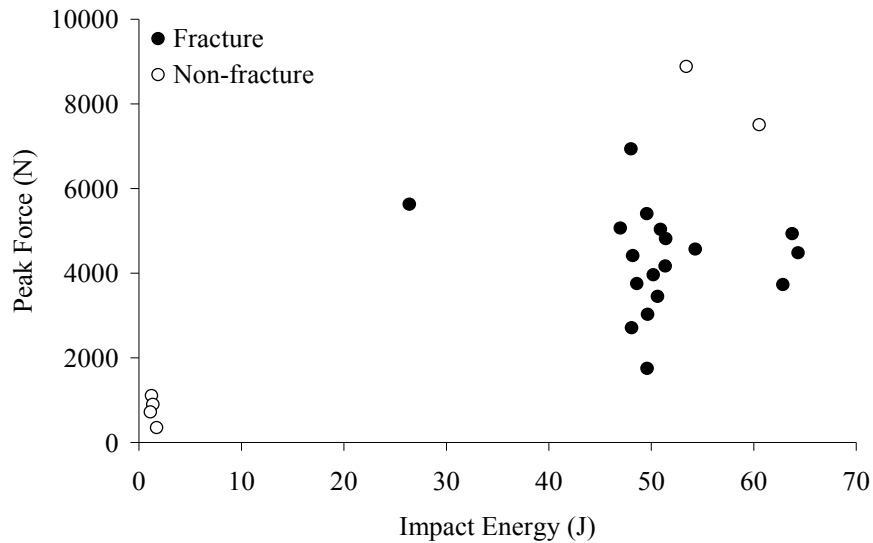
Figure 75: Peak force achieved by fracture status for frontal bone impacts.
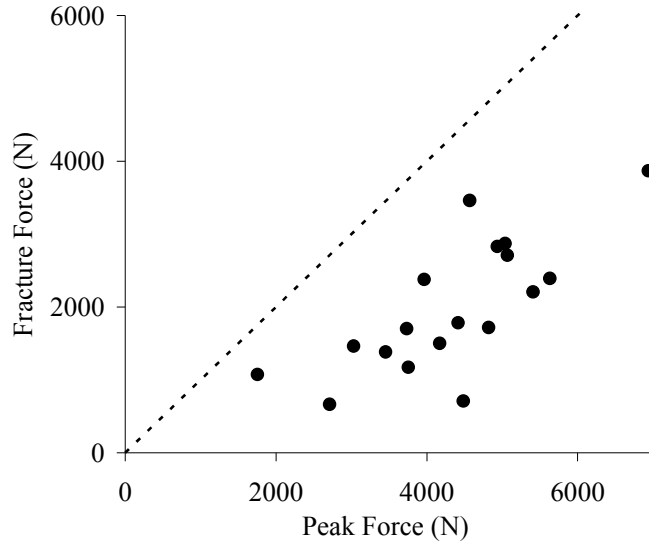
Figure 76: Relationship between peak force and fracture force identified using AE data.

The lateral frontal bone impacts had an average pulse duration of 12 ms. A few of the tests contained a single peak in the force response (Figure 77); however, the majority of the tests contained multiple peaks within the force data (Figure 78). Differences in the force-displacement response were correlated with the resulting fracture. Tests resulting in lower impactor displacement (Figure 79) created non-depressed radiating fractures (Figure 80). In comparison, depressed and comminuted fractures (Figure 81) resulted in more extensive impactor motion due to the deeper penetration (Figure 82). The inferior portion of the fracture lines tended to follow the inferior temporal line. Fractures resulting in depression of the skull tended to exhibit radiating fractures to a lesser extent.
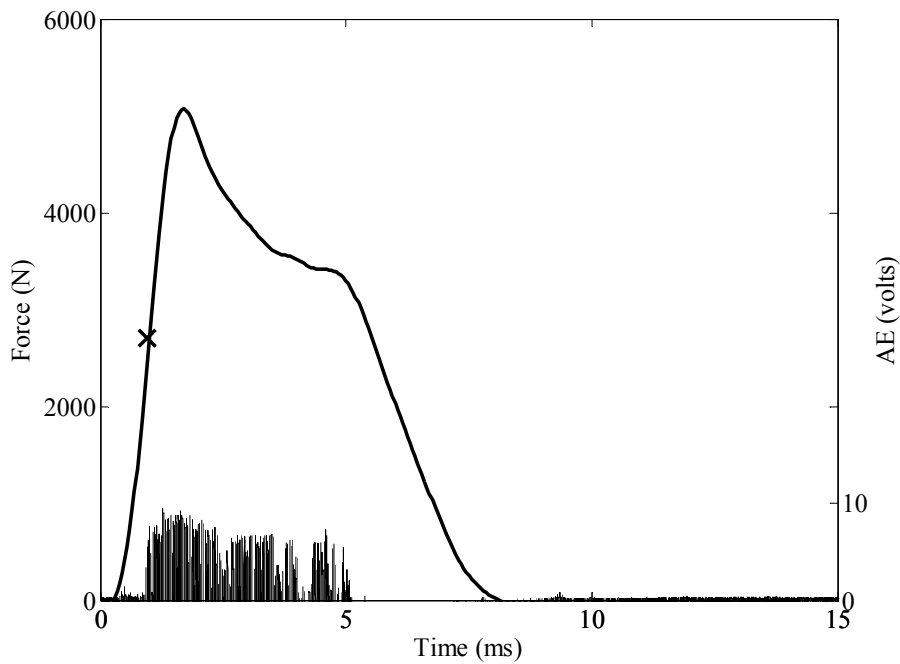
Figure 77: Subject 42 fracture producing impact with AE.
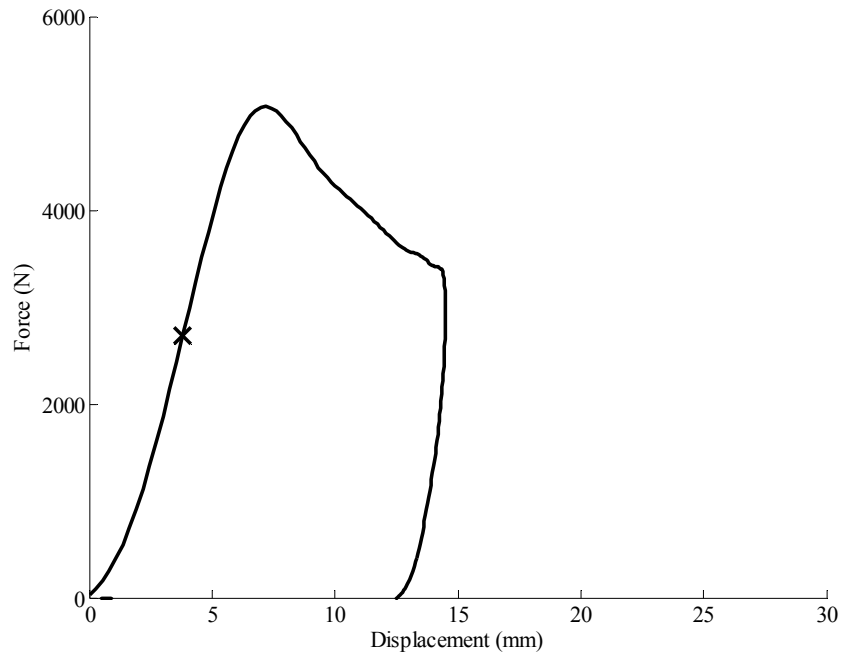
Figure 78: Subject 42 fracture producing impact force-displacement response ("X" denotes force at fracture).
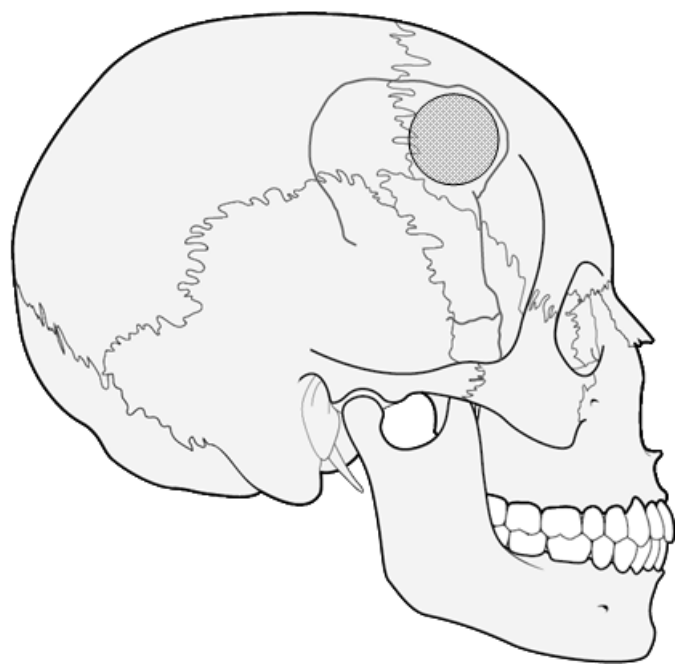
Figure 79: Frontal bone fracture pattern and impact location for subject 42.
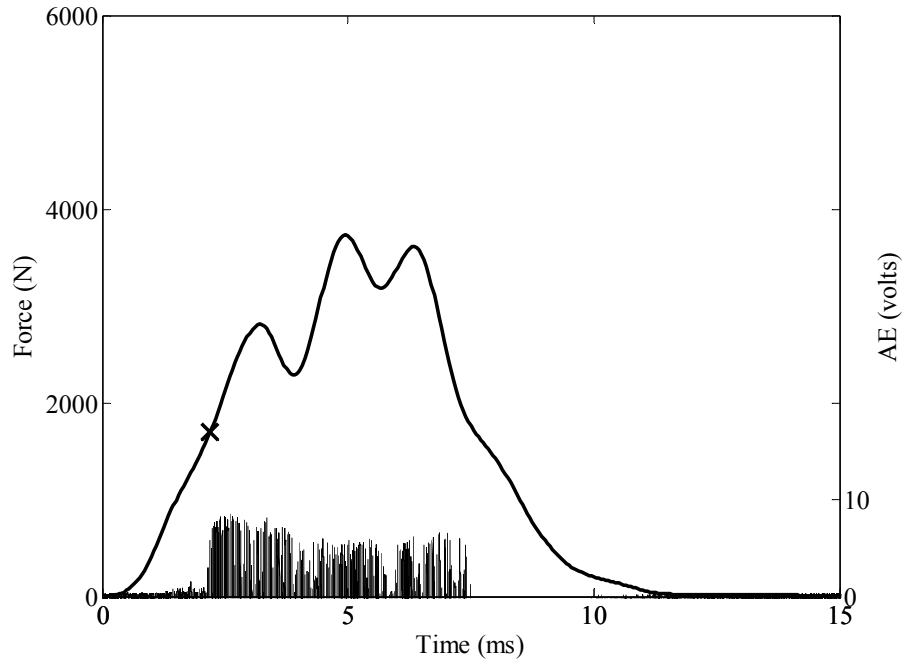
Figure 80: Subject 48 fracture producing impact with AE.
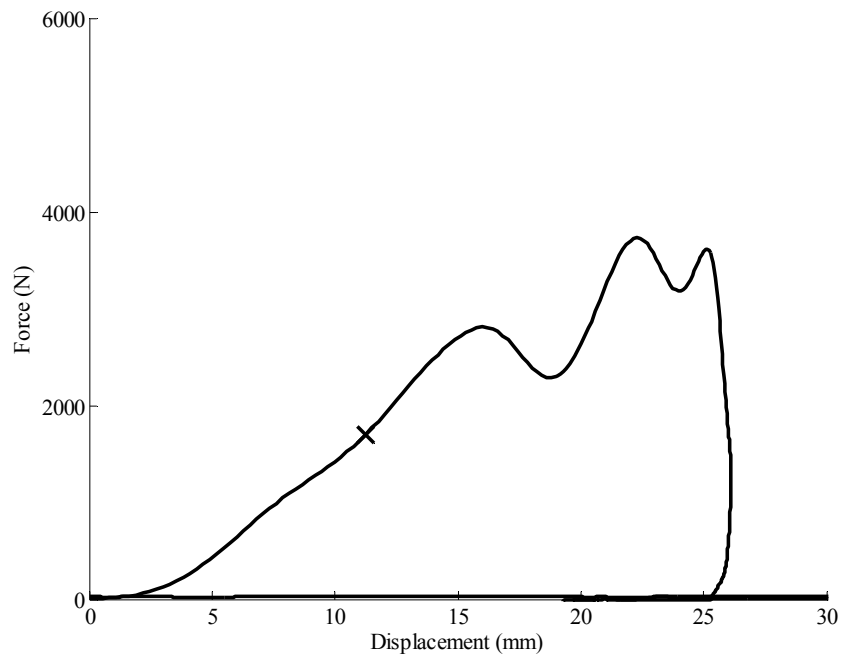
Figure 81: Subject 48 fracture producing impact force-displacement response ("X" denotes force at fracture).
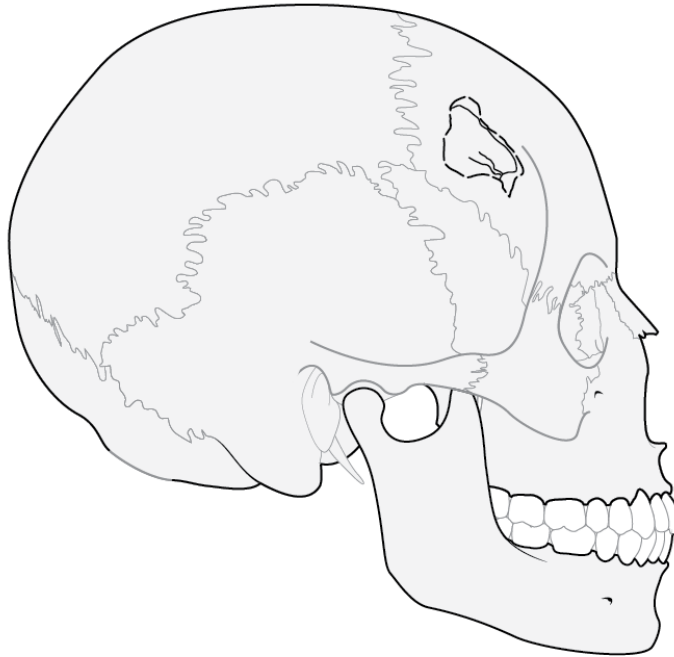
Figure 82: Frontal bone fracture pattern for subject 48.

The high-speed video was used to select tests that did not exhibit slippage of the impactor with respect to the skull and would be useful for characterizing the force-displacement response. Sixteen tests were selected to be used in developing a stiffness corridor to describe the average response of the frontal bone (Figure 83). The average maximum displacement achieved during the corridor tests was 18 mm (SD: 9).
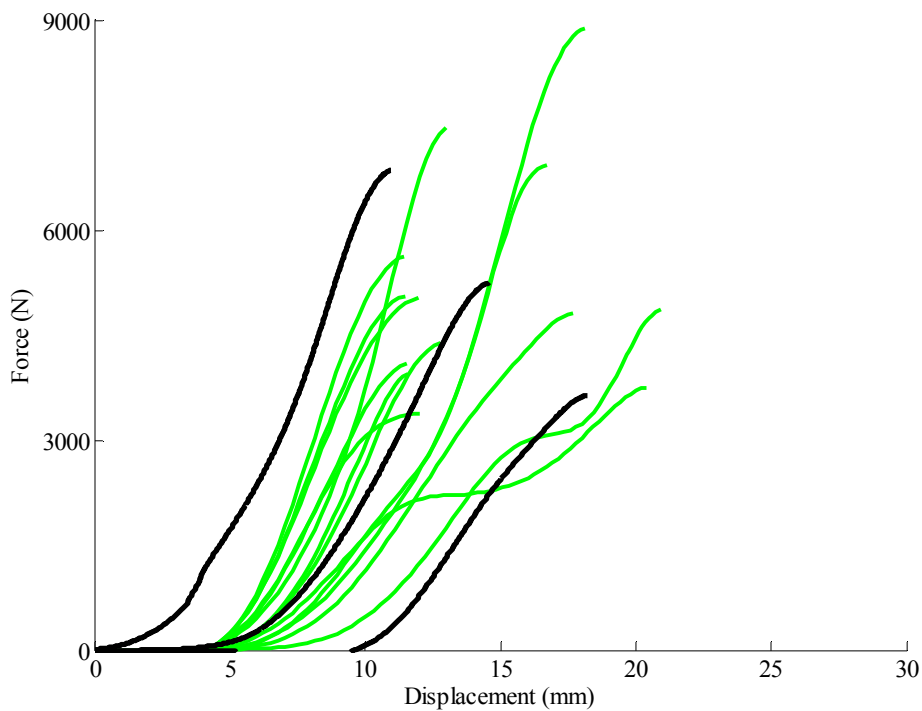
Figure 83: Frontal bone response and corresponding average corridor response and standard deviation.

The risk of frontal fracture was estimated using a Weibull distribution (Table 29) and the Kaplan-Meier non-parametric technique. Both models predict similar risk values up to the 50% risk level. Beyond the 50% risk level, the Kaplan-Meier estimate predicts a higher level of risk than the Weibull model. Age was found to be a statistically significant factor in the risk of frontal bone fracture. For a 10 year increase in age between 70 and 80 years, the force necessary to create a 50% risk of fracture decreases by approximately 1000 N (3000 N vs. 2000 N) (Figure 84). The Weibull survival function is given below.

Table 29: Parameter estimates for Weibull model of frontal bone fracture force.

Parameter	Estimate	95% Confidence Interval	
		Lower	Upper
Intercept	11.07	8.58	13.56
Shape	1.63	1.16	2.30
Age	1.07	1.18	1.01

$$S = 1 - \exp(-\exp(-\gamma(Intercept + Age\beta_{age})Force^{\gamma}$$
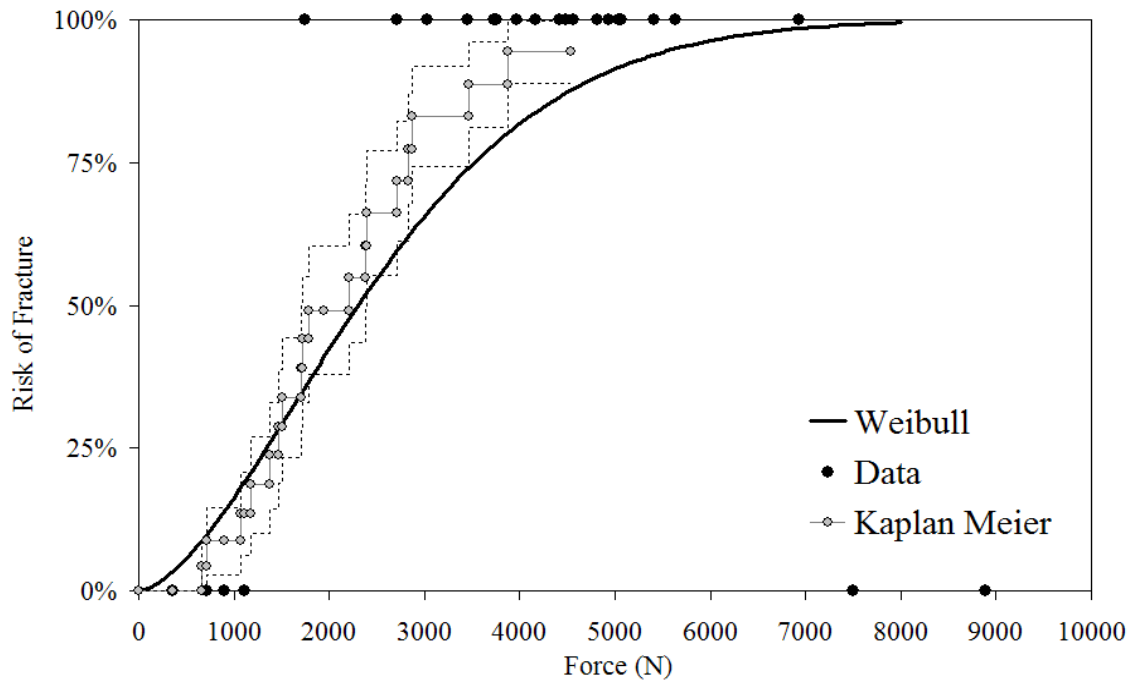
Figure 84: Risk of frontal bone fracture due to lateral impact.

Nasal Bone

A total of 19 lateral nasal impact tests were performed using male cadaver specimens (Table 30). The average impact velocity was 2.2 m/s which resulted in energy at impact of 7 to 10 J, with an average of 8 J. The peak force ranged from 76 to 723 N with an average of 368 N. Only one test did not result in fracture, which was the test resulting in the lowest peak force of 76 N. A threshold for the Acoustic Emission (AE) data associated with fracture was set to 5 volts. This threshold was higher than the maximum value of AE recorded during the non-fracture frontal bone tests (0.6 v) performed on the same subjects. The maximum AE measured during fracture producing impacts for the nasal and frontal bone impacts had an average value of 8.1 and 8.7 respectively. The slightly lower value for the nasal bone impacts is consistent with the AE sensor being farther away from the nasal bone than frontal bone impact locations. On average, fracture force was equal to 32% of the peak force achieved during the fracture tests (Figure 85). The peak force achieved during each test did not demonstrate a relationship to the initial impactor energy (Figure 86).

Table 30: Results of lateral nasal bone impacts.

Specimen Number	Impact Velocity (m/s)	Impact Energy (J)	Peak Force (N)	Fracture Force (N)
38	2.2	7.6	355	79
39	2.1	7.0	298	138
40	2.3	8.2	243	102
41	2.1	7.1	271	143
42	2.2	7.4	241	71
43	2.3	8.3	375	114
44	2.5	9.6	352	89
45	2.1	7.0	360	61
46	2.2	7.6	76	-
47	2.1	7.3	253	84
48	2.2	7.6	308	86
49	2.1	6.9	615	138
50	2.4	9.3	397	146
52	2.1	7.2	378	378*
53	2.2	7.4	657	87
54	2.3	8.0	320	320*
55	2.1	6.7	723	410
56	2.1	6.7	356	76
57	2.4	9.3	414	130

* AE data not available
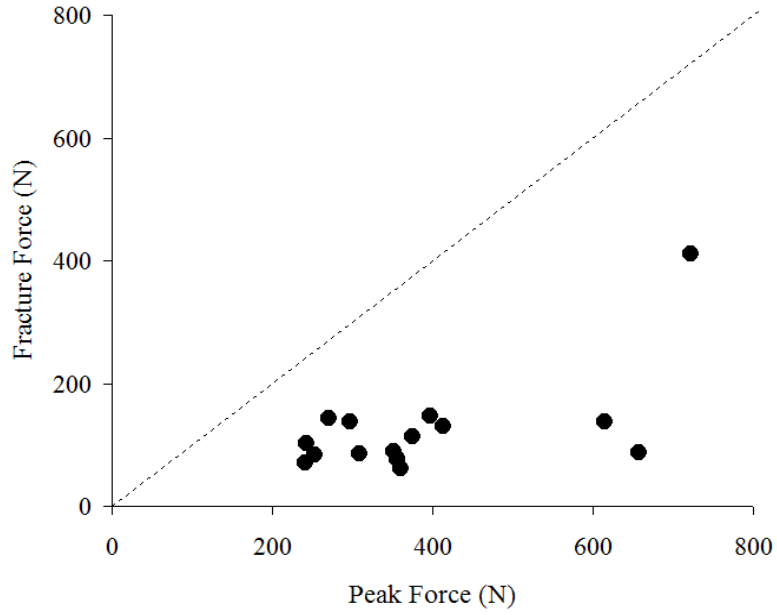
Figure 85: Corresponding fracture and peak forces for lateral nasal bone impacts.
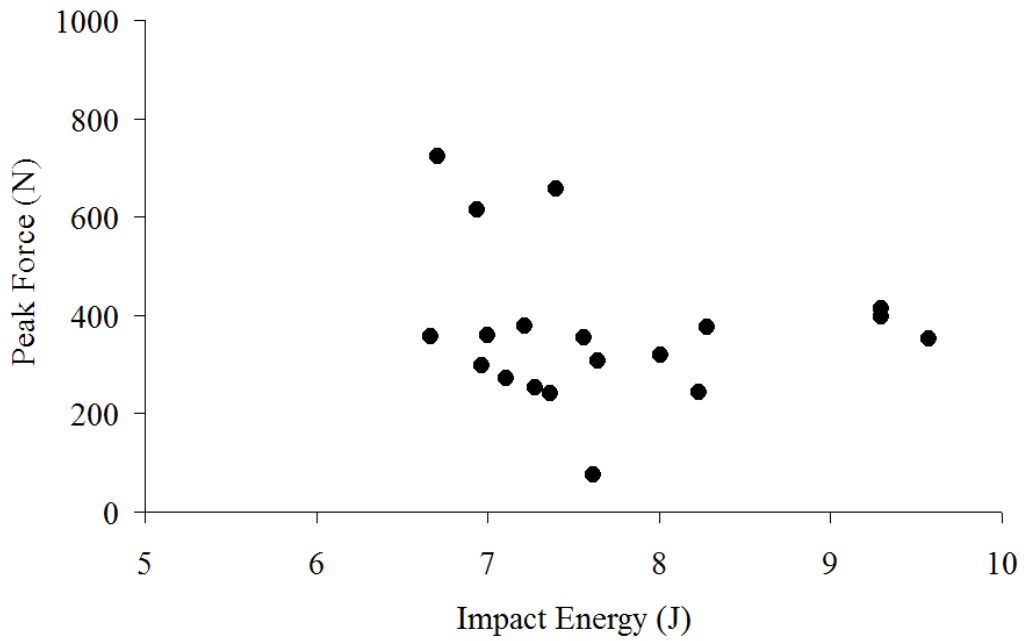
Figure 86: Impactor energy and resulting peak force for all nasal bone tests.

The response of the nasal structure to the lateral impacts consisted of lateral translation of the nose and a bending of the soft structures in the direction of the impact. The displacement of the impactor was calculated for every test by double integrating the accelerometer data. The pre-impact velocity of the impactor was determined using high-speed video. Using the calculated displacement response and high speed video, tests with inaccurate force-displacement data were identified. These tests were not used for the force-displacement response because initial contact between the impactor and other facial structures of the subject caused the impactor to slow a minute amount. This made it difficult to determine the exact time the impactor struck the nose. Twelve tests were utilized to evaluate the force-displacement response of the nasal bone to lateral impact. The distribution of the force-displacement response was characterized using the characteristic average and its standard deviation (Figure 87).
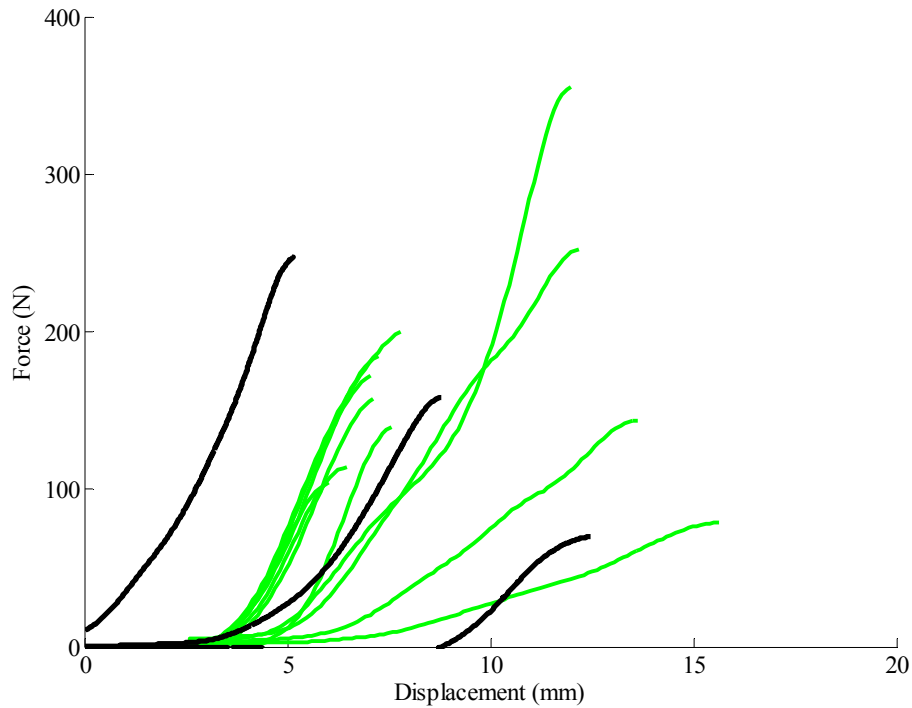
Figure 87: Force-displacement response of lateral nasal bone impacts with corresponding characteristic average and standard deviation.

In 11 of the 19 tests, the fracture force identified by the AE was coincident with a local peak in the force response (Figure 88), while in the remaining tests fracture was identified prior to a single peak in the force response (Figure 89). In tests with a local peak around the fracture force, the difference in magnitude between fracture force and the local peak was 14 N on average. Based on the AE data, fracture occurred fairly early in the event, before the extensive motion of the major structure of the nose. On average, the AE signal began after approximately 4 mm (std dev = 1.2) of impactor travel. In two tests resulting in fracture, AE data were not available; therefore, the peak force was utilized in the survival analysis and treated as a left censored data point. The remaining fracture force values were treated as non-censored values in the survival analyses.
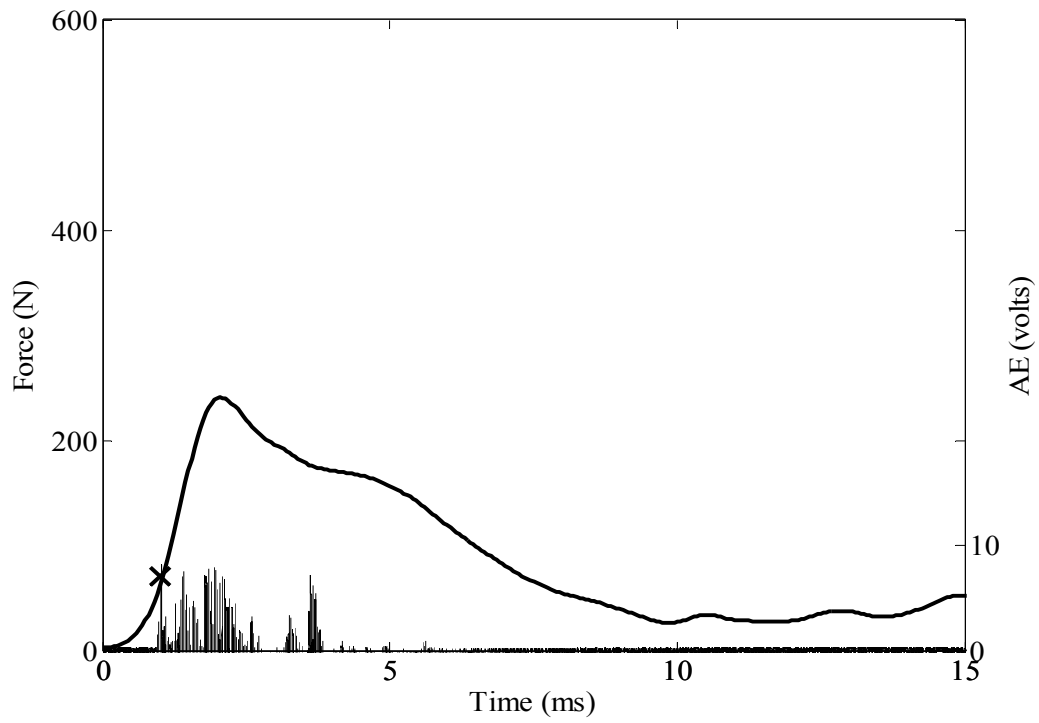
Figure 88: Force and AE response for subject 43.
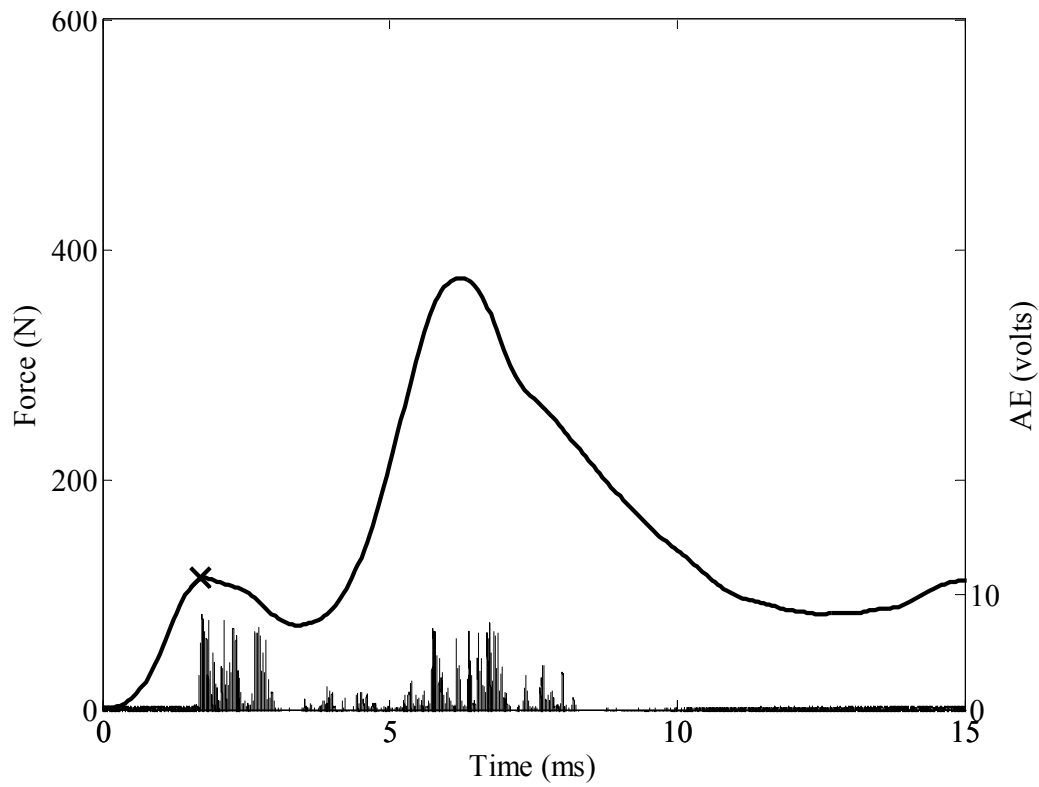
Figure 89: Force and AE response for subject 44.

119

The risk of fracture was estimated using a Weibull distribution (Table 31) and the Kaplan-Meier non-parametric technique. The Weibull and Kaplan Meier methods estimated similar values for risk between 30 and 70% risk. Since no fracture was recorded at a force below 61 N, the Kaplan Meier estimate predicts a risk of zero until this force level is reached. In order to fit the data the Weibull model must continually increase the risk estimate from zero; therefore, it predicts a higher level of risk at forces less than 61 N (Figure 90). Subject age was not a statistically significant factor in predicting the risk of nasal bone fracture. Based on the Kaplan Meier estimate, a 50% risk of nasal bone fracture corresponds to an applied force between 90 and 130 N.

Table 31: Parameter estimates for Weibull model for nasal bone fracture.

Parameter	Estimate	95% Confidence Interval	
		Lower	Upper
Scale	1.59E-04	1.26E-05	1.16E-03
Shape	1.77	1.29	2.42
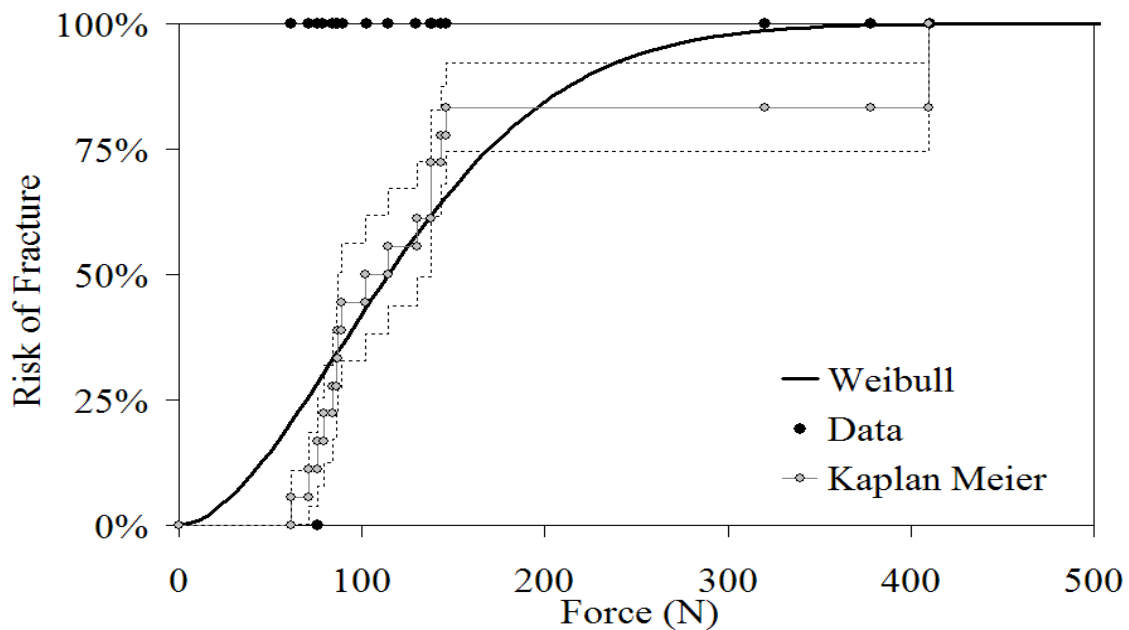
Figure 90: Risk of nasal bone fracture due to lateral impact.

The nasal bone fracture patterns exhibited by the subjects were fairly consistent. All subjects incurred fractures to the nasal bones and the majority also exhibited a fracture propagating inferiorly along the frontal process of the maxilla. The fracture of the medial aspect of the maxilla mostly occurred on the same side as the impact, (Figure 91) but in some cases the maxilla was fracture on the contralateral side (Figure 92). This suggests that the fracture to the frontal process of the maxilla is due to an avulsion process from forces applied by the nasal structures.
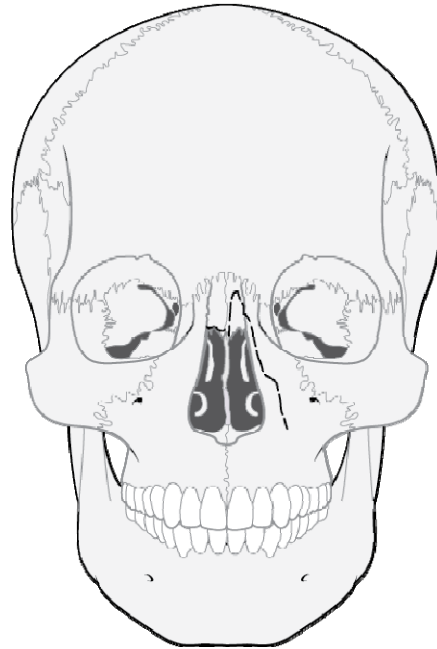
Figure 91: Fracture pattern in subject 43 due to right sided impact shown in Figure 88.
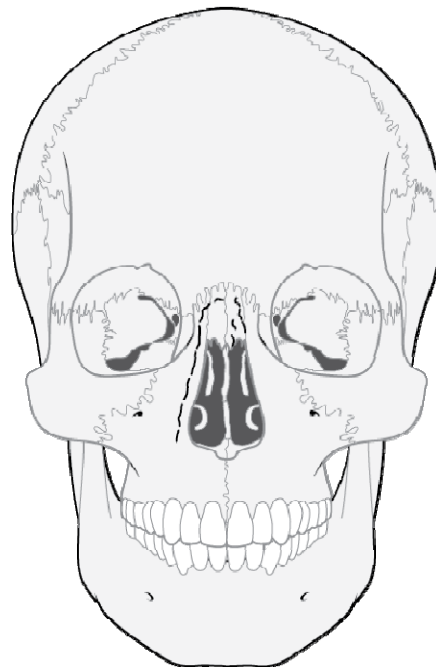
Figure 92: Fracture pattern in subject 44 due to right sided impact shown in Figure 89.

Zygoma

A total of 17 lateral zygoma impact tests were performed using male cadaver specimens (Table 32). The average impact velocity was 4 m/s which corresponded to an impactor energy of 22 to 33 J with an average of 29 J. Peak force during the zygoma impacts ranged from 913 to 2835 N with an average of 495 N. All 17 tests resulted in a fracture with an average fracture force of 906 N. A threshold for the Acoustic Emission (AE) data associated with fracture was set to 5 volts. The maximum AE measured during fracture producing impacts for the zygoma and frontal bone impacts had an average value of 8.2 and 8.7 respectively. On average, fracture force was equal to 60% of the peak force achieved during the fracture tests (Figure 93). Frequently, the fracture occurred near a deviation in force resulting in a local peak. On average, the fracture force was approximately 77% of the local peak force. Fracture force did not demonstrate a relationship with impactor energy.

Table 32: Results of lateral zygoma impacts.

Specimen Number	Impact Velocity (m/s)	Impact Energy (J)	Peak Force (N)	Fracture Force (N)
39	4.4	31.2	1257	579
40	4.3	28.7	1030	563
41	3.8	22.4	1295	504
42	4.4	30.1	1741	603
43	3.9	24.4	1221	560
44	4.4	30.7	1743	1238
45	4.1	26.8	2021	1301
46	4.3	29.3	2204	1479
49	4.1	27.0	1777	928
50	4.2	27.9	947	898
51	4.2	28.4	1343	860
52	4.4	31.0	1417	656
53	4.2	27.4	1568	553
54	4.6	32.7	913	511
55	4.3	29.5	1424	697
56	4.5	31.6	2835	2792
58	4.4	30.2	1198	673
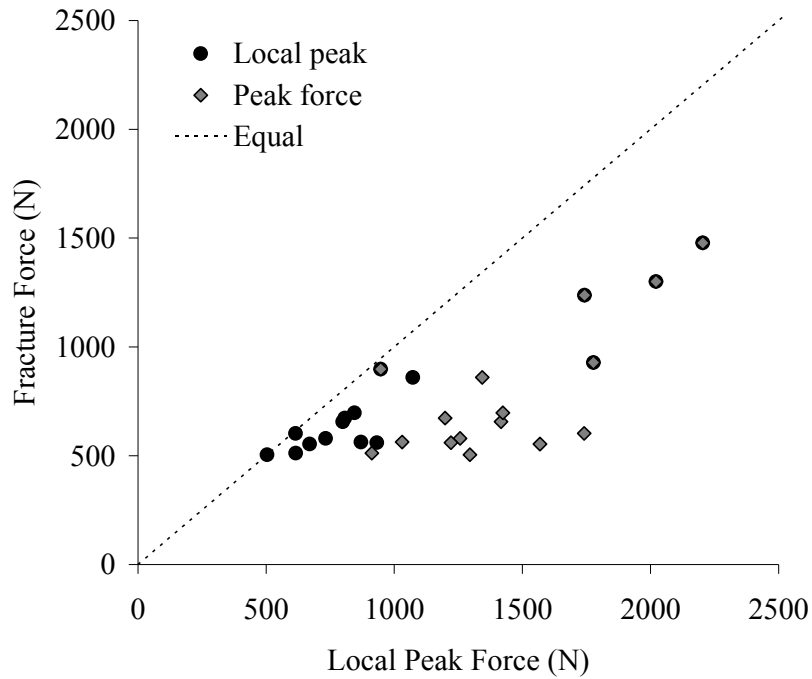
Figure 93: Relationship between peak, local peak and fracture forces.

The occurrence of fracture near a local peak was observed in both the force-time and force-displacement responses (Figure 94). In the remaining tests, fracture occurred prior to peak force without a deviation in force prior to the peak. On average, the difference between fracture force and a local peak force was 90 N. After initial impactor contact, fracture was identified at 5 to 14 mm of displacement with an average of 7 mm.
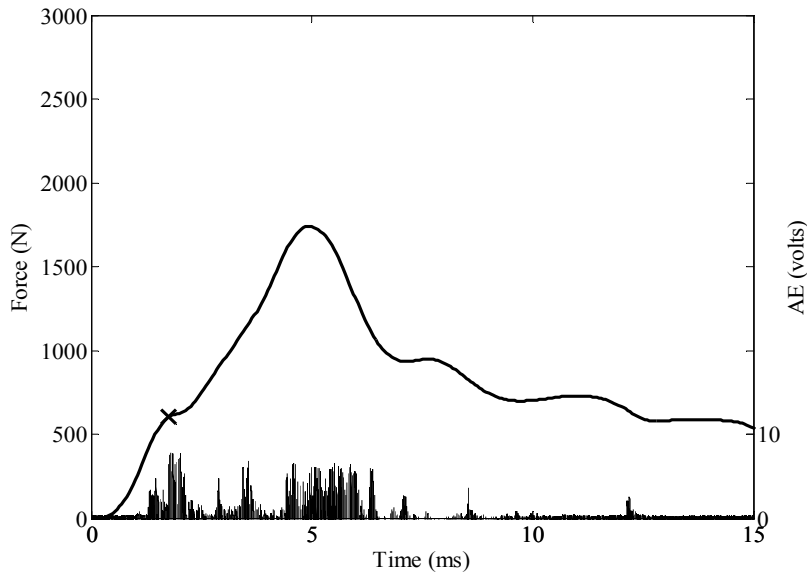
Figure 94: Subject 42 force and acoustic emission response.

123

The response of the zygoma to lateral impact consisted of deformation of the zygomatic arch, lateral aspect of the zygoma and displacement of the impactor into the maxillary sinus. The displacement of the impactor was calculated for every test by double integrating the accelerometer data. The pre-impact velocity of the impactor was determined using high-speed video. All but one test was used to create a force-displacement corridor for the zygoma impacts using the characteristic average and standard deviation (Figure 95). The single test was removed due to difficulty in assessing the time of contact.
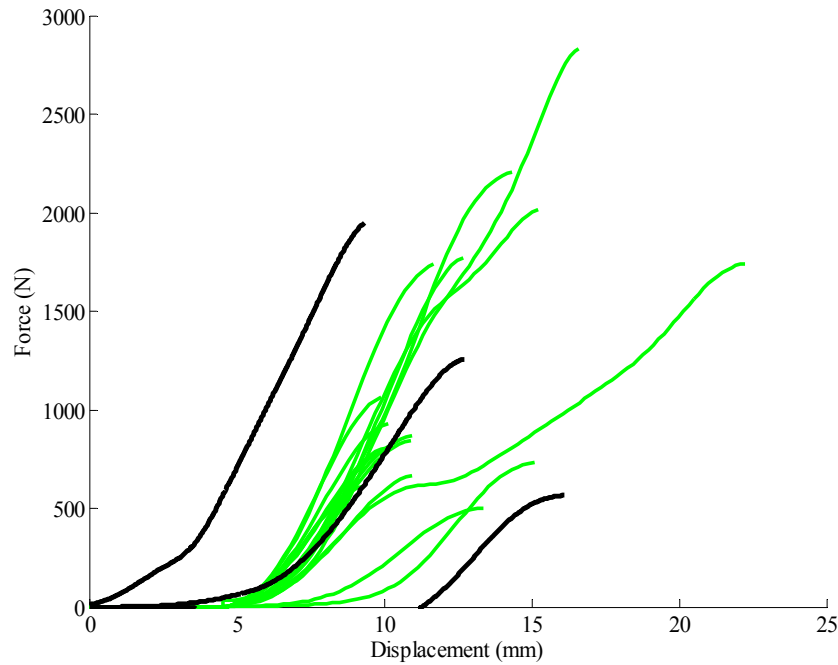
Figure 95: Zygoma force displacement response to peak force and corresponding corridors.

The fracture patterns observed during the zygoma impacts was fairly consistent among tests (Figure 96). Medially, the fractures typically propagated along the suture line between the zygoma and frontal process of the maxilla. Laterally, the fracture typically occurred at the zygomatic arch and frontal process.
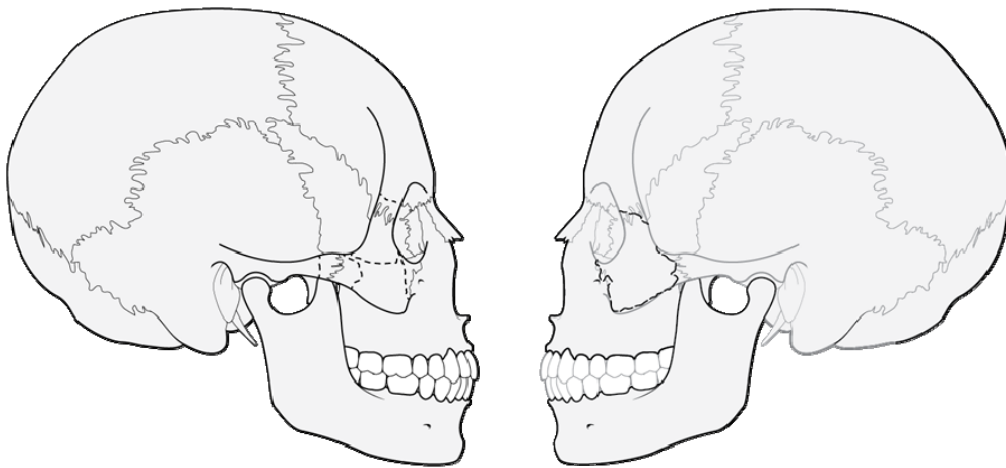
Figure 96: Fracture pattern observed in subject 42 (left) and 49.

The risk of fracture was estimated using a Weibull distribution (Table 33) and the Kaplan-Meier non-parametric technique (Figure 97). Since no fracture occurred until a force of 500 N, the Kaplan-Meier model indicates zero risk up to this force. Both models predict similar risk of fracture between 25 and 50 percent, and then diverge slightly thereafter. Subject age was not a statistically significant factor for predicting zygoma fracture. Using the Kaplan-Meier estimate a 50% risk of zygoma fracture occurs at a force between 650 and 700 N.

Table 33: Parameter estimates for Weibull model for zygoma fracture.

Parameter	Estimate		95% Confidence Interval	
			Lower	Upper
Scale	3.44E-06		5.86E-08	7.58E-05
Shape	1.81		1.31	2.50
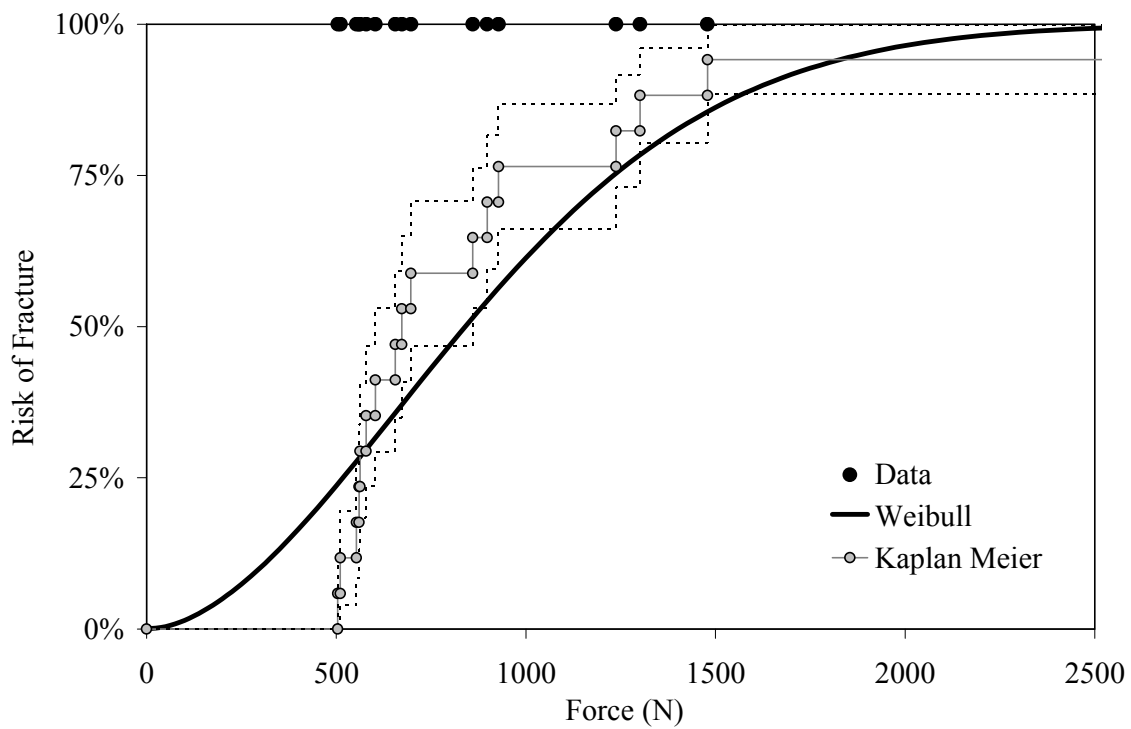
Figure 97: Risk of zygoma fracture due to lateral impact.

Discussion

This study is a continuation of previously published work on the response of the facial bones to Anterior-Posterior (AP) impacts (Cormier et al., 2010a; Cormier et al., 2011a, b; Cormier et al., 2011c). The previous study was performed using the exact methods and impactor and with respect to the frontal bone, produced similar peak forces with respect to impact severity (Figure 98). Also of interest is that the force at fracture onset identified using AE data was similar in both studies. The average fracture force in the current study was 2119 N (SD: 1032) and during the AP testing, the average fracture force was 1982 (SD: 765).
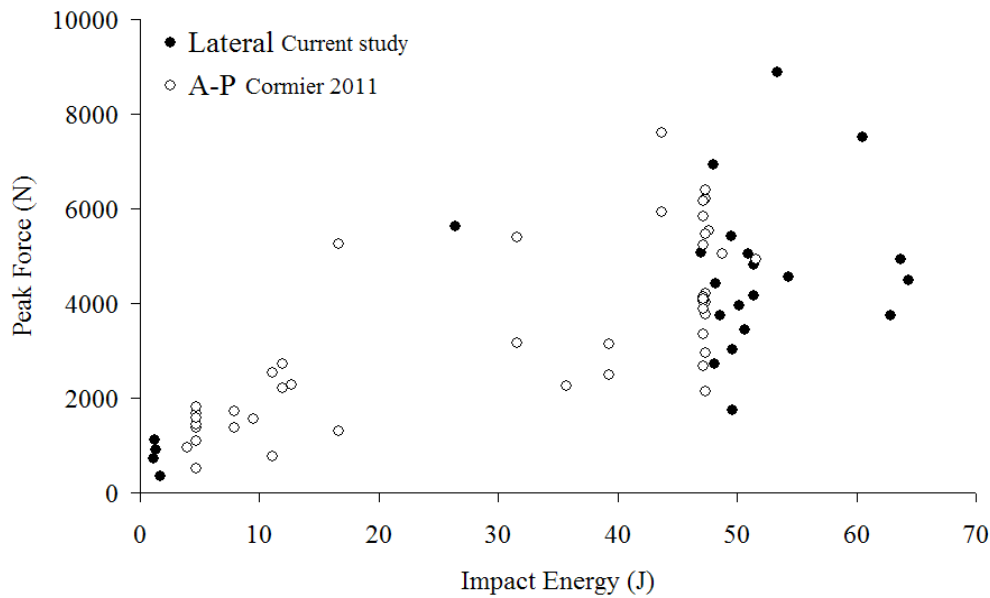
Figure 98: Peak forces produced during current and previous study by impact direction on frontal bone.

The peak forces generated in this study are also similar to those of previous studies utilizing a similar impactor size (with padding) in the AP direction (Nahum, 1975a; Nahum et al., 1968) (Figure 99). Two of the non-fracture tests in the current study exhibited the highest peak force which is consistent with the ability to support more force if fracture does not occur. As a result of the testing performed by Nahum *et al.* (1968, 1975), they proposed a tolerance of the frontal bone to A-P impacts of 3560 to 7120 N. Based on the non-parametric risk curve developed in the current study, these forces correspond to a 74 to 99% risk of fracture. The proposed tolerances are on the upper end of the risk curve because they are based on peak force and not the force at fracture onset. Also, the force to cause fracture in the current study may be lower due to the lack of padding compared to the Nahum *et al.* studies.
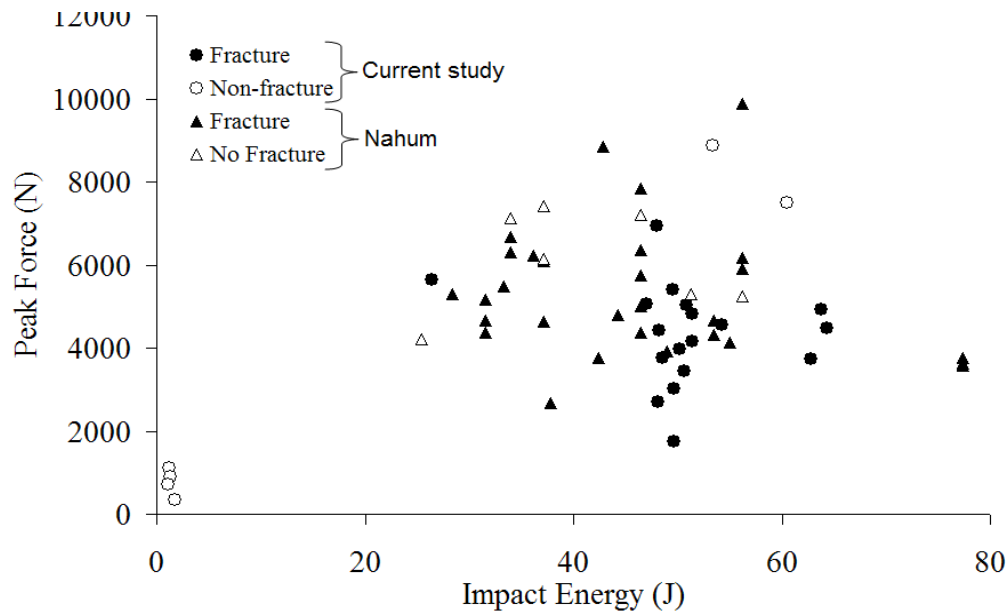
Figure 99: Impactor energy and peak force for current and previous studies on frontal bone impacts.

The Bermond *et al.* (1999) study which used a cylindrical impactor to perform oblique (30°) impacts to the frontal bone measured average peak forces of 4050 N during non-impact producing tests. The risk curve created during the current study suggests that force level represents a fracture risk of 82%. This suggests that the cylindrical impactor may present a less aggressive impacting surface than the flat, rounded shape used in the current and the Nahum *et al.* studies. These results are consistent with those of Allsop *et al.* (1988) who found an average force of fracture onset of 4800 N when performing A-P impacts using a cylindrical impactor. The higher force to fracture is likely due to the cylindrical impactor and the A-P direction distributed the force across a greater area on the frontal bone than the oblique impacts.

The tolerance of the nasal bone was estimated using a Weibull parametric model and the Kaplan Meier estimate which is a non-parametric estimate. Both methods estimated similar risk values near the 50% point, but deviate toward the lower end of fracture force. Considering the geometry of the nasal bones, it is expected that its tolerance would be lower in the lateral direction than the AP direction. Therefore, it is likely that oblique impacts to the nasal bones would result in fracture at lower forces than a purely AP directed impact.

The fracture patterns observed during this study were interesting in that direct impact to the frontal process of the maxilla was not necessary to cause fracture. Also, the occurrence of fracture on the frontal process contralateral to the impacted side demonstrated the avulsion mechanism of creating these fractures. This demonstrates that the facial fracture patterns should be examined carefully when attempting to determine the direction of impact.

The force-displacement response of the zygoma to lateral impact was described using the characteristic average. Some comparisons can be made to previous studies on the impact tolerance of the zygoma (Figure 100). Caution should be used when evaluating the risk of fracture however, since the previous work is limited to peak force while the current study utilized acoustic emission sensors to identify the force at fracture onset. The impacts in the current study were performed at slightly higher energies than previous work; however the peak force achieved during each study was similar. This demonstrates that lateral zygoma impacts are a load-limiting event due to the loss of integrity to the underlying structures.
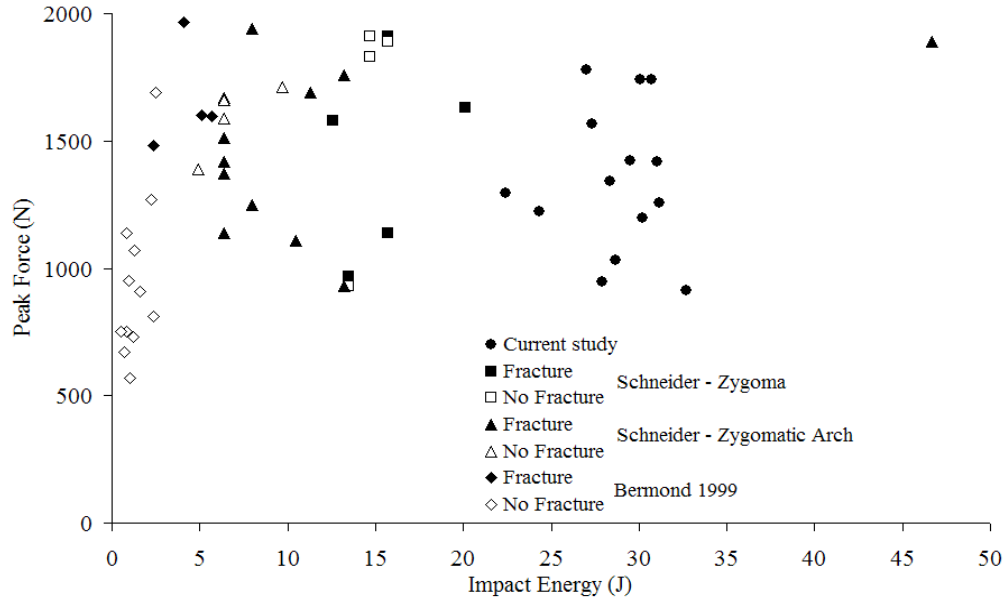
Figure 100: Peak force achieved in zygoma impacts during current and previous studies.

The previous work by Schneider et al. (1972) consisted of oblique impacts to the zygoma using a similar sized impactor with nickel padding. Their study produced average peak forces of 1640 and 1680 N for the no-fracture and fracture tests respectively. According to the Kaplan-Meier estimates of the current study, these forces correspond to a fracture risk of 88 to 99%. The high risk without fracture is likely due to the oblique nature of the Schneider impacts which may be a stronger loading direction for the zygoma. Additionally, the lower fracture forces obtained in the current study results from the use of acoustic emission to determine fracture onset since this will occur with little change in the structural integrity of the bone (Rajachar et al., 1999). Age was not found to be significantly correlated with the risk of fracture for the lateral zygoma impacts.

Conclusions

The purpose of this study was to examine the biomechanical response and tolerance of facial bones to lateral impact. The force at fracture onset was determined using acoustic emission sensors. Survival analyses were performed to determine the risk of fracture as a function of impact force. Non-parametric techniques estimated a 10 and 50% risk of fracture at 1073 and 2200 N respectively for the frontal bone. The Weibul model generated for frontal bone fracture risk found that age was a statistically significant factor. The 50% risk for the nasal bone fracture was between 90 and 130 N and between 650 and 700 N for the zygoma. Force-deflection data are also provided which can provide information necessary to evaluate the biofidelity of facial surrogates. The fracture patterns encountered during testing is also discussed which provides insight into the variability of fracture location by impact direction. The force-displacement response of the zygoma frequently demonstrated a deviation near the time of fracture onset identified using the acoustic emission sensor. Compared to previous work at lower impactor energy, this study produced similar peak forces which demonstrates that zygoma fracture is a load-limiting process. Fracture patterns are discussed and frequently followed the zygomatic suture lines with the maxilla, temporal and frontal bones. Overall, this study provides a model for predicting facial fracture due to lateral impact as well as a measure of its force-displacement response which can be useful in assessing the biofidelity of physical and computational models.

FINITE ELEMENT MODELING

In collaboration with the Global Human Bodies Modeling Consortium and the Wake Forest University Neurosurgery department four (n=4) independent finite element modeling studies were conducted to evaluate response of the cervical spine and the effects of cervical arthrodesis and arthroplasty during simulated automobile collisions and rotary-wing aircraft impacts. Below are summary abstracts of the four finite element modeling studies that were conducted and published. The full articles are provided as an Appendix.

Effects of Cervical Arthrodesis and Arthroplasty on Neck Response during a Simulated Frontal Automobile Collision

Abstract

While arthrodesis is the most common surgical intervention for treatment of symptomatic cervical degenerative disc disease (CDDD), arthroplasty has become increasingly more popular over the past decade. While literature exists comparing the effects of anterior cervical discectomy and fusion (ACDF) and cervical total disc replacement (CTDR) on neck kinematics and loading, the vast majority of these studies apply only quasi-static, non-injurious loading conditions to a segment of the cervical spine. The objective of this study was to investigate the effects of arthrodesis and arthroplasty on biomechanical neck response during a simulated frontal automobile collision with airbag deployment. This study uses a full-body, 50th percentile seated male finite element (FE) model to study neck response during a dynamic impact event. The cervical spine was modified to simulate either an arthrodesis or arthroplasty procedure at C5-6. Five simulations of a belted driver, subjected to a 13.3 m/s ΔV frontal impact with airbag deployment, were run in LS-DYNA with the Global Human Body Models Consortium (GHBMC) full-body FE model. The first simulation used the original model, with no modifications to the neck, while the remaining four were modified to represent either interbody arthrodesis or arthroplasty of C5-6. Cross-sectional forces and moments at the C5 and C6 cervical level of the neck, along with interbody and facet forces between C5 and C6, were reported. Adjacent-level, cross-sectional neck loading was maintained in all simulations without exceeding any established injury thresholds. Interbody compression was greatest for the CTDRs, and interbody tension occurred only in the fused and non-modified spines. Some interbody separation occurred between the superior and inferior components of the CTDRs during flexion-induced tension of the cervical spine, increasing the facet loads. This is the first study to evaluate the effects of a C5-6 cervical arthrodesis and arthroplasty on neck response during a simulated frontal automobile impact. While cervical arthrodesis and arthroplasty at C5-6 did not appear to significantly alter the adjacent-level, cross-sectional neck responses during a simulated frontal automobile impact, key differences were noted in the interbody and facet loading.

Head and Neck Response of a Finite Element Anthropomorphic Test Device and Human Body Model during a Simulated Rotary-Wing Aircraft Impact

Abstract

A finite element simulation environment has been developed to investigate aviator head and neck response during simulated rotary aircraft crashes using both an anthropomorphic test device (ATD) and a human body model. The simulation setup was based on a series of experimental sled tests reported in the literature which studied the effects of ATD size, head-supported mass, and sled pulse on neck response during such an event. The first ATD simulation was successfully validated against one of these experimental sled tests. The majority of the transducer time histories received a CORrelation and Analysis (CORA) rating of 0.7 or higher, indicating good overall correlation between the simulation and the experiment response. A second ATD simulation was conducted to examine the effects of initial position on head and neck response. Neck angle and foot-to-floor contact were found to influence the magnitude of the head and neck response, but not the timing. The human body model simulated a more biofidelic head and neck response than the ATD model, including the change in neck curvature. Shear force, axial force, and bending moment were reported for each level of the cervical spine, providing further insight into the biomechanical loading of the neck during a rotary aircraft crash.

Cross-Section Neck Response of a Total Human Body FE Model during Simulated Frontal and Side Automobile Impacts

Abstract

Human body finite element models are beginning to play a more prevalent role in the advancement of automotive safety. A methodology has been developed to evaluate neck response at multiple levels in a human body finite element model during simulated automotive impacts. Three different impact scenarios were simulated: a frontal impact of a belted driver with airbag deployment, a frontal impact of a belted passenger without airbag deployment, and an unbelted side impact sled test. Cross-sections were created at each vertebral level of the cervical spine to calculate the force and moment contributions of different anatomical components of the neck. Adjacent level axial force ratios varied between 0.74 and 1.11 and adjacent level bending moment ratios between 0.55 and 1.15. The present technique is ideal for comparing neck forces and moments to existing injury threshold values, calculating injury criteria, and for better understanding the biomechanical mechanisms of neck injury and load-sharing during sub-injurious and injurious loading.

Effects of Cervical Arthroplasty on Neck Response during a Simulated Rotary-Wing Aircraft Impact

TITLE: Effects of Cervical Arthroplasty on Neck Response during a Simulated Rotary-Wing Aircraft Impact
AUTHORS: White NW, Danelson KA, Gayzik FS, HSU W, Powers AK, and Stitzel JD
JOURNAL: International Journal of Crashworthiness
STATUS: Published 2016

Abstract

Three simulations were conducted using a human body finite element model to study the effects of cervical arthroplasty on neck response during a rotary-wing aircraft ground impact. One simulation was run as a baseline with no modifications to the neck. The remaining two simulations included neck modifications to represent a C5-6 interbody arthroplasty with either a Prestige ST or ProDisc-C cervical total disc replacement (CTDR). Cross sections were implemented at each cervical level to capture neck loading. In the three simulations, neck injury criteria (Nij) ranged between 0.35 and 0.36 for the upper neck and the Beam Criterion (BC) ranged between 0.98 and 1.05 for the lower neck. The adjacent-level, cross-sectional loading for the C5-6 segment was not greatly altered by the CTDRs, as indicated by CORrelation and Analysis (CORA) ratings of 0.988 for the Prestige ST and 0.909 for the ProDisc-C. The CTDRs increased the interbody range of motion, altering both the interbody and cervical facet loading. While the facet capsules experienced increased tension in both CTDR simulations, established injury threshold levels were not reached. Overall, cervical arthroplasty at the C5-6 level did not appear to have a deleterious effect on the dynamic neck response during a simulated rotary-wing aircraft impact.

EXPERIMENTAL TESTING

BIOMECHANICAL RESPONSE OF CERVICAL SPINE IMPLANTS

The comparison of anterior cervical discectomy and fusion (ACDF) and cervical total disc replacement (CTDR) has been intensely researched. Pending long-term clinical follow up on CTDR, it has been found that CTDR is at least equal to, if not superior to ACDF. However, while many different implants have been compared to fusion, no biomechanical studies and very few clinical studies have evaluated different implants with the same experimental boundary conditions and fixturing. A major argument against CTDR is its potential to cause serious injury. Preserved physiological range of motion and reduced rigidity in these cases may be beneficial for preventing adjacent segment syndrome, however it may be a concern during high dynamic acceleration, traumatic loading, and rapid complex motion that is common among the pilot population. This is especially important to military pilots who get cervical degenerative disc disease more frequently, benefit more from the preserved ROM of CTDR over ACDF, and are more likely to experience significant trauma than the average population. In addition, few cadaveric studies have looked at the failure of these implants. It would be valuable to see both the anatomical location of initial injury and the magnitude of loading at which failure occurs. A study which evaluates several implants in a controlled will aid the military in restoring pilot quality of life and longevity of service.

This study aims to evaluate the biomechanical response of the cervical spine while preserving the complexity of natural spine motion. Nearly every biomechanical study of the spine test one three loading directions independently and sequentially: flexion/extension, lateral bending, and axial torsion. However, movement of the spine is very complex and usually consists of motion in multiple planes simultaneously. By testing and analyzing the spine in more physiological complex loading vectors, a more complete picture of the biomechanical response can be obtained. The initial interest in this study came from the work done as part of Dr. Nick White's finite element analysis of rotary-wing aircraft crashes, which are discussed in the previous section of this report. Logically, biomechanical testing performed on intact cervical spines as well as cervical spines with ACDF and CTDR would provide valuable validation data that could improve the accuracy of these modeling efforts.

The FDA does not test prosthetic disks of the spine at the level of activity and loading that is experienced in the armed services. Due to the high acceleration maneuvers of pilots during normal operation of their aircraft and the even higher acceleration situations caused by emergency maneuvers and collisions, surgeries such as spinal fusion and disk prosthetics to the cervical neck need an additional level of scrutiny to show that they are viable solutions to extending the service period of injured pilots. The aims of this study are intended to aid in the evaluation of these prosthetics for what is considered off label high loading situations. We also seek to discover common modes of failure for different prosthetic designs to evaluate threat to life and potential design improvements. Our aims also seek to provide validation data for FE modeling of neck loading and kinematics. Finally, we are planning on validating a novel testing method that will provide easily understood and displayed 3D complex motion information previously unknown to the spine biomechanics arena. Through a complex multi-axis matlab generated motion or torque control signal our robotic system will be able to test the full range of motion. This data can be processed to show a full profile of disk motion performance.

Kuka Robot and Cervical Spine Testing Fixture

The Wake Forest laboratory space has been outfitted with a Kuka 300 R2500 ultra, 6-axis industrial robotic arm with an ATI 6 axis multiple range load cell and KRC4 robot controller (Figure 101). The robot provides upwards of 3500N of static force with a position resolution of +/-0.06mm (at full range). The Robotic Biomechanics simulation laboratory will be used to test both large scale multi-joint testing of cadaveric and animal biomechanical models as well as provide more focused single-joint small scale testing. The robot provides complex motion paths and force/torque control in six degrees of freedom to more accurately simulate physiological movement and loading. Data generated from this laboratory can help determine native tissue static and dynamic properties, quantify joint mechanics, specify injury metrics in impact (low velocity) and sports injury, and help to quantitatively evaluate orthopedic, neurological, trauma, and general surgical techniques and resulting outcomes. Ultimately, this robotic testing system will allow complex loading experiments to be performed on cervical spines implanted with prosthetic disk devices in order to measure stiffness, range of motion, and stability under physiologic loading. This information can be used to validate complex loading using finite element analysis. Lessons learned from the initial fixture design and robotic system tests have been implemented into the new design of a cervical/thoracic spine fixture system (Figure 102). The system takes advantage of secure fixturing through the use of a low viscosity urethane potting technique, modular design, and quick mounting features.

Figure 101: Kuka 300 R2500 ultra, 6-axis industrial robot.
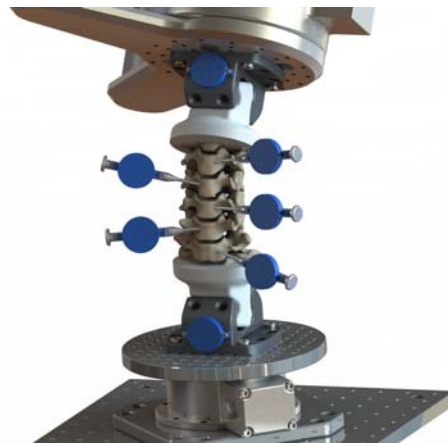
Figure 102: CAD rendered image of the cervical fixture, testing table, 6-axis loadcell (bottom), and robot end effector (top).

The benefits of complex 2 and 3 axis simultaneous moment/force control to perform full field stiffness measurements of all possible moments and directions of bending were assessed using matlab to generate complex loading curves and to analize the resulting data. Three different field measurement methods have been evaluated: spiral, rotating spike, and rotating circular. The curves will supply the control signals to the robotic system through the SimVitro software to map a full polar 2D measurement field as seen in Figure 103, Figure 104, and Figure 105. These figures show varying methods of path generation for filling out the moment field of 0-2Nm from 0 to 360 degrees around the central axis of the spine. The control curve is created through a Mx and My input. Mx represents the flexion extension axis moment, and My represents the lateral bending axis moment. Additional application of Mz and Fz may be applied as needed representing axial torsion and compression.
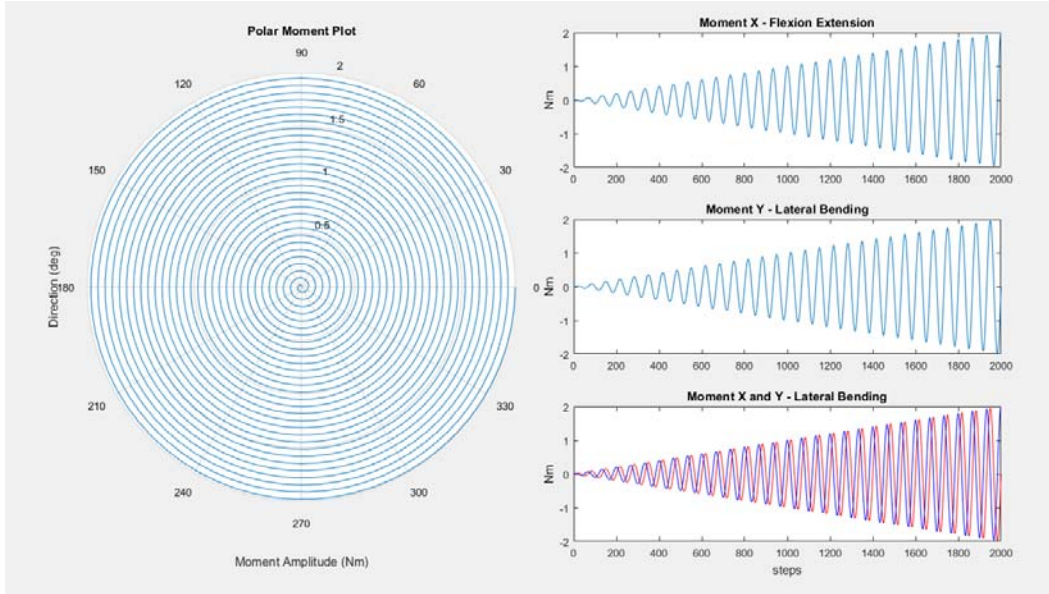
Figure 103: Spiral method of field measurement.
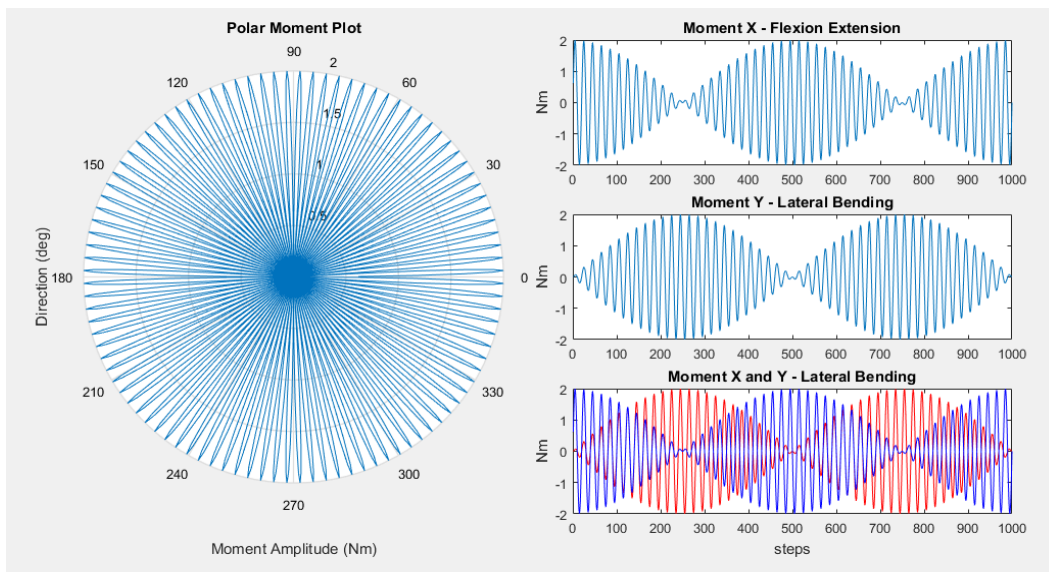
Figure 104: Rotating Spike method of field measurement.

134
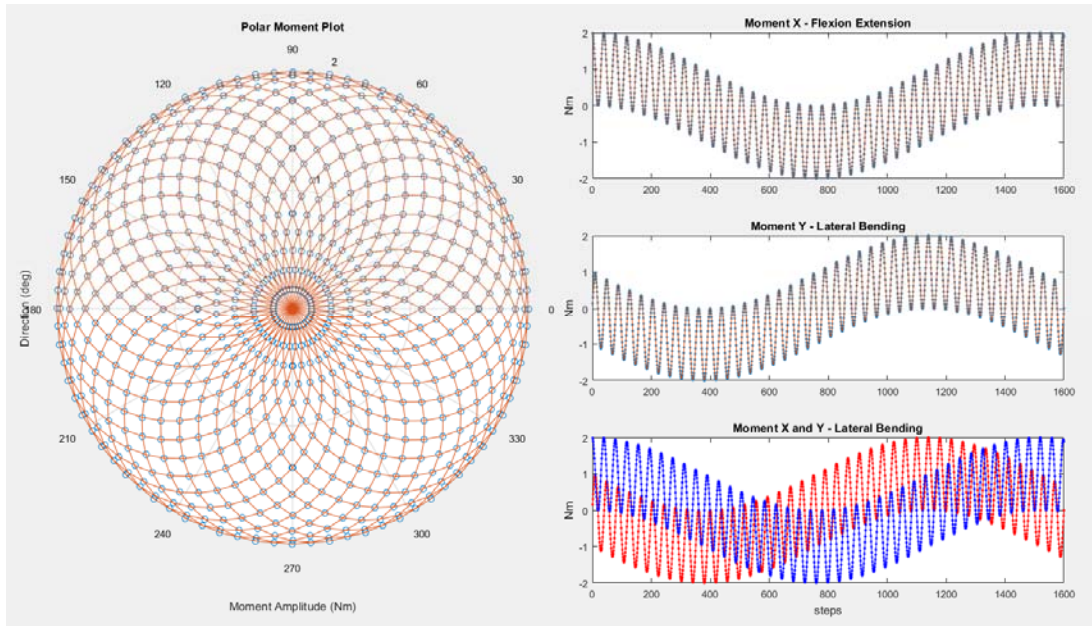
Figure 105: Rotating circular passes method of field measurement.

The rotating circular passing method of field measurement appears to have the most smooth trajectory and allows the added benefit of multiple passes through a single measurement point with a change in direction of trajectory coming from the second pass through the same point. The path generation algorithm will divide the 360 degree polar field into n number of circular passes rotating about the origin. Below in Figure 106 is a simulated stiffness measurement output plot. This simulation supplied a randomly generated stiffness value to each analysis points seen in Figure 105. Three different methods of fringe plots are displayed to show the added benefit of a full field bending test over a standard single axis bending test.
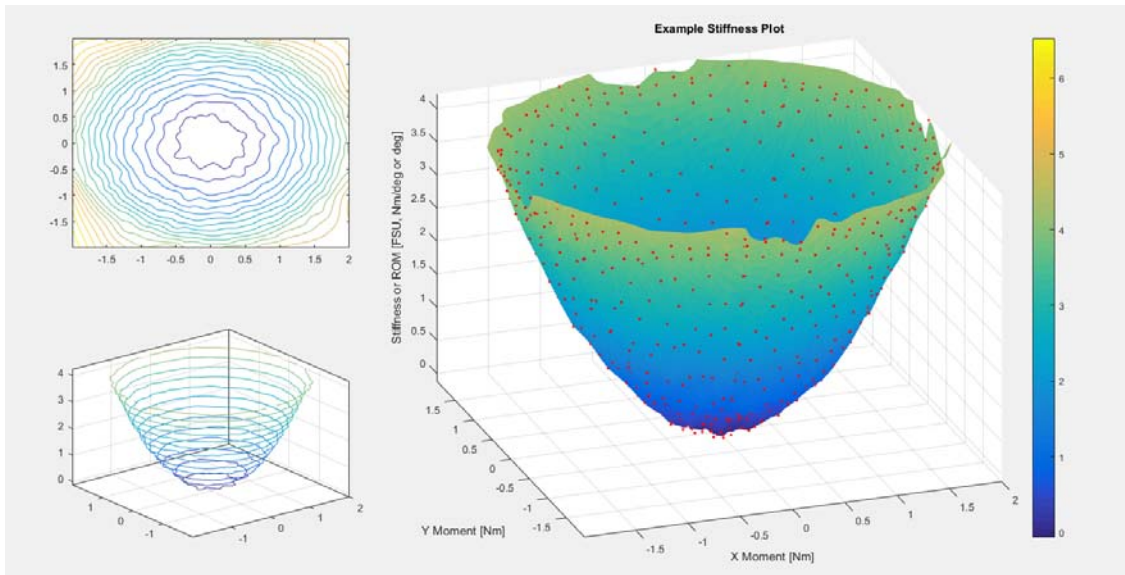
Figure 106: Simulated stiffness analysis.

135

The plan of action is to proceed with each aim as it continues to benefits the over all goal; to provide detailed and useful experimental data and analysis for the evaluation of performance and safety of cervical prosthetics. Initially we will seek to test the novel complex biomechanics loading methodology of physiological loading alongside the more traditional single bending axis testing method employed in standard literature publications. Pending its usefulness and repeatability, we will continue with either the standard testing method or our novel complex loading method. Our intended testing protocol calls for physiologic bending testing followed by the most likely complex failure-loading scenario.

Study Design

Considered Implants for testing:
- **<u>Medtronic Prestige</u>**
- Synthes ProDisc-C
- **<u>Medtronic Bryan</u>**
- Globus Secure-C
- NuVasive PCM
- LDR Mobi-C

Number of specimens:
- Will depend on the number of implants we can obtain (likely 2 implants)
- 5-8 specimens per type of implant (likely 8)

Measured Variables:
- Mx, My, Mz
- Rx, Ry, Rz (for each functional spinal unit)
- Intravertebral disk pressure

Calculated variables:
- Energy expenditure
- Stiffness
- Range of motion
- Failure energy
- Injury/failure mode and location

Medical Imaging and BMD Measurement:
- Phantom and QTC will be used to image cadaver bones
- Mimics will be used for mapping Bone Mineral Density

Specimen Mounting:
- All specimens will be potted on both ends in a custom fixture with polyurethane (SmoothOn 300)
- C2 and C7 partially submerged
- C2 will be mounted to a load cell attached to the Robot
- C7 will be secured to the table

Motion Tracking:
- Northern Digital Inc. (NDI) camera
- Track each vertebra using active LED 3D investigator motion tracking system
- Including C2 and C7
- Relative motion of each FSU can be calculated

Loading Scenarios:

- Simulate FE, LB, AR with Force Torque Control to limits of 2Nm in each direction on the native tissue and then once more on the surgically augmented specimen after disk installation.
    - o Prosthetic Disk implantation will occur in the C5-C6 Disk by a trained neurosurgeon.
    - o Nearly all studies load to 1.5 Nm [1-7] or 2 Nm [8-12] moments in flexion/extension, lateral bending, & axial torsion.
- Simulate complex multi-axis loading using the cylindrical fringe method in non-implanted specimens
    - o This method will measure all output measures from 0-2Nm from 0-360 degrees around the vertical axis of the spine.
- After stiffness and ROM testing, specimens will be loaded to failure
    - o Significant engagement of the implant will occur in over compression and over flexion. A simulated complex motion including both applied forces and moments will be used to evaluate cervical neck failure.

Study Progress and Future Plans

The construction and operation of our robotic test bed has been a long process. Due to the complexity of the system, the development of system integration and control software, and relative newness of freshly released robot control hardware our system has been seeing many incremental upgrades to address issues in control and data acquisition. Recent fixes to the control system include the upgrade of our control PC. The PC was built with a multi core AMD processor that did not run efficiently with our National Instruments Labview based control software SimVitro (Figure 107). We replaced the motherboard and processer with an equivalent Intel processor. In addition, we installed several Ethernet network cards to manage fixed IP addresses to communicate with our Ethernet based systems. This system change did not completely fix our control issues of jumpy incremental movement of the robot. This issue arises from the mismatch of trajectory generation and robot controller refresh rate. To solve this issue another upgrade to the SimVitro platform was completed to transition from displacement-control to velocity-control. This type of control is a much more forgiving and smooth control method for robotics.
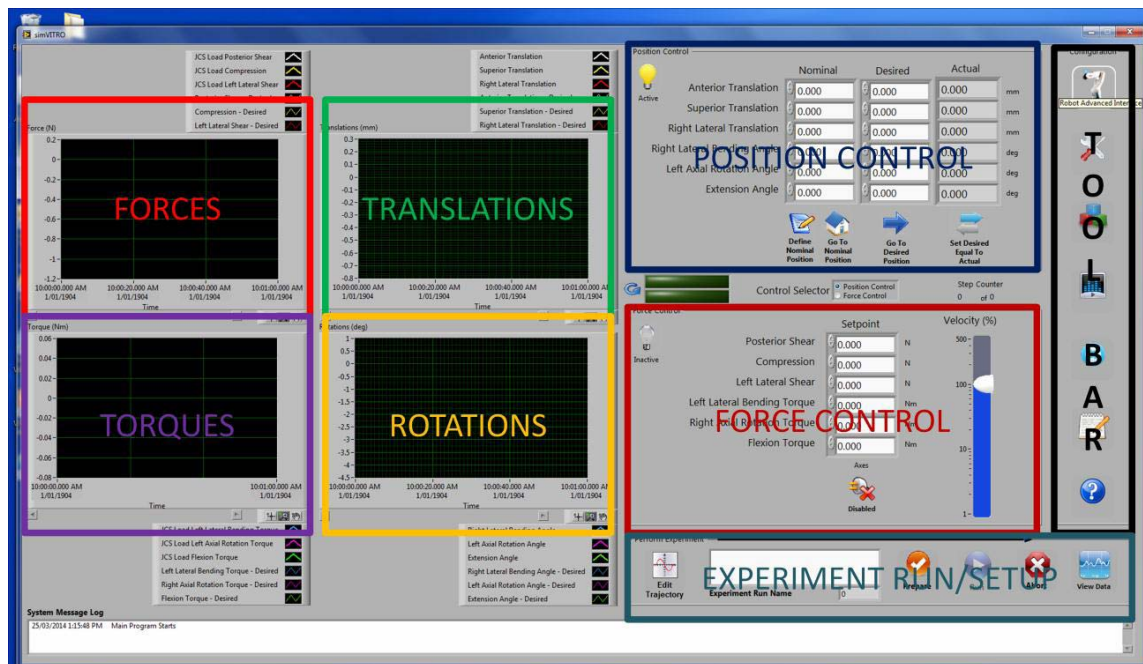
Figure 107: SimVitro main screen showing both kinematic and kinetic control and monitoring.

We have also acquired a National Instruments cDAQ system with quarter Wheatstone bridge amplifier and signal conditioning modules along with Precision measurements Model 060S low profile MEMS based pressure sensors (Figure 108 and Figure 109). The sensors will be installed into biopsy needles for insertion into the disk space (Figure 110). This system will easily integrate into our SimVitro environment to provide synchronized cervical disk pressure measurements. These measurements will be helpful in evaluating the changes above and below the disk prosthetic after implantation in addition to providing additional FEA validation data.

Figure 108: National Instruments cDAQ data acquisition system for strain gage based pressure measurement.

Models 060 and 060S
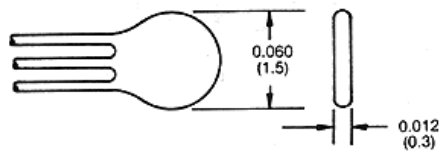
Model 060: Material; BeCu - Output: F.S. 0.7 mv/v nominal in all models.						
Pressure Range - *Non-metallic diaphragm						
psi	0 - 20*	0 - 50	0 - 200	0 - 500	0 - 1000	0 - 2000
kPa	0 - 140	0 - 350	0 - 1.4k	0 - 3.4k	0 - 6.9k	0 - 13.8k
Model 060S: Material; Stainless Steel - Output: F.S. 0.5 mv/v nominal in all models.						
Pressure Range - *Non-metallic diaphragm						
psi	0 - 20*	0 - 100	0 - 500	0 - 1000	0 - 2000	0 - 4000
kPa	0 - 140	0 - 690	0 - 3.4k	0 - 6.9k	0 - 13.8k	0 - 28k

Figure 109: Precision measurements Model 060S size and pressure readings.

138

Figure 110: Example of biopsy needle used for disk pressure when combined with a Model 060S pressure sensor.

Tissue acquisition

We have scheduled incremental acquisition of 20 cervical neck samples C2-T1 from the Wake Forest Center for Applied Learning. Specimens will be under the age of 72 and have no history of mechanical cervical neck surgery.

Implant Acquisition

We have attempted contact with several cervical disk prosthetic manufacturing companies including the following: Medtronic (Prestige, Bryan), Synthes (ProDisc-C), Globus (Secure-C), NuVasive (PCM), and LDR (Mobi-C). In our discussions with company research representatives there appears to be little benefit and a substantial risk to the companies to proceed with a comparative study between brands or a study involving loading considered to be off label (ie. high loading). For this reason we are pursuing support of Medtronic as they see some benefit in our study and have two distinctive implant systems that are fairly representative of the various designs within the field. These models are the Prestige and the Bryan (Figure 111 to Figure 113). The Prestige was one of the models evaluated in earlier FE modeling and is a metal on metal ball and trough design with three degrees of rotational freedom and a single anterior-posterior translation degree of freedom. The Bryan is an anatomical inspired design containing two oesteointegrative titanium endplates with a polyurethane shell and a duel spherical gliding surface polyurethane nucleolus. This design provides three degrees of rotational freedom and two translational degrees of freedom. It also has a changing center of rotation and some spring force provided by the outer shell more accurately replicating the function of the biological disk.

Figure 111: Medtronic Prestige cervical disk prosthetic.

Figure 112: Medtronic Bryan cervical disk prosthetic.

Titanium Alloy Shell

Commercially Pure (CP) Titanium Porous Coating

Flexible Polyurethane Outer Shell

Polyurethane Inner Nucleus

Titanium Alloy Shell

Commercially Pure (CP) Titanium Porous Coating

Figure 113: Medtronic Bryan cervical disk prosthetic (exploded view).

Overall Project Status , Summary, and Future Work

In collaboration with the Global Human Bodies Modeling Consortium and the Wake Forest University Neurosurgery department our group has conducted 4 independent finite element studies simulating automobile collisions and rotary-wing aircraft impact. In addition we have constructed a test bed for complex simulation of cadaveric spine segments for physical evaluation of cervical prosthetic discs and validation of the above mentioned simulation work. Our experimental phase is still in progress as our system is finishing its control upgrade, as fixture hardware is created and delivered by third party vendors, as we acquire specimens from the center for applied learning, and as we evaluate our testing methodology for robustness. We are also engaged with Medtronic with regards to the supply of disc implant devices for evaluation. Future work will include the experimental testing of two groups of 8 cervical spine (Medtronic Prestige, Medtronic Bryan) in physiologic stiffness and range of motion followed by load to failure testing and a biomechanical/clinical evaluation of the mode of failure and risk to life. Data will be post processed to evaluate biofidelic properties of the implant, the modes of failure, and the clinical safety of these implants, and any resulting surgical implications from failure.

TASK 4.3: MILITARY BIOMECHANICS- NATIONAL RESEARCH SYMPOSIUM

The Military Biomechanics National Research Symposium was successfully held on October 29th of 2015 in Blacksburg, VA. This year's meeting built upon the International State-of-the-Science Meeting on the Biomedical Basis for mTBI Environmental Sensor Threshold Values by focusing on our work with head impact sensors (Figure 114). This meeting highlighted the importance of evaluating the ability of head impact sensors to capture head kinematics during loading events. Such work can help inform future decisions on sensors, how to interpret these data, and appropriately analyze risk. This forum allowed for interactions and collaborative discussions that will lead to new partnerships and ultimately better protection for soldiers. The success of this symposium highlights the importance of these symposiums to assist in the translation of the research to practice. Figure 114 displays the agenda and lecture content of the Military Biomechanics National Research Symposium.

Figure 114: October 29, 2015 Military Biomechanics National Research Symposium Program.

The research under this cooperative agreement has generated a considerable amount of novel data that will add to the literature. To date, this research has yielded nine (n=9) refereed publications and six (n=6) conference publications. Three (n=3) additional manuscripts have been submitted to peer reviewed journals and are currently under review. Finally, five (n=5) more manuscripts will be submitted to peer reviewed journals within the next six months.

REFEREED PUBLICATIONS

Task 1.3: Blast Eye Modeling/ Blast Eye Injury Criteria

Alphonse VD, Kemper AR, Strom BT, Beeman SM, and Duma SM. Mechanisms of Eye Injuries from Fireworks. *Journal of the American Medical Association*, 308(1): 33-34, 2012.

Alphonse VD, Kemper AR, Strom BT, Beeman SM, and Duma SM. Exposure to Fireworks and Eye Injuries - Reply. *Journal of the American Medical Association*. 308(15): 1523-1524, 2012. DOI:10.1001/jama.2012.11907.

Alphonse VD, Kemper AR, and Duma SM. Effects of Filtering on Experimental Blast Overpressure Measurements. *Biomedical Sciences Instrumentation*. 2015;51:143-50.

Task 1.3.1: Brain Injury: Biomechanics of the Head /Brain

Cobb BR, MacAlister A, Young TJ, Kemper AR, Rowson S, and Duma SM. Quantitative Comparison of Hybrid III and NOCSAE Headform Shape Characteristics and Implications on Football Helmet Fit. Proceedings of the Institution of Mechanical Engineers, Part P: *Journal of Sports Engineering and Technology*, 229(1): 39-46, 2015. DOI: 10.1177/1754337114548245.

Cobb BR, Zadnik AM, Rowson S. Comparative analysis of helmeted impact response of Hybrid III and National Operating Committee on Standards for Athletic Equipment headforms. Proceedings of the Institution of Mechanical Engineers, Part P: Journal of Sports Engineering and Technology. 2016;230(1):50-60. doi: 10.1177/1754337115599133

Task 2.3: Evaluation of Cervical Spine Implants

White NW, Moreno DP, Brown PJ, Gayzik FS, Hsu W, Powers AK, Stitzel JD. Effects of Cervical Arthrodesis and Arthroplasty on Neck Response during a Simulated Frontal Automobile Collision. The Spine Journal. 2014; 14(9):3195-207.

White NW, Danelson KA, Gayzik FS, and Stitzel JD**.** Head and Neck Response of a Finite Element Anthropomorphic Test Device and Human Body Model during a Simulated Rotary-Wing Aircraft Impact. *J Biomech Eng.* 2014; 136(11),111001.

White NW, Moreno DP, Gayzik FS, Stitzel JD. Cross-Section Neck Response of a Total Human Body FE Model during Simulated Frontal and Side Automobile Impacts – Computer Methods in Biomechanics and Biomedical Engineering. Computer Methods in Biomechanics and Biomedical Engineering. 2015;18(3):293-315.

White NW, Danelson KA, Gayzik FS, HSU W, Powers AK, and Stitzel JD. Effects of Cervical Arthroplasty on Neck Response during a Simulated Rotary-Wing Aircraft Impact. International Journal of Crashworthiness. 2016;21(4):323-337.

CONFERENCE PUBLICATIONS

Task 1.3: Blast Eye Modeling/ Blast Eye Injury Criteria

Kemper AR, Alphonse VD, McNally C, Herring IP, Brown PJ, Stitzel JD, and Duma SM. Response of Porcine Eyes to Blast Overpressure: Effects of Overpressure Severity and Boundary Conditions. *Proceedings of the 41st International Workshop on Human Subjects for Biomechanical Research*, National Highway Traffic Safety Administration (NHTSA), US DOT, 2013.

Alphonse VD, Kemper AR, and Duma SM. Effect of Orbital Geometry on Eye Response to Survivable Primary Blast Overpressure. *Proceedings of the 2014 Biomedical Engineering Society Annual Meeting*, San Antonio, TX, 2014.

Alphonse VD, Kemper AR, and Duma SM. Blast Simulator Considerations for Biological Specimens. *Proceedings of the 40th Annual Northeast Bioengineering Conference*, Boston, MA, 2014.

Alphonse VD, Kemper AR, and Duma SM. Eye and Face Response to Blast Overpressure: An Experimental Study Using a 3D-Printed Human Face. *Proceedings of the 2015 Biomedical Engineering Society Annual Meeting*, Tampa, FL, 2015.

Task 1.3.1: Brain Injury: Biomechanics of the Head /Brain

Rowson S, Cobb BR, Daniel RW, MacAlister A, Young T, Kemper AR, and Duma SM. Rotational Head Acceleration Measurement Techniques and Headform Characteristics: Implication on Helmet Impact Testing. *Proceedings of the 41st International Workshop on Human Subjects for Biomechanical Research*, National Highway Traffic Safety Administration (NHTSA), US DOT, 2013.

Cobb BR, MacAlister A, Young TJ, Kemper AR, Rowson S, and Duma SM. Quantitative Analysis of Dummy Headform Shape for Impact Testing with Football Helmets. *Proceedings of the 2014 Biomedical Engineering Society Annual Meeting*, San Antonio, TX, 2014.

SUBMITTED MANUSCRIPTS CURRENTLY UNDER REVIEW

Task 1.3: Blast Eye Modeling/ Blast Eye Injury Criteria

Weaver AA, Stitzel SM, Stitzel JD. Injury Risk Prediction from Computational Simulations of Ocular Blast Loading. Biomechanics and Modeling in Mechanobiology. (Under Review).

Task 1.3.1: Brain Injury: Biomechanics of the Head /Brain

Cormier JM, Rowson S, McNally C, Bolte J, and Duma SM, "The tolerance and biomechanical response of facial bones to lateral impact," Journal of the Mechanical Behavior of Biomedical Materials. (Under Review).

Tyson AM, Rowson S, and Duma SM, "Development and implementation of laboratory test methods for the evaluation of wearable head impact sensors," Annals of Biomedical Engineering. (Under Review).

MANUSCRIPTS UNDER PREPARATION

Task 1.3: Blast Eye Modeling/ Blast Eye Injury Criteria

TITLE: Injury risk from primary blast overpressure to the unprotected porcine eye
AUTHORS: Alphonse VD, Kemper AR, and Duma SM
PROPOSED JOURNAL: Journal of Biomechanics
STATUS: Manuscript will be submitted August 2016

TITLE: Effects of spectacles and goggles on eye injury risk from primary blast overpressure exposure
AUTHORS: Alphonse VD, Kemper AR, and Duma SM
PROPOSED JOURNAL: Archives of Ophthalmology
STATUS: Manuscript will be submitted by December 2016

TITLE: Intraorbital and facial response corridors for primary blast overpressure exposure
AUTHORS: Alphonse VD, Kemper AR, and Duma SM
PROPOSED JOURNAL: Biomechanics and Modeling in Mechanobiology
STATUS: Manuscript will be submitted December 2016

TITLE: Evaluating the FOCUS headform for exposure to primary blast overpressure
AUTHORS: Alphonse VD, Kemper AR, and Duma SM
PROPOSED JOURNAL: Biomedical Sciences Instrumentation
STATUS: Manuscript will be submitted February 2017

TITLE: An area-sensitive synthetic eye that differentiates between blunt and blast loading
AUTHORS: Alphonse VD, Kemper AR, and Duma SM
PROPOSED JOURNAL: Journal of Trauma
STATUS: Manuscript will be submitted February 2017

References

Agel J, Olson DE, Dick R, et al. Descriptive epidemiology of collegiate women's basketball injuries: National collegiate athletic association injury surveillance system, 1988-1989 through 2003-2004. J Athl Train. 2007;42:202-10.

Alphonse VD, Kemper AR, Strom BT, Beeman SM, and Duma SM. Mechanisms of Eye Injuries from Fireworks. Journal of the American Medical Association. 2012;308(1):33-34.

Allison MA, Kang YS, Maltese MR, et al. Measurement of hybrid III head impact kinematics using an accelerometer and gyroscope system in ice hockey helmets. Ann Biomed Eng. 2015;43(8):1896-906.

Allison PD. Survival Analysis Using SAS: A Practical Guide. SAS Press, Cary , 1995.

Allsop D, and Kennett K. Skull and Facial Bone Trauma, in: Nahum, A., Melvin, J. (Eds.), Accidental Injury: Biomechanics and Prevention. Springer-Verlag, New York, 2002:254-276.

Allsop D, Warner C, Wille M, Schneider D, Nahum A. Facial Impact Response – A Comparison of the Hybrid 3 Dummy and Human Cadaver. Society of Automotive Engineers. 1988. SAE Paper Number 881719.

Alvi A, Doherty T, Lewen G. Facial Fractures and Concomitant Injuries in Trauma Patients. The Laryngoscope 2003;113:102-6.

Authorized Protective Eyewear List (APEL). July 13, 2015 Available: http://www.peosoldier.army.mil/equipment/eyewear/

Bailoor S, Bhardwaj R, and Nguyen TD. Effectiveness of eye armor during blast loading. Biomechanics and modeling in Mechanobiology. 2015;14(6):1227-37.

Bartsch A, Benzel E, Miele V, et al. Impact test comparisons of 20th and 21st century american football helmets. J Neurosurg. 2012;116:222-33.

Beckwith JG, Greenwald RM and Chu JJ. Measuring head kinematics in football: Correlation between the head impact telemetry system and hybrid iii headform. Ann Biomed Eng. 2012;40:237-48.

Belmont PJ, Schoenfeld AJ, Goodman G. Epidemiology of combat wounds in Operation Iraqi Freedom and Operation Enduring Freedom: orthopaedic burden of disease. J Surg Orthop Adv. 2010;19:2-7.

Berger RE. A model for evaluating the ocular contusion injury potential of propelled objects. J Bioeng. 1978;2:345-358.

Bermond F, Kallieris D, Mattern R, Ramet M, Bouquet R, Caire Y, Voiglio E. Human Face Response at an Angle to the Fore-aft Vertical Plane Impact. Proceedings of the IRCOBI Conference, 1999:121-132.

Bhardwaj, R, et al., A computational model of blast loading on the human eye. Biomech Model Mechanobiol. 2014; 13(1): 123-40.

Bisplnghoff J, Cormier J, Duma S, Kennedy E, Depinet P, Brozoski F. Development and Validation of Eye and Facial Fracture Criteria for the FOCUS headform. Proceedings of the 26th Army Science Conference. Orlando, FL, 2008.

Bisplinghoff JA, Duma SM. Evaluation of eye injury risk from projectile shooting toys using the focus headform. Biomedical sciences instrumentation. 2009;45:107-112.

Bisplinghoff JA, McNally C, Duma SM. High-rate internal pressurization of human eyes to predict globe rupture. Arch Ophthalmol. 2009;127:520-523.

Bricker-Anthony C, Hines-Beard J, D'Surney L, Rex TS. Exacerbation of blast-induced ocular trauma by an immune response. J Neuroinflammation. 2014a;11:192.

Bricker-Anthony C, Hines-Beard J, Rex TS. Molecular changes and vision loss in a mouse model of closed-globe blast trauma. Invest Ophthalmol Vis Sci. 2014b;55:4853-4862.

Campbell KR, Warnica MJ, Levine IC, et al. Laboratory evaluation of the gforce tracker™, a head impact kinematic measuring device for use in football helmets. Annals of biomedical engineering. 2015;1-11.

Cantor AB. Analysis Techniques for Medical Research, 2nd ed. SAS Press, Cary, 2003.

Carroll SM, Jawad MA, West M, O'Connor TP. One hundred and ten sports related facial fractures. Br J Sports Med. 1995; 29:194-195.

Carvalho TB, Cancian LR, Marques CG, Piatto VB, Maniglia JV, Molina FD. Six years of facial trauma care: an epidemiological analysis of 355 cases. Braz J Otorhinolaryngol. 2010;76: 565-574.

Cesari D, Ramet M, Welbourne E.. Experimental Evaluation of Human Facial Tolerance to Injuries. Proceedings of the IRCOBI Conference. Stockholm, Sweden. 1989.

Choi JH, Greene WA, Johnson AJ, Chavko M, Cleland JM, McCarron RM, Wang HC. Pathophysiology of blast-induced ocular trauma in rats after repeated exposure to low-level blast overpressure. Clin Experiment Ophthalmol. 2015;43:239-246.

Crisco JJ, Chu JJ and Greenwald RM. An algorithm for estimating acceleration magnitude and impact location using multiple nonorthogonal single-axis accelerometers. J Biomech Eng. 2004;126:849-54.

Cobb BR, Urban JE, Davenport EM, et al. Head impact exposure in youth football: Elementary school ages 9–12 years and the effect of practice structure. Ann Biomed Eng. 2013;41:2463-2473.

Cobb BR, MacAlister A, Young TJ, et al. Quantitative comparison of hybrid iii and nocsae headform shape characteristics and implications on football helmet fit. Proceedings of the Institution of Mechanical Engineers, Part P: Journal of Sports Engineering and Technology. 2014;DOI: 10.1177/1754337114548245:

Cobb BR, MacAlister A, Young TJ, et al. Quantitative comparison of hybrid iii and national operating committee on standards for athletic equipment headform shape characteristics and implications on football helmet fit. Proceedings of the Institution of Mechanical Engineers, Part P: Journal of Sports Engineering and Technology. 2015;229:39-46.

Cobb BR, Zadnik AM and Rowson S. Comparative analysis of helmeted impact response of hybrid iii and national operating committee on standards for athletic equipment headforms. Proceedings of the Institution of Mechanical Engineers, Part P: Journal of Sports Engineering and Technology. 2016;230:50-60.

Cormier J, and Duma S, Epidemiology of Facial Fractures in Automotive Collisions. Annals of the Advancement of Automotive Medicine. 2009;53:169-176.

Cormier J, Manoogian S, Bisplinghoff J, Rowson S, Santago A, McNally C, Duma S, Bolte J, The tolerance of the nasal bone to blunt impact. Ann Adv Automot Med. 2010a.;54,: 3-14.

Cormier J, Manoogian S, Bisplinghoff J, Rowson S, Santago A, McNally C, Duma S, Bolte J. The tolerance of the frontal bone to blunt impact. J Biomech Eng. 2011a;133, 021004.

Cormier J, Manoogian S, Bisplinghoff J, Rowson S, Santago A, McNally C, Duma S, Bolte J. The tolerance of the maxilla to blunt impact. J Biomech Eng 2011b;133, 064501.

Cormier J, Manoogian S, Bisplinghoff J, Rowson S, Santago A, McNally C, Duma S, Bolte J. The tolerance of the frontal bone to blunt impact. J Biomech Eng. 2011c:133.

Cormier J, Manoogian S, Bisplnghoff J, McNally C, Duma S. The Use of Acoustic Emission in Facial Fracture Detection. Biomed. Sci. Instrum. 2008;44:147-152.

Cormier J, Manoogian S, Bisplnghoff J, Rowson S, Santago A, McNally C, Duma S, Bolte J,. Biomechanical Response of the Human Face and Corresponding Biofidelity of the FOCUS Headform, Society of Automotive Engineers. 2010b. SAE Paper Number 2010-01-1317.

Cormier JM, Stitzel JD, Hurst WJ, Porta DJ, Jones J, Duma SM. Predicting zygoma fractures from baseball impact. Biomedical sciences instrumentation. 2006;42:142-147.

Covassin T, Schatz P and Swanik CB. Sex differences in neuropsychological function and post-concussion symptoms of concussed collegiate athletes. Neurosurgery. 2007;61:345-351.

Daniel RW, Rowson S and Duma SM. Head impact exposure in youth football. Ann Biomed Eng. 2012;40:976-981.

Duma SM, Schreiber P, McMaster J, Crandall J, Bass C, Pilkey W. Dynamic Injury Tolerance for Long Bones in the Female Upper Extremity. J Anatomy. 1999;194:463-471.

Duma SM, Crandall JR. Eye injuries from airbags with seamless module covers. J Trauma. 2000;48:786-789.

Duma SM, Jernigan M, Stitzel J, Herring I, Crowley J, Brozoski F, Bass C. The Effect of Frontal Air Bags on Eye Injury Patterns in Automibile Crashes. Arch Ophthalmol. 2002;120:1517-1522.

Duma SM, Jernigan M. The effects of airbags on orbital fracture patterns in frontal automobile crashes. Ophthal Plast Reconstr Surg. 2003;19:107-111.

Duma SM, Ng TP, Kennedy EA, Stitzel JD, Herring IP, Kuhn F. Determination of significant parameters for eye injury risk from projectiles. J Trauma. 2005a;59:960-964.

Duma SM, Manoogian SJ, Bussone WR, et al. Analysis of real-time head accelerations in collegiate football players. Clin J Sport Med. 2005b;15:3-8.

Duma SM and Rowson S. Every newton hertz: A macro to micro approach to investigating brain injury. Conf Proc IEEE Eng Med Biol Soc. 2009;1:1123-6.

Duma SM, Bisplinghoff JA, Senge DM, McNally C, and Alphonse VD. Evaluating the risk of eye injuries: intraocular pressure during high speed projectile impacts. Current Eye Research. 2012; 37: 43-49.

Esposito L, Clemente C, Bonora N, Rossi T. Modelling human eye under blast loading. Computer methods in biomechanics and biomedical engineering. 2015;18:107-115.

Fischer H. A guide to U.S. military casualty statistics: Operation New Dawn, Operation Iraqi Freedom, and Operation Enduring Freedom. 2015. Available: www.fas.org/sgp/crs/natsec/RS22452.pdf

Funk J, Crandall J, Tourret L, MacMahon C, Bass C, Patrie J, Khaewpong N, Eppinger R. The Axial Injury Tolerance of the Human Foot/Ankle Complex and the Effect of Achilles Tension. Journal of Biomechanical Engineering. 2002;124:1-8.

Funk JR, Duma SM, Manoogian SJ, et al. Development of concussion risk curves based on head impact data from collegiate football players. Injury Biomechanics Research, Proceedings of the 34th International Workshop. 2006.

Funk JR, Rowson S, Daniel RW, et al. Validation of concussion risk curves for collegiate football players derived from hits data. Ann Biomed Eng. 2012;40:79-89.

Gadd CW. Use of a weighted-impulse criterion for estimating injury hazard. Proceedings of the 10th Stapp Car Crash Conference. 1966;10:164-174. SAE Paper Number 660793:

Gassner R, Tuli T, Hächl O, Rudisch A, Ulmer H. Cranio-Maxillofacial Trauma: A 10 Year Review of 9543 cases with 21067 Injuries. Cranial and Maxillofacial Surgery. 2003; 31: 51-61.

Guskiewicz KM and Mihalik JP. Biomechanics of sport concussion: Quest for the elusive injury threshold. Exerc Sport Sci Rev. 2011;39:4-11.

Gwin JT, Chu JJ, Diamond SG, et al. An investigation of the nocsae linear impactor test method based on in vivo measures of head impact acceleration in american football. J Biomech Eng. 2010;132:011006.

Hardy WN, Mason MJ, Foster CD, et al. A study of the response of the human cadaver head to impact. Stapp Car Crash J. 2007;51:17-80.

Hackle W, Hausberger K, Sailer R, Ulmer H, Gassner R. Prevalence of Cervical Spine Injuries in Patients with Facial Trauma. Oral and Maxillofacial Surgery. 2001;92:370-376.

Higgins M, Halstead PD, Snyder-Mackler L, et al. Measurement of impact acceleration: Mouthpiece accelerometer versus helmet accelerometer. Journal of athletic training. 2007;42:5.

Hines-Beard J, Marchetta J, Gordon S, Chaum E, Geisert EE, Rex TS. A mouse model of ocular blast injury that induces closed globe anterior and posterior pole damage. Exp Eye Res. 2012;99:63-70.

Hodgson VR. National operating committee on standards for athletic equipment football helmet certification program. Medicine and science in sports. 1975;7:225.

Hodgson VR, Brinn J, Thomas LM, Greenberg SW. Fracture Behavior of the Skull Frontal Bone Against Cylindrical Surfaces. Proceedings of the 14th Stapp Car Crash Conference. 1970;14:341-355. SAE Paper number 700909.

Hubbard RP and McLeod DG. Definition and development of a crash dummy head. Proceedings of the 18th Stapp Car Crash Conference. 1974;18:599-628. SAE Paper Number 741193:

Huelke DF, Compton CP. Facial injuries in automobile crashes. Journal of oral and maxillofacial surgery : official journal of the American Association of Oral and Maxillofacial Surgeons. 1983;41:241-244.

Jadischke R, Viano DC, Dau N, et al. On the accuracy of the head impact telemetry (hit) system used in football helmets. Journal of biomechanics. 2013;46(13):2310-5.

Jayamanne DGR, Gillie RF. Do Patients with Facial Trauma to the Orbito-Zygomatic Region also Sustain Significant Ocular Injuries? Coll. Surg. Eding. 1996;41: 200-203.

Karimi A, Razaghi R, Navidbakhsh M, Sera T, Kudo S. Computing the stresses and deformations of the human eye components due to a high explosive detonation using fluid-structure interaction model. Injury. 2016;47(5):1042-50.

Karlson TA. The incidence of hospital-treated facial injuries from vehicles. J Trauma. 1982;22: 303-310.

Kemper AR, McNally C, Duma SM. Acquiring non-censored pelvic bone fracture data during dynamic side impact loading - biomed 2009. Biomedical sciences instrumentation. 2009;45:395-400.

Kendall M, Walsh ES and Hoshizaki TB. Comparison between hybrid iii and hodgson–wsu headforms by linear and angular dynamic impact response. Proceedings of the Institution of Mechanical Engineers, Part P: Journal of Sports Engineering and Technology. 2012;226:260-265.

Kennedy EA, and Duma SM. Eye injury risk functions for human and FOCUS eyes: hyphema, lens dislocation, and retinal damage, Prepared for: US Army Medical Research and Materiel Command, 2011.

Kennedy EA, Ng TP, McNally C, Stitzel JD, Duma SM. Risk functions for human and porcine eye rupture based on projectile characteristics of blunt objects. Stapp Car Crash J. 2006;50:651-671.

Kennedy EA, et al. Development and validation of a synthetic eye and orbit for estimating the potential for globe rupture due to specific impact conditions. Stapp Car Crash J. 2007;51:381-400.

Kennedy EA, Stitzel JD, Duma SM. Matched experimental and computational simulations of paintball eye impacts. Biomedical sciences instrumentation. 2008;44:243-248.

Kent R, Stacey S, Parenteau C. Dynamic Pinch Tolerance of the Phalanges and Interphalangeal Joints. Traffic Injury Prevention. 2008;9:83-88.

Kingery CN, Bulmash G. Air-Blast Parameters from TNT Spherical Airburst and Hemispherical Surface Burst. U.S. Army Ballistic Research Laboratory, Aberdeen Proving Ground, MD. April, 1984.

Kisielewicz LT, Kodama N, Ohno S, Uchio E. Numerical Prediction of Airbag Caused Injuries on Eyeballs After Radial Keratotomy. Society of Automotive Engineers. 1998. SAE Paper 980906.

Kleinbaum D and Klein M. Survival Analysis: A Self-Learning Text, 2nd ed. Springer Science, New York. 2005.

Laituri T, El-jawahri R. Fracture Modeling Inputs for a Human Body Model via Inference from a Risk Curve: Application for Skull Fracture Potential, Society of Automotive Engineers. 2012. SAE Paper Number 2012-01-0562.

Lessley D, Crandall J, Shaw G, Kent R, Funk J. A Normalization Technique for Developing Corrdors from Individual Subject Responses. Society of Automotive Engineers. 2004. SAE Paper Number 2004-01-0288.

Lim LH, Lam LK, Moore MH, Trott JA, David DJ. Associated Injuries in Facial Fractures: A Review of 839 Patients. British J. Plast. Surg. 1993;46:365-338.

Liu X, Wang L, Wang C, Fan J, Liu S, Fan Y (2015) Prediction of globe rupture caused by primary blast: a finite element analysis. Computer methods in biomechanics and biomedical engineering. 2015;18:1024-1029.

Mader TH, Carroll RD, Slade CS, George RK, Ritchey JP, Neville SP. Ocular war injuries of the Iraqi insurgency, January-September 2004. Ophthalmology. 2006;113:97-104.

Manoogian S, Kennedy E, Wilson K, Duma S. Prevention of facial fractures from night vision goggle impact. Biomedical sciences instrumentation. 2006;42: 13-18.

Muraoka M, Nakai Y, Nakagawa K, Yoshioka N, Nakaki Y, Yabe T, Hyodo T, Kamo R, Wakami S. Fifteen-year statistics and observation of facial bone fracture. Osaka City Med J. 1995a;41: 49-61.

Muraoka M, Nakai Y, Nakagawa K, Yoshioka N, Nakaki Y, Yabe T, Hyodo T, Kamo R, Wakami S. Fifteen – Year Statistics and Observation of Facial Bone Fracture. Osaka City Med. J. 1995b;41:49-61.

Nahum AM. The biomechanics of facial bone fracture. Laryngoscope. 1975a;85: 140-156.

Nahum AM. The biomechanics of maxillofacial trauma. Clin Plast Surg. 1975b; 2:59-64.

Nahum AM, Gatts JD, Gadd CW, Danforth J. Impact Tolerance of the Skull and Face, Proceedings of the 12th Stapp Car Crash Conference, New York. 1968:302-316.

National Operating Committee on Standards for Athletic Equipment. Standard test method and equipment used in evaluating the performance characteristics of protective headgear/equipment. 2011;NOCSAE DOC (ND)001-11m11.

Nevins D, Smith L and Kensrud J. Laboratory evaluation of wireless head impact sensor. Procedia Engineering. 2015;112:175-179.

Newman JA, Beusenberg MC, Shewchenko N, et al. Verification of biomechanical methods employed in a comprehensive study of mild traumatic brain injury and the effectiveness of american football helmets. J Biomech. 2005;38:1469-81.

Ommaya AK. Biomechanics of head injuries: Experimental aspects. In: A. N. a. J. W. Melvin. Biomechanics of trauma. Eat Norwalk, CT. Appleton-Century-Crofts; 1985.

Owens BD, Kragh JF, Wenke JC, Macaitis J, Wade CE, Holcomb JB,. Combat wounds in operation Iraqi Freedom and operation Enduring Freedom. The Journal of Trauma. 2008;64: 295-299.

Nyquist GW, Cavanaugh JM, Goldberg SJ, King AI. Impact Tolerance and Response of the Face, Proceedings of the Advances in Bioengineering Conference, Anaheim, CA, 1986:75-81.

Padgaonkar AJ, Kreiger KW and King AI. Measurement of angular acceleration of a rigid body using linear accelerometers. J Appl Mech. 1975;42:552-556.

Pellman EJ, Viano DC, Tucker AM, et al. Concussion in professional football: Reconstruction of game impacts and injuries. Neurosurgery. 2003;53:799-812; discussion 812-4.

Pellman EJ, Viano DC, Withnall C, et al. Concussion in professional football: Helmet testing to assess impact performance--part 11. Neurosurgery. 2006;58:78-96; discussion 78-96.

Power ED, Duma SM, Stitzel JD, Herring IP, West RL, Bass CR, Crowley JS, Brozoski FT. Computer modeling of airbag-induced ocular injury in pilots wearing night vision goggles. Aviat Space Environ Med. 2002; 73: 1000-1006.

Press JN and Rowson S. Quantifying head impact exposure in collegiate women's soccer. Clinical Journal of Sport Medicine. 2016.

Rajachar RM, Chow DL, Curtis CE, Weissman NA, Kohn DH. Use of Acoustic Emission to Characterize Focal and Diffuse Microdamage in Bone. Acoustic Emission: Standards and Technology Update ASTM STP 1353, Ed. Vahaviolos SJ, ASTM. 1999.

Rowson S, Brolinson G, Goforth M, et al. Linear and angular head acceleration measurements in collegiate football. J Biomech Eng. 2009;131:061016.

Rowson S, Duma SM, Beckwith JG, et al. Rotational head kinematics in football impacts: An injury risk function for concussion. Ann Biomed Eng. 2012;40:1-13.

Rowson S and Duma SM. Development of the star evaluation system for football helmets: Integrating player head impact exposure and risk of concussion. Ann Biomed Eng. 2011;39:2130-40.

Rowson S and Duma SM. The temperature inside football helmets during head impact: A five-year study of collegiate football games. Proceedings of the Institution of Mechanical Engineers, Part P: Journal of Sports Engineering and Technology. 2013;227:12-19.

Rowson S, Daniel RW and Duma SM. Biomechanical performance of leather and modern football helmets: Technical note. Journal of neurosurgery. 2013;119:805-809.

Rowson B, Rowson S and Duma SM. Hockey star: A methodology for assessing the biomechanical performance of hockey helmets. Annals of biomedical engineering. 2015;43(10):2429-43.

Rudd R, Crandall J, Millington S, Hurwitz S, Hoglund N. Injury Tolerance and Response of the Ankle Joint in Dynamic Dorsiflexion. Stapp Car Crash Journal. 2004;48:1-26.

Schneider DC, Nahum AM. Impact Studies of Facial Bones and Skull, Proceedings of the 16th Stapp Car Crash Conference. 1972;16:186-203. SAE Paper Number 720965.

Schwer L. Air Blast - Engineering Models. Schwer Engineering & Consulting Services, March, 2009.

Scott WR, Lloyd WC, Benedict JV, Meredith R. Ocular injuries due to projectile impacts. Annu Proc Assoc Adv Automot Med. 2000;44:205-217.

Shain KS, Madigan ML, Rowson S, Bisplinghoff J, Duma SM. Analysis of the ability of catcher's masks to attenuate head accelerations on impact with a baseball. Clinical journal of sport medicine: official journal of the Canadian Academy of Sport Medicine. 2010;20:422-427.

Shaprio AJ, Johnson RM, Miller SF, McCarthy MC. Facial Fractures in a Level I Trauma Centre: The Importance of Protective Devices and Alcohol Abuse. Injury Int. J. Care Injured. 2001;32:353-356.

Sherwood D, et al. Anatomical manifestations of primary blast ocular trauma observed in a postmortem porcine model. Invest Ophthalmol Vis Sci. 2014;55:1124-1132.

Siegmund GP, Guskiewicz KM, Marshall SW, et al. A headform for testing helmet and mouthguard sensors that measure head impact severity in football players. Annals of biomedical engineering. 2014;42:1834-1845.

Stitzel JD, Duma SM, Cormier JM, Herring IP. A nonlinear finite element model of the eye with experimental validation for the prediction of globe rupture. Stapp Car Crash Journal. 2002;46:81-102.

Stitzel JD, Hansen GA, Herring IP, Duma SM. Blunt trauma of the aging eye: injury mechanisms and increasing lens stiffness. Arch Ophthalmol. 2005;123:789-794.

Stitzel JD and Weaver AA. Computational simulations of ocular blast loading and prediction of eye injury risk. in ASME Summer Bioengineering Conference. 2012. Fajardo, Puerto Rico.

Stuhmiller JH, Phillips, YY, Richmond, DR. Conventional Warfare: Ballistic, Blast, and Burn Injuries. Chapter 7: The Physics and Mechanisms of Primary Blast Injury. bordeninstitute.army.mil, 1991.

Sullivan JP, et al. Jane's Unconventional Weapons Response Handbook. Jane's Information Group, Alexandria, VA. 2002.

Thomas R, McManus JG, Johnson A, Mayer P, Wade C, and Holcomb JB. Ocular injury reduction from ocular protection use in current combat operations. Journal of Trauma and Acute Care Surgery. 2009;66:S99-S103.

Uchio E, Kadonosono K, Matsuoka Y, Goto S. Simulation of air-bag impact on an eye with transsclerally fixated posterior chamber intraocular lens using finite element analysis. J Cataract Refract Surg. 2004;30:483-490.

Uchio E, Ohno S, Kudoh J, Aoki K, Kisielewicz LT. Simulation model of an eyeball based on finite element analysis on a supercomputer. Br J Ophthalmol. 1999;83:1106-1111.

Uchio E, Ohno S, Kudoh K, Kadonosono K, Andoh K, Kisielewicz LT. Simulation of air-bag impact on post-radial keratotomy eye using finite element analysis. J Cataract Refract Surg. 2001;27:1847-1853.

Versace J. A review of the severity index. Proceedings of the 15th Stapp Car Crash Conference. 1971;15:771-796. SAE Paper Number 710881:

Viano DC, Withnall C and Wonnacott M. Football helmet drop tests on different fields using an instrumented hybrid iii head. Ann Biomed Eng. 2012a;40:97-105.

Viano DC, Withnall C and Halstead D. Impact performance of modern football helmets. Ann Biomed Eng. 2012b;40:160-74.

Vinger P, Duma S, Crandall J. Baseball Hardness as a Risk Factor for Eye Injuries. Arch Ophthalmol. 1999;117.

Walsh ES, Rousseau P and Hoshizaki TB. The influence of impact location and angle on the dynamic impact response of a hybrid iii headform. Sports Engineering. 2011;13:135-143.

Weaver AA, Kennedy EA, Duma SM, Stitzel JD. Evaluation of different projectiles in matched experimental eye impact simulations. J Biomech Eng. 2011a ;133:031002.

Weaver AA, Loftis KL, Duma SM, Stitzel JD. Biomechanical modeling of eye trauma for different orbit anthropometries. Journal of biomechanics. 2011b;44:1296-1303.

Wong RH, Wong AK and Bailes JE. Frequency, magnitude, and distribution of head impacts in pop warner football: The cumulative burden. Clinical Neurology and Neurosurgery. 2014;118:1-4.

Wu LC, Nangia V, Bui K, et al. In vivo evaluation of wearable head impact sensors. Annals of biomedical engineering. 2015;1-12.

Yoganandan N, Fintar F, Sances A, Myklebust J, Schmaltz D. Steering Wheel Induced Facial Trauma, Proceedings of the 32nd Stapp Car Crash Conference. 1988;32:45-69. SAE Paper Number 881712.

APPENDIX - PUBLISHED FEM PAPERS FOUSED ON EVAULATING THE RESPONSE OF THE CERVICAL SPINE DURING AUTOMOBILE COLLISIONS AND ROTARY-WING AIRCRAFT IMPACTS

Basic Science

Effects of cervical arthrodesis and arthroplasty on neck response during a simulated frontal automobile collision

Nicholas A. White, PhD[a], Daniel P. Moreno, MS[a], Philip J. Brown, MS[a], F. Scott Gayzik, PhD[a], Wesley Hsu, MD[b], Alexander K. Powers, MD[b], Joel D. Stitzel, PhD[a],*

[a]Center for Injury Biomechanics, Virginia Tech-Wake Forest University, 575 N. Patterson Ave., Suite 120, Winston-Salem, NC 27157, USA
[b]Department of Neurosurgery, Wake Forest University School of Medicine, Medical Center Blvd., Winston-Salem, NC 27157, USA

Abstract

BACKGROUND CONTEXT: Whereas arthrodesis is the most common surgical intervention for the treatment of symptomatic cervical degenerative disc disease, arthroplasty has become increasingly more popular over the past decade. Although literature exists comparing the effects of anterior cervical discectomy and fusion and cervical total disc replacement (CTDR) on neck kinematics and loading, the vast majority of these studies apply only quasi-static, noninjurious loading conditions to a segment of the cervical spine.

PURPOSE: The objective of this study was to investigate the effects of arthrodesis and arthroplasty on biomechanical neck response during a simulated frontal automobile collision with air bag deployment.

STUDY DESIGN: This study used a full-body, 50th percentile seated male finite element (FE) model to evaluate neck response during a dynamic impact event. The cervical spine was modified to simulate either an arthrodesis or arthroplasty procedure at C5–C6.

METHODS: Five simulations of a belted driver, subjected to a 13.3 m/s ΔV frontal impact with air bag deployment, were run in LS-DYNA with the Global Human Body Models Consortium full-body FE model. The first simulation used the original model, with no modifications to the neck, whereas the remaining four were modified to represent either interbody arthrodesis or arthroplasty of C5–C6. Cross-sectional forces and moments at the C5 and C6 cervical levels of the neck, along with interbody and facet forces between C5 and C6, were reported.

RESULTS: Adjacent-level, cross-sectional neck loading was maintained in all simulations without exceeding any established injury thresholds. Interbody compression was greatest for the CTDRs, and interbody tension occurred only in the fused and nonmodified spines. Some interbody separation occurred between the superior and inferior components of the CTDRs during flexion-induced tension of the cervical spine, increasing the facet loads.

CONCLUSIONS: This study evaluated the effects of C5–C6 cervical arthrodesis and arthroplasty on neck response during a simulated frontal automobile impact. Although cervical arthrodesis and arthroplasty at C5–C6 did not appear to significantly alter the adjacent-level, cross-sectional neck responses during a simulated frontal automobile impact, key differences were noted in the interbody and facet loading.   © 2014 Elsevier Inc. All rights reserved.

Keywords: Arthrodesis; Arthroplasty; ProDisc-c; Prestige ST; Finite element analysis; GHBMC

Introduction

The use of finite element (FE) methods for orthopedic applications, particularly those involving the cervical spine, began over 20 years ago with a simple two-dimensional model used to study postlaminectomy deformities [1]. The first FE study of an anterior cervical spine fusion was conducted by Kumaresan et al. [2] to evaluate the effects of fusion materials and surgical procedure on the biomechanical response of a C4–C6 spine model. Since this publication, close to two-dozen additional FE studies have been conducted, evaluating the effects of both anterior cervical discectomy and fusion (ACDF) and cervical total disc replacement (CTDR) on the biomechanics of the cervical spine [3–25]. Typically, the implant was modeled between either C4–C5 or C5–C6, and the simulations were run as quasi-static events using an implicit FE solver (Table 1). The present study uses a state-of-the-art full-body FE model to evaluate dynamic neck kinematics and loading, with simulated arthrodesis and arthroplasty at the C5–C6 level, during a frontal automobile collision.

Materials and methods

General model overview

The Global Human Body Models Consortium (GHBMC) 50th percentile seated male FE model (version 3.5) was used to study the cervical spine response because of a simulated arthrodesis and arthroplasty [26,27]. The biofidelity of the neck (Fig. 1) has been rigorously validated both at individual cervical segment levels and for the full cervical spine [28–31]. Additionally, whole body validation

has been conducted for a number a different impact scenarios [32–35]. Neck muscle activation, based on the experimental volunteer studies, was included in the current simulations [36]. The flexor and extensor muscles were activated 74 ms after impact and remained active for 100 ms.

Cervical spine modifications for ACDF and CTDR

To mimic actual surgical technique for both these procedures, the intervertebral disc (IVD), end plates, and anterior longitudinal ligaments (ALL) associated with this level of the cervical spine were removed from the model. Vertebral body (VB) geometric modifications consistent with these surgeries were accomplished through a combination of select element deletion and advanced morphing techniques using HyperMesh version 11.0 (Altair Engineering, Troy, MI, USA). The geometries of both CTDRs used in this study were reverse engineered from the corresponding physical implants. The ACDF and CTDRs were secured to the VBs using tied nodes to surface offset contacts. Material properties for the IVDs, ACDF, and CTDRs are reported in Table 2 [24,37–42].

Arthrodesis at the C5–C6 cervical level was modeled using two different methods, one involving constrained nodal rigid bodies (CNRBs) and the other a cage, core, and anterior plate (ACDF). The CNRB fusion rigidly constrained more than 100 individual node sets from the inferior VB surface of C5 to the superior VB surface of C6. The geometries of VB surfaces were not modified, and no additional contacts were required because a physical implant was not modeled. The ACDF was modeled as a 14×15×6 mm solid organic polymer polyether ether ketone cage, 1 mm thick, and a solid trabecular bone core (Fig. 2, Top Left). The C5 and C6 VBs were modified to create surfaces parallel to

Table 1
Literature review of FE simulations involving cervical arthrodesis and arthroplasty

Reference	Implant	Implant location	Model	FE code
Kumaresan et al. [2]	Fusion	C4–C5	C4–C6	NASTRAN
Maiman et al. [3]	Fusion	C4–C5, C5–C6	C4–C6	NASTRAN
Natarajan et al. [4]	Fusion	C5–C6	C5–C6	ADINA
Galbusera et al. [5]	Bryan	C5–C6	C5–C6	ABAQUS
Ha [6]	Elastomer Disc, Fusion	C4–C5	C3–C6	ANSYS
Lopez-Espina et al. [7]	Fusion	C3–C4, C4–C5, C5–C6, C6–C7	C3–C7	ANSYS
		C3–C5, C4–C6, C5–C7		
Dang et al. [8]	Fusion	C2–C3, C3–C4, C4–C5, C5–C6, C6–C7	THUMS	LS-DYNA
		C2–C4, C3–C5, C4–C6, C5–C7		
Galbusera et al. [9]	Bryan	C5–C6	C4–C7	ANSYS
Rousseau et al. [10]	Ball and Socket	C5–C6	C5–C6	ANSYS
Faizan et al. [11]	Ball and Socket	C5–C6	C3–C7	ABAQUS
Lin et al. [12]	Bryan, Prestige LP, ProDisc-C	C5–C6	C5–C6	Voxelcon
Womack [13]	ProDisc-C	C4–C5	C3–C7	ABAQUS
Crawford et al. [14]	Prestige ST, ProDisc-C, Synergy	C5–C6	C3–C7	ABAQUS
Galbusera et al. [15]	Spherical Joint	C5–C6	C5–C6	ANSYS
Kang et al. [16]	Bryan, Prestige LP, ProDisc-C	C5–C6	C5–C6	Voxelcon
Kulkarni [17]	Prestige ST, ProDisc-C, Synergy	C5–C6	C3–C7	ABAQUS
Li and Lewis [18]	Fusion, Nucleus	C5–C6	C1–C7	ABAQUS
Bhattacharya [19]	Prestige ST, ProDisc-C	C5–C6	C5–C6	ABAQUS
Bhattacharya et al. [20]	ProDisc-C	C5–C6	C5–C6	ABAQUS
Faizan et al. [21]	Discover, Fusion	C4–C5, C5–C6	C3–C7	ABAQUS
Fernandes et al. [22]	Fusion	C5–C6	C5–C6	ABAQUS
Lee et al. [23]	ProDisc-C, Mobi-C	C5–C6	C2–C7	ABAQUS
Womack et al. [24]	ProDisc-C	C4–C5	C3–C7	ABAQUS
Zhao et al. [25]	ProDisc-C, Fusion	C4–C5, C5–C6, C4–C6	C3–C7	ABAQUS

FE, finite element; THUMS, Toyota Human Model for Safety.

and coincident with the implant. Titanium shell elements were used to model a simplified anterior plate by again connecting the anterior-inferior VB surface of C5 to the anterior-superior VB surface of C6.

Arthroplasty at the C5–C6 cervical level was modeled with the Prestige ST and ProDisc-C CTDRs. The Prestige ST is a two-piece, ball-and-trough design with one point of articulation. This stainless steel, metal-on-metal implant is capable of rotation in all three axes and translation in the anterior-posterior (AP) direction, allowing for a mobile, instantaneous center of rotation. The nominally 16-mm-deep, 7-mm-high CTDR was modeled with rigid shells, with the ball positioned at the center of the trough (Fig. 2, Top Right). The C5 and C6 VBs were modified to create surfaces parallel and coincident with the implant.

The ProDisc-C is a three-piece, ball-and-socket design with one point of articulation. The end plates are constructed of cobalt-chromium-molybdenum and the polymer insert of ultra–high-molecular weight polyethylene, creating a metal-on-polymer articulation. This design encourages three-axis rotation, thus establishing a nearly fixed center of rotation. The CTDR is a press fit between adjoining vertebrae, with central keels nested into the VBs. The nominal dimensions of this implant were $14 \times 15 \times 6$ mm (Fig. 2, Bottom). The end plates were modeled with rigid shells and the semispherical inlay with deformable tetrahedrons. The C5 and C6 VBs were modified to create surfaces parallel and coincident with the implant and channels matching the geometry of the central keels.

Simulation

Five simulations of a belted driver, subjected to a 13.3 m/s ΔV frontal impact with air bag deployment, were run with the GHBMC model in LS-DYNA R4.2.1 (LSTC, Livermore, CA, USA) (Fig. 3) [43]. The first simulation used the original model, with no modifications to the neck. The remaining four simulations included a CNRB fusion, ACDF, Prestige ST implant, or ProDisc-C implant at the C5–C6 cervical level. A series of cross-sections were included to capture the forces and moments at each cervical level of the neck in their respective local coordinate systems (LCSYS) using a methodology previously described by White et al. [44]. Cross-sections were also used to capture forces transmitted though the C5–C6 IVD of the non-modified neck, the cage, core, and plate of the ACDF neck, and the C5–C6 facets for all neck models.

Data analysis

The simulation results were postprocessed using Oasys T/HIS 10.2-64 bit (Arup, London, UK). Cross-sectional forces were filtered at CFC (Channel Frequency Class) 1,000 and moments at CFC 600 [45]. The outputs from the nodal force groups were filtered at CFC 1,000 and the nodal displacements used to calculate VB rotation at CFC 60. The filtered data were then processed using in-house code written in Matlab version 7.12.0 (R2011a; Math-Works, Natick, MA, USA). A quantitative validation
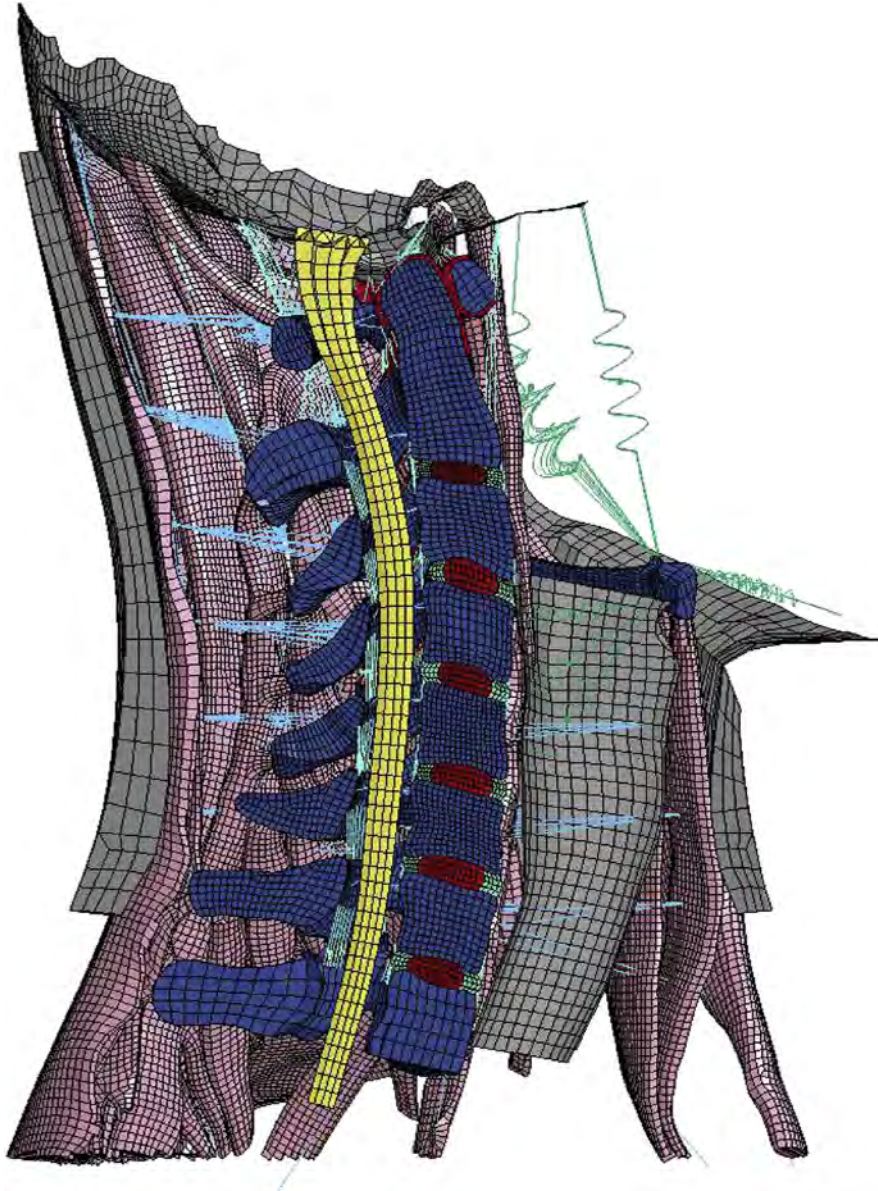
Fig. 1. Midsagittal cross-section of the Global Human Body Models Consortium neck including the C1–T1 vertebrae, intervertebral discs, ligaments, musculature, and soft tissue.

method developed by Sprague and Geers [46] was used to compare time history plots. This method computes the magnitude (M) and phase (P) contributions to the total error

(difference between the benchmark and experimental curves) and combines these metrics into a single comprehensive (C) metric [47,48]. For example, a magnitude error

Table 2
Material and model properties for the FE models of the ACDF, Prestige ST, and ProDisc-C

Implant	Part	Material	ASTM standard	Material model	Element type	Density (kg/mm³)	Elastic modulus (GPa)	Poisson ratio	Reference
ACDF	Cage	PEEK	F2026-02	Elastic	Solid Hex	1.30×10^{-6}	3.6	0.4	[40,41]
	Core	Trabecular bone	N/A	Plastic-Kinematic	Solid Hex	1.10×10^{-6}	0.4	0.3	[27]
	Plate	Ti-6Al-4V	F136	Elastic	Shell	4.43×10^{-6}	116.0	0.3	[38,41]
Prestige ST	End plates	316L SST	F138	Rigid	Shell	8.00×10^{-6}	190.0	0.3	[39,41]
ProDisc-C	End plates	CoCrMo	F75	Rigid	Shell	8.30×10^{-6}	210.0	0.3	[37,42]
	Insert	UHMWPE	F648	Elastic	Solid Tet	9.36×10^{-7}	1.3	0.3	[24,37,41]

ACDF, anterior cervical discectomy and fusion; ASTM, American Society for Testing and Materials; CoCrMo, cobalt-chromium-molybdenum; FE, finite element; N/A, not available; PEEK, polyether ether ketone; UHMWPE, ultra–high-molecular weight polyethylene.
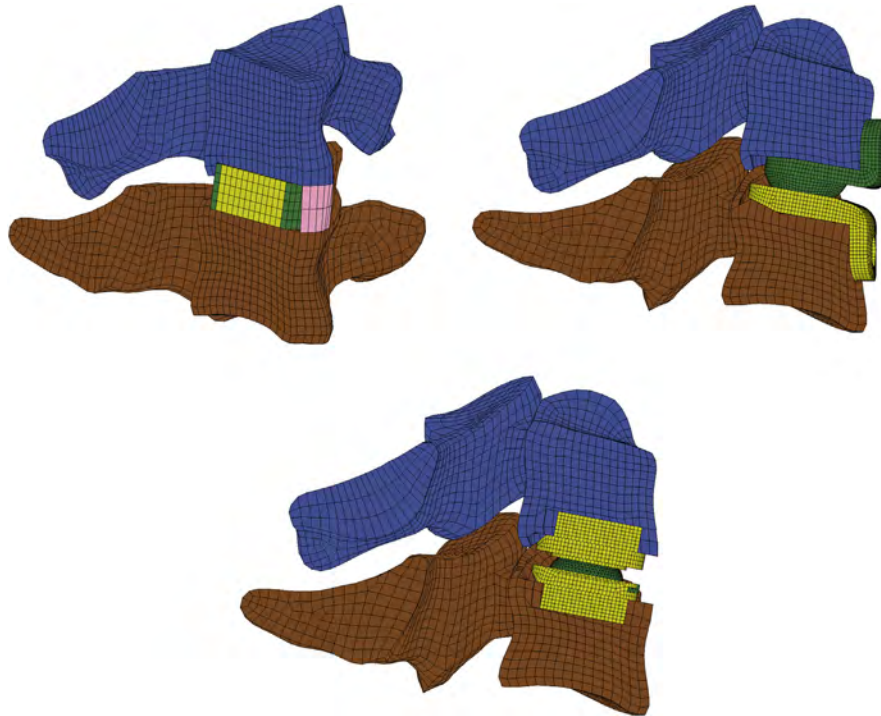
Fig. 2. Midsagittal cross-section of the C5 and C6 vertebrae with an (Top Left) anterior cervical discectomy and fusion (ACDF), (Top Right) Prestige ST cervical total disc replacement (CTDR), and (Bottom) ProDisc-C CTDR. The cross-section extends through the ACDF showing the cage, core, and plate, whereas CTDRs were left intact for better visualization.

of 10% would indicate that the magnitude of the experimental curve is 10% greater than the magnitude of the benchmark curve. A phase error of 50% would indicate that the experimental curve was 50% (90°) out of phase with the benchmark curve. The comprehensive error is the square root of the sum of the squares of the magnitude and phase errors.

Results

Overview

The simulation time histories are separated into two categories, fusion (CNRB/ACDF) and CTDR (Prestige ST/ProDisc-C), with the nonmodified (IVD) simulation
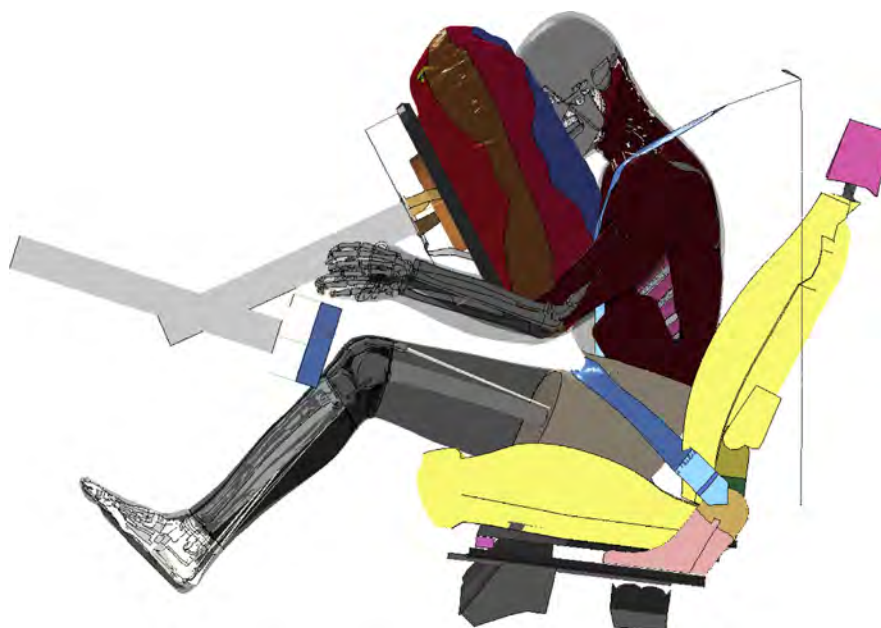
Fig. 3. Belted driver subjected to a frontal impact with 13.3 m/s ΔV and air bag deployment [43].

results reported in both categories as a baseline. Positive polarities for the different loading modes reported in these time histories are illustrated in Fig. 4 [45]. Each time history plot includes vertical lines indicating the approximate time of maximum shoulder belt loading (70 ms) and maximum contact force between the air bag and the occupant (85 ms) (Fig. 5). Each time history plot also includes two vertical dotted lines indicating the window of time (t=119–124 ms) where the maximum C5 and C6 cross-sectional bending moments occurred for all simulations.

Midsagittal rotations of C5 and C6 about their respective center of gravity are reported in Fig. 6 with peak rotations reported in Table 3. Interbody loading with respect to the C6 LCSYS is reported in Fig. 7. The sum of the right and left facet forces, referred to as the total facet force, is reported with respect to C6 in Fig. 8. Peak interbody and total facet forces are reported in Table 4. Adjacent-level, cross-sectional AP shear and axial forces and flexion/extension moments about VB CGs are reported at the C5 and C6 cervical levels in their respective LCSYS (Figs. 9–11) with peak loading reported in Table 3. Pertinent results are described in a time line fashion, broken into three distinct phases based on the maximum occupant/restraint contact times: Phase 1 from 0 to 70 ms, Phase 2 from 70 to 85 ms, and Phase 3 from 85 to 150 ms. Phase 1 begins at the onset of sled acceleration, continuing up to the approximate time of maximum shoulder belt loading. At this point in time, Phase 2 begins and continues up to the time of maximum contact force between the air bag and the occupant. Phase 3 represents the remainder of the simulation time.

Phase 1 (0–70 ms)

Midsagittal rotations of both C5 and C6 VBs begin early in this phase and are almost identical for all simulations (Fig. 6). An exception to this observation occurs between 50 and 70 ms where the C5 VB rotations from the CTDR simulations are slightly lower than the other VB rotations.

Anterior-posterior shear and axial interbody loading (Fig. 7) is negligible for the CTDRs in this phase. Negative AP shear interbody loading in the IVD and ACDF begins at approximately 55 ms, becoming more noticeable just before the end of the phase. Interbody tension in both the IVD and ACDF begins at approximately 50 ms, reaching global peaks of 325.8 and 517.3 N, respectively.

Total AP shear facet loading (Fig. 8) is negligible for the CTDRs in this phase. Total positive AP shear facet loading in the IVD and ACDF begins at approximately at 55 ms, reaching global peaks of 12.1 and 5.2 N, respectively. Peak total facet global tension is achieved for all simulations toward the end of the phase. The CTDR total facet tension traces are almost identical, reaching a peak value of 159.5 N for the Prestige ST and 158.4 N for the ProDisc-C. Peak total facet tension for the IVD and ACDF are 79.4 and 33.0 N, respectively.

Cross-sectional negative AP shear (Fig. 9) begins at approximately 55 ms for all simulations. Cross-sectional tension (Fig. 10) is produced for all simulations with global peaks reached at the end of the phase. Peak tension ranged between 1,052.6 and 1,059.1 N at the C5 VB level and between 1,121.2 and 1,127.5 N at the C6 VB level. A cross-sectional flexion-bending moment (Fig. 11) is experienced at both levels in all simulations, with a noticeable increase at approximately 50 ms.
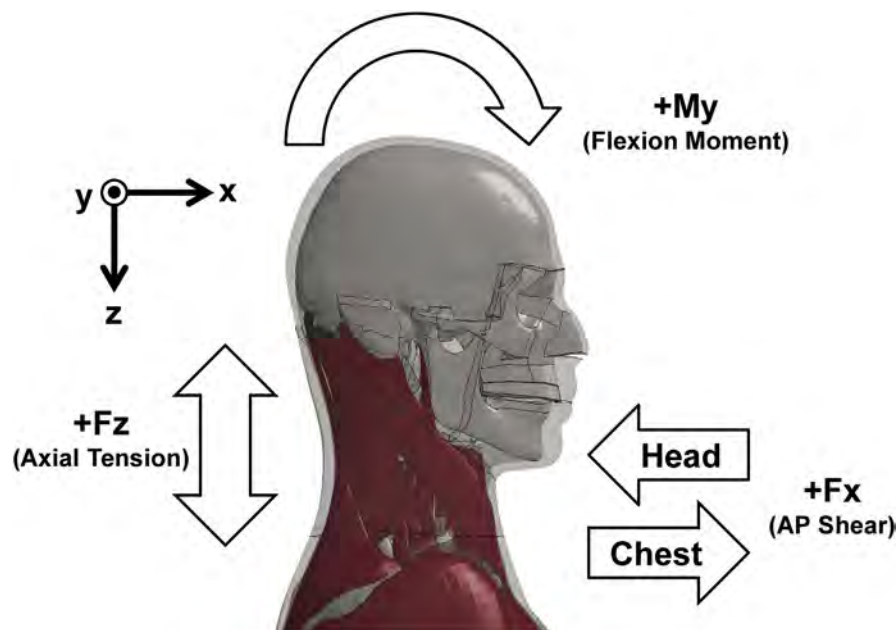
Fig. 4. Relative head and chest motion corresponding to SAEJ211 standards for positive neck anterior-posterior (AP) shear force, axial force, and bending moment [45].
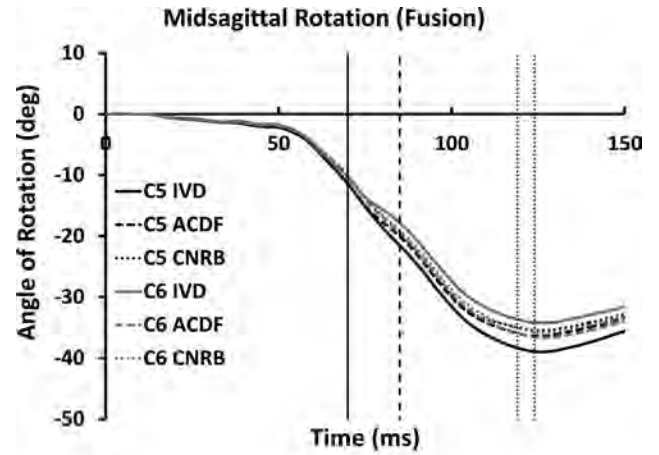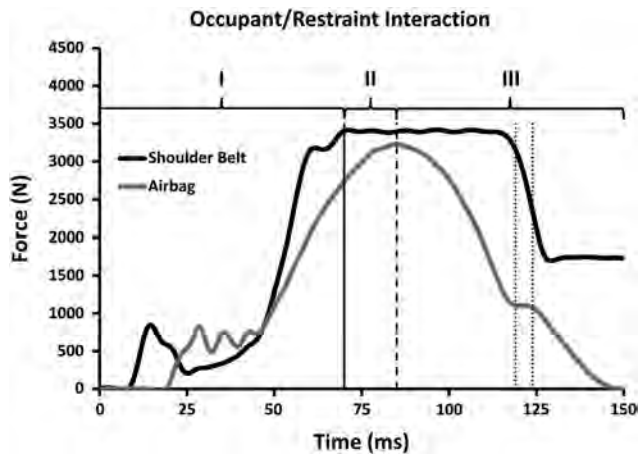
Fig. 5. Representative time histories of the shoulder belt loading and contact force between the air bag and occupant.

Phase 2 (70–85 ms)

During this phase, the C5 and C6 rotations of the IVD VBs begin to differentiate, with C6 rotating less than C5 (Fig. 6). The relative difference in rotations between C5 and C6 in both fusion simulations remains negligible, with the traces running midway between the IVD C5 and C6 traces. The C5 rotations of the CTDRs surpass the C6 rotations during this phase.

Approximately halfway through this phase, the CTDRs begin to experience interbody negative AP shear loading and compression (Fig. 7). Interbody tension decreases to approximately zero for both the IVD and ACDF by the end of this phase. The combined AP shear facet loading for the IVD changes polarity during this phase, whereas the ACDF loading approaches zero (Fig. 8). The global peak negative total AP shear facet loads for the CTDRs are achieved during this phase: −49.6 N for the Prestige ST and −39.1 N for the ProDisc-C. Whereas the total facet axial loading is decreasing during this phase for all simulations, tension is maintained. The same is true for the adjacent-level, cross-sectional axial loading (Figs. 9–11).

Phase 3 (85–150 ms)

Peak rotations of C5 and C6 occur between 121 and 128 ms for all simulations (Fig. 6). For the IVD, rotation of C5 is always greater than C6, with a maximum relative difference of 4.8° between to the two VBs. As would be expected, C5 and C6 rotations are almost identical for the fusions. The fusion traces run midway between the IVD C5 and C6 rotations. The CTDR traces follow the IVD traces much closer. The maximum relative difference in rotation between C5 and C6 is 2.4° for the Prestige ST and 4.6° for the ProDisc-C.

Peak negative AP shear interbody loading occurs between 118 and 128 ms and peak compressive interbody loading between 130 and 132 ms for all simulations (Fig. 7). Peak
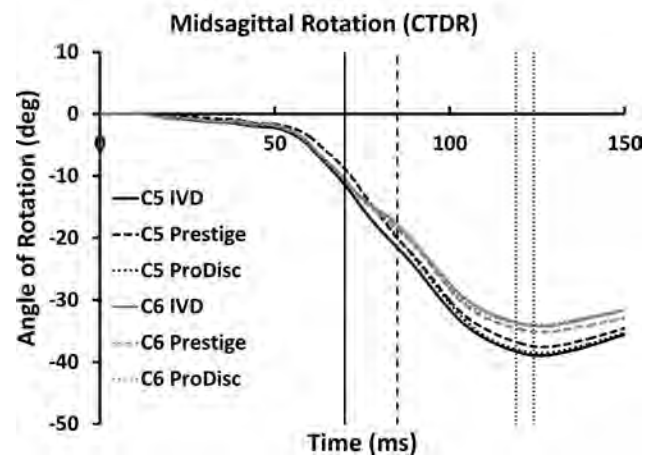
Fig. 6. Midsagittal rotation of C5 and C6 about their center of gravity for the (Top) fusion and (Bottom) cervical total disc replacement simulations. ACDF, anterior cervical discectomy and fusion; CNRB, constrained nodal rigid body; CTDR, cervical total disc replacement; IVD, intervertebral disc.

negative AP shear ranged from −405.4 N for the IVD to −527.7 N for the ACDF, whereas peak compression ranged from −1,091.7 N for the ACDF to −1,351.9 N for the ProDisc-C.

The peak adjacent-level, cross-sectional negative AP shear force occurs between 118 and 124 ms for all simulations (Fig. 9). The peak flexion moment occurs between 119 and 124 ms (Fig. 11). The larger negative AP shear force occurs at the C5 level, ranging from −365.6 N for the IVD to −415.5 N for the CNRB. The greatest flexion moment occurs at the C6 level, ranging from 64.6 Nm for the IVD to 65.7 Nm for the CNRB.

During the 5-second window where the maximum cross-sectional C5 and C6 bending moments occurs (t=119–124 ms), shoulder belt loading sharply decreases, whereas occupant to air bag contact force plateaus (Fig. 5). The majority of the peak adjacent-level, cross-sectional negative AP shear forces occur within this window (Fig. 9). A point of inflection in the total AP shear facet loading occurs for all simulations immediately after this window (Fig. 8, Top).

Table 3
Peak adjacent-level, cross-sectional loading through the C5 and C6 VB level with respect to the corresponding local coordinate systems

Simulation	VB	±AP Shear (N)		Ten/comp (N)		Flex/ext (Nm)		Rot (°)
IVD	C5	5.7	−365.6	1,053.4	−2.1	63.4	−0.4	−39.0
	C6	28.6	−236.8	1,121.2	−4.8	64.6	−0.3	−34.2
ACDF	C5	8.5	−403.1	1,053.2	−2.4	62.6	−0.4	−36.4
	C6	35.3	−234.6	1,121.9	−4.2	65.0	−0.3	−36.6
CNRB	C5	13.5	−415.5	1,059.1	−2.2	62.8	−0.4	−35.5
	C6	37.9	−222.3	1,125.2	−3.9	65.7	−0.3	−35.8
Prestige ST	C5	8.7	−395.8	1,052.6	−3.1	62.8	−0.3	−37.6
	C6	31.2	−247.3	1,125.7	−6.9	64.9	−0.3	−35.2
ProDisc-C	C5	10.2	−397.0	1,058.3	−2.2	62.8	−0.3	−38.6
	C6	35.7	−268.7	1,127.5	−2.7	65.1	−0.3	−34.0

ACDF, anterior cervical discectomy and fusion; AP, anterior-posterior; CNRB, constrained nodal rigid body; flex/ext, flexion/extension; IVD, intervertebral disc; rot, rotation; ten/comp, tension/compression; VB, vertebral body.

Note: Maximum midsagittal rotation was taken about the VB center of gravity.

Quantitative comparison

Two separate quantitative comparisons of the adjacent-level, cross-sectional loading and VB rotational time histories were conducted using the method by Sprague and Geers [46]. The first analysis compares the ACDF (benchmark) to the CNRB (experiment) with the results reported in Table 5. The largest comprehensive errors occur at the C6 level with errors ranging from 4.53% for AP shear loading to 0.78% for moment loading. The magnitude was underestimated by the CNRBs for AP shear loading, axial loading, and midsagittal rotation. The second analysis compares the IVD (benchmark) to the fusions and CTDRs (experiments) with the results reported in Table 6. The largest errors for the adjacent-level, cross-sectional AP shear loading occur at the C5 level with 11.82% for the CNRB and 10.22% for the Prestige ST. In both cases, the magnitudes overestimate the IVD response. The largest errors for the adjacent-level, cross-sectional axial loading occur at the C5 level with 3.83% for the CNRB and 3.26% for the Prestige ST. The largest compressive error for flexion/extension moment is 2.24% for the CNRB and 1.54% for the Prestige ST, both occurring at the C6 level. In both cases, the magnitudes overestimate the IVD response.

Discussion

ACDF versus CNRBs

Implementation of CNRBs into the neck to simulate a fusion between adjacent VBs was a less time-consuming and computationally less expensive approach than modeling an ACDF. One of the major drawbacks of the CNRB method was that interbody shear and axial forces were not available for comparison with IVD results. For adjacent-level, cross-sectional loading, the comprehensive errors were less than
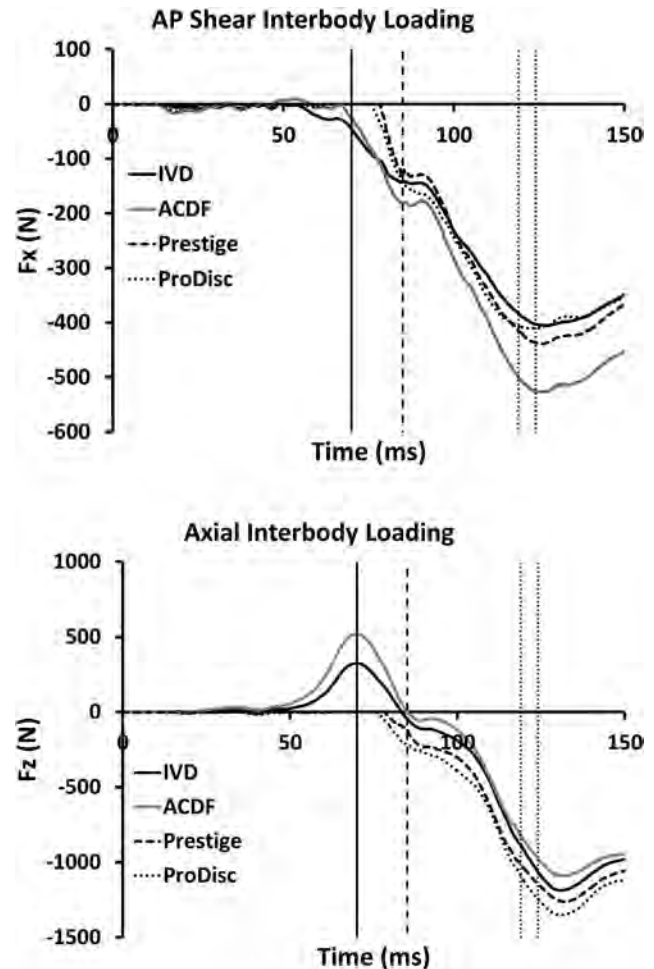
Fig. 7. Interbody (Top) anterior-posterior (AP) shear and (Bottom) axial force time histories between C5 and C6 reported in the C6 local coordinate systems. The forces for the intervertebral disc (IVD) and anterior cervical discectomy and fusion (ACDF) are reported from cross-sections and the constrained nodal rigid bodies from contact forces.

2% for the axial loading and 1% for the moment for both vertebral levels. Difference in bending moment was negligible for both VB levels.

Prestige ST versus ProDisc-C

Rotation of both VB levels matched between CTDRs up to the time of maximum occupant/air bag interaction: the end of Phase 2. The simulation kinematics revealed that the Prestige ST reached its maximum AP translation at this time. The ProDisc-C allowed more rotation and some additional AP translation because of deformation of the semispherical inlay. The maximum relative rotational difference between C5 and C6 of the ProDisc-C was within 0.2° of the IVD rotation, closer than for the Prestige ST.

For adjacent-level, cross-sectional loading, the peak negative AP shear forces for both CTDRs were almost identical at the C5 level and 8.0% greater for the ProDisc-C at the C6 level. Peak negative AP interbody shear force was 6.8% greater for the Prestige ST than for the ProDisc-C. At the
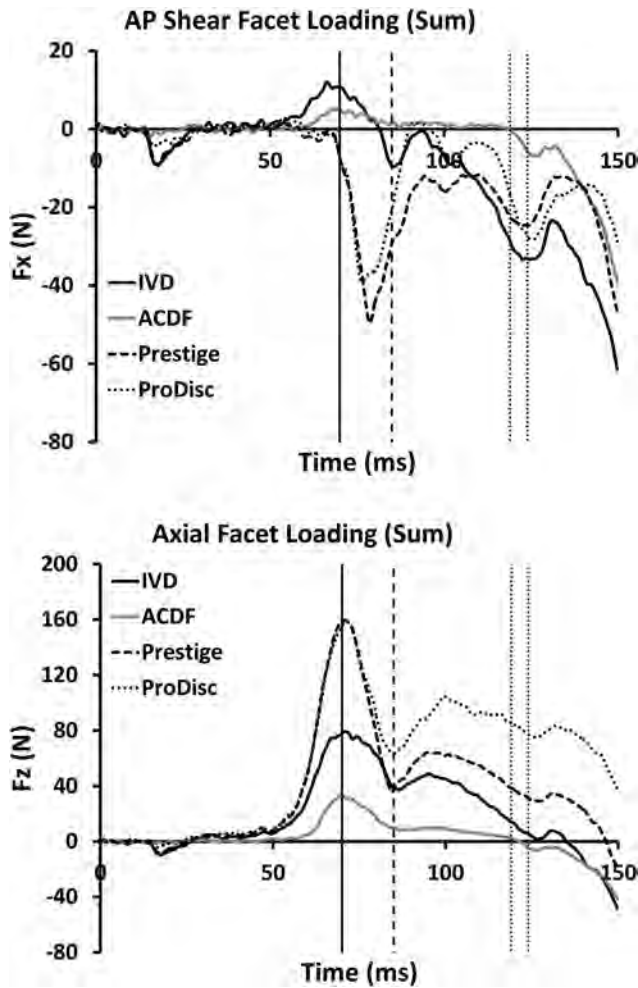
Fig. 8. Facet (Top) anterior-posterior (AP) shear and (Bottom) axial force time histories between C5 and C6 reported in the C6 local coordinate systems. The reported forces are the sum of both the left and right facet forces. ACDF, anterior cervical discectomy and fusion; IVD, intervertebral disc.
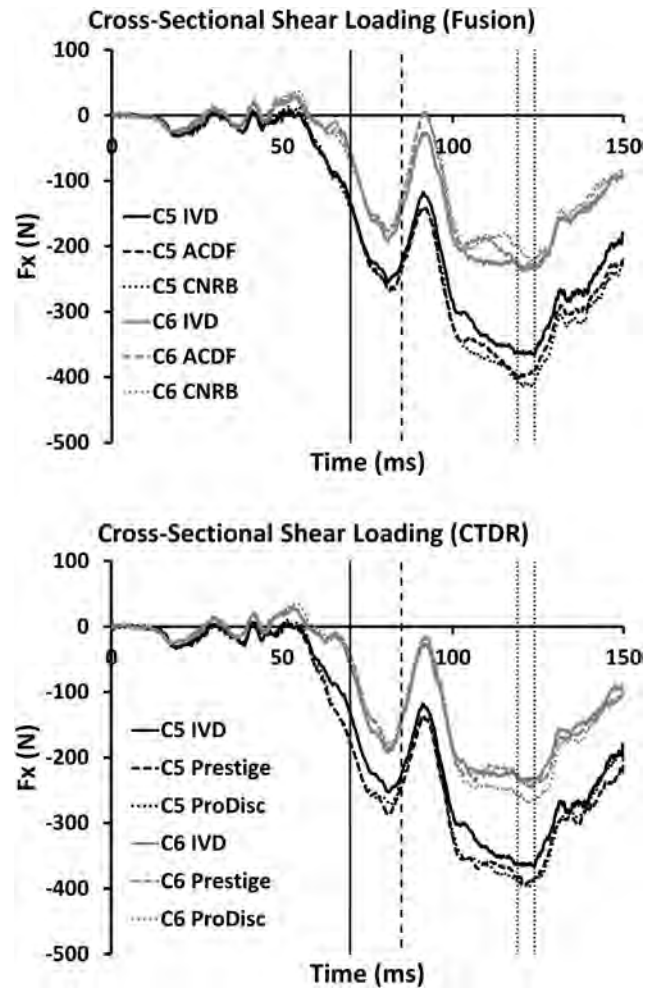
Fig. 9. Adjacent-level, cross-sectional anterior-posterior (AP) shear force time histories for the (Top) fusion and (Bottom) cervical total disc replacement (CTDR) simulations. The forces are reported in their respective vertebral body local coordinate systems. ACDF, anterior cervical discectomy and fusion; CNRB, constrained nodal rigid body; IVD, intervertebral disc.

time of peak negative AP shear, the simulation kinematics reveal the superior socket of the ProDisc-C catching on the semisphere inlay, deforming it slightly. The nondeformable Prestige ST reached its maximum AP translation much earlier and was purely rotating at this point in time.

The peak adjacent-level, cross-sectional tensile force was almost identical between CTDRs and IVD for both VB

levels. As neither of the CTDRs was capable of supporting interbody tension, the axial interbody forces remained negligible until compression occurred. During this period, a physical separation between the inferior and superior CTDR components was visualized in the simulation. Interbody compression followed a similar trend for both CTDRs with

Table 4
Peak interbody and peak total facet AP shear and axial loading between C5 and C6 with respect to the C6 local coordinate systems

Simulation	Peak interbody load (N)				Peak facet total load (N)			
	±AP shear		Ten/comp		± AP shear		Ten/comp	
IVD	0.5	−405.4	325.8	−1,187.0	12.1	−61.5	79.4	−48.3
ACDF	9.6	−527.4	517.3	−1,091.7	5.2	−39.3	33.0	−41.4
Prestige ST	0.4	−439.0	0.6	−1,263.3	1.6	−49.6	159.5	−19.5
ProDisc-C	0.1	−411.0	0.0	−1,351.9	2.9	−39.1	158.4	−4.3

ACDF, anterior cervical discectomy and fusion; AP, anterior-posterior; flex/ext, flexion/extension; IVD, intervertebral disc; ten/comp, tension/compression.

Note: Cross-sections were used to capture the interbody loading for the IVD and ACDF and contact forces for the cervical total disc replacements. Cross-sections were used to capture the left and right superior C6 facet cartilage and ligaments and then summed for the total loading.
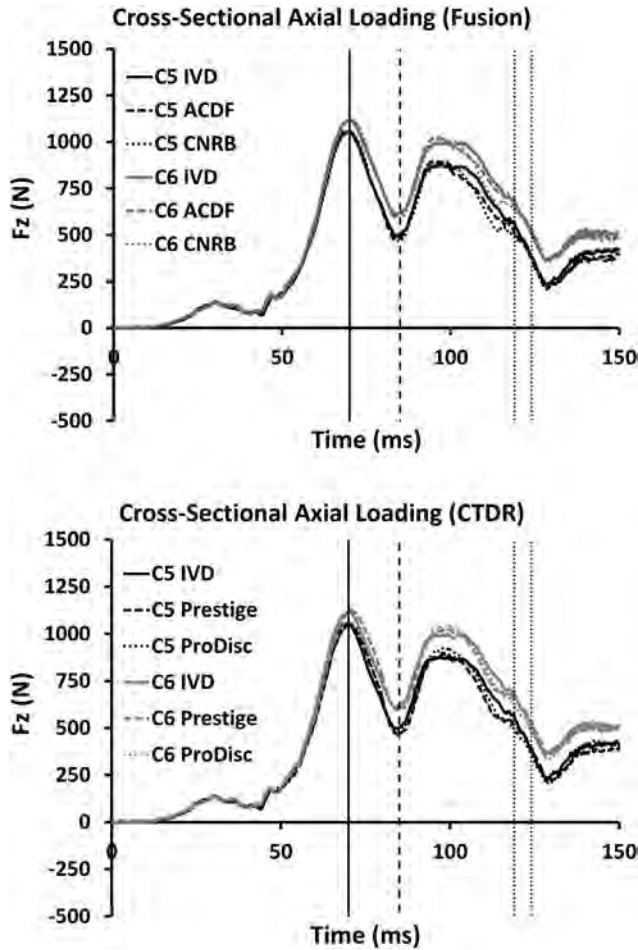
Fig. 10. Adjacent-level, cross-sectional axial force time histories for the (Top) fusion and (Bottom) cervical total disc replacement (CTDR) simulations. The forces are reported in their respective vertebral body local coordinate systems. ACDF, anterior cervical discectomy and fusion; CNRB, constrained nodal rigid body; IVD, intervertebral disc.

Fig. 11. Adjacent-level, cross-sectional bending moment time histories for the (Top) fusion and (Bottom) cervical total disc replacement (CTDR) simulations. The moments are taken about the vertebral body (VB) center of gravity and are reported in their respective VB local coordinate systems. ACDF, anterior cervical discectomy and fusion; CNRB, constrained nodal rigid body; IVD, intervertebral disc; ext, extension; flex, flexion.

a peak compression force 7.0% greater for the ProDisc-C than for the Prestige ST.

For adjacent-level, cross-sectional loading, the peak bending moment was almost identical between CTDRs and IVD for both VB levels. The comprehensive errors were all less than 2%, indicating minimal difference in bending moment between the modified and nonmodified cervical spines.

Fusion versus CTDRs

Biomechanical injury assessment reference values (IARVs) for the upper and lower neck of the 50th percentile male occupant have been previously defined [49]. Peak loading below these thresholds minimizes the risk of neck injury. The peak adjacent-level, cross-sectional loading at C5 and C6 were well below these IARVs for all simulations. As would be expected, the CTDRs maintained mid-sagittal rotation of the C5 and C6 VBs closer to the IVD than the fusions. Rotation was best preserved by the ProDisc-C in terms of peak rotation, peak relative rotation,

and comprehensive error. The largest comprehensive error was less than 12% for all adjacent-level, cross-sectional loading time histories with the majority less than 5%. This indicates that the overall neck loading time histories adjacent to a simulated arthrodesis or arthroplasty were not greatly altered. There was negligible difference between simulations for peak bending moment and peak tension. The largest comprehensive errors for all simulations occurred for AP shear loading. Both fusions created a stiff interface between adjacent VBs, thereby altering the shear loading. When the translation of the superior ball of the Prestige ST reached the anterior end of the trough, only rotation could occur, increasing the shear force at the C5 and C6 VB levels. The ProDisc-C did not allow for translation, other than that because of minor deformation of the semispherical inlay that increased the shear force at adjacent VB levels.

The largest interbody AP shear force occurred in the ACDF, followed by the Prestige ST, ProDisc-C, and then IVD. The cage, core, and anterior plate of the ACDF

Table 5
Quantitative comparison analysis of the two fusion simulations

Loading	C5			C6		
	M	P	C	M	P	C
AP Shear	2.70	0.94	2.86	−4.06	2.02	4.53
Axial	−1.13	1.09	1.57	−1.30	0.99	1.64
Moment	0.19	0.50	0.53	0.63	0.47	0.78
Rotation	−1.82	0.24	1.83	−2.28	0.08	2.28

AP, anterior-posterior.

Note: Magnitude (M), phase (P), and comprehensive (C) Sprague and Geers error factors [46] are expressed as a percentage for the cross-sectional loading and vertebral body rotation time histories. The corresponding anterior cervical discectomy and fusion curve was defined as the benchmark data and the constrained nodal rigid body curve as the experimental data.

prevented relative AP displacement between C5 and C6, therefore creating the greatest shear forces. The Prestige ST allowed for some AP translation; however, once maximum translation was reached, shear force increased. The Prestige ST shear force remained lower than the ACDF.

Although the ProDisc-C is not designed to allow AP translation, the increased VB rotation and some deformation of the semispherical inlay created a shear force larger than the IVD but less than the ACDF and Prestige ST. The increase in adjacent-level translation in both CTDRs increased the combined AP shear facet loading. Interbody tension occurred only in ACDF and IVD. Without a firm connection between the inferior C5 and superior C6 VB surfaces, interbody tension was not supported through the CTDRs, allowing for a period of VB separation during the simulations. This separation almost doubled the amount of tension measured in the facets versus the tension measured in the IVD simulation. Lee and Winkelstein [50] reported the response of the human cervical facet capsular ligament during failure from quasi-static retraction of one joint. Average gross failure was reported at 61.81±26.40 N, partial failure at 45.81±22.99 N, and ligament yielding at 30.65±25.54 N. The reported facet tension for the present study was the summation of the left and right joints. If the axial total facet loading is equally distributed

between both the left and right facets in the present study, the peak tensile values for the CTDR simulations potentially fall within an injurious range.

The ACDF experienced the least amount of interbody compression, even less than the IVD. However, it is important to note that the peak shear and tension occurred at approximately the same time for the IVD and ACDF. The difference in the resultant force between the IVD and ACDF interbody forces is much less than the difference in individual force components, indicating similar loading through the interbody space. The difference in relative rotations between the VBs in these two simulations most likely accounts for the mismatch in peak shear and compression. Both CTDRs produced greater interbody axial compression than the IVD and ACDF, potentially because of the change in center of rotation and combined facet loading.

Comparison with quasi-static experiments

Although the vast majority of cervical arthrodesis and arthroplasty experimental studies are quasi-static, they give insight into the change in kinematics and loading from these procedures. Attention is given to flexion as it was the primary bending mode in the present study. Biomechanical studies conducted by DiAngelo et al. [51,52] investigated the change in motion patterns of C2–T1 cadaveric cervical spines after surgical implantation of an ACDF, Prestige ST, and ProDisc-C at C5–C6 using a displacement controlled method. The motion patterns at the operated and adjacent levels were not altered during physiological flexion for both CTDRs, unlike the ACDF in which motion was decreased. The motion preservation experimentally observed in the CTDR specimens corresponds well with observations from the present study. Chang et al. [53] conducted a series of tests on C3–T2 cadaveric cervical spines using a load-control, pure-moment method to investigate the effect on load transmission through the IVDs and facets after surgical implantation of an ACDF, Prestige ST, and ProDisc-C at C6–C7. The adjacent-level IVD pressure did not vary greatly between the intact spine and CTDRs; however, the pressure did increase for the ACDF in flexion at the

Table 6
Quantitative comparison analysis of the nonmodified and modified neck simulations

VB level	Simulation	AP Shear			Axial			Moment			Rotation		
		M	P	C	M	P	C	M	P	C	M	P	C
C5	ACDF	8.80	1.09	8.87	−2.28	1.23	2.59	0.34	0.49	0.59	−5.96	0.39	5.98
	CNRB	11.73	1.39	11.82	−3.38	1.80	3.83	0.53	0.65	0.84	−7.67	0.59	7.70
	Prestige ST	10.08	1.68	10.22	−2.80	1.67	3.26	1.13	0.62	1.29	−4.59	1.13	4.73
	ProDisc-C	8.78	1.64	8.93	−0.78	1.64	1.82	−1.13	0.85	1.41	−2.37	1.31	2.71
C6	ACDF	−5.77	2.66	6.35	−0.85	0.86	1.21	1.51	0.55	1.61	7.05	0.42	7.07
	CNRB	−9.59	3.21	10.12	−2.14	1.41	2.56	2.14	0.66	2.24	4.61	0.46	4.63
	Prestige ST	1.13	2.08	2.37	−1.06	1.41	1.77	1.47	0.46	1.54	3.11	0.16	3.12
	ProDisc-C	7.73	2.87	8.25	−0.36	1.45	1.49	−0.31	0.86	0.91	0.59	0.46	0.75

ACDF, anterior cervical discectomy and fusion; CNRB, constrained nodal rigid body; VB, vertebral body.

Note: Magnitude (M), phase (P), and comprehensive (C) error factors by Sprague and Geers [46] are expressed as a percentage for the cross-sectional loading and VB rotation time histories. The corresponding intervertebral disc curve was defined as the benchmark to which all others curves were compared.

proximal level. There was no significant change in facet loading noted in flexion. Cadaveric studies conducted by Jaumard et al. [54] and Bauman et al. [55] reported that a ProDisc-C arthroplasty did not significantly alter facet joint contact pressure during lateral, axial, or sagittal bending.

Although adjacent-level IVDs were not investigated in the present study, the cross-sectional axial loading gives insight into the change in adjacent-level loading. The peak tension adjacent to the implant site was almost identical for the IVD, fusions, and CTDRs, indicating that there would be little change in adjacent IVD pressure. It is important to note, however, that the reported cross-sectional forces include contributions from other load-bearing tissue structures besides the skeleton. A FE study by Womack et al. [24] used a C3–C7 lower cervical spine model to investigate alterations in kinematics and load transmission from a ProDisc-C modeled between C4–C5. Implant size was found to strongly affect the facet and interbody implant forces. The increase in CTDR interbody loading for the present study may be explained by this finding.

Conclusions

This study evaluated the effects of C5–C6 cervical arthrodesis and arthroplasty on neck response during a simulated frontal automobile impact. Cross-sectional loading above and below C5–C6 interbody space was maintained in all simulations without exceeding any IARVs. The midsagittal rotations of the C5 and C6 VBs were maintained well with the CTDRs. Interbody compression was greatest for the CTDR cases, possibly because of a change in center of rotation and its effects on facet loading. Interbody tension occurred only in the ACDF and IVD, as the superior and inferior components of the CTDRs were independent of one another. The design of the CTDRs allowed for some interbody separation to occur between the superior and inferior components during flexion-induced tension of the cervical spine subsequently increasing the total facet tension. According to the existing knowledge regarding the injury tolerance of the facet joints, this additional tension may increase the risk of injury to the facet capsule ligaments. Although cervical arthrodesis and arthroplasty at C5–C6 did not appear to significantly alter the adjacent-level, cross-sectional neck responses during a simulated frontal automobile impact, key differences were noted in the interbody and facet loading.

Acknowledgments

References

[1] Saito T, Yamamuro T, Shikata J, et al. Analysis and prevention of spinal column deformity following cervical laminectomy. I. Pathogenetic analysis of postlaminectomy deformities. Spine 1991;16: 494–502.

[2] Kumaresan S, Yoganandan N, Pintar FA. Finite element analysis of anterior cervical spine interbody fusion. Biomed Mater Eng 1997;7: 221–30.

[3] Maiman DJ, Kumaresan S, Yoganandan N, Pintar FA. Biomechanical effect of anterior cervical spine fusion on adjacent segments. Biomed Mater Eng 1999;9:27–38.

[4] Natarajan RN, Chen BH, An HS, Andersson GB. Anterior cervical fusion: a finite element model study on motion segment stability including the effect of osteoporosis. Spine 2000;25:955–61.

[5] Galbusera F, Fantigrossi A, Raimondi MT, et al. Biomechanics of the C5-C6 spinal unit before and after placement of a disc prosthesis. Biomech Model Mechanobiol 2006;5:253–61.

[6] Ha SK. Finite element modeling of multi-level cervical spinal segments (C3-C6) and biomechanical analysis of an elastomer-type prosthetic disc. Med Eng Phys 2006;28:534–41.

[7] Lopez-Espina CG, Amirouche F, Havalad V. Multilevel cervical fusion and its effect on disc degeneration and osteophyte formation. Spine 2006;31:972–8.

[8] Dang AB, Hu SS, Tay BK. Biomechanics of the anterior longitudinal ligament during 8 g whiplash simulation following single- and contiguous two-level fusion: a finite element study. Spine 2008;33:607–11.

[9] Galbusera F, Bellini CM, Raimondi MT, et al. Cervical spine biomechanics following implantation of a disc prosthesis. Med Eng Phys 2008;30:1127–33.

[10] Rousseau MA, Bonnet X, Skalli W. Influence of the geometry of a ball-and-socket intervertebral prosthesis at the cervical spine: a finite element study. Spine 2008;33:E10–4.

[11] Faizan A, Goel VK, Garfin SR, et al. Do design variations in the artificial disc influence cervical spine biomechanics? A finite element investigation. Eur Spine J 2012;21(5 Suppl):S653–62.

[12] Lin CY, Kang H, Rouleau JP, et al. Stress analysis of the interface between cervical vertebrae end plates and the Bryan, Prestige LP, and ProDisc-C cervical disc prostheses: an in vivo image-based finite element study. Spine 2009;34:1554–60.

[13] Womack WJ. Computational modeling of the lower cervical spine facet cartilage distribution and disc replacement. Fort Collins, CO: Colorado State University, 2009.

[14] Crawford NR, Arnett JD, Butters JA, et al. Biomechanics of a posture-controlling cervical artificial disc: mechanical, in vitro, and finite-element analysis. Neurosurg Focus 2010;28:E11.

[15] Galbusera F, Anasetti F, Bellini CM, et al. The influence of the axial, antero-posterior and lateral positions of the center of rotation of a ball-and-socket disc prosthesis on the cervical spine biomechanics. Clin Biomech (Bristol, Avon) 2010;25:397–401.

[16] Kang H, Park P, La Marca F, et al. Analysis of load sharing on uncovertebral and facet joints at the C5-6 level with implantation of the Bryan, Prestige LP, or ProDisc-C cervical disc prosthesis: an in vivo image-based finite element study. Neurosurg Focus 2010;28:E9.

[17] Kulkarni N. Effects of implant design parameters on cervical disc arthroplasty performance and sagittal balance—a finite element investigation. Toledo, OH: The University of Toledo, 2010.

[18] Li Y, Lewis G. Influence of surgical treatment for disc degeneration disease at C5-C6 on changes in some biomechanical parameters of the cervical spine. Med Eng Phys 2010;32:595–603.

[19] Bhattacharya S. Predictive finite element modeling of artificial cervical discs in a ligamentous functional spinal unit. Toledo, OH: The University of Toledo, 2011.

[20] Bhattacharya S, Goel VK, Liu X, et al. Models that incorporate spinal structures predict better wear performance of cervical artificial discs. Spine J 2011;11:766–76.

[21] Faizan A, Goel VK, Biyani A, et al. Adjacent level effects of bi level disc replacement, bi level fusion and disc replacement plus fusion in cervical spine—a finite element based study. Clin Biomech (Bristol, Avon) 2012;27:226–33.

[22] Fernandes PC, Fernandes PR, Folgado JO, Levy Melancia J. Biomechanical analysis of the anterior cervical fusion. Comput Methods Biomech Biomed Engin 2012;15:1337–46.

[23] Lee SH, Im YJ, Kim KT, et al. Comparison of cervical spine biomechanics after fixed- and mobile-core artificial disc replacement: a finite element analysis. Spine 2011;36:700–8.

[24] Womack W, Leahy PD, Patel VV, Puttlitz CM. Finite element modeling of kinematic and load transmission alterations due to cervical intervertebral disc replacement. Spine 2011;36:E1126–33.

[25] Zhao Y, Li Q, Mo Z, et al. Finite element analysis of cervical arthroplasty combined with fusion against 2-level fusion. J Spinal Disord Tech 2013;26:347–50.

[26] Gayzik FS. Completion of phase 1 development of the global human body consortium mid-sized male full body finite element model. SAE Government Industry Meeting: Society of Automotive Engineers; Warrendale, PA: 2012.

[27] Stitzel JD. Global human body models consortium (GHBMC) male 50th percentile (M50) occupant model manual. Virginia Tech-Wake Forest University Center for Injury Biomechanics, December 19, 2011. Report No.: GHBMC-FBM-Manual-01. Virginia Tech-Wake Forest University Center for Injury Biomechanics; Winston-Salem, NC.

[28] DeWit JA, Cronin DS. Cervical spine segment finite element model for traumatic injury prediction. J Mech Behav Biomed Mater 2012;10:138–50.

[29] Fice JB, Cronin DS. Investigation of whiplash injuries in the upper cervical spine using a detailed neck model. J Biomech 2012;45:1098–102.

[30] Fice JB, Cronin DS, Panzer MB. Cervical spine model to predict capsular ligament response in rear impact. Ann Biomed Eng 2011;39:2152–62.

[31] Mattucci SF, Moulton JA, Chandrashekar N, Cronin DS. Strain rate dependent properties of younger human cervical spine ligaments. J Mech Behav Biomed Mater 2012;10:216–26.

[32] Gayzik FS, Moreno DP, Vavalle NA, et al. Development of a full human body finite element model for blunt injury prediction utilizing a multi-modality medical imaging protocol. 12th International LS-DYNA User Conference, Dearborn, MI, USA. 2012.

[33] Hayes AR, Vavalle NA, Moreno DP, et al. Validation of simulated chestband data in frontal and lateral loading using a human body finite element model. Traffic Inj Prev 2014;15:181–6.

[34] Vavalle NA, Jelen BC, Moreno DP, et al. An evaluation of objective rating methods for full-body finite element model comparison to PMHS tests. Traffic Inj Prev 2013;14(Suppl):S87–94.

[35] Vavalle NA, Moreno DP, Rhyne AC, et al. Lateral impact validation of a geometrically accurate full body finite element model for blunt injury prediction. Ann Biomed Eng 2013;41:497–512.

[36] Panzer MB, Fice JB, Cronin DS. Cervical spine response in frontal crash. Med Eng Phys 2011;33:1147–59.

[37] DIN ISO 5834–5842:2007-12. Implants for surgery: ultra-high-molecular-weight-polyethylene, part 2: moulded forms (iso 5834-2:2006). Berlin, Germany, 2007.

[38] eFunda. Ti-6al-4v. Sunnyvale, CA. Available at: http://www.efunda.com/materials/alloys/titanium/show_titanium.cfm?ID=T18_AB&prop=all&Page_Title=Ti-6Al-4V. Accessed April 8, 2013.

[39] eFunda. Aisi type 316l. Sunnyvale, CA. Available at: http://www.efunda.com/materials/alloys/stainless_steels/show_stainless.cfm?ID=AISI_Type_316L&show_prop=all&Page_Title=AISI%20Type%20316L. Accessed April 8, 2013.

[40] Goyal RK, Tiwari AN, Mulik UP, Negi YS. Novel high performance Al2O3/poly(ether ether ketone) nanocomposites for electronics applications. Compos Sci Technol 2007;67:1802–12.

[41] Hallab NJ, Wimmer M, Jacobs JJ. Material properties and wear analysis. In: Yue JJ, Bertagnoli R, McAfee PC, An HS, eds. Motion preservation surgery of the spine: advanced techniques and controversies. Philadelphia, PA: Saunders, 2008:52–62.

[42] ASM International. Materials and coatings for medical devices—cardiovascular. 1st ed. Materials Park, OH: ASM International, 2009.

[43] Forman J, Lessley D, Kent R, et al. Whole-body kinematic and dynamic response of restrained PMHS in frontal sled tests. Stapp Car Crash J 2006;50:299–336.

[44] White NA, Moreno DP, Gayzik FS, Stitzel JD. Cross-sectional neck response of a total human body FE model during simulated frontal and side automobile impacts. Comput Methods Biomech Biomed Engin 2013 Aug 9. [Epub ahead of print].

[45] Society of Automotive Engineers. Sae j211/1. Instrumentation for impact test—part 1. Electronic instrumentation. Atlantic City, NJ: October 29 – November 1, 2007.

[46] Sprague MA, Geers TL. A spectral-element method for modelling cavitation in transient fluid–structure interaction. Int J Numer Methods Eng 2004;60:2467–99.

[47] Mongiardini M, Ray M, Anghileri M. Development of a software for the comparison of curves during the verification and validation of numerical models. 7th European LS-DYNA Conference; Milan, Italy: DYNAmore GmbH; 2009.

[48] Moorcroft D. Selection of validation metrics for aviation seat models. The Fifth Triennial International Aviation Fire and Cabin Safety Research Conference; 2007.

[49] Mertz HJ, Irwin AL, Prasad P. Biomechanical and scaling bases for frontal and side impact injury assessment reference values. Stapp Car Crash J 2003;47:155–88.

[50] Lee DJ, Winkelstein BA. The failure response of the human cervical facet capsular ligament during facet joint retraction. J Biomech 2012;45:2325–9.

[51] DiAngelo DJ, Foley KT, Morrow BR, et al. In vitro biomechanics of cervical disc arthroplasty with the ProDisc-C total disc implant. Neurosurg Focus 2004;17:E7.

[52] DiAngelo DJ, Roberston JT, Metcalf NH, et al. Biomechanical testing of an artificial cervical joint and an anterior cervical plate. J Spinal Disord Tech 2003;16:314–23.

[53] Chang UK, Kim DH, Lee MC, et al. Changes in adjacent-level disc pressure and facet joint force after cervical arthroplasty compared with cervical discectomy and fusion. J Neurosurg Spine 2007;7:33–9.

[54] Jaumard NV, Bauman JA, Guarino BB, et al. Prodisc cervical arthroplasty does not alter facet joint contact pressure during lateral bending or axial torsion. Spine 2013;38:E84–93.

[55] Bauman JA, Jaumard NV, Guarino BB, et al. Facet joint contact pressure is not significantly affected by prodisc cervical disc arthroplasty in sagittal bending: a single-level cadaveric study. Spine J 2012;12:949–59.

Nicholas A. White
Mem. ASME
Virginia Tech-Wake Forest University,
Center for Injury Biomechanics,
575 N. Patterson Avenue, Suite 120,
Winston-Salem, NC 27101
e-mail: whiten@vt.edu

Kerry A. Danelson
Mem. ASME
Virginia Tech-Wake Forest University,
Center for Injury Biomechanics,
575 N. Patterson Avenue, Suite 120,
Winston-Salem, NC 27101
e-mail: kdanelso@wakehealth.edu

F. Scott Gayzik
Virginia Tech-Wake Forest University,
Center for Injury Biomechanics,
575 N. Patterson Avenue, Suite 120,
Winston-Salem, NC 27101
e-mail: sgayzik@wakehealth.edu

Joel D. Stitzel[1]
Mem. ASME
Virginia Tech-Wake Forest University,
Center for Injury Biomechanics,
575 N. Patterson Avenue, Suite 120,
Winston-Salem, NC 27101
e-mail: jstitzel@wakehealth.edu

Head and Neck Response of a Finite Element Anthropomorphic Test Device and Human Body Model During a Simulated Rotary-Wing Aircraft Impact

A finite element (FE) simulation environment has been developed to investigate aviator head and neck response during a simulated rotary-wing aircraft impact using both an FE anthropomorphic test device (ATD) and an FE human body model. The head and neck response of the ATD simulation was successfully validated against an experimental sled test. The majority of the head and neck transducer time histories received a CORrelation and Analysis (CORA) rating of 0.7 or higher, indicating good overall correlation. The human body model simulation produced a more biofidelic head and neck response than the ATD experimental test and simulation, including change in neck curvature. While only the upper and lower neck loading can be measured in the ATD, the shear force, axial force, and bending moment were reported for each level of the cervical spine in the human body model using a novel technique involving cross sections. This loading distribution provides further insight into the biomechanical response of the neck during a rotary-wing aircraft impact. [DOI: 10.1115/1.4028133]

Introduction

Since WWII, rotary-wing aircraft have become a staple in all major military conflicts including the Korean War, Vietnam War, Gulf War, and the War on Terror [1]. Aviator training is a very time-consuming and expensive process, typically requiring 1.5–2.5 yr of preparation and costing U.S. taxpayers as much as $2 million per pilot [2]. Due to the large investment required to produce these highly skilled pilots, as well as the obvious concern for loss of life or injury, it is very important that these individuals be protected in the event of crash. Occupant response during rotary-wing aircraft crashes have been studied through full-scale, sled, and surrogate component-level experimental testing [3–11]. In many cases, the head and neck response were the focus of these studies.

Bass et al. conducted several series of ATD and cadaver tests to study and to evaluate the effects of head-supported mass (HSM) on neck injury risk during experimentally simulated rotary-wing aircraft impacts [3,4]. The results from a variety of head-neck component and whole-body experiments were used to both further elucidate the overall neck response and to develop a new injury criterion, the beam criterion (BC), for the lower neck [3,4]. For the component tests, injury severity was found to be less sensitive to the location of the HSM as compared to the initial neck angle and the peak sled acceleration. However, a linear relationship existed between the length of the moment arm, from the HSM to the lower neck, and both the peak force and moment. Lower neck anteroposterior (AP) shear force was not found to be a significant factor in injury predication, unlike axial force and flexion moment. In the whole-body cadaver tests, the cervical spine experienced sigmoid bending after the initial impact, due to gross

shearing motion in the lower neck, followed by a transition into C-shaped, simple bending.

Paskoff and Sieveka conducted an extensive series of rotary-wing aircraft sled tests to study the effects of ATD size, helmet mass properties, and impact severity on neck response [10,11]. Testing included a 50th percentile male, 95th percentile male, and 5th percentile female Hybrid III ATD with varying HSM configurations and three different severity sled pulses. The HSM did not have a statistically significant effect on the magnitude of the neck forces or moments for a given ATD size. However, both ATD size and pulse severity were found to have a statistically significant effect on most neck loading parameters.

The primary goal of this study was to evaluate the head and neck response of the Global Human Body Models Consortium (GHBMC) FE human body model during a simulated rotary-wing aircraft impact. The forces and moments at each cervical level of the neck were captured using a novel technique previously described by White et al. [12]. The seat geometry, belt configuration, and sled pulse were based on one of the experimental sled tests conducted by Paskoff and Sieveka [10,11]. The boundary conditions of this simulation were first validated through simulation of the experimental sled test with an FE ATD model. The head, neck, and chest response of the FE ATD model were quantitatively compared to the reported experimental results.

Materials and Methods

Overview. In the current study, two low-severity rotary-wing aircraft impact simulations were conducted using LS-DYNA R4.2.1 (LSTC, Livermore, CA) to examine the head and neck response of an ATD and human body FE model. The sled pulse, sled configuration, seat geometry, and belt preload were based on the low-severity, 7.62 m/s delta-V, sled test (#530) conducted by Paskoff and Sieveka [10,11]. This particular experimental test simulated a 30 deg pitch-down helicopter ground impact using a
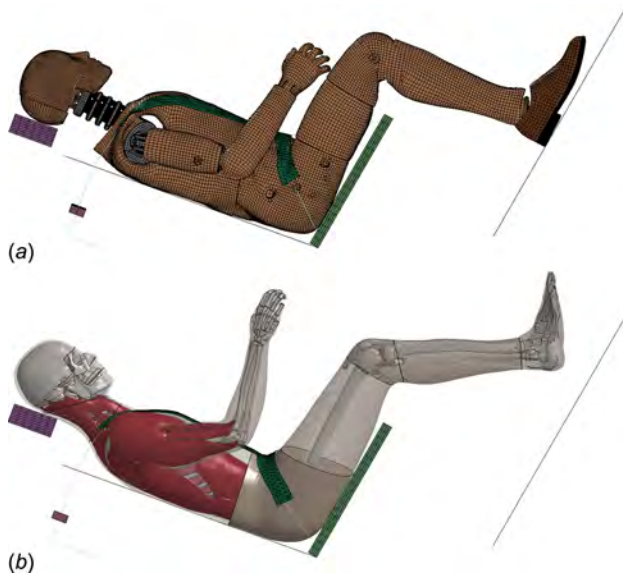
Fig. 1 Positioning at the time of sled pulse initiation ($t = 70$ ms) for the (*a*) ATD and (*b*) GHBMC simulations

50th percentile Hybrid III ATD with 1.8 kg of HSM proximate to the head center of gravity (CG). A generic five-point restraint system was then modeled according to established military aircraft personnel restraint design principles [13]. In order to simulate the experimental preloading of the restraint system, modeled pretensioners applied approximately 181 N of belt loading prior to any sled acceleration. To allow this initial belt tension to be achieved, as well as model settling due to gravity, both simulations were run for 70 ms prior to the initiation of the sled pulse (Fig. 1).

ATD FE Model. The Humanetics (Plymouth, MI) 50th percentile Hybrid III ATD FE model (v8.0) was used to validate the boundary conditions of the simulation by comparing the model and experimental responses. This FE model has been extensively validated on the component, subassembly, and whole ATD levels [14]. The original seated, driving posture of the ATD model was modified, increasing the neck extension angle by 15 deg and the thorax extension angle by 3 deg. The upper arms were rotated until they were in line with the torso and the lower legs were flexed until the feet were parallel with the sled floor. These modifications aligned the ATD model more closely to the experimental test initial position. Lumped mass elements were equally distributed around the head accelerometer mounting block, representing the HSM in the experimental test. Neck forces and moments were extracted from the upper and lower load cell transducers and transformed to the occipital condyle and base of the neck, respectively.

Prior to data analysis, the experimental data was zeroed and time shifted 70 ms, matching the start time of the simulation sled pulse. The time intervals for analysis were defined from 70 to 270 ms for acceleration and force data and 70–290 ms for moment data. These time intervals were chosen since they focus on the most relevant parts of the respective time histories. A quantitative comparison analysis was then conducted to compare the experimental results with the ATD simulation results using CORA, v3.6.1 (Partnership for Dummy Technology and Biomechanics, Germany).

The CORA analysis uses two different methods to quantitatively compare signals [15–17]. The corridor method rates, from 0 to 1, how well the subject curve fits within a narrow inner corridor and a wide outer corridor, both defined about the benchmark curve. For purposes of the current study, the subject curve is the simulation time history and the benchmark curve is the experimental test time history. A rating of 1 is assigned if the subject curve falls completely within the narrow corridor and a 0 if it falls completely outside of the wide corridor. The cross-correlation method analytically

analyzes the characteristics of the signal including phase shift, size, and shape using individual weighing factors. For each of these three submethods, a rating between 0 and 1 is also calculated. An overall, global rating is then calculated as the weighted sum of the corridor and correlations ratings, ranging from 0 for a poor match to 1 for a perfect match. While there is no definitive rating indicative of a "good" match, correlations with a rating of 0.7 or greater have been designated as a good match in past studies [16]. It is important to note that the CORA rating is dependent on the control variables within the program. Default global settings were used for both the corridor and cross-correlation methods.

Human Body FE Model. The GHBMC seated, 50th percentile male FE model (v3.5) was used to simulate the experimental ATD sled test [18–20]. This state-of-the-art human body model was developed by an international team of research institutions to investigate injury to the human body during dynamic impact events. It has been validated on both segmental and full cervical spine levels [21–24]. Additionally, whole-body validation has been conducted in a number of different impact scenarios [25–28]. The model, as a whole, is composed of 1.3×10^6 nodes, 1.95×10^6 elements, and 847 parts. The neck model includes the seven cervical vertebrae, intervertebral discs, ligaments, and muscles. The cancellous bone is modeled with hexahedral solid elements and the cortical bone with shell elements; both with plastic-kinematic material behavior. The intervertebral discs include the annulus fibrosis and nucleus pulposus. The fiber layers of the annulus fibrosis are modeled with a series of shell layers and the ground substance between fiber layers with an Ogden-rubber solid component. The nucleus pulposus is modeled as a solid, visco-elastic material. Multiple 1D nonlinear rate dependent tension-only beam elements represent the ligaments. The facet joint articular cartilage is modeled as a superior and inferior layer of visco-elastic solid elements. The joint synovial fluid is simulated using a squeeze-film model. Twenty-six neck muscles are modeled with solid elements using an Ogden-rubber material, representing the passive response. Active response is simulated with corresponding embedded Hill-type 1D elements.

The LS-PrePost (v4.0, LSTC, Livermore, CA) mass trimming function was used to equally distribute the additional head mass about the skull while maintaining the original head CG. Unlike in ATDs, there are no load cells to directly measure neck forces and moments in the GHBMC model since it is based off of the human anatomy. To capture this neck loading, cross sections were defined at each cervical level of the neck using a methodology
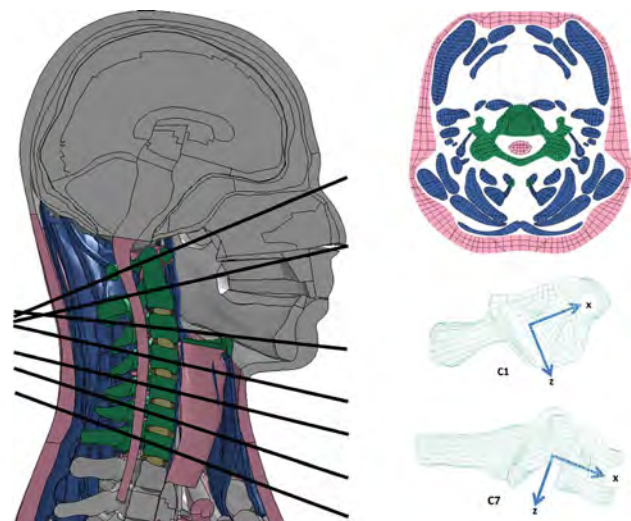
Fig. 2 Midsagittal cut of the GHBMC head and neck with transverse cross sections indicated by the solid lines. The LCSYS for C1 and C7 is visualized, along with the cross section at the level of C5.

Table 1 Quantitative comparisons between the benchmark experimental data and the ATD simulation data

Transducer		CORA		
		Corridor	Correlation	Overall
Acceleration (magnitude)	Head	0.761	0.803	0.782
	Chest	0.826	0.849	0.838
Upper neck loading	F_X	0.736	0.903	0.819
	F_Z	0.721	0.751	0.736
	M_Y	0.589	0.818	0.704
Lower neck loading	F_X	0.578	0.577	0.578
	F_Z	0.698	0.701	0.700
	M_Y	0.803	0.914	0.858

previously developed by White et al. [12]. Effectively, each of these seven cross sections represents a virtual load cell in the GHBMC model neck. For each cervical level, a local coordinate system (LCSYS) was defined according to SAEJ211 sign convention [29] with the origin located at the CG of the corresponding vertebra (Fig. 2). The positive x-direction was directed along the midsagittal plane from the origin to the midpoint of the anterior vertebral body. The positive z-direction was directed inferiorly from the origin, orthogonal to the local x-axis. A cross section was then defined in the local xy-plane for each level of the cervical spine using the appropriate LS-DYNA keywords. The axial and shear forces reported for each of these planes is the summation of the internal nodal forces from the respective cross-sectional interface, reported in the respective LCSYS. The moments reported for each of these planes is calculated as the cross product of the internal nodal force and the vector from the centroid of the given cross section to the location of this force. The moment about the respective local origin was then calculated using the concept of equivalent force systems. These forces and moments include the cross-sectional loading contributions from the bones, ligaments, active muscles, passive muscles, and surrounding flesh for a given cervical level.

The upper neck loading was reported at the C1 level with bending moment reported about the CG of the C1 vertebra. Unlike the upper neck load LCSYS in the ATD, which rotated with the head, the C1 loads were reported in a LCSYS that rotated with the vertebra. This method of reporting upper neck loading provided a more realistic load response in the human body model since the majority of the neck loading was transmitted through the bony skeleton, either directly or indirectly through muscle and ligament attachments. The lower neck loading was reported at the C7 level with bending moment reported about the CG of the C7 vertebra.

Data Analysis. The results of each simulation were postprocessed using Oasys T/HIS (v11, Arup, London, UK). For consistency with the reported experimental results, all simulation data was filtered using a 100 Hz, eight-pole Butterworth filter. The filtered cross-sectional force and moment results from the GHBMC model were then processed using in-house code written in MATLAB (v7.12.0, R2011a, MathWorks, Natick, MA).

Results

Overview. The head and neck response is reported for the experimental and simulated rotary-wing aircraft impacts, with the upper and lower neck load polarities reported in accordance with SAE J211 sign convention [29]. Data is only reported prior to the time of head to head restraint contact. Results of the quantitative comparison analyses between the experimental test and corresponding ATD simulation are reported in Table 1. Global extrema for upper and lower neck loading, as well as N_{ij} (neck injury criteria) and BC values are reported in Table 2 for the experimental test and both simulations.

Table 2 Maximum upper and lower neck loads for the experiment and simulation along with established IARVs. Time is reported in milliseconds.

Loading mode		IARV	Parameter	Experiment	ATD	GHBMC
Upper neck loading	AP shear F_x (N)	3100	t max	132	124	136
			F_x max	496.6	371.6	790.3
		−3100	t min	204	204	176
			F_x min	−538.6	−690.2	−678.8
	Tension/compression F_z (N)	4170	t max	178	174	182
			F_z max	665.5	809.4	735.5
		−4000	t min	134	121	134
			F_z min	−1604.5	−1560.1	−898.2
	Flexion/extension moment M_y (Nm)	190	t max	192	211	189
			M_y max	53.7	63.8	77.2
		−96	t min	142	146	149
			M_y min	−34.1	−20.9	−1.6
	N_{ij}	1	t max	136	122	188
			N_{ij} max	0.36	0.32	0.35
Lower neck loading	AP shear F_x (N)	3100	t max	126	90	180
			F_x max	182.9	46.1	198.8
		−3100	t min	202	204	136
			F_x min	−731.7	−594.3	−491.9
	Tension/compression F_z (N)	4170	t max	178	174	179
			F_z max	752.3	908.3	1416.7
		−4000	t min	133	121	134
			F_z min	−1945.4	−2261.5	−1312.7
	Flexion/extension moment M_y (Nm)	380	t max	213	206	196
			M_y max	128.8	155.8	110.5
		−192	t min	127	127	146
			M_y min	−33.2	−25.6	−25.5
	BC	1	t max	208	205	193
			BC max	0.93	1.19	0.98
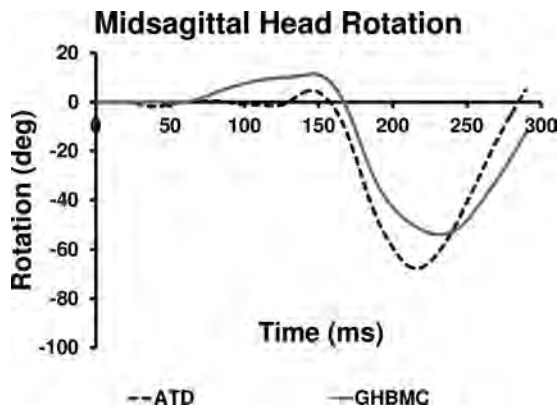
Fig. 3 Midsagittal head rotation for the two FE simulations. Head rotation from the experimental test was not available for comparison.
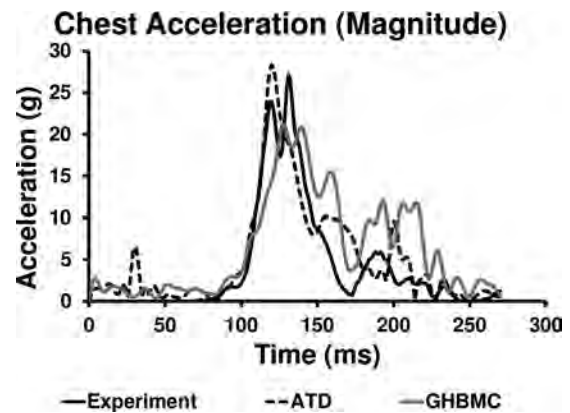
Fig. 5 Resultant chest acceleration for the experimental test and simulations
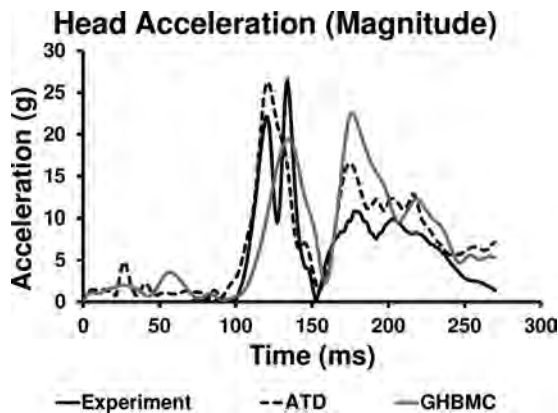
Fig. 4 Resultant head CG acceleration for the experimental test and simulations
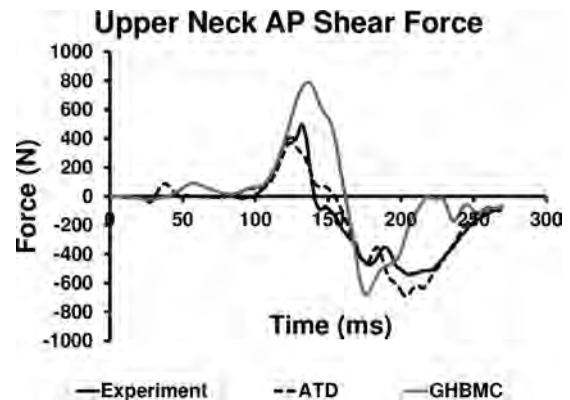
Fig. 6 Upper neck AP shear force for the experimental test and simulations

Head and Chest Response. While not reported in the experimental test, midsagittal head rotations for the two simulations are presented in Fig. 3. Head rotation remained minimal prior to 70 ms, during the settling phase of the simulations. While the GHBMC head underwent approximately 11 deg of extension during the beginning of the sled acceleration, head flexion was the primary form of rotation for both simulations. Maximum head flexion occurred 16 ms later for the GHBMC simulation than in the ATD simulation. Chin-to-chest contact did not occur in either of the simulations.

The resultant head CG accelerations are presented in Fig. 4. The global peak accelerations occurred during the first half of the time history plot for both the experimental test and ATD simulation and were almost identical in magnitude. Unlike the ATD simulation, the global peak in the experimental test exhibited bimodal-behavior. The overall CORA rating between the head accelerations in the experimental test and ATD simulation indicates good correlation between the two time histories. While the resultant head acceleration in the GHBMC simulation followed a similar trend to both ATD time histories, the global peak acceleration occurred during the second half of the simulation.

The peak chest resultant linear accelerations were very similar in magnitude between the experimental test and ATD simulation (Fig. 5). The overall CORA rating indicated good correlation between the two acceleration time histories. A bimodal-peak occurred for both the experimental test and GHBMC simulation, around the time of peak chest acceleration.

Upper and Lower Neck Response. Upper neck loading is reported in Figs. 6–8. The CORA analysis of the upper neck

loading showed good agreement between the experimental test and ATD simulation time histories for all loading modes. A period of positive AP shear and compression followed by a period of negative AP shear and tension occurred in the experimental test and both simulations. The change in load direction appeared to correlate with head rotation for the simulations. During compression, the experimental test exhibited bimodal-behavior, similar to the head acceleration time history. The experimental test and ATD simulations experienced a short period of extension followed by a more pronounced flexion moment, while the GHBMC simulation experienced primarily a flexion moment. The N_{ij} for the upper neck was calculated using critical intercepts defined in FMVSS 208 [30]. Neither the peak loading values nor the N_{ij} values approached established injury assessment reference values (IARVs).

Lower neck loading is reported in Figs. 9–11. The CORA analysis of the lower neck loading showed good agreement between the experimental test and ATD simulation for both the axial force and bending moment time histories. The degree of agreement between AP shear time histories was less clear. The experimental test and simulations experienced a period of compression followed by tension, similar to the upper neck axial loading. Again, the change in load direction appeared to correlate with head rotation. A small extension moment occurred in the experimental test and simulations, followed by a more pronounced flexion moment. While the peak loading values did not approach established IARVs, the BC value approached or exceeded 1, indicating approximately a 50% risk of a moderate injury to the lower cervical spine [3,4].
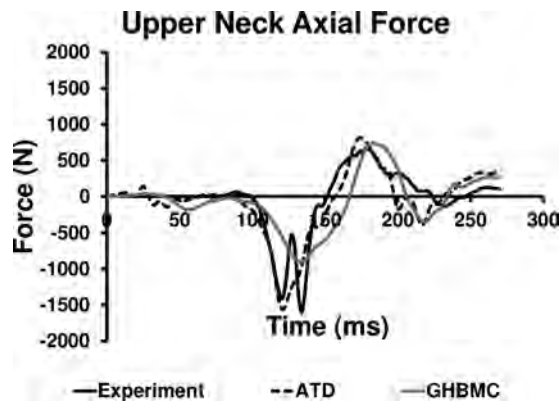
Fig. 7 Upper neck axial force for the experimental test and simulations

Fig. 8 Upper neck bending moment for the experimental test and simulations
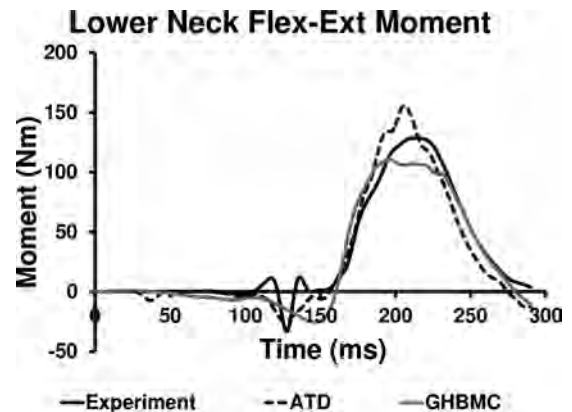
Fig. 9 Lower neck AP shear force for the experimental test and simulations

Fig. 10 Lower neck axial force for the experimental test and simulations

Fig. 11 Lower neck bending moment for the experimental test and simulations
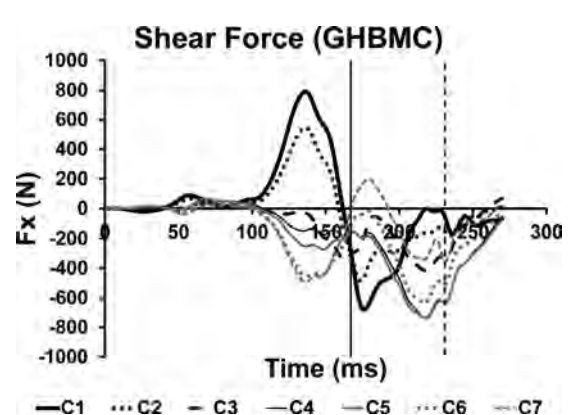
Fig. 12 Cross-sectional AP shear force for each cervical level of the GHBMC simulation. The forces are reported in their respective LCSYS.

GHBMC Cervical Column Response. While only the upper and lower neck loading can be reported from the ATD, loading throughout the cervical column can be captured in the GHBMC model. To further investigate the loading distribution throughout the entire neck, cross-sectional AP shear forces (Fig. 12), axial forces (Fig. 13), and bending moments (Fig. 14) are reported for each cervical level in the GHBMC simulation with peak axial and moment values reported in Table 3. The solid vertical line ($t = 167$ ms) indicates the initiation of primary head rotation and the dashed vertical line ($t = 231$ ms) indicates maximum head rotation. The lower cervical levels tended to experience greater axial forces and bending moments than the upper levels. During

the first 150 ms a marked difference is noted between both the polarity and peak values of the AP shear force between the upper and lower cervical levels. Incremental, midsagittal neck kinematics with respect to the C7 local origin are presented in Fig. 15, illustrating the change in cervical spine curvature during the different phases of loading.

Discussion

Simulation Configuration. Each simulation was allowed to settle under the effects of gravity and belt pretensioning for 70 ms,
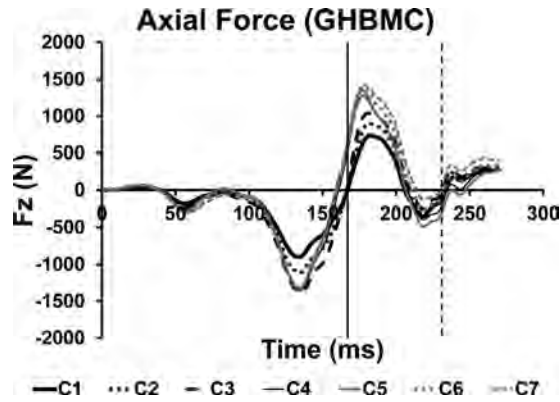
Fig. 13 Cross-sectional axial force for each cervical level of the GHBMC simulation. The forces are reported in their respective LCSYS.
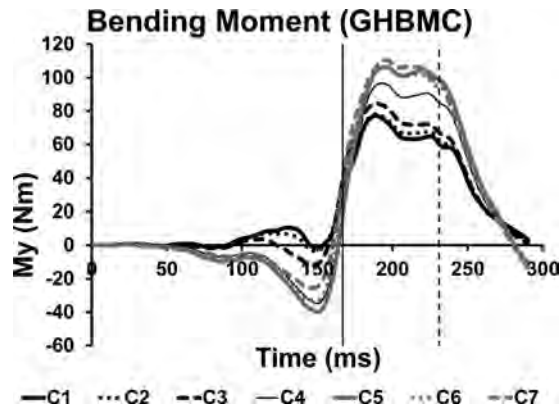
Fig. 14 Cross-sectional bending moment for each cervical level of the GHBMC simulation. Each moment is reported about the CG of its LCSYS.

Fig. 15 Incremental, midsagittal neck kinematics of the GHBMC simulation. The position of the local origin for each vertebra is plotted with respect to the C7 local origin at different points in time.

prior to the onset of the sled acceleration pulse. While some head and chest acceleration and neck loading occurred during the settling phase of the simulation, almost all of the time histories returned to zero at the onset of the sled acceleration pulse ($t = 70$ ms). Combining both the settling and sled acceleration into a single simulation allowed for the initial stresses, particularly the belt pretensioning, to be maintained. This process avoided some of the complications associated with applying initial stress and nodal positioning obtained from separate settling runs.

Only one HSM-configuration was evaluated in the current study with the location of the CG remaining relatively close to the original head CG. Since added head mass and CG location had no statistically significant effect of the magnitude of the measured forces or moments for the experiments as reported by Paskoff and

Sieveka [10,11], any minor differences in CG location for the simulations were considered negligible.

Numerical Validation of the ATD Simulation. From a visual standpoint, the salient features of the experimental time histories appeared to be adequately simulated by the ATD model. This observation is supported by the quantitative analysis where an overall CORA rating of 0.7 or greater was achieved for all acceleration, force, and moment time histories, except for lower neck shear loading. The chest acceleration, upper neck shear loading, and lower neck bending moment received an overall rating of greater than 0.8. This relatively high degree of correlation validates the boundary conditions of this simulated rotary-wing aircraft impact.

Between 100 and 150 ms, distinct bimodal-peaks occurred in the experimental head and chest accelerations, as well as the upper and lower neck axial loading. The magnitude of the second peak was always larger than the first peak and the local minimum between these peaks occurred at approximately 130 ms. Even though this bimodal-peak behavior was not reproduced by the ATD model, the simulation peaks always aligned in time with the first, smaller peaks of the experimental bimodal-response. While the experimental belt loading was not reported in the literature, it was examined in the ATD simulation. It appeared that the ATD began to pitch forward and load the shoulder harness at around 130 ms, the same time the local minimum occurs in the experimental bimodal-response. Due to the high degree of correlation between the experimental test and simulation in terms of head and neck response, it is reasonable to deduce that the simulated belt loading approximated the experimental loading. Therefore, the bimodal-response in the experiment data may be the result of the initial shoulder harness interaction with the ATD, creating a sharp, momentary deceleration of the upper torso. Minor differences in

Table 3 Maximum cross-sectional axial force and bending moment for each cervical level in the GHBMC simulation

Level	Compression		Tension		Extension		Flexion	
	Time (ms)	F_z (N)	Time (ms)	F_z (N)	Time (ms)	M_y (Nm)	Time (ms)	M_y (Nm)
C1	134	−898.2	182	735.5	149	−1.6	189	77.2
C2	134	−1110.9	182	900.3	149	−3.6	189	78.1
C3	135	−1383.9	181	1040.4	148	−11.8	190	84.5
C4	135	−1352.0	178	1271.6	150	−34.8	193	96.7
C5	134	−1319.9	177	1344.3	150	−39.9	195	106.5
C6	134	−1334.0	178	1399.6	149	−33.0	195	106.4
C7	134	−1312.7	179	1416.7	146	−25.5	196	110.5

belt placement, pretensioning, and friction properties may explain why the bimodal-response was not produced in the simulation.

The largest discrepancy between the experimental test and simulation response occurred for the lower neck AP shear, as was evident by the low overall CORA rating. A clear, visual difference between the experimental test and simulation responses occurred between 100 and 150 ms. In the experimental test, a short duration positive AP shear peak occurred at 126 ms, just prior to a large, almost instantaneous reverse in polarity at approximately 130 ms. The simulation produced neither this distinct positive AP shear peak nor such a sharp polarity change. The disparity in simulation and experiment responses was most likely due to a difference in initial shoulder harness interaction with the ATD.

GHBMC Biomechanical Response. The GHBMC model produced a more biofidelic neck response during the simulated impact. Similar to the upper and lower neck loads reported at the C1 and C7 levels, the AP shear, axial, and bending moment loads were also reported for the C2–C6 levels; effectively capturing the response of the entire GHBMC neck. Prior to onset of head flexion rotation, all levels underwent axial compression with peak levels occurring at approximately the same time, between 134 and 135 ms. Maximum compression was noticeably larger for C3–C7 levels than for the C1 and C2 levels. At approximately 136 ms, the C1 and C2 levels experienced maximum positive AP shear as the C3–C7 levels experienced a local peak negative AP shear. From the incremental kinematics (Fig. 15), it appeared that the cervical spine takes on an S-shaped curvature during this period of time, with the transition in curvature occurring between the C3 and C4 levels. This transition was even more pronounced at the time of maximum extension moment. Similar observations in spinal curvature were reported in the cadaver component and sled tests by Bass et al. [4]. This S-shaped curvature can be explained using basic beam deflection theory. From the simulation animation, it was observed that the global head CG translation from the onset of the sled pulse to the onset of head flexion occurred almost exclusively in the horizontal direction. This creates a paradigm where the neck can be represented as a beam fixed at the C7 level and free, but guided, at the C1 level. From the corresponding beam deflection equation, it can be shown that the beam, in this case the neck, will bend into a sigmoidal shape. Transition of the curvature occurs at the midpoint of the beam, which would correspond most closely to the C4 level.

The onset of axial tension began at approximately 160 ms for the C4–C7 levels and 167 ms for C1–C3 levels. This delay between the lower and upper levels appeared in the incremental kinematics illustration, where the lower vertebrae began to straighten out prior to the onset of head flexion. Straightening in the upper levels occurred by the time of maximum tension, creating a C-shaped curve in the cervical spine, indicative of simple beam bending. Maximum tension was reached at approximately the same time for all levels, with the C4–C7 levels reaching greater peak values than the C1–C3 levels. Shortly after maximum tension occurred, maximum flexion moment was achieved for all levels. The largest peak moments were achieved at the C5–C7 levels, due to the longer moment arm from these levels to the head. Peak flexion moments were smallest for the C1–C3 levels, due to the shorter moment arm.

To assess injury risk, the N_{ij} was calculated for the upper neck and the BC for the lower neck. The N_{ij} was originally developed to assess the risk of upper neck injury during a frontal automotive crash through a linear combination of normalized axial force and sagittal bending moment. Federal regulations set a threshold of 1.0 for the N_{ij} in the upper neck, corresponding to a 22% risk of a serious injury [30]. Using the axial loading and bending moment from the C1 cross section, the calculated N_{ij} value was well below this injury threshold. The BC was developed to assess the risk of lower neck injury during combined vertical-frontal crashes with through a linear combination of normalized axial force and

sagittal flexion moment [3]. Using the axial loading and flexion moment from the C7 cross section, the calculated BC value approached a value of 1, indicating a 50% risk of moderate injury to the lower cervical spine.

Limitations. The current work is not without limitations. One is that there is no direct method to validate the cross-sectional forces and moments calculated at the different levels of the GHBMC neck. Even if experimental cadaver tests were conducted using the same setup as the ATD, these values could not be measured in the actual cadavers. While it is possible to use inverse kinematic methods in to estimate the forces and moments at the occipital condyle [31] and T1 [32] in cadavers, there is no direct measurement method. Traditionally, inverse kinematic approaches have been acceptable. Cross sections are a predictive tool, as is the model itself, which estimate the loading response of the cervical spine during a simulated dynamic impact. A second limitation is that there is no intrinsic method to position the joints of the GHBMC model so that the initial position perfectly matches that of the ATD in the experimental sled test. However, given the overall head, neck, chest response of the GHBMC model followed that of the ATD, any difference in model response due to initial positioning is considered minimal.

Conclusions

The head and neck response of an FE ATD during a simulated rotary-wing aircraft impact was successfully validated against experimental test data. A quantitative analysis was conducted to compare the responses of the simulation and experimental test. All but one time history received a CORA rating of 0.7 or higher, indicating good overall correlation. The neck response of a human body FE model was also investigated during a simulated rotary-wing aircraft impact. Detailed neck loading for each cervical level was reported. While the maximum axial and AP shear forces and bending moments did not exceed existing IARVs, the BC value calculated from the C7 axial loading and flexion moment indicated a 50% risk of moderate injury to the lower cervical spine. The loading distribution throughout the cervical spine may help to explain the kinematic response, including change in spinal curvature. Sigmoidal curvature of the cervical spine was most prominent during the early part of the simulation when compression and extension moment were greatest. At this time, the AP shear force was positive in the upper cervical spine and negative in the lower cervical spine. Relating load distribution in the cervical spine to kinematic response has potential to explain the mechanism of injury during dynamic impact. These observations highlight the importance of human body modeling in understanding the underlying biomechanics of potential neck injury, a much harder task to complete when using an ATD.

References

[1] Dorr, R., 2005, Chopper: *A History of American Military Helicopter Operations From WWII to the War on Terror*, The Berkley Publishing Group, New York.
[2] Gebicke, M. E., and Farrell, B. S., 1999, "Military Personnel: Actions Needed to Better Define Pilot Requirements and Promote Retention," U.S. General Accounting Office, Report No. B-283075.
[3] Bass, C. R., Donnellan, L., Salzar, R., Lucas, S., Folk, B., Davis, M., Rafaels, K., Planchak, C., Meyerhoff, K., Ziemba, A., and Alem, N. M., 2006, "A New Neck Injury Criterion in Combined Vertical/Frontal Crashes With Head

Supported Mass," International Research Council on Biomechanics of Injury, Madrid, Spain.

[4] Bass, C. R., Salzar, R., Donnellan, L., and Lucas, H., 2004, "Injury Risk From HSM Loading (HM 2,3,4,5 Series)," University of Virginia Center for Applied Biomechanics, Charlottesville, VA, Report No. HEADMASS2.

[5] Coltman, J. W., 1983, "Design and Test Criteria for Increased Energy-Absorbing Seat Effectiveness," Report No. USAAVRADCOM-TR-82-D-42.

[6] Coltman, J. W., Van Ingen, C., and Selker, F., 1986, "Crash-Resistant Crewseat Limit-Load Optimization Through Dynamic Testing With Cadavers," U.S. Army Aviation Systems Command, Fort Eustis, VA, Report No. USAAVSCOM TR-85-D-11.

[7] Haley, J. L., Jr., and McEntire, B. J., 1994, "OH-58 Pilot Display Unit (PDU) Simulated Crash Tests," United States Army Aeromedical Research Laboratory, Fort Rucker, AL, USAARL Report No. 95-10.

[8] Haley, J. L., Jr., and Palmer, R. W., 1994, "Evaluation of a Retrofit OH-58 Pilot's Seat to Prevent Back Injury," U.S. Army Aeromedical Research Laboratory, Fort Rucker, AL, USAARL Report No. 95-9.

[9] Jackson, K. E., Boitnott, R. L., Fasanella, E. L., Jones, L. E., and Lyle, K. H., 2004, "A History of Full-Scale Aircraft and Rotorcraft Crash Testing and Simulation at NASA Langley Research Center," Fourth Triennial International Fire and Cabin Safety Research Conference, Lisbon, Portugal.

[10] Paskoff, G. R., 2004, "Cervical Injury Risk Resulting From Rotary Wing Impact: Assessment of Injury Based Upon Aviator Size, Helmet Mass Properties and Impact Severity," Patuxent River, MD, Report No. NAWCADPAX/RTR-2004/86.

[11] Paskoff, G. R., and Sieveka, E., 2004, "Influence of Added Head Mass Properties on Head/Neck Loads During Standard Helicopter Impact Conditions," Forty Second Annual SAFE Association Symposium, SAFE Association, Salt Lake City, UT, pp. 20–40.

[12] White, N. A., Moreno, D. P., Gayzik, F. S., and Stitzel, J. D., 2013, "Cross-Sectional Neck Response of a Total Human Body FE Model During Simulated Frontal and Side Automobile Impacts," Comput. Methods Biomech. Biomed. Eng. (Epub ahead of print).

[13] Zimmerman, R. E., and Merritt, N. A., 1989, "Aircraft Crash Survival Design Guide. Volume 1. Design Criteria and Checklists," Simula Inc., Phoenix, AZ, Report No. USAAVSCOM TR 89-D-22A.

[14] Humanetics, 2013, "Hybrid III 50th Dummy DYNA Model Technical Report, Release Version 8.0," Plymouth, MI.

[15] Gehre, C., Gades, H., and Wernicke, P., 2009, "Objective Rating of Signals Using Test and Simulation Responses," 21st International Technical Conference on the Enhanced Safety of Vehicles, Stuttgart, Germany.

[16] Gehre, C., and Stahlschmidt, S., 2011, "Assessment of Dummy Models by Using Objective Rating Methods," 22nd International Technical Conference on the Enhanced Safety of Vehicles, Washington, DC.

[17] Thunert, C., 2012, "CORA Release 3.6 User's Manual," GNS mbH, Germany.

[18] Gayzik, F. S., Moreno, D. P., Danelson, K. A., McNally, C., Klinich, K. D., and Stitzel, J. D., 2012, "External Landmark, Body Surface, and Volume Data of a Mid-Sized Male in Seated and Standing Postures," Ann. Biomed. Eng., **40**(9), pp. 2019–2032.

[19] Gayzik, F. S., Moreno, D. P., Geer, C. P., Wuertzer, S. D., Martin, R. S., and Stitzel, J. D., 2011, "Development of a Full Body CAD Dataset for Computational Modeling: A Multi-Modality Approach," Ann. Biomed. Eng., **39**(10), pp. 2568–2583.

[20] Stitzel, J. D., 2011, "Global Human Body Models Consortium (GHBMC) Male 50th Percentile (M50) Occupant Model Manual," Virginia Tech—Wake Forest University Center for Injury Biomechanics.

[21] DeWit, J. A., and Cronin, D. S., 2012, "Cervical Spine Segment Finite Element Model for Traumatic Injury Prediction," J. Mech. Behav. Biomed. Mater., **10**, pp. 138–150.

[22] Fice, J. B., and Cronin, D. S., 2012, "Investigation of Whiplash Injuries in the Upper Cervical Spine Using a Detailed Neck Model," J. Biomech., **45**(6), pp. 1098–1102.

[23] Fice, J. B., Cronin, D. S., and Panzer, M. B., 2011, "Cervical Spine Model to Predict Capsular Ligament Response in Rear Impact," Ann. Biomed. Eng., **39**(8), pp. 2152–2162.

[24] Mattucci, S. F., Moulton, J. A., Chandrashekar, N., and Cronin, D. S., 2012, "Strain Rate Dependent Properties of Younger Human Cervical Spine Ligaments," J. Mech. Behav. Biomed. Mater., **10**, pp. 216–226.

[25] Gayzik, F. S., Moreno, D. P., Vavalle, N. A., Rhyne, A. C., and Stitzel, J. D., 2012, "Development of a Full Human Body Finite Element Model for Blunt Injury Prediction Utilizing a Multi-Modality Medical Imaging Protocol," 12th International LS-DYNA User Conference, Dearborn, MI.

[26] Hayes, A. R., Vavalle, N. A., Moreno, D. P., Stitzel, J. D., and Gayzik, F. S., 2013, "Validation of Simulated Chestband Data in Frontal and Lateral Loading Using a Human Body Finite Element Model," Traffic Inj. Prev., **15**(2), pp. 181–186.

[27] Vavalle, N. A., Jelen, B. C., Moreno, D. P., Stitzel, J. D., and Gayzik, F. S., 2013, "An Evaluation of Objective Rating Methods for Full-Body Finite Element Model Comparison to PMHS Tests," Traffic Inj. Prev., **14**(Suppl 1), pp. S87–S94.

[28] Vavalle, N. A., Moreno, D. P., Rhyne, A. C., Stitzel, J. D., and Gayzik, F. S., 2013, "Lateral Impact Validation of a Geometrically Accurate Full Body Finite Element Model for Blunt Injury Prediction," Ann. Biomed. Eng., **41**(3), pp. 497–512.

[29] Society of Automotive Engineers, 2007, "SAE J211/1—Instrumentation for Impact Test-Part 1-Electronic Instrumentation," Warrendale, PA.

[30] National Highway Traffic Safety Administration, 2008, "Title 49 Code of Federal Regulations (CFR) Part 571 Section 208, Occupant Crash Protection."

[31] Mertz, H. J., and Patrick, L., 1971, "Strength and Response of the Human Neck," SAE Technical Paper No. 710855.

[32] Pintar, F. A., Yoganandan, N., and Maiman, D. J., 2010, "Lower Cervical Spine Loading in Frontal Sled Tests Using Inverse Dynamics: Potential Applications for Lower Neck Injury Criteria," Stapp Car Crash J., **54**, pp. 133–166.

Taylor & Francis
Taylor & Francis Group

Cross-sectional neck response of a total human body FE model during simulated frontal and side automobile impacts

Nicholas A. White[1], Daniel P. Moreno[2], F. Scott Gayzik[3] and Joel D. Stitzel*

Virginia Tech-Wake Forest University Center for Injury Biomechanics, 575 N. Patterson Avenue, Suite 120, Winston-Salem, NC 27157, USA

Human body finite element (FE) models are beginning to play a more prevalent role in the advancement of automotive safety. A methodology has been developed to evaluate neck response at multiple levels in a human body FE model during simulated automotive impacts. Three different impact scenarios were simulated: a frontal impact of a belted driver with airbag deployment, a frontal impact of a belted passenger without airbag deployment and an unbelted side impact sled test. Cross sections were created at each vertebral level of the cervical spine to calculate the force and moment contributions of different anatomical components of the neck. Adjacent level axial force ratios varied between 0.74 and 1.11 and adjacent level bending moment ratios between 0.55 and 1.15. The present technique is ideal for comparing neck forces and moments to existing injury threshold values, calculating injury criteria and for better understanding the biomechanical mechanisms of neck injury and load sharing during sub-injurious and injurious loading.

Keywords: finite element methods; cross section; cervical spine; neck; biomechanics; injury

Introduction and background

Neck injury biomechanics and tolerances

Motor vehicle collisions (MVCs) are the most common cause of cervical spine fracture and dislocation (McElhaney et al. 2002). According to the National Spinal Cord Injury Statistical Center (2011), MVCs were responsible for 39.2% of all reported spinal cord injuries between 2005 and 2011. A previous review of epidemiological data from clinical and accident database files found MVC-related cervical spine injuries tended to manifest between the occipital condyle (OC) and C2 of the upper region and C5–C6 in the lower region (Yoganandan et al. 1989). Upper cervical spine injuries were commonly associated with fatalities and lower cervical spine injuries with survivors. Of the serious injuries reported, 20% were of the spinal cord and 65% of the bone. Still, the majority of MVC-related injuries to the cervical spine are minor soft tissue injuries usually resulting from low-speed, rear-end impacts (Schmitt et al. 2010). Although not life-threatening, these injuries are associated with high-socioeconomic costs on a global level (White et al. 2009).

In 1976, General Motors introduced the Hybrid III 50th percentile male anthropomorphic test device (ATD) as a biofidelic surrogate to study occupant protection in simulated frontal and rear MVCs (Mertz 2002). In the following years, scaled versions of the ATD were developed, representing the small 5th percentile female, large 95th percentile male, 3- and 6-year-old child, and a 6-, 12- and 18-month infant. Each of these ATDs is instrumented with a single six degree of freedom load cell in both the upper and lower neck. These load cells allow for forces and moments to be calculated at the levels of the OC–C1 junction and at T1 and compared with defined injury assessment reference values (IARVs) (Mertz 2002; Mertz et al. 2003). These IARVs were selected so that the risk of associated injuries would be minimised for a particularly sized occupant, as long as the IARVs are not exceeded. To account for the viscoelastic properties of tissue, time-dependent loading criteria for the neck in tension, compression and shear have also been developed in the form of exceedence plots (Society of Automotive Engineers 2010).

The N_{ij} neck injury criterion (NIC) is the primary method to evaluate the risk of neck injury from a frontal MVC, including any airbag interaction (Klinich et al. 1996; Kleinberger et al. 1998; Eppinger et al. 1999; Eppinger et al. 2000). The criterion is based on matched 3-year-old ATD and animal airbag interaction tests that linearly combine normalised axial and sagittal bending moments from the upper neck load cell (Mertz and Weber 1982; Mertz et al. 1982; Prasad and Daniel 1984). Four possible loading scenarios are evaluated: tension/extension, tension/flexion, compression/extension and compression/flexion. Rear-end impact criterion includes the NIC, neck protection criterion (N_{km}) and lower neck load index (LNL). The NIC value is calculated from the relative acceleration and velocity between the upper and lower neck in the anterior–posterior (AP) direction (Bostrom et al. 1996). It is based on the hypothesis that transient pressure changes in the cervical

*Corresponding author. Email: jdstitzel@gmail.com

spinal canal, caused by a quick extension/flexion motion of the neck, lead to ganglion injuries. The N_{km} value is based on the summation of normalised shear loads in the AP direction and flexion/extension moments, similar to the N_{ij} (Schmitt et al. 2002). The critical intercepts used to normalise the load and moment were based on non-injurious volunteer studies (Mertz and Patrick 1971; Goldsmith and Ommaya 1984). The LNL value takes into account three force components and two bending moments of the lower neck load cell normalised by critical intercept values (Heitplatz et al. 2003).

Government-mandated occupant crash protection regulations differ from region to region around the world. In the USA, Federal Motor Vehicle Safety Standards (FMVSS) 208 sets peak reaction forces and moments and N_{ij} critical intercept values for the upper neck during frontal crash tests for different ATD sizes (NHTSA 2008a). In Europe, the Economic Commission for Europe (ECE) R94 sets thresholds for maximum neck extension moment, as well as time-dependent loading criteria for neck tension and shear for frontal impact test (United Nations Economic Commission for Europe 2007).

Brief review of finite element neck models

Although physical crash testing with ATDs is the standard for evaluating the safety of new vehicles, computer simulations have become more and more prevalent in studying the potential for MVC-induced injury. Mathematical modelling of occupant kinematics during a vehicle crash was born close to 50 years ago with the advent of computers (McHenry 1963; Prasad and Chou 2002). Extensive reviews of human body computational models used to study impact biomechanics exist in the literature (Prasad and Chou 2002; Yang et al. 2006; Hu 2007). One of the first finite element (FE) neck models developed was a simplified geometry 2D model to study laminectomy deformity (Saito et al. 1991). As technology has progressed, more complex 3D FE neck models with detailed geometries based on CT and MRI scans were developed with numerous injury biomechanics applications, including frontal, lateral and rear impacts (Kleinberger 1993; Dauvilliers et al. 1994; de Jager et al. 1996; Nitsche et al. 1996; Camacho et al. 1997; Kumaresan et al. 1997; Maurel et al. 1997; van der Horst et al. 1997; Yang et al. 1998; Deng et al. 1999; Halldin et al. 2000; Deng and Fu 2002; Meyer et al. 2004; Zhang et al. 2005; Hu 2007).

This study utilised the Global Human Body Models Consortium 50th percentile male model (GHBMC M50, v3-5-rev-03 g), a state-of-the-art FE model of a seated average-sized male built for LS-DYNA, R4.2.1 (LSTC, Livermore, CA, USA) (Figure 1) (Gayzik et al. 2011; Stitzel 2011; Gayzik et al. 2012). The model was
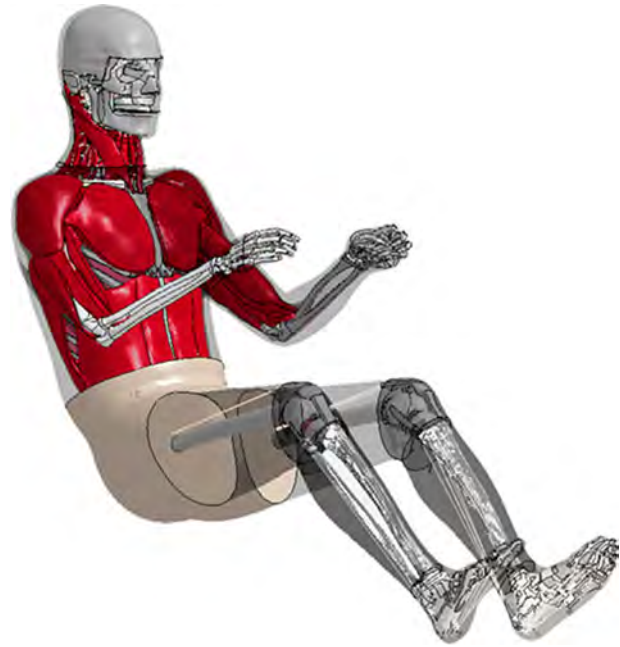
Figure 1. The GHBMC 50th percentile seated male model.

developed by a team of research university centres of excellence (COEs) around the world with the Full Body Model COE model integration centre located at Wake Forest University School of Medicine and the Virginia Tech – Wake Forest Center for Injury Biomechanics. The GHBMC neck model was developed at the Neck COE, the University of Waterloo, in Ontario, Canada (Fice et al. 2011; DeWit and Cronin 2012; Fice and Cronin 2012; Mattucci et al. 2012). It is composed of seven cervical vertebrae with detailed facet joints and accompanying intervertebral discs (IVDs), as well as nonlinear rate-dependent ligaments, 3D passive muscles and 1D active muscles (Figure 2). Element types include hexahedral solids, shells, 1D beams and discrete springs with a 1.5-mm representative mesh size for the vertebrae and neck muscles and 1.0-mm size for the IVDs. The neck model has been rigorously validated both at individual cervical segment levels and for the full cervical spine (Stitzel 2011; Vavalle et al. 2012). At the segmental level, non-injurious axial, lateral, shear, flexion, extension, compression and tension loading mode validations were carried out. Traumatic flexion, extension, compression and tension-loading mode validations have also been completed. The full cervical spine has been validated against lateral, frontal and rear-end car crash events, as well as in tension.

Cross sections

The purpose of this study is to describe a methodology to evaluate neck forces and moments at multiple levels of a human body FE model during simulated MVCs. Cross
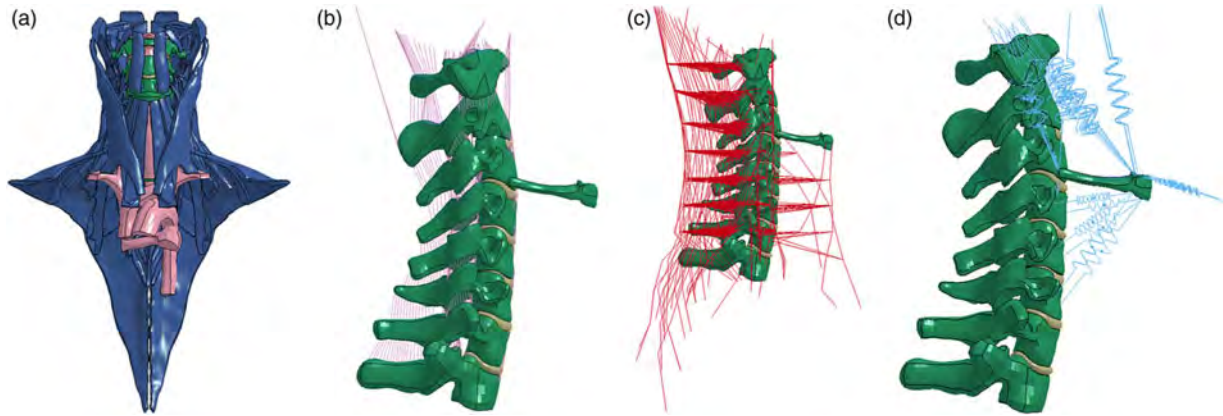
Figure 2. Breakdown of the GHBMC neck model including (a) passive muscles and vasculature, (b) ligaments, (c) active muscles and (d) supportive discrete elements.

sections were implemented in the neck to capture loading contributions of different anatomical components. For each cervical level, transverse cutting planes were created according to a locally defined coordinate system. Cross-sectional interfaces were then automatically calculated using LS-DYNA. Each of these interfaces contained a node set defining the cutting surface and one or more element sets. Only deformable elements to one side of the interface were selected. Forces and moments for each anatomical component, at every cervical level, were reported in the corresponding local coordinate system (LCSYS) and compared with the current IARVs and injury criteria.

Methodology

Simulations

The GHBMC whole-body model was validated against various regional impacts and full body cadaver sled tests (Stitzel 2011; Vavalle et al. 2012). Three of these validation simulations, two frontal and one side impact, have been repeated in this study to examine the neck response at each cervical level using cross sections. The first simulation was of a force-limited, three-point belted driver subjected to a 13.3-m/s ΔV frontal impact with airbag deployment (Forman et al. 2006). The second simulation was of a three-point belted (no retractor) passenger subjected to an 11.1-m/s ΔV frontal impact without airbag deployment (Shaw et al. 2009). The third simulation was a 6.7-m/s ΔV lateral impact using a Heidelberg-type seat fixture with no side wall padding (Cavanaugh et al. 1990a, 1990b; Cavanaugh et al. 1993). The simulations were run under LS-DYNA, (R4.2.1) on the WFU DEAC Cluster, a high-performance computing environment with 238 computational nodes containing 1904 processors, 11.4TB of total memory and 100TB of disk storage.

Local coordinate system

A LCSYS (Figure 3) was defined for vertebral bodies C1–T1 in accordance with SAE J211 sign convention (Society of Automotive Engineers 2007). The centre of gravity (CG) for each vertebra, including both shell and solid elements, was computed with the Mass Trimming interface in LS-PrePost (LSTC, Livermore, CA, USA). The local origin of the vertebra was defined by a node placed at this CG. A second node was defined at the midpoint of the superior and inferior portion of the anterior vertebral body, in the same sagittal plane as the CG, indicating the positive x-direction. A third node was then defined in the local xy-plane, with the positive y-direction to the right, orthogonal to the sagittal plane. Constrained nodal rigid bodies (∗CNRBs) were used to rigidly attach the LCSYS to a node on its corresponding vertebra, allowing local axes to rotate with the vertebra. The global coordinates of these nodes were output at 0.1-ms increments.

Cross sections

Six part sets were created, separating the neck into anatomical components including bones, IVDs, ligaments, soft tissue, active muscles and passive muscles. Database cross section planes (∗DCSPs), parallel with the local xy-plane, were defined at each cervical level (Figure 4). These cross sections were centred at the vertebral local origin and extended radially, just past the outer surface of the neck skin. The same plane was defined six times for each vertebra, allowing capture of the six part sets individually. The model was run for a single time step, allowing for LS-DYNA to automatically capture all elements and nodes associated with each cross-sectional interface, reporting them in the D3HSP (high-speed printer) ASCII output file under the heading 'interface definition'. The captured elements and nodes for each interface were extracted and
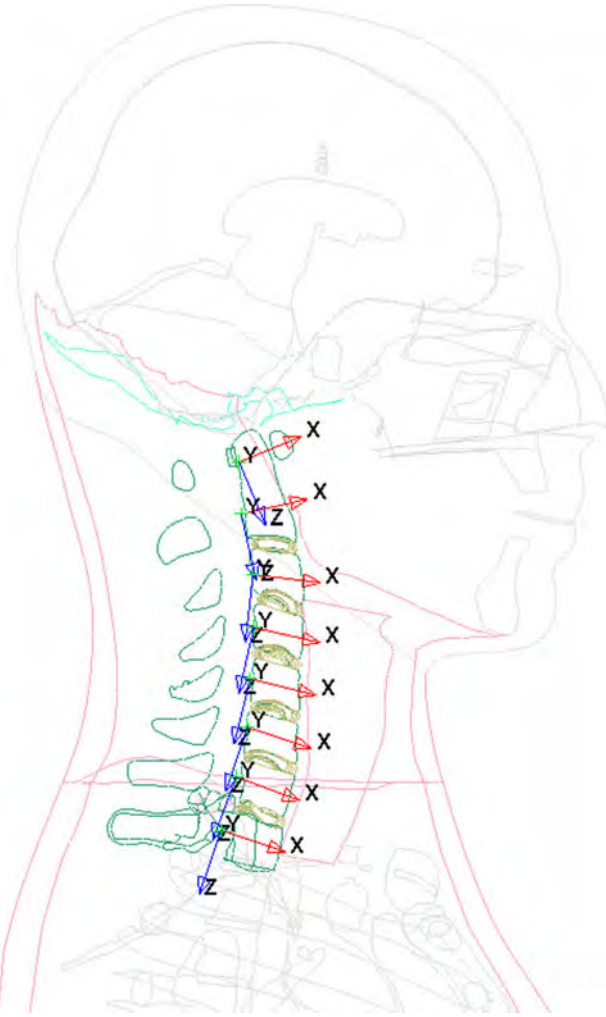
Figure 3. LCSYS for each vertebral level with the origin at the CG for each vertebrae and axes oriented according to SAE J211 convention (Society of Automotive Engineers 2007).

placed into individual sets. Database cross section sets (∗DCSSs) were then created based on these element sets and incorporated into the model (Figure 5). Projected views of the cross-sectional cuts are presented in Appendix A. It is important to note that only deformable bodies are included in cross sections, not rigid bodies.

Cross section force (CSF), cross section moment (CSM) and cross section centroid (CSC) data were output at 0.1-ms increments for each ∗DCSS. The CSF is the summation of the internal node forces defined at the cross-sectional interface. The moment contribution from each node defined in the cross-sectional interface is calculated as the cross product of the internal nodal force and the vector from the CSC to the location of this force. The CSM is the summation of these cross products, representing the total moment about the CSC, not the local origin. Because the CSC varies throughout time and is dependent on which part set is defined in the ∗DCSS, the reported moments
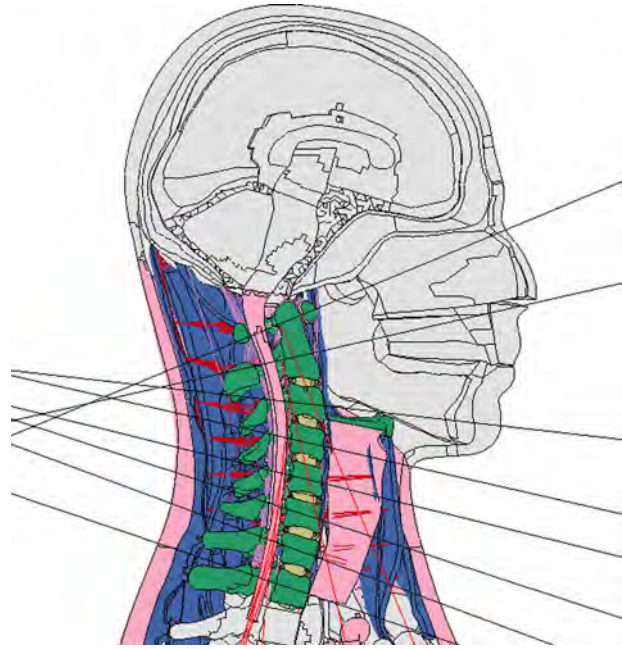
Figure 4. View of the GHBMC head and neck along the mid-sagittal plane. Cross-sectional planes were defined coplanar with each LCSYS *xy*-plane, capturing only elements and nodes within the neck and trying to avoid redundant measurement (overlapping section planes).

require transformation to the local origins. Using the concept of equivalent force systems, the moments about the local origins were calculated by adding the CSM to the cross product of the CSF and vector from the local origin to the CSC.

Although the CSF and CSM can be directly reported in the specified LCSYS, a problem lies with the CSC which is only reported in global coordinates, regardless of how the ∗DCSS is defined. Even though this issue may be resolved in newer versions of LS-DYNA, currently the GHBMC model is stable only in R4.2.1. To properly transform the CSMs to the local origin, a 3×3 direction cosine rotation matrix was constructed from the global coordinate time histories of the nodes used to define the vertebral LCSYSs. The CSC data were transformed into the LCSYS using this matrix prior to moment correction. For consistency, this rotation matrix was used to rotate both the CSF and CSM global results into LCSYSs.

Discrete elements

Because version R4.2.1 of LS-DYNA does not capture discrete elements using either ∗DCSP or ∗DCSS, the force and moment contributions of these elements must be added to the CSF and CSM results for each cervical level. The global forces and nodal coordinates of each discrete element were output at 0.1-ms increments. Analytical geometry was used to calculate the intersection points of
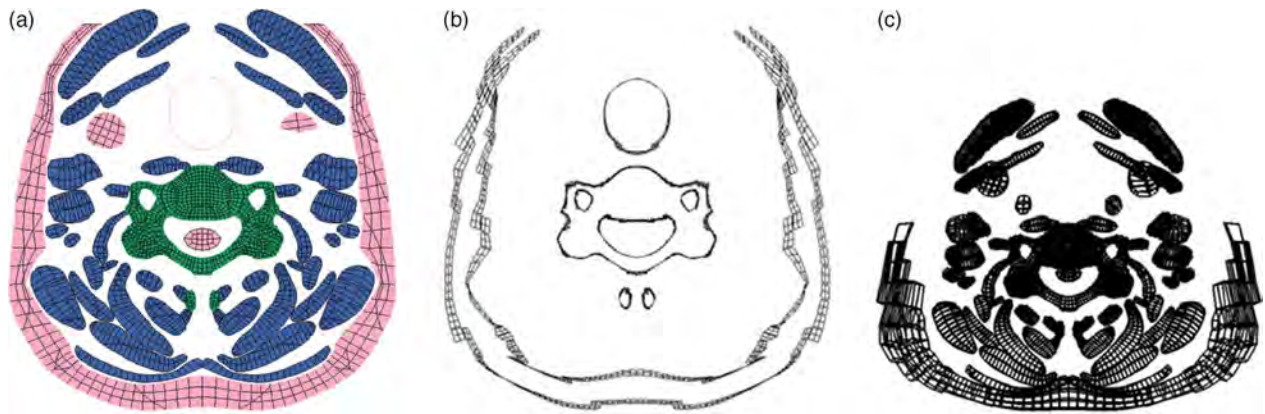
Figure 5. Projected cross-sectional view of the (a) bone, passive muscles and soft tissue, (b) *SET_SHELL and (c) *SET_SOLID captured at the level of C6.

the discrete elements with the cross-sectional interfaces. The coordinates of any point, l_n, along a discrete element can be calculated using Equation (1), where l_a and l_b correspond to the coordinates of the two nodes defining the element. Although the value of t may be any real number, it must remain between 0 and 1 for l_n to lie within the physical boundaries of the discrete element. The coordinates of any point, p_n, on the plane defined by three, non-collinear points p_0, p_1 and p_2, can be calculated using Equation (2). These three points correspond to the coordinates of the three nodes defining the *xy*-plane of a vertebral LCSYS. A parametric equation can be created by equating Equations (1) and (2), where t can be solved and then plugged back into Equation (1) to calculate the point of intersection. For each cervical level, the cross product of the vector from the local origin to the point of intersection and discrete element force was used to calculate the moment contribution from each discrete element. These individual moments were summed and rotated into the LCSYS using the rotation matrix.

$$l_n = l_a + (l_b - l_a)t; \quad t \in R \tag{1}$$

$$p_n = p_0 + (p_1 - p_0)u + (p_2 - p_0)v; \quad u, v \in R \tag{2}$$

Data processing

The binary output files were post-processed using Oasys T/HIS 10.2-64 bit (Arup, London, UK). The CSF results were filtered at CFC 1000 and CSM results at CFC 600 according to SAE J211 specifications for neck load cells in the Hybrid III ATD (Society of Automotive Engineers 2007). For purposes of N_{ij} calculation, both the CFC and CSM results were filtered at CFC 600 according to FMVSS regulation (NHTSA 2008a). The nodal displacements and CSC results were filtered at CFC 60. Seatbelt and airbag loading with the occupant were also filtered at CFC 60 (Society of Automotive Engineers 2007). The occupant–wall interaction forces measured in the Cavanaugh side impact simulation were filtered with CFC 300. All of the filtered data were then processed using in-house code written in MATLAB 7.12.0 (R2011a, MathWorks, Natick, MA, USA).

Results

Animated results of the overall occupant kinematics are presented as individual d3plots for the start, middle and end of each simulation (Figures 6–8). Total force and moment time histories were created for each simulation
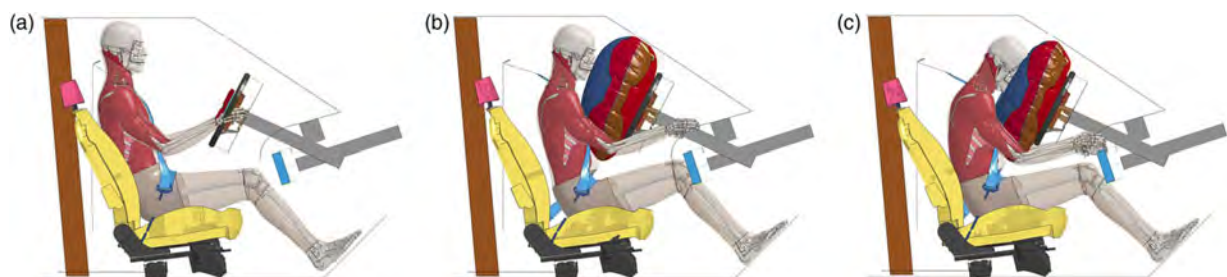
Figure 6. Simulation d3plots for the Forman 13.3 m/s ΔV force-limited, three-point belted driver frontal impact with airbag deployment at (a) $t = 0$ ms, (b) $t = 75$ ms and (c) $t = 150$ ms (Forman et al. 2006).
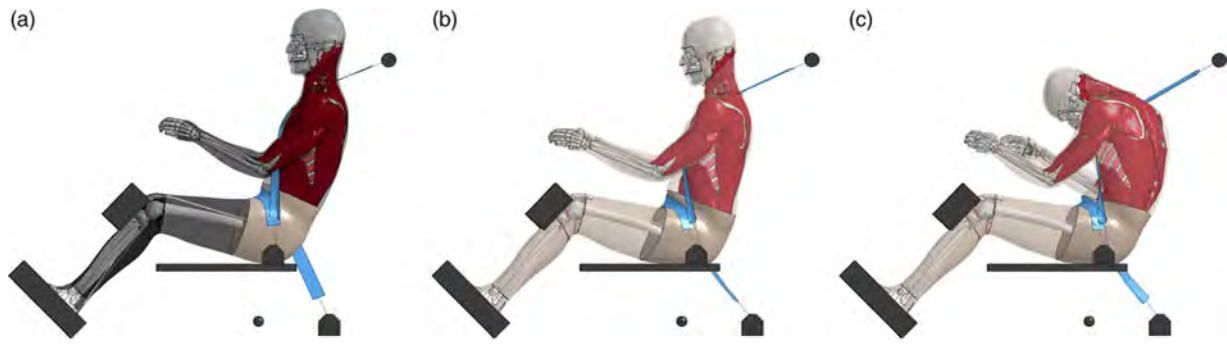
Figure 7.   Simulation d3plots for the Shaw 11.1 m/s ΔV three-point belted (no retractor) passenger frontal impact at (a) $t = 0$ ms, (b) $t = 75$ ms and (c) $t = 150$ ms (Shaw et al. 2009).

from the summation of bone, ligament, active muscle, passive muscle and soft tissue anatomical components and discrete element loading contributions, in the rotated LCSYS for each respective cervical level (Figures 9–11). A summary of force and moment polarity with respect to head and chest motion based on SAE J211 is presented in Table 1 (Society of Automotive Engineers 2007). Maximum and minimum neck forces and moments are summarised in Table 2. The individual force and moment contributions of the anatomical components and discrete elements are reported in the Appendices B–D. Force time histories of occupant–restraint systems and occupant–wall interaction are reported in Figures 12–14.

For purposes of this study, only the total forces and moments (Figures 9–11) will be reported in this section. Many of the local extrema in the force and moment curves correlate with occupant–restraint interactions. In the Forman simulation, maximum engagement of the upper

shoulder belt occurred at 70 ms and maximum occupant–airbag interaction at 85 ms. Prior to maximum airbag interaction, the time of maximum engagement with the upper shoulder belt coincided with the largest negative AP shear force in the upper cervical spine and the largest axial tension force at all levels. Although AP shear force decreased in magnitude for both C1 and C2 just after the maximum engagement of the upper shoulder belt, an inflection point was noted for both cervical levels at the time of maximum occupant–airbag interaction, where AP shear subsequently increased in magnitude (larger negative value). At the approximate time of maximum occupant–airbag interaction, a local axial tension force minimum and local axial moment maximum were reached for all cervical levels.

In the Shaw simulation, maximum engagement of the upper shoulder belt occurred at 90 ms and of the lower shoulder belt at 116 ms. A force plateau was noted
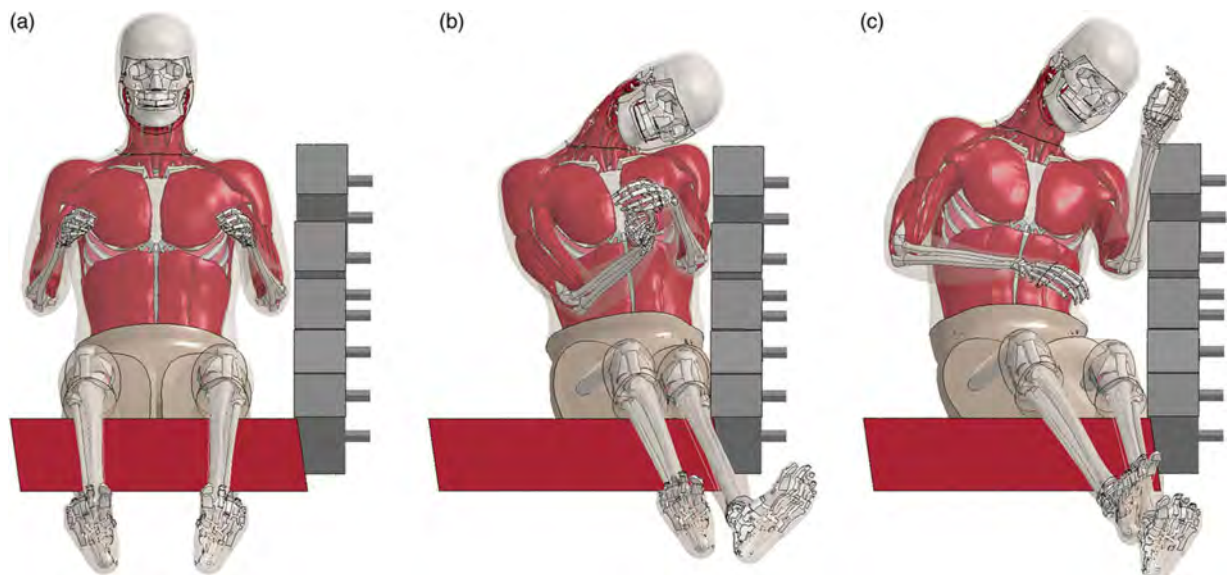
Figure 8.   Simulation d3plots for the Cavanaugh 6.7 m/s ΔV lateral impact using a Heidelberg-type seat fixture with no side wall padding at (a) $t = 0$ ms, (b) $t = 50$ ms and (c) $t = 100$ ms (Cavanaugh et al. 1990a, 1990b; Cavanaugh et al. 1993).
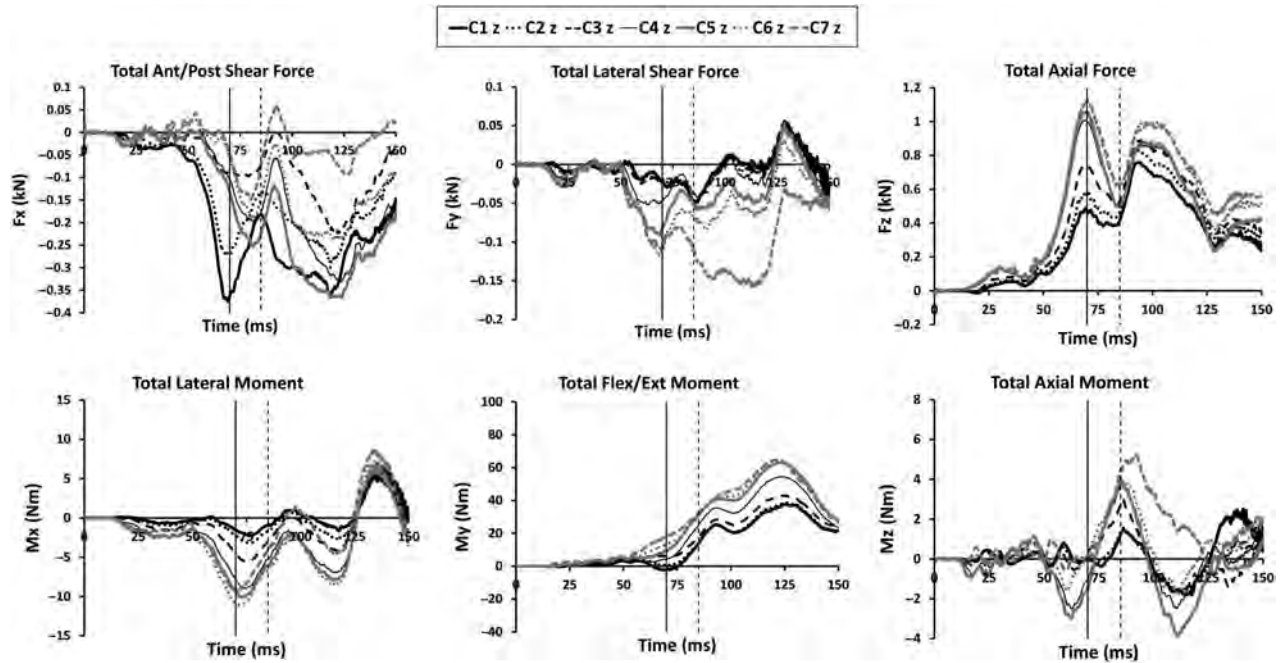
Figure 9. Total force and moment time histories from the Forman frontal impact simulation. These total load curves are the summation of bone, ligament, active muscle, passive muscle, soft tissue and discrete element anatomical component contributions in the rotated, LCSYS for each respective vertebral level. The vertical solid line corresponds to the time of maximum engagement of the upper shoulder belt ($t = 70$ ms) and the vertical dashed line to the time of maximum occupant–airbag interaction ($t = 85$ ms).
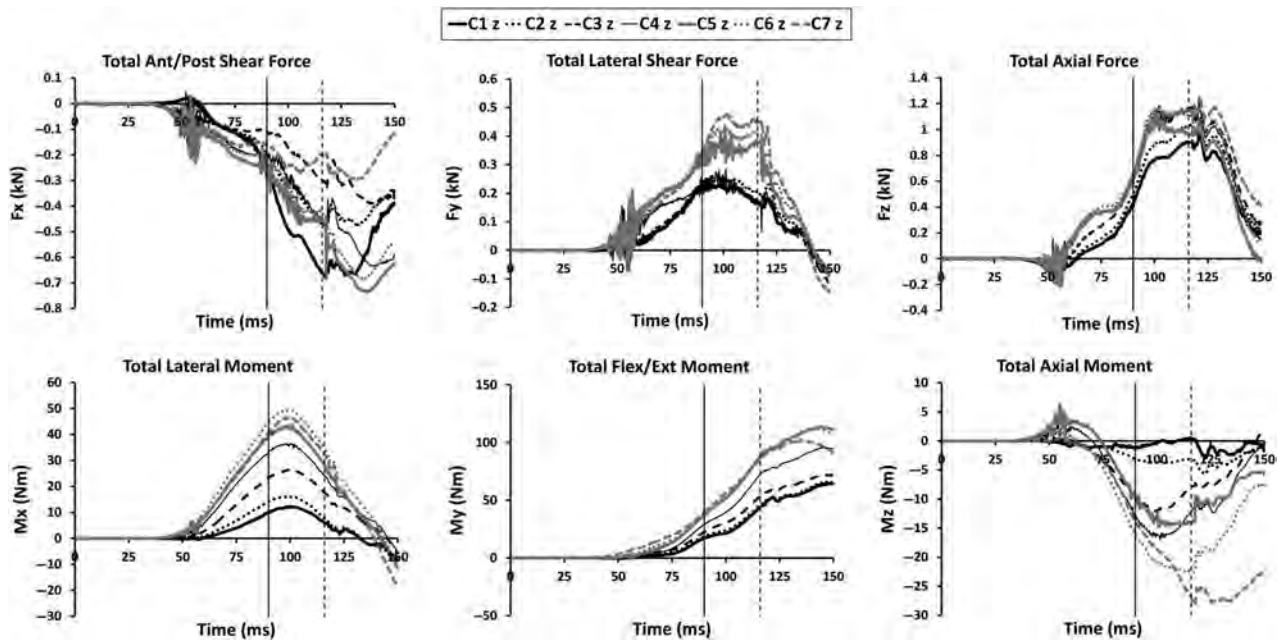
Figure 10. Total force and moment time histories from the Shaw frontal impact simulation. These total load curves are the summation of bone, ligament, active muscle, passive muscle, soft tissue and discrete element anatomical component contributions in the rotated, LCSYS for each respective vertebral level. The vertical solid line corresponds to the time of maximum engagement of the upper shoulder belt ($t = 90$ ms) and the vertical dashed line to of maximum engagement of the lower shoulder belt ($t = 116$ ms).
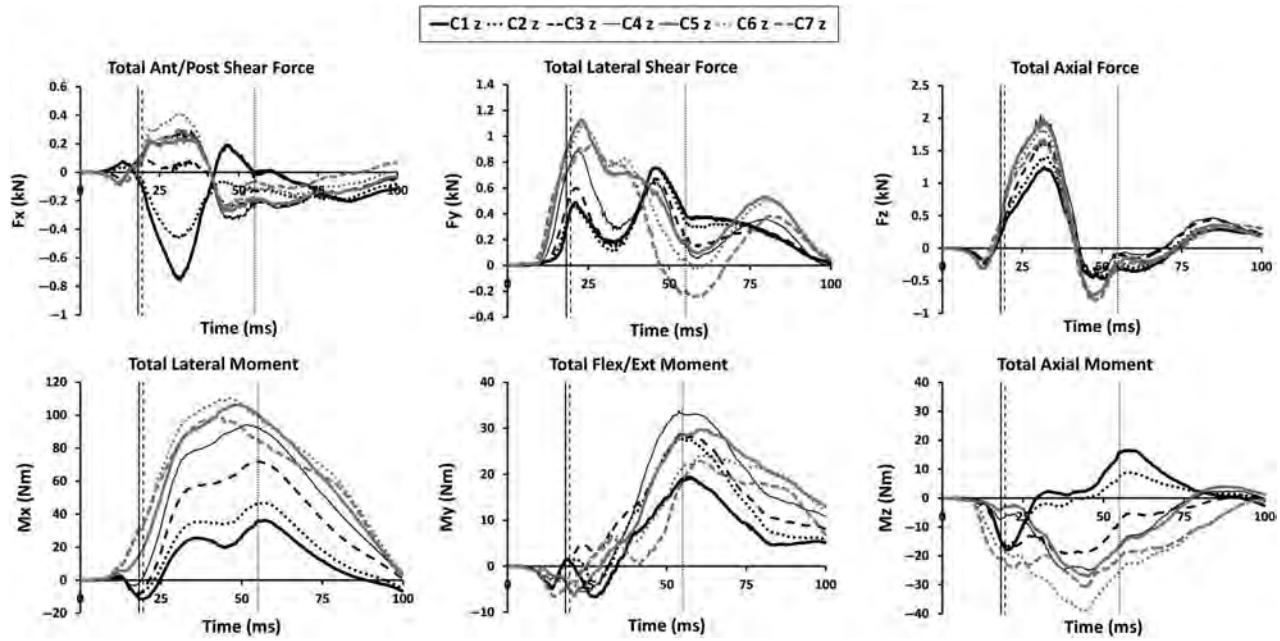
Figure 11. Total force and moment time histories from the Cavanaugh side impact simulation. These total load curves are the summation of bone, ligament, active muscle, passive muscle, soft tissue and discrete element anatomical component contributions in the rotated, LCSYS for each respective vertebral level. The vertical solid line corresponds to the time of maximum upper body-to-wall contact force ($t = 18$ ms), the vertical dashed line to the time of maximum pelvis-to-wall contact force ($t = 19.5$ ms) and the vertical dotted line to the approximate time of the maximum lateral rotation of C1 with respect to C7 in the frontal plane ($t = 55$ ms).

between both of these points in time for the lateral shear and axial force, for all levels of the cervical spine. The magnitude of the AP shear force began to increase (larger negative value) at a faster rate from the time of maximum engagement of the upper shoulder belt to that of the lower belt. All levels of the cervical spine experienced a flexion moment for the entire simulation. At maximum engagement of the lower shoulder belt, peak axial moments were experienced in the lower cervical spine (C4–C7).

Although there were no restraints in the Cavanaugh simulation, time of maximum occupant-to-wall interaction and estimated maximum lateral neck rotation were reported. Occupant-to-wall force time histories were reported for the upper body (shoulder, thorax and abdomen forces) and pelvis. The maximum force between the upper body and wall occurred at $t = 18$ ms and that between the pelvis and wall at $t = 19.5$ ms. Lateral rotation of the cervical spine in the frontal plane was approximated in

LS-PrePost. This estimated maximum lateral rotation was measured between C1 and C7 and occurred at $t = 55$ ms. Lateral shear forces first peaked shortly after pelvis-to-wall contact at all levels of the cervical spine. Peak axial force occurred for all levels at approximately the same time, between maximum pelvis-to-wall contact and maximum lateral cervical spine rotation. Peak lateral moments occurred roughly 10 ms prior to the time of maximum rotation for the lower cervical spine (C5–C7) and at the approximate time of maximum rotation for the upper cervical spine (C1–C4).

The time of maximum total axial force and the time of maximum total bending moment were determined for each simulation. Force and moment values for each cervical level corresponding to these two times are presented in Figures 15–16. Adjacent vertebral level ratios, C1/C2, C2/C3, C3/C4, C4/C5, C5/C6 and C6/7, were calculated using these force and moment values (Figures 17 and 18).

Table 1. Polarity relative to sign convention for the measured neck loads and moments (Society of Automotive Engineers 2007).

Parameter	Measurement	Head–neck motion	Manipulation for positive polarity
Neck load	F_x	Anterior/posterior shear	Head rearward, chest forward
	F_y	Lateral shear	Head leftward, chest rightward
	F_z	Axial	Head upward, chest downward
Neck moment	M_x	Lateral	Left ear towards left shoulder
	M_y	Flexion/extension	Chin towards sternum (flexion)
	M_z	Axial (torsion)	Chin towards left shoulder

Table 2. Peak neck forces and moments calculated for each cervical spine level for the (F) Forman, (S) Shaw and (C) Cavanaugh simulations. The IARVs for each loading mode at the OC–C1 and C7–T1 junctions are included for reference (Mertz et al. 2003).

Peak loading	OC–C1	C7–T1	ID[a]	C1	C2	C3	C4	C5	C6	C7
AP shear F_x (N)	±3100	±3100	F	2.3 / −375.1	1.5 / −299.2	2.5 / −224.6	7.6 / −330.8	5.7 / −365.6	28.6 / −236.8	58.9 / −148.5
			S	24.2 / −683.5	1.6 / −487.6	2.6 / −391.1	45.2 / −634.7	28.6 / −736.4	3.9 / −687.4	22.4 / −297.0
			C	190.2 / −755.0	45.7 / −463.8	97.6 / −261.7	295.1 / −332.5	236.8 / −271.5	416.1 / −288.0	299.2 / −243.7
Lateral shear F_y (N)	±3100	±3100	F	52.9 / −49.1	55.5 / −47.6	57.3 / −50.2	55.8 / −51.6	52.8 / −90.9	30.0 / −118.7	3.5 / −158.0
			S	245.8 / −82.4	255.2 / −78.3	255.0 / −116.7	284.3 / −64.9	436.2 / −89.7	428.2 / −89.5	476.7 / −147.5
			C	756.6 / −0.8	753.2 / −0.9	672.1 / −2.2	887.5 / −2.0	1132.4 / −1.6	1084.7 / −26.7	924.2 / −241.4
Ten/Comp F_z (N)	4170/ −4000	4170/ −4000	F	758.3 / −12.8	827.7 / −11.4	888.4 / −3.1	1007.8 / −1.3	1053.4 / −2.1	1121.2 / −4.8	1118.0 / −19.6
			S	970.0 / −112.3	1088.9 / −113.3	1199.7 / −112.7	1185.5 / −224.9	1107.2 / −210.8	1232.4 / −43.9	1257.1 / −54.7
			C	1245.2 / −471.8	1397.5 / −436.3	1665.0 / −354.7	2044.4 / −418.8	1969.0 / −743.9	1829.8 / −757.8	1669.3 / −809.4
Lateral moment M_x (Nm)	±143	±286	F	6.6 / −2.2	6.3 / −3.2	6.6 / −5.6	6.1 / −9.0	6.7 / −10.1	7.3 / −11.1	8.6 / −9.4
			S	12.2 / −8.6	16.2 / −10.9	26.3 / −5.8	36.4 / −5.1	43.7 / −11.6	49.5 / −11.4	46.5 / −18.7
			C	36.2 / −11.4	47.0 / −8.0	71.9 / −9.4	94.2 / −3.3	106.2 / −0.1	110.3 / −0.1	98.3 / −0.1
Flex/Ext moment M_y (Nm)	190/ −96	380/ −192	F	37.8 / −2.4	38.7 / −0.1	43.0 / 0.0	54.6 / −0.5	63.4 / −0.4	64.6 / −0.3	64.6 / −0.1
			S	64.8 / −0.4	65.9 / −0.1	72.1 / −0.1	95.5 / −1.0	113.5 / −0.5	111.7 / −0.1	101.7 / −0.1
			C	19.4 / −6.7	28.0 / −4.6	28.8 / −5.0	33.8 / −6.1	29.7 / −6.4	24.2 / −3.8	22.9 / −6.7
Axial moment M_z (Nm)	±96	±96	F	2.5 / −1.8	1.6 / −1.6	3.0 / −1.8	3.9 / −2.5	4.0 / −3.9	4.0 / −1.8	5.3 / −0.8
			S	0.5 / −2.9	0.1 / −5.6	2.0 / −12.1	3.5 / −16.9	6.3 / −14.8	2.1 / −22.6	0.9 / −28.2
			C	16.5 / −17.9	9.0 / −16.7	0.9 / −19.2	2.4 / −25.1	3.9 / −27.1	0.2 / −39.2	0.1 / −31.4

[a]F: driver, frontal impact, 13.3 m/s ΔV, three-point force-limited belt, airbag deployment; S: passenger, frontal impact, 11.1 m/s ΔV, three-point belt with no retractor, no airbag deployment; C: Heidelberg-type sled test, lateral impact, 6.7 m/s ΔV, no side wall padding.
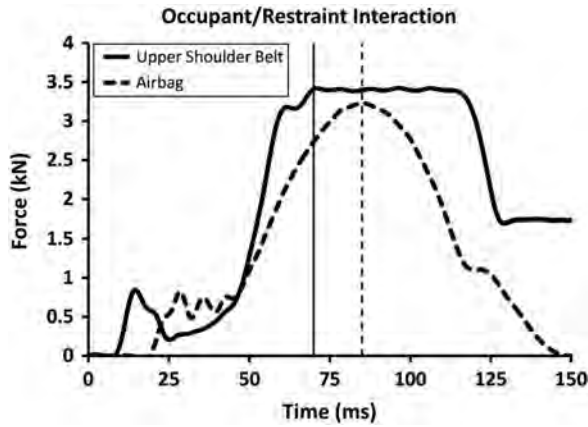
Figure 12. Reported interface force time histories of the occupant with the upper shoulder belt and airbag in the Forman simulation. The vertical solid line corresponds to the time of maximum engagement of the upper shoulder belt ($t = 70$ ms) and the vertical dashed line to the time of maximum occupant–airbag interaction ($t = 85$ ms).

D3plot images for these two times (approximate) are presented in Figure 19. The Forman simulation produced a maximum axial force of 1.1 kN at the C7 vertebral level ($t = 70.2$ ms) and a maximum flexion moment of 64.6 Nm at the C6 vertebral level ($t = 122.4$ ms). The adjacent vertebral level axial force and flexion moment ratios were 0.80, 0.79, 0.74, 0.95, 0.94, 1.00 kN and 0.96, 0.88, 0.78, 0.87, 0.97, 1.00 Nm, respectively. The Shaw simulation produced a maximum axial force of 1.3 kN at the C7 vertebral level ($t = 121.3$ ms) and a maximum flexion moment of 113.5 Nm at the C5 vertebral level ($t = 144.9$ ms). The adjacent vertebral level axial force and flexion moment ratios were 0.89, 0.91, 1.04, 1.07,
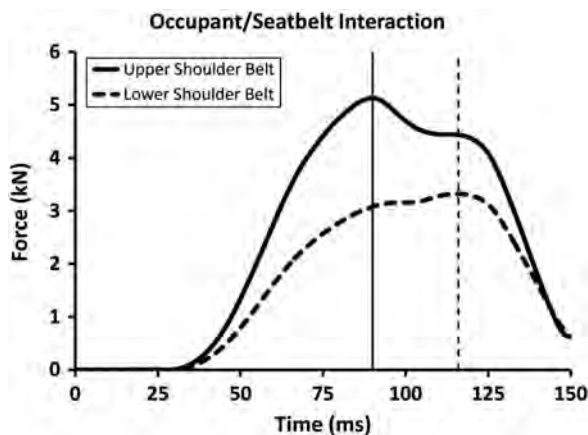
Figure 13. Reported interface force time history of the occupant with the upper and lower shoulder belt in the Shaw simulation. The vertical solid line corresponds to the time of maximum engagement of the upper shoulder belt ($t = 90$ ms) and the vertical dashed line to the time of maximum engagement of the lower shoulder belt ($t = 116$ ms).
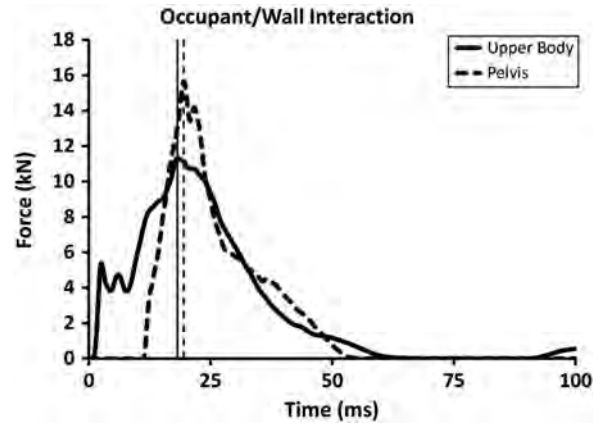
Figure 14. Reported interface force time history of the occupant with the wall in the Cavanaugh simulation. The vertical solid line corresponds to the time of maximum upper body-to-wall contact force ($t = 18$ ms) and the vertical dashed line to the time of maximum pelvis-to-wall contact force ($t = 19.5$ ms).

0.87, 0.97 kN and 0.98, 0.91, 0.75, 0.84, 1.02, 1.15 Nm, respectively. The Cavanaugh simulation produced a maximum axial force of 2.0 kN at the C4 vertebral level ($t = 30.8$ ms) and a maximum lateral moment of 1104 Nm at the C6 vertebral level ($t = 46.2$ ms). The adjacent vertebral level axial force and lateral moment ratios were 0.87, 0.84, 0.80, 1.05, 1.07, 1.11 kN and 0.60, 0.55, 0.69, 0.85, 0.95, 1.14 Nm, respectively.

Neck tension time-dependent curves were calculated for each simulation at each cervical level (Figure 20). None of the calculated curves exceeded the injury tolerance threshold, indicating that serious injury due to neck tension was unlikely.

The N_{ij} value was calculated at each cervical level using the axial force and flexion/extension moment for both frontal sled tests and the corresponding critical intercepts (Table 3) as specified in FMVSS 208 (NHTSA
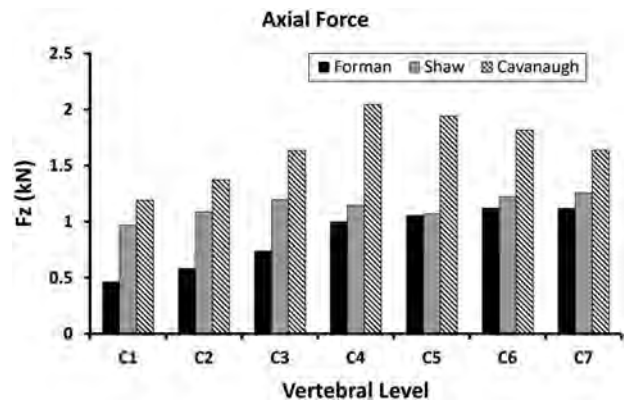
Figure 15. Distribution of axial forces for each vertebral level at the time of overall maximum axial force. Time of maximum axial force for the Forman, Shaw and Cavanaugh simulations occurred at $t = 70.2$, 121.3 and 30.8 ms, respectively.
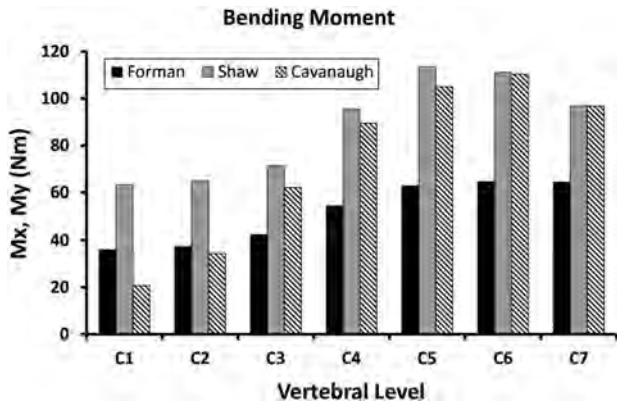
Figure 16. Distribution of bending moments for each vertebral level at the time of overall maximum bending moment. Time of maximum bending moment for the Forman, Shaw and Cavanaugh simulations occurred at $t = 122.4$, 144.9 and 46.2 ms, respectively. The flexion moment, My, was reported for the frontal Forman and Shaw simulations and the lateral bending moment, Mx, for the lateral Cavanaugh simulation.

2008a). The lateral moment replaced the flexion/extension moment in the calculation for the side impact test, and the critical moment intercept was changed to match that used in previous lateral impact tests (Soltis 2001; Green and Barth 2006; DeWeese et al. 2007).

For every point in time, only one of four loading scenarios exists when calculating N_{ij} (Table 4). The combined N_{ij} calculations are presented as time histories for each simulation at each cervical level (Figure 21). Maximum N_{ij} values for each cervical level are reported in Table 5. The maximum N_{ij} values for both frontal simulations were below the FMVSS 208 threshold of 1, corresponding to approximately 22% risk of serious (AIS $3 +$) injury (Figure 22) (Eppinger et al. 1999; Association for the Advancement of Automotive Medicine 2008). The maximum N_{ij} value for the Forman and Shaw simulations

Figure 17. Adjacent vertebral level axial force ratio at the time of overall maximum axial force. Time of maximum axial force for the Forman, Shaw and Cavanaugh simulations occurred at $t = 70.2$, 121.3 and 30.8 ms, respectively.

Figure 18. Adjacent vertebral level bending moment ratio at the time of overall maximum bending moment. Time of maximum bending moment for the Forman, Shaw and Cavanaugh simulations occurred at $t = 122.4$, 144.9 and 46.2 ms, respectively. The flexion moment ratio was reported for the frontal Forman and Shaw simulations and the lateral bending moment ratio for the lateral Cavanaugh simulation.

was 0.313 and 0.492 at C7, respectively. The maximum value for the Cavanaugh lateral impact simulation was 1.958 at C6. Neither FMVSS 208 nor its lateral impact counterpart, FMVSS 214 (NHTSA 2008b), specifies a maximum N_{ij} for lateral impacts.

Figure 19. D3plots corresponding to the approximate times of maximum neck force and moment for Forman: (a) axial force and (b) flexion moment; Shaw: (c) axial force and (d) flexion moment; Cavanaugh: (e) axial force and (f) lateral moment.
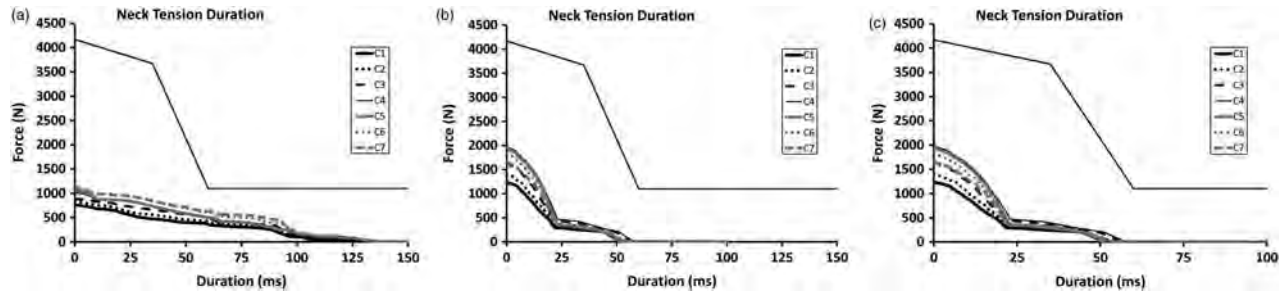
Figure 20. Neck tension duration results at each vertebral level with threshold boundary for the (a) Forman, (b) Shaw and (c) Cavanaugh simulations.

Table 3. N_{ij} critical intercept values for the OC–C1 junction as specified FMVSS 208 (NHTSA 2008a) and for the OC–C1 and C7–T1 junctions as specified by Mertz et al. (2003).

N_{ij} intercept	OC–C1 (FMVSS 208)	OC–C1 (IARV)	C7–T1 (IARV)
Ft	6806	6780	6780
Fc	−6160	−6200	−6200
Mf[a]	310	305	610
Me[a]	−135	−133	−266

[a] Replaced with ±60 for Cavanaugh lateral impact simulation (DeWeese et al. 2007; Green and Barth 2006; Soltis 2001).

Table 4. Summary of the four possible loading modes of the neck used in calculating N_{ij}.

N_{ij}	Loading mechanism	Force	Moment
N_{CF}	Compression/flexion	$F < 0$	$M > 0$
N_{CE}	Compression/extension	$F < 0$	$M < 0$
N_{TF}	Tension/flexion	$F > 0$	$M > 0$
N_{TE}	Tension/extension	$F > 0$	$M < 0$

Discussion

Methodology

This study created and utilised cross sections to calculate forces and moments within the neck of a total human body FE model during simulated frontal and lateral impacts. The local vertebral body coordinate systems were defined in a manner which can be easily replicated in any FE neck model. The nodes defining a LCSYS were constrained to their respective vertebra using *CNRBs, allowing the LCSYS to rotate. Even though the vertebrae were deformable bodies, no deformation was expected to
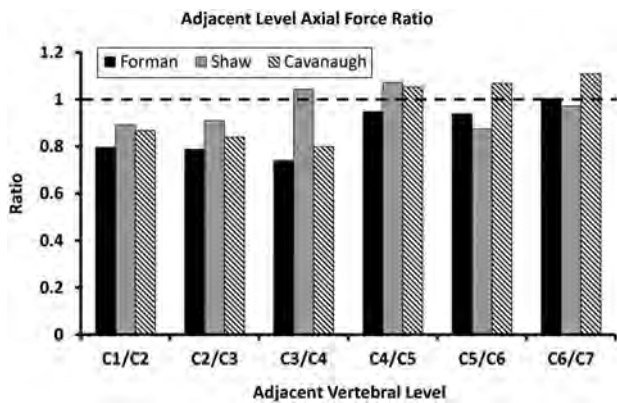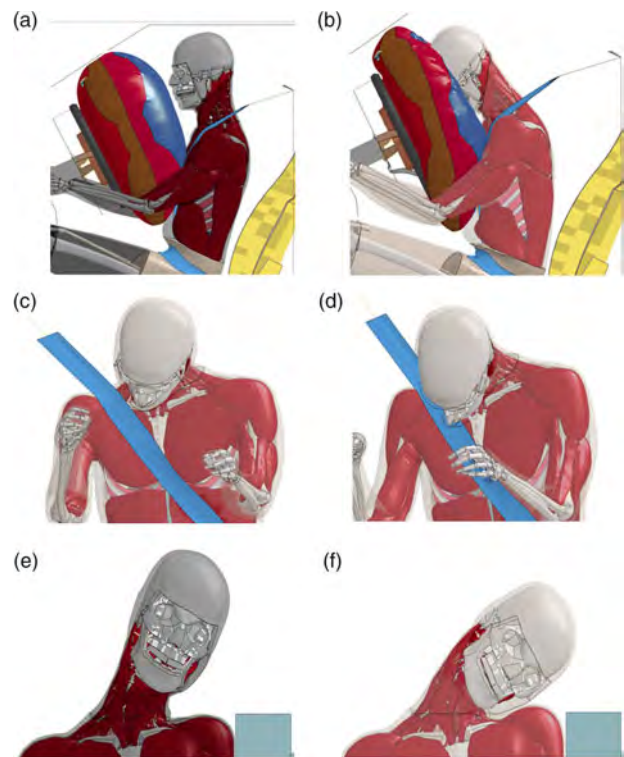
occur for the loading scenarios. Should comparison need to be made between tracked motion of the cadaver cervical spine using high-speed, biplane X-rays, an alternative LCSYS defined by Padgaonkar (1976) and utilised by White (2008, 2009) can be implemented. Using this alternative method, the local origin is placed at the anterior–superior vertebral body in the sagittal plane, not requiring the location of the CG.

The interface definitions created by the *DCSPs contain the elements and nodes associated with the cross sections, ensuring that elements are captured from only one side of each cut. Although the best results are obtained when the *DCSP cuts cleanly through the middle of all elements, this automatic interface definition handles irregularities quite well. The captured elements and nodes depend on the part sets defined by the user, as well as the placement of the *DCSPs. For this study, part sets were created based on anatomical components within the neck, including bones, IVDs, ligaments, soft tissue, active muscles and passive muscles. Because none of the *DCSPs cut through the IVDs, no forces or moments were reported for this component. The user can always add in additional *DCSPs to capture IVDs or other structures of interest. Once the nodes and elements for each cross section are captured, they are separated into element sets and used to define *DCSSs. This step allows the user even more control over which elements are included in a cross section. In addition, the creation of these element sets allows for visualisation and inspection of the elements and nodes automatically selected by the *DCSPs.

In LS-PrePost, the SPlane option is an interactive method to report cross-sectional data. Unlike *DCSPs or *DCSSs, the SPlane option reports cross-sectional forces and moments calculated from element stress resultants in

Table 5. Maximum N_{ij} value calculated at each cervical level.

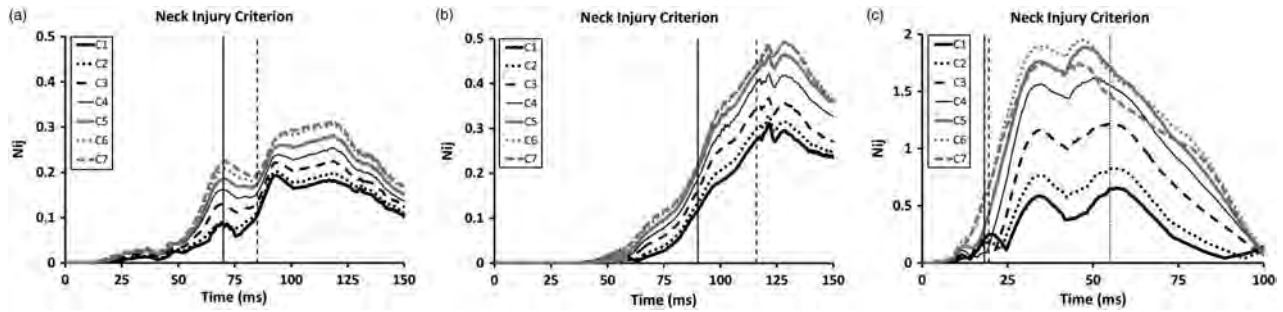| Simulation	C1	C2	C3	C4	C5	C6	C7
Forman	0.193	0.202	0.225	0.255	0.281	0.307	0.313
Shaw	0.312	0.329	0.367	0.422	0.464	0.491	0.492
Cavanaugh	0.656	0.826	1.217	1.618	1.887	1.958	1.744

Figure 21. N_{ij} time histories at each vertebral level for the (a) Forman, (b) Shaw and (c) Cavanaugh simulations. For the Forman simulation, the vertical solid line corresponds to the time of maximum engagement of the upper shoulder belt ($t = 70$ ms) and the vertical dashed line to the time of maximum occupant–airbag interaction ($t = 85$ ms). For the Shaw simulation, the vertical solid line corresponds to the time of maximum engagement of the upper shoulder belt ($t = 90$ ms) and the vertical dashed line to that of maximum engagement of the lower shoulder belt ($t = 116$ ms). For the Cavanaugh simulation, the vertical solid line corresponds to the time of maximum upper body-to-wall contact force ($t = 18$ ms), the vertical dashed line to the time of maximum pelvis-to-wall contact force ($t = 19.5$ ms) and the vertical dotted line to the approximate time of the maximum lateral rotation of C1 with respect to C7 in the frontal plane ($t = 55$ ms).

the d3plot data. There are three different methods of defining a cross-sectional cut with SPlane. The first two methods allow the section plane to be fixed in space so that it does not move once defined or to be fixed to the model so that it moves with the nodes used to define it. The Lagrangian cut option, most like *DCSP and *DCSS, captures a group of elements in the plane and tracks them throughout the d3plot animation, even if the elements move out of the plane. The SPlane options are considered less accurate than *DCSS or *DCSP which use nodal forces not included in the d3plots to calculate section forces. In addition, the sampling rate for the SPlane data is limited by the time interval between outputs for the d3plots, which are typically lower than the ASCII outputs due to the large data size of the file.

Figure 22. N_{ij} risk curves for AIS 3 + to AIS 5 + neck injuries. The FMVSS 208 maximum allowable N_{ij} value of 1 indicates approximately 22% risk for serious (AIS 3 +) injury (Eppinger et al. 1999; NHTSA 2008a).

Simulation results

Several interesting observations can be made from the force and moment time histories of the three simulations. Axial force tended to progressively increase from the upper to lower cervical levels. A sharp decrease in axial tension occurred at the time of maximum occupant–airbag interaction in the Forman simulation, attributed to interaction with the airbag. No such decrease in axial loading was noted in the Shaw simulation, which did not include an airbag. Significant AP shear forces were observed in C1 and C2 for both the Forman and Cavanaugh simulations. The main contributors of these forces were the ligaments. Unlike C3–C7, more extensive ligamentous structures exist between OC–C1–C2. In general, the flexion moment in the frontal simulations and the lateral moment in the side impact increased caudally. This was expected as the moment arm to the head increases from C1 to C7.

The reported force and moment ratios allow for comparison between adjacent vertebral levels. A ratio less than unity indicates that the force or moment at the superior vertebral level is less than the inferior level, whereas a ratio greater than unity indicates that the force or moment at the superior vertebral level is greater than the inferior level. The force ratios for the Forman and Cavanaugh simulations suggested a load distribution difference between the upper (C1–C3) and lower (C4–C7) neck. The Forman force ratios indicated that the axial forces increased caudally whereas the Cavanaugh ratios indicated that the axial forces increased caudally in the upper neck and cephalically in the lower neck. The force ratios for the Shaw simulation suggested a load distribution difference between the upper (C1–C3), middle (C4–C5) and lower (C6–C7) neck. This simulation used a generic three-point seatbelt with no retractor or load limiter, producing a more abrupt deceleration of the occupant than the load limiting retractor in the Forman simulation.
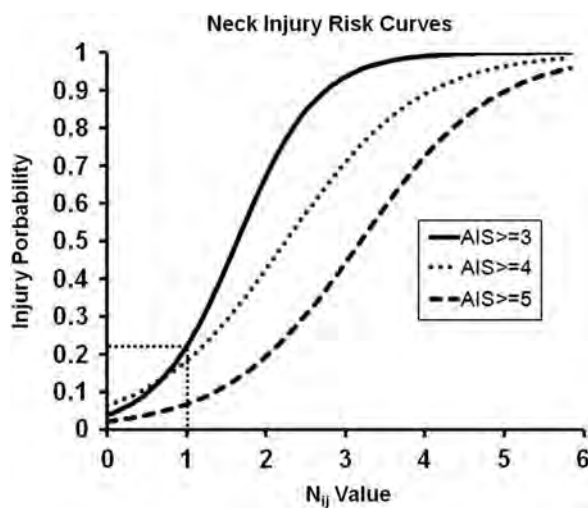
The maximum shoulder belt force for the Shaw simulation was approximately 5 kN whereas it was approximately 3.5 kN in the Forman simulation. The force ratios indicated that the axial forces increased caudally in the upper and lower neck and cephalically in the middle neck. This point of inflection in the middle neck may indicate a rotation point where the head begins to wrap around the shoulder belt with no airbag to counteract this motion.

For the Forman and Shaw frontal simulations, the moment ratios decreased between C1/C2 and C3/C4 and then increased up to C6/C7, whereas the Cavanaugh lateral simulation produced a steady increase in moment ratios from C2/C3 to C6/C7. The moment ratio concavity in the frontal simulations is most likely due to passive restraint interactions with the occupant. The occupant torso and pelvis in the lateral simulation were not restrained. The moment ratios also indicated that the moments increased caudally for all levels of the neck in all simulations, except the Cavanaugh C6/C7 and the Shaw C5/C6 and C6/C7 adjacent levels, where they increased cephalically.

None of the maximum or minimum forces and moments reported in Table 2 exceeded corresponding IARVs, indicating that significant injury to the neck was unlikely. The neck tension duration results were also well below the threshold boundaries. Although axial compression and AP shear duration plots could have also been created, it is unlikely that the corresponding injury thresholds would have been exceeded. Only minimal axial compression was noted and AP shear tended to be about half that of axial tension in the simulations. Although the N_{ij} criteria are currently used to evaluate injury risk at the OC-C1 junction per FMVSS 208 (NHTSA 2008a), lower neck critical intercepts do exist (Mertz et al. 2003). In this study, the N_{ij} criteria were applied to levels of the neck between the OC-C1 junction and T1. Because no critical intercept values currently exist for these levels, the FMVSS 208 specified force and moment intercepts were utilised for all levels of the neck as a worst-case scenario. Although the overall efficacy of N_{ij} in lateral impacts is unknown, it was modified slightly for use in the lateral Cavanaugh simulation (Soltis 2001; Green and Barth 2006; DeWeese et al. 2007).

It is important to note the contribution of the discrete spring elements to the overall cross-sectional results. As described in the section Methods', the force and moment contributions of these discrete elements were manually added to the total force and moment plots for completeness. These discrete elements represent the suprahyoid and infrahyoid muscles which suspend the hyoid bone in the GHBMC model. The stiffness values of these elements were chosen for computational purposes only. In a human, the primary actions of these muscles are to elevate and depress the hyoid bone during speaking and swallowing (Moore and Agur 2002), playing a minimal role in the kinematics of the neck. Although these muscles can actively create tension in the neck, they do not support compressive loads. The implementation of these discrete elements may seem counterintuitive. For example, during head flexion, the discrete elements develop a restoring force that counteracts the flexion moment, creating an extension moment. This is apparent when comparing the discrete element force and moment time histories with the anatomical component time histories. However, both the force and moment contributions of these discrete elements compose only a small fraction of the total forces and moments and are, therefore, considered negligible. The purpose of this study was to present a method to measure forces and moments at various levels of an FE human body model neck and demonstrate how these data can be used to evaluate the risk of injury based on IARVs and injury criteria. The described method can always be modified to exclude these discrete elements at the discretion of the user.

Limitations and future work

There are several limitations to this work. One is that there is no direct method to validate the forces and moments calculated at the different levels of the neck, as these values could not be measured in the actual cadaveric experiments. Although it is possible to estimate the forces and moments at the OC (Mertz and Patrick 1971) and T1 (Pintar et al. 2010) using inverse kinematic methods in cadavers, there is no direct measurement method. Traditionally, the inverse kinematic approaches have been acceptable and are, therefore, the best available data for comparison. The GHBMC T1 is modelled as a rigid body and, therefore, cannot be included in the cross-sectional definition. Modifications to the GHBMC neck model are underway to make T1 deformable. Converting T1 to a deformable body requires changing not only the material definition, but also any associated attachment points. Lastly, the elements initially defined in the ∗DCSSs for a particular cross section may potentially move out of plane as the neck deforms. Unless there is direct impact to the neck or extreme head motion, the potential for this to occur should be minimal. The reader is cautioned that the force and moment results depend on how the cross-sectional plane, captured elements and LCSYS are defined. Care was taken to choose the best cross sections for the intended purpose and to avoid redundant load measurement axially through the entire neck.

Future work includes studying the effects of both anterior cervical discectomy and fusion and cervical total disc replacement (CTDR) on adjacent vertebral levels using the described cross-sectional technique. The current literature debates whether cervical fusion deleteriously alters the loading of the adjacent segments, increasing adjacent-segment disease (ASD). By preserving motion

and loading distribution, some consider CTDRs a method to reduce the likelihood of ASD (Galbusera et al. 2008; Baaj et al. 2009; Bartels et al. 2010; Fekete and Porchet 2010; Kishen and Diwan 2010; Uschold et al. 2011). The use of cross sections to measure load contributions from the cervical zygapophysial and uncovertebral joints will also be investigated in future studies.

Conclusions

This paper described and implemented a method to determine cross-sectional forces and moments at various levels of a human body FE model neck during simulated frontal and lateral MVCs. Total force and moment time histories were reported for each vertebral and compared with established IARVs to determine whether significant injury was likely to occur. Adjacent level axial force ratios varied between 0.74 and 1.11 and adjacent level bending moment ratios varied between 0.55 and 1.15. The individual contribution of neck anatomical components to the total cross-sectional forces and moments was also evaluated. Neck tension time-dependent curves and N_{ij} time histories were calculated for each cervical level and compared with injury threshold standards. The procedure presented in this paper can be applied not only to the neck, but also to other regions of the body. It is helpful for full body FE models to provide transducer data similar to their physical counterparts, ATDs, to properly evaluate the safety of an automobile.

Acknowledgements

Notes

1. Email: niwhite@wakehealth.edu
2. Email: dmoreno@wakehealth.edu
3. Email: sgayzik@wakehealth.edu

References

Association for the Advancement of Automotive Medicine. 2008. Abbreviated Injury Scale © 2005 Update 2008. Barrington, IL.

Baaj AA, Uribe JS, Vale FL, Preul MC, Crawford NR. 2009. History of cervical disc arthroplasty. Neurosurg Focus. 27(3):E10.

Bartels RH, Donk R, Verbeek AL. 2010. No justification for cervical disk prostheses in clinical practice: a meta-analysis of randomized controlled trials. Neurosurgery. 66(6): 1153–1160, discussion 1160.

Bostrom O, Svensson M, Aldman B, Hansson H, Haland Y, Lovsund P, Seeman T, Suneson A, Saljo A, Ortengren T. 1996. A new neck injury criterion candidate based on injury findings in the cervical ganglia after experimental neck extension trauma. IRCOBI. p. 123–136.

Camacho D, Nightingale R, Robinette J, Vanguri S, Coates D, Myers B. 1997. Experimental flexibility measurements for the development of a computational head-neck model validated for near-vertex head impact. SAE Technical Paper 973345.

Cavanaugh J, Walilko T, Malhotra A, Zhu Y, King A. 1990a. Biomechanical response and injury tolerance of the pelvis in twelve sled side impacts. SAE Technical Paper 902305:1–12.

Cavanaugh J, Walilko T, Malhotra A, Zhu Y, King A. 1990b. Biomechanical response and injury tolerance of the thorax in twelve sled side impacts. SAE Technical Paper 902307:23-38.

Cavanaugh J, Zhu Y, Huang Y, King A. 1993. Injury and response of the thorax in side impact cadaveric tests. SAE Technical Paper 933127:199-221.

Dauvilliers F, Bendjellal F, Weiss M, Lavaste F, Tarrière C. 1994. Development of a finite element model of the neck. SAE Technical Paper 942210.

de Jager M, Sauren A, Thunnissen J, Wismans J. 1996. A global and a detailed mathematical model for head-neck dynamics. SAE Technical Paper 962430.

Deng YC, Fu J. 2002. Simulation and identification of the neck muscle activities during head and neck flexion whiplash. SAE Technical Paper 2002-01-0017.

Deng YC, Li X, Liu Y. 1999. Modeling of the human cervical spine using finite element techniques. SAE Technical Paper 1999-01-1310.

DeWeese R, Moorcroft D, Green T, Philippens MMGM. 2007. Assessment of injury potential in aircraft side-facing seats using the ES-2 anthropomorphic test dummy. Federal Aviation Administration, DOT/FAA/AM-07/13.

DeWit JA, Cronin DS. 2012. Cervical spine segment finite element model for traumatic injury prediction. J Mech Behav Biomed Mater. 10:138–150.

Eppinger R, Sun E, Bandak F, Haffner M, Khaewpong N, Maltese M, Kuppa S, Nguyen T, Takhounts E, Tannous R, et al. 1999. Development of improved injury criteria for the assessment of advanced automobile restraint systems – II. NHTSA, Docket No. 1999-6407-5.

Eppinger R, Sun E, Kuppa S, Saul R. 2000. Development of improved injury criteria for the assessment of advanced automobile restraint systems – II. NHTSA, Docket No. 2010-03-19.

Fekete TF, Porchet F. 2010. Overview of disc arthroplasty-past, present and future. Acta Neurochir (Wien). 152(3):393–404.

Fice JB, Cronin DS. 2012. Investigation of whiplash injuries in the upper cervical spine using a detailed neck model. J Biomech. 45(6):1098–1102.

Fice JB, Cronin DS, Panzer MB. 2011. Cervical spine model to predict capsular ligament response in rear impact. Ann Biomed Eng. 39(8):2152–2162.

Forman J, Lessley D, Kent R, Bostrom O, Pipkorn B. 2006. Whole-body kinematic and dynamic response of restrained PMHS in frontal sled tests. Stapp Car Crash J. 50:299–336.

Galbusera F, Bellini CM, Brayda-Bruno M, Fornari M. 2008. Biomechanical studies on cervical total disc arthroplasty: a

literature review. Clin Biomech (Bristol, Avon). 23(9):1095–1104.

Gayzik FS, Moreno DP, Danelson KA, McNally C, Klinich KD, Stitzel JD. 2012. External landmark, body surface, and volume data of a mid-sized male in seated and standing postures. Ann Biomed Eng. 40(9):2019–2032.

Gayzik FS, Moreno DP, Geer CP, Wuertzer SD, Martin RS, Stitzel JD. 2011. Development of a full body CAD dataset for computational modeling: a multi-modality approach. Ann Biomed Eng. 39(10):2568–2583.

Goldsmith W, Ommaya A. 1984. Head and neck injury criteria and tolerance levels. In: Aldman B, Chapon A, editors. The biomechanics of impact trauma. Amsterdam: Elsevier Science Publisher. p. 149–187.

Green T, Barth T. 2006. Injury evaluation and comparison of lateral impacts when using conventional and inflatable restraints. Creswell, OR: SAFE Association.

Halldin PH, Brolin K, Kleiven S, von Holst H, Jakobsson L, Palmertz C. 2000. Investigation of conditions that affect neck compression-flexion injuries using numerical techniques. Stapp Car Crash J. 44:127–138.

Heitplatz F, Sferco R, Fay P, Reim J, Kim A, Prasad P. 2003. An evaluation of existing and proposed injury criteria with various dummies to determine their ability to predict the levels of soft tissue neck injury seen in real world accidents. In: 18th International Technical Conference on the Enhanced Safety of Vehicles (ESV).

Hu J. 2007. Neck injury mechanism in rollover crashes – a systematic approach for improving rollover neck protection. [Detroit, MI]: Wayne State University.

Kishen TJ, Diwan AD. 2010. Fusion versus disk replacement for degenerative conditions of the lumbar and cervical spine: quid est testimonium? Orthop Clin North Am. 41(2):167–181.

Kleinberger M. 1993. Application of finite element techniques to the study of cervical spine mechanics. SAE Technical Paper 933131.

Kleinberger M, Sun E, Eppinger R, Kuppa S, Saul R. 1998. Development of improved injury criteria for the assessment of advanced automobile restraint systems. NHTSA, Docket No. 1998-4405-9.

Klinich K, Saul R, Auguste G, Backaitis S, Kleinberger M. 1996. NHTSA Child Protection Team. Techniques for Developing Child Dummy Protection Reference Values. NHTSA, Docket No. 74-14, Notice 97, Item 069.

Kumaresan S, Yoganandan N, Pintar F. 1997. Age-specific pediatric cervical spine biomechanical responses: three-dimensional nonlinear finite element models. SAE Technical Paper 973319.

Mattucci SF, Moulton JA, Chandrashekar N, Cronin DS. 2012. Strain rate dependent properties of younger human cervical spine ligaments. J Mech Behav Biomed Mater. 10:216–226.

Maurel N, Lavaste F, Skalli W. 1997. A three-dimensional parameterized finite element model of the lower cervical spine. Study of the influence of the posterior articular facets. J Biomech. 30(9):921–931.

McElhaney J, Nightingale R, Winkelstein B, Chancey V, Myers B. 2002. Biomechanical aspects of cervical trauma. In: Nahum A, Melvin J, editors. Accidental injury: biomechanics and prevention. New York: Springer. p. 324–373.

McHenry R. 1963. Analysis of the dynamics of automobile passenger-restraint systems. In: 7th Stapp Car Crash Conference.

Mertz HJ. 2002. Anthropomorphic test device. In: Nahum A, Melvin J, editors. Accidental injury: biomechanics and prevention. New York: Springer.

Mertz HJ, Irwin AL, Prasad P. 2003. Biomechanical and scaling bases for frontal and side impact injury assessment reference values. Stapp Car Crash J. 47:155–188.

Mertz HJ, Nyquist GW, Hodgson VR, Weber DA. 1982. Response of animals exposed to deployment of various passenger inflatable restraint system concepts for a variety of collision severities and animal positions. SAE Technical Paper 826047.

Mertz HJ, Patrick L. 1971. Strength and response of the human neck. SAE Technical Paper 710855.

Mertz HJ, Weber DA. 1982. Interpretations of the impact responses of a 3-year-old child dummy relative to child injury potential. SAE Technical Paper 826048.

Meyer F, Bourdet N, Deck C, Willinger R, Raul JS. 2004. Human neck finite element model development and validation against original experimental data. Stapp Car Crash J. 48:177–206.

Moore KL, Agur AMR. 2002. Essential clinical anatomy. New York: Lippincott, Williams and Wilkins. p. 592–642.

National Spinal Cord Injury Statistical Center. 2011. The 2011 annual statistical report for the spinal cord injury model. University of Alabama at Birmingham.

NHTSA. 2008a. Title 49 Code of Federal Regulations (CFR) Part 571 Section 208, Occupant Crash Protection. Washington, DC: Office of the Federal Register, National Archives and Records Administration.

NHTSA. 2008b. Title 49 Code of Federal Regulations (CFR) Part 571 Section 214, Side Impact Protection. Washington, DC: Office of the Federal Register, National Archives and Records Administration.

Nitsche S, Krabbel G, Appel H, Huag E. 1996. Validation of a finite-element model of the human neck. In: International IRCOBI Conference on the Biomechanics of Impacts. Dublin, Ireland.

Padgaonkar AJ. 1976. Validation study of a three-dimensional crash victim simulator for pedestrian-vehicle impact. [Detroit, MI]: Wayne State University.

Pintar FA, Yoganandan N, Maiman DJ. 2010. Lower cervical spine loading in frontal sled tests using inverse dynamics: potential applications for lower neck injury criteria. Stapp Car Crash J. 54:133–166.

Prasad P, Chou CC. 2002. A review of mathematical occupant simulation models. In: Nahum A, Melvin J, editors. Accidental injury: biomechanics and prevention. 2nd ed. New York: Springer. p. 121–186.

Prasad P, Daniel RP. 1984. A biomechanical analysis of head, neck, and torso injuries to child surrogates due to sudden torso acceleration. SAE Technical Paper 841656.

Saito T, Yamamuro T, Shikata J, Oka M, Tsutsumi S. 1991. Analysis and prevention of spinal column deformity following cervical laminectomy. I. Pathogenetic analysis of postlaminectomy deformities. Spine (Phila Pa 1976). 16(5):494–502.

Schmitt K-U, Muser M, Walz F, Niederer P. 2002. N_{km} – a proposal for a neck protection criterion for low speed rear-end impacts. Traffic Injury Prevent. 3(2):117–126.

Schmitt K-U, Niederer P, Muser M, Walz F. 2010. Trauma biomechanics: accidental injury in traffic and sports. New York: Springer.

Shaw G, Parent D, Purtsezov S, Lessley D, Crandall J, Kent R, Guillemot H, Ridella SA, Takhounts E, Martin P. 2009. Impact response of restrained PMHS in frontal sled tests:

skeletal deformation patterns under seat belt loading. Stapp Car Crash J. 53:1–48.

Society of Automotive Engineers. 2007. SAE J211/1 – Instrumentation for Impact Test-Part 1-Electronic Instrumentation.

Society of Automotive Engineers. 2010. SAE J1727 – Calculation Guidelines for Impact Testing.

Soltis S. 2001. An overview of existing and needed neck impact injury criteria for sideward facing aircraft seats. In: Proceedings of the Third Triennial International Aircraft Fire and Cabin Safety Research Conference.

Stitzel JD. 2011. Global Human Body Models Consortium (GHBMC) Male 50th Percentile (M50) Occupant Model Manual. Virginia Tech – Wake Forest University Center for Injury Biomechanics.

United Nations Economic Commission for Europe. 2007. Addendum 93, Regulation No. 94, Uniformed provisions concerning the approval of vehicles with regard to the protection of the occupants in the event of a frontal collision.

Uschold TD, Fusco D, Germain R, Tumialan LM, Chang SW. 2011. Cervical and lumbar spinal arthroplasty: clinical review. AJNR Am J Neuroradiol. 33(9):1631–1641.

van der Horst M, Thunnissen J, Happee R, van Haaster R. 1997. The influence of muscle activity on head-neck response during impact. SAE Technical Paper 973346.

Vavalle NA, Moreno DP, Rhyne AC, Stitzel JD, Gayzik FS. 2012. Lateral impact validation of a geometrically accurate full body finite element model for blunt injury prediction. Ann Biomed Eng. 41(3):497–512.

White NA, Begeman P, Hardy W, Yang KH, Ono K, Sato F, Kamiji K, Yasuki T, Bey M. 2009. Investigation of upper body and cervical spine kinematics of post mortem human subjects (PMHS) during low-speed, rear-end impacts. SAE Technical Paper 2009-01-0387.

White NA, Hu J, Yang KH. 2008. Conceptual development of a personalised whiplash protection system. Int J Veh Saf. 3(2):163–178.

Yang KH, Hu J, White NA, King AI, Chou CC, Prasad P. 2006. Development of numerical models for injury biomechanics research: a review of 50 years of publications in the Stapp Car Crash Conference. Stapp Car Crash J. 50:429–490.

Yang KH, Zhu F, Luan F, Zhao L, Begeman P. 1998. Development of a finite element model of the human neck. Technical Paper 983157.

Yoganandan N, Haffner M, Maiman DJ, Nichols H, Pintar F, Jentzen J, Weinshel S, Larson SJ, Sances A. 1989. Epidemiology and injury biomechanics of motor vehicle related trauma to the human spine. SAE Technical Paper 892438.

Zhang QH, Teo EC, Ng HW. 2005. Development and validation of a CO-C7 FE complex for biomechanical study. J Biomech Eng. 127(5):729–735.

Appendix A

Projected cross-sectional visualisation of the neck at each vertebral level (C1–T1) including the bone, passive muscles and soft tissue. Beam (ligaments and active muscles) and discrete elements are not shown. Although included for completeness, forces and moments were not calculated at the level of T1 because this vertebra is currently defined as a rigid body and cannot be included in a cross section.
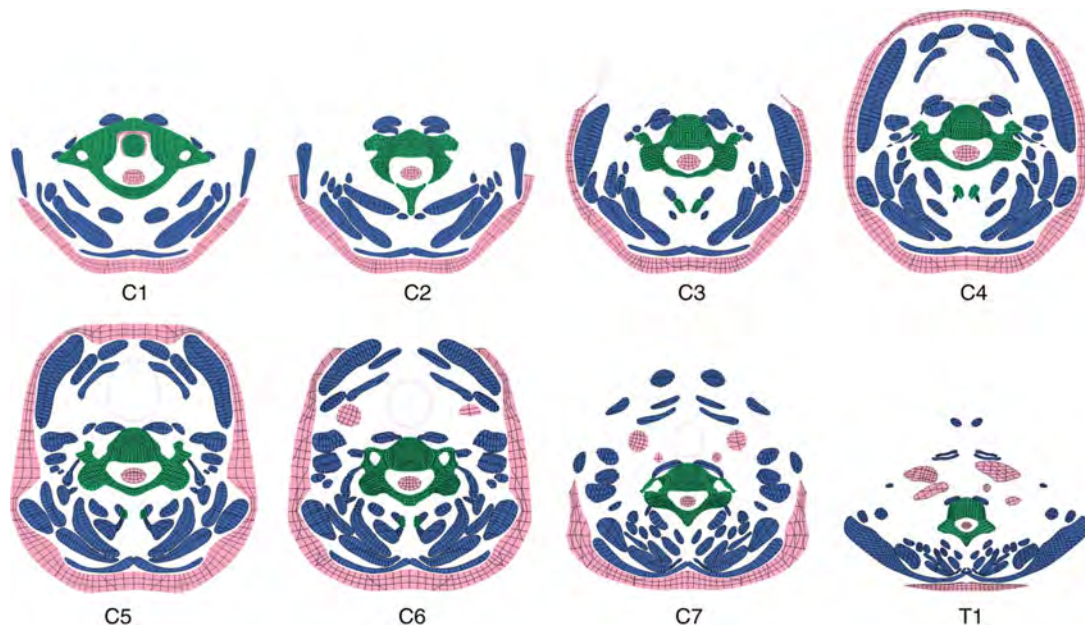
Appendix B

Forman frontal impact simulation – individual force and moment time histories of bone, ligament, active muscle, passive muscle, soft tissue anatomical components and discrete elements loading contributions in the rotated, LCSYS for each respective vertebral level.

—C1 z ··· C2 z --C3 z —C4 z —C5 z ··· C6 z --C7 z

—C1 z ··· C2 z --C3 z —C4 z —C5 z ··· C6 z --C7 z
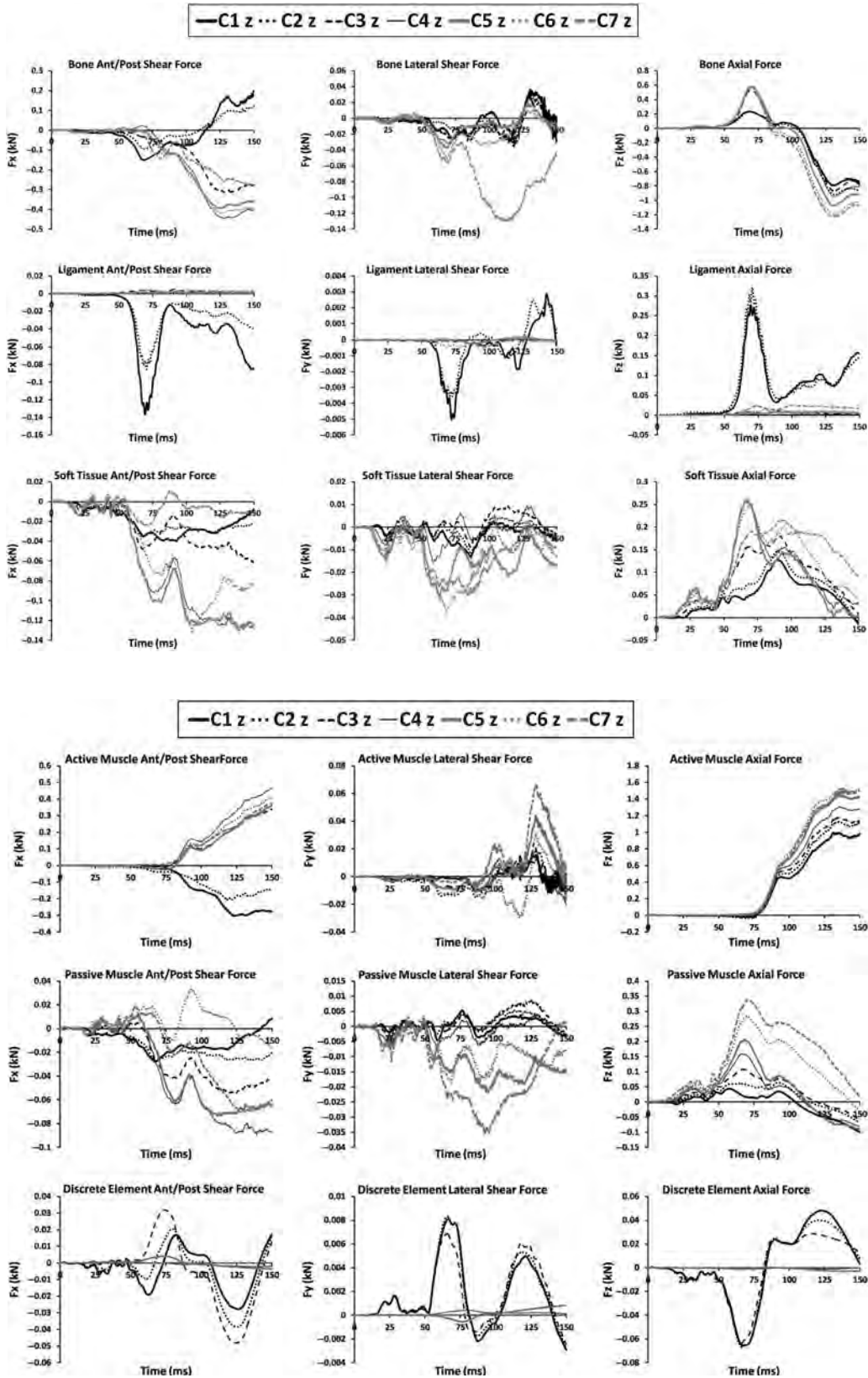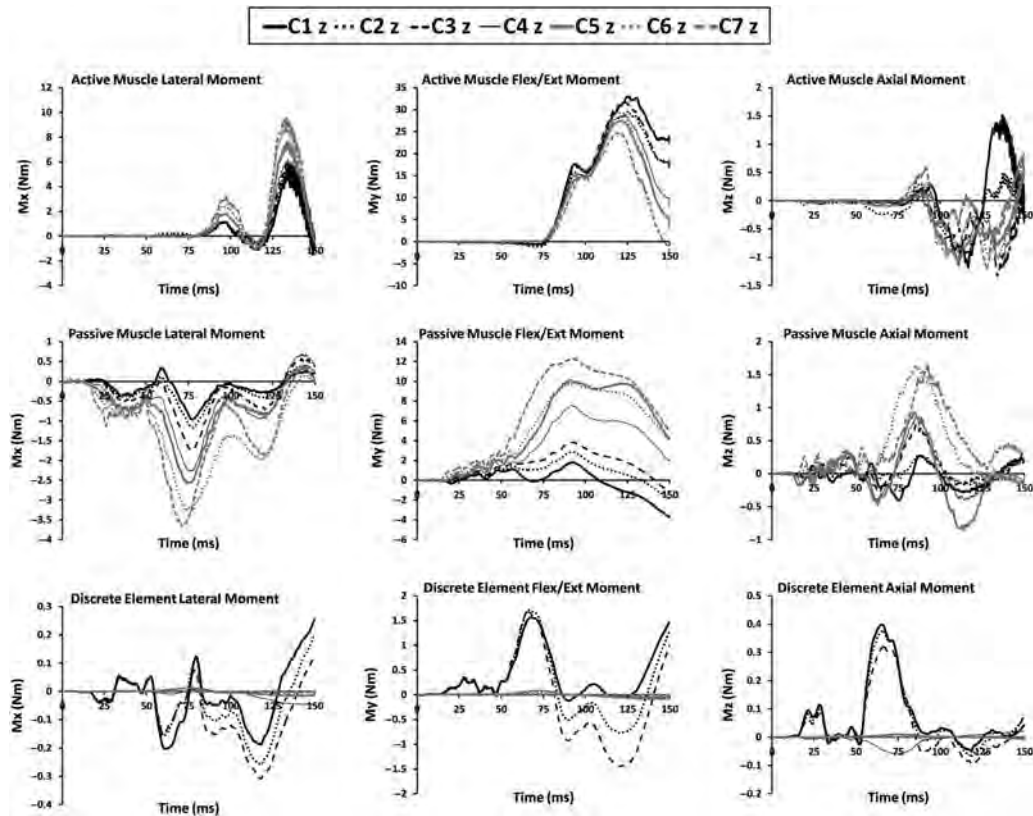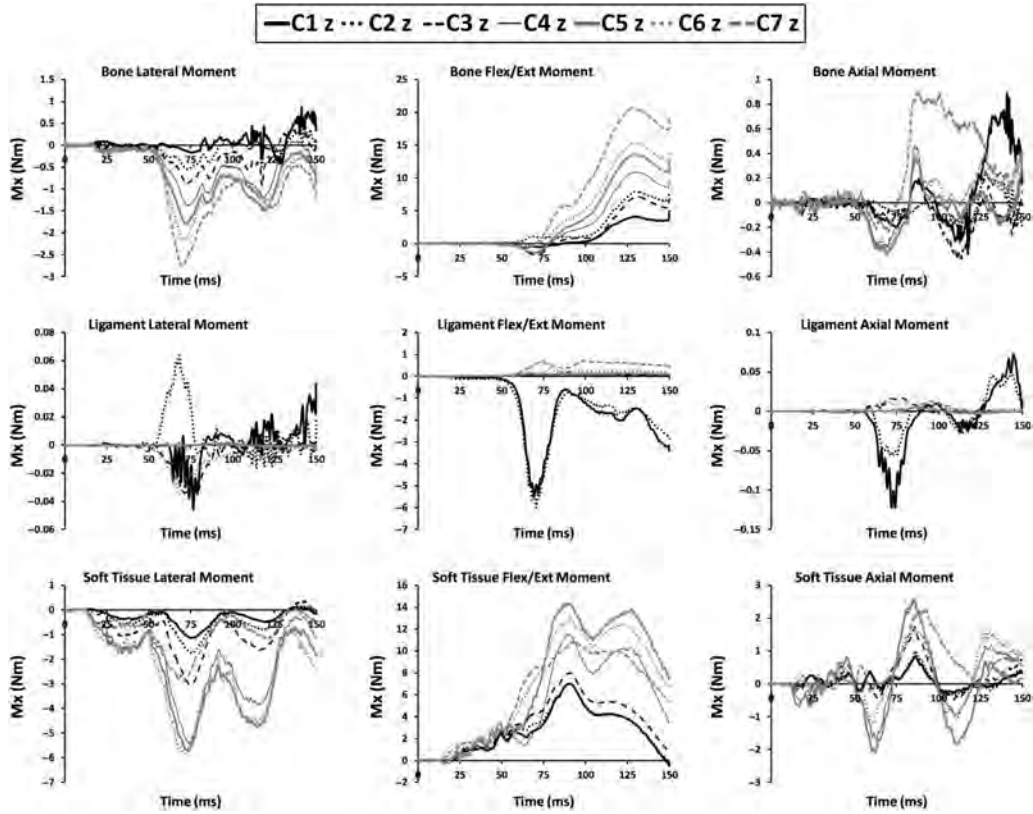
Appendix C

Shaw frontal impact simulation – individual force and moment time histories of bone, ligament, active muscle, passive muscle, soft tissue anatomical components and discrete elements loading contributions in the rotated, LCSYS for each respective vertebral level.
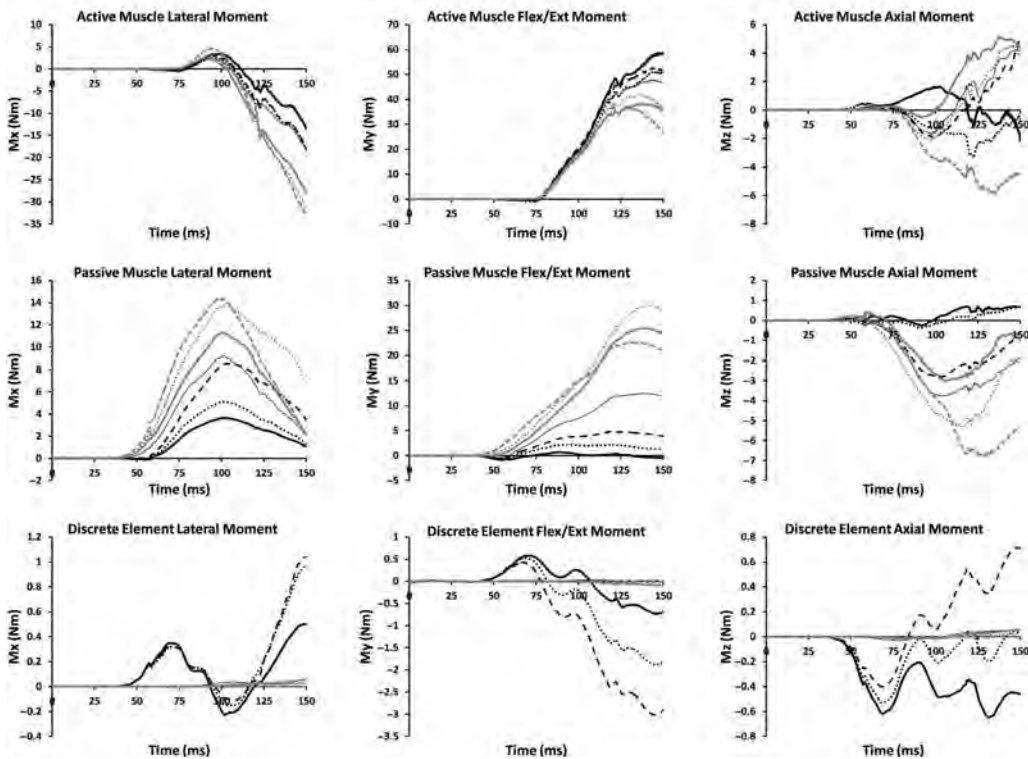
Appendix D

Cavanaugh lateral impact simulation – individual force and moment time histories of bone, ligament, active muscle, passive muscle, soft tissue anatomical components and discrete elements loading contributions in the rotated, LCSYS for each respective vertebral level.

Taylor & Francis
Taylor & Francis Group
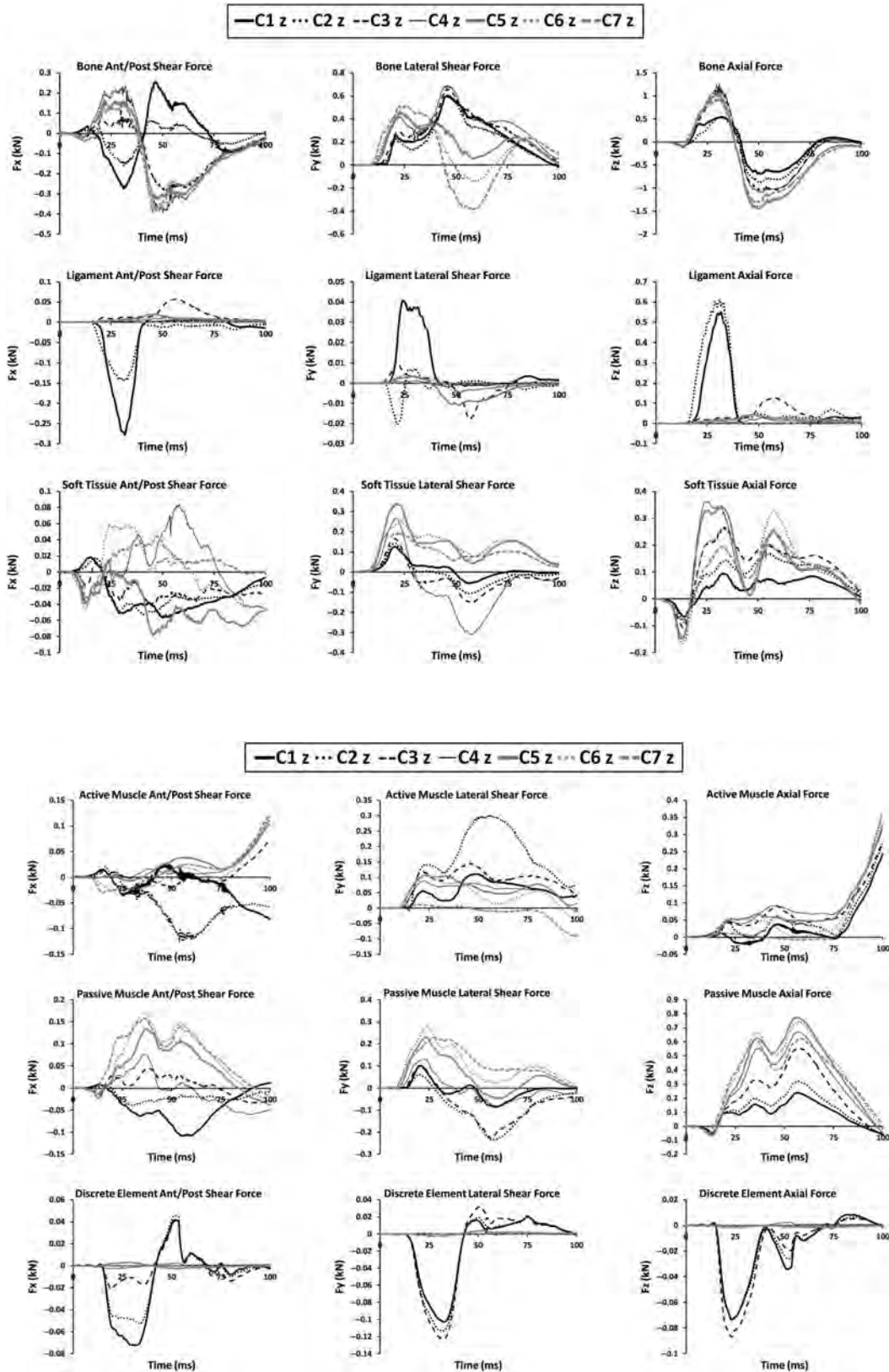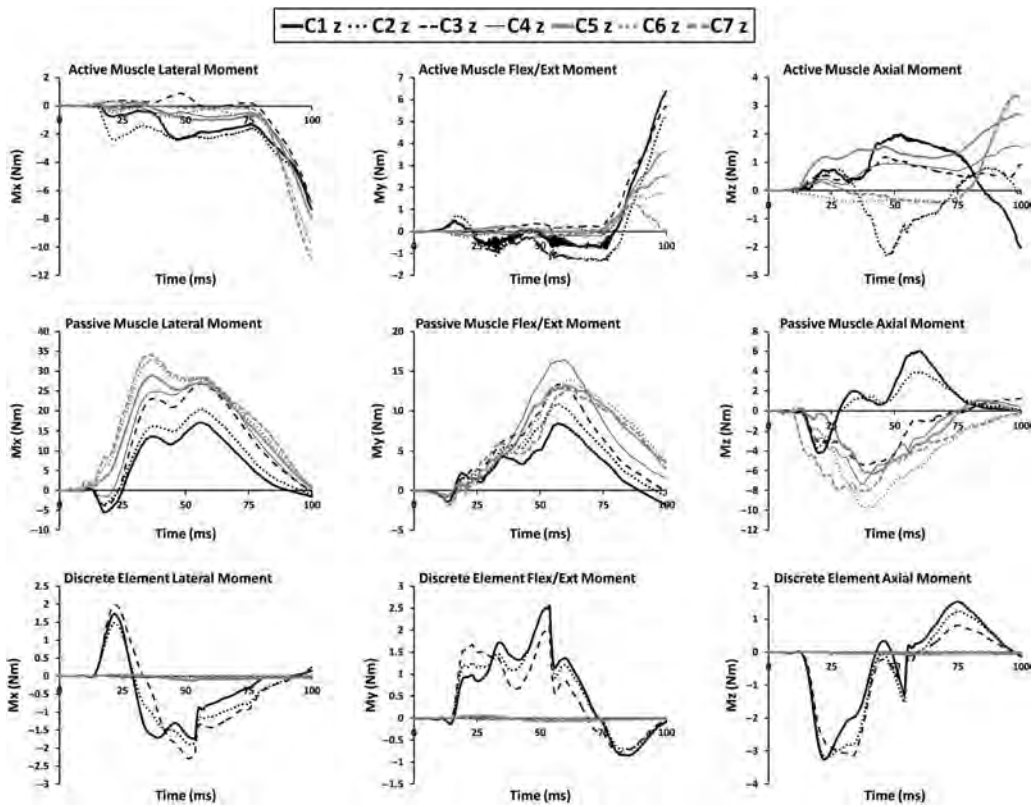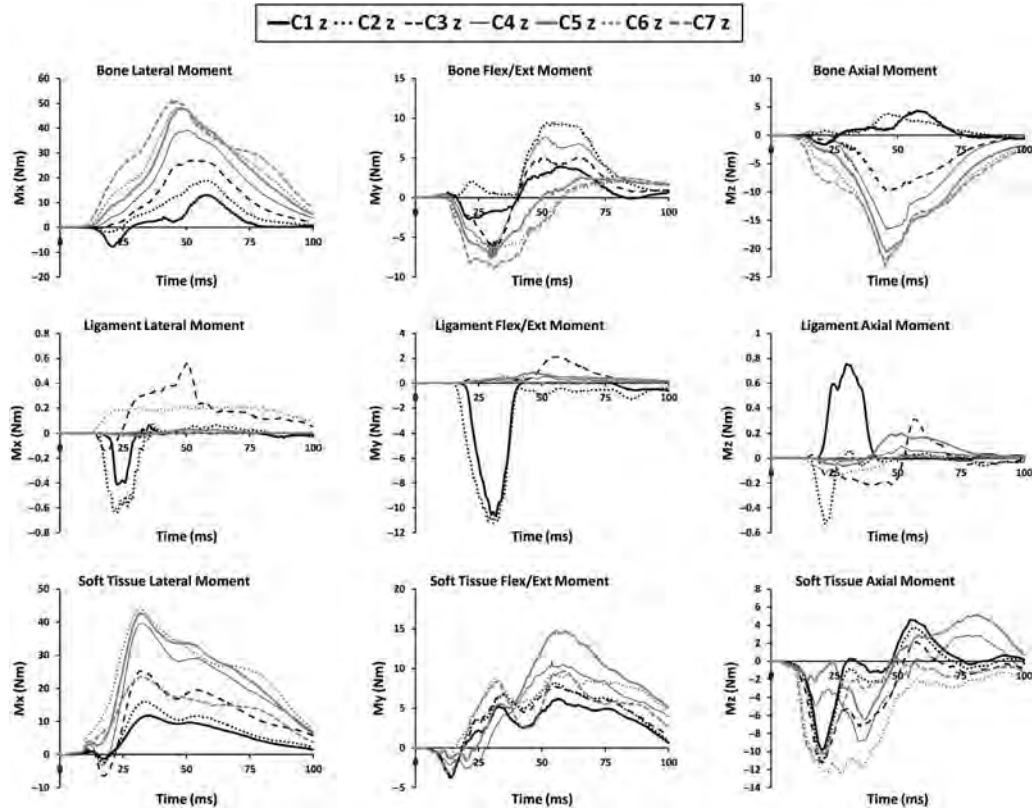
Effects of cervical arthroplasty on neck response during a simulated rotary-wing aircraft impact

Nicholas A. White [ID][a], Kerry A. Danelson[a], F. Scott Gayzik[a], Wesley Hsu[b], Alexander Powers[b] and Joel D. Stitzel[a]

[a]Virginia Tech-Wake Forest University Center for Injury Biomechanics, Winston-Salem, NC, USA; [b]Department of Neurosurgery, Wake Forest University School of Medicine, Winston-Salem, NC, USA

ABSTRACT

A computational finite element analysis was performed to evaluate the effects of C5-6 cervical total disc replacement (CTDR) on cross-sectional neck loading and cervical spine kinematics during a simulated rotary-wing aircraft ground impact. The neck of a human body finite element model was modified to include a C5-6 interbody arthroplasty with either a Prestige ST or ProDisc-C CTDR. The adjacent-level, cross-sectional loading for the C5-6 segment was not greatly altered by the CTDRs, as indicated by CORrelation and Analysis (CORA) ratings of 0.988 for the Prestige ST and 0.909 for the ProDisc-C. The CTDRs increased the interbody range of motion, altering both the interbody and cervical facet loading. While the facet capsules experienced inc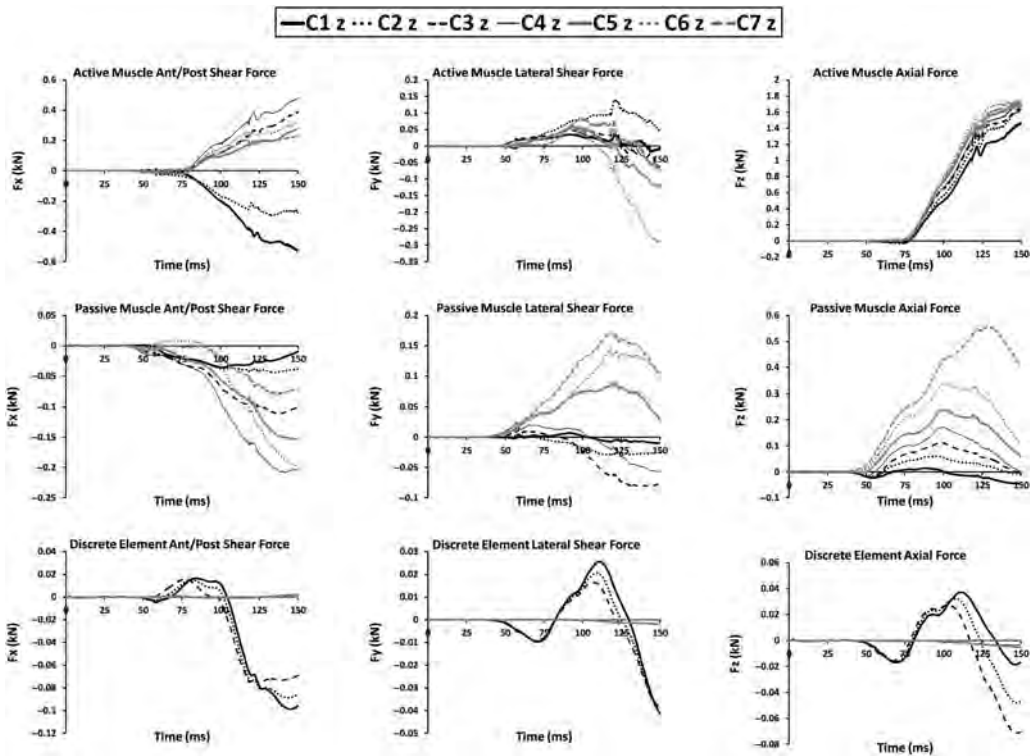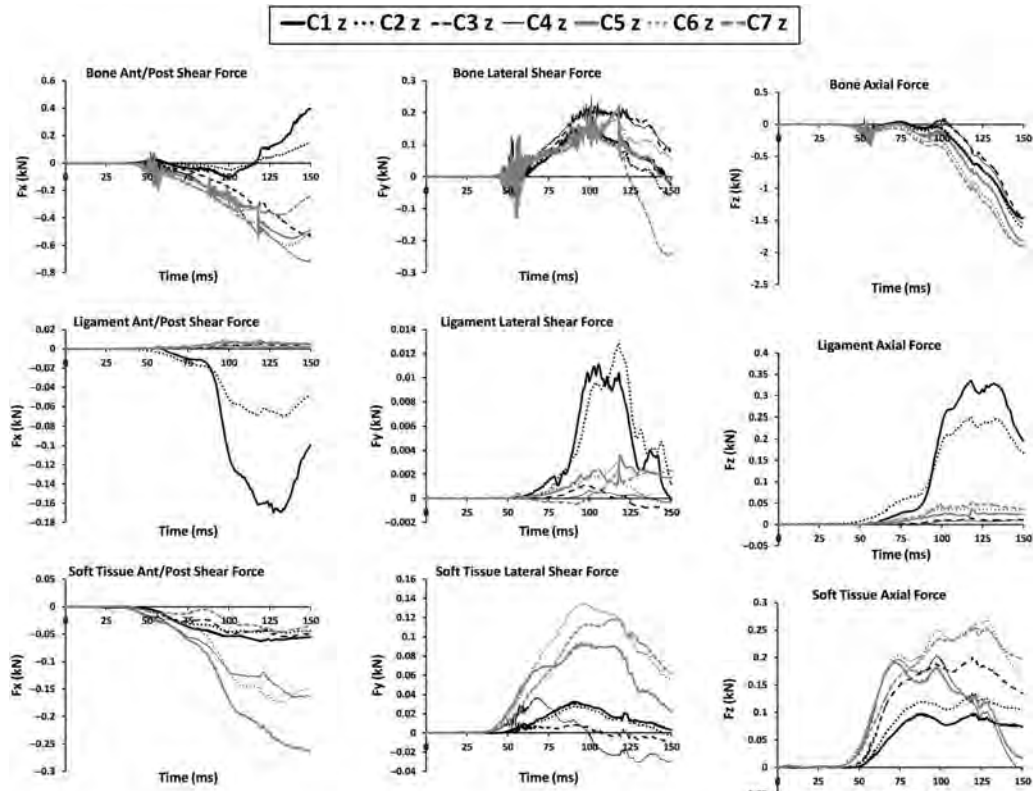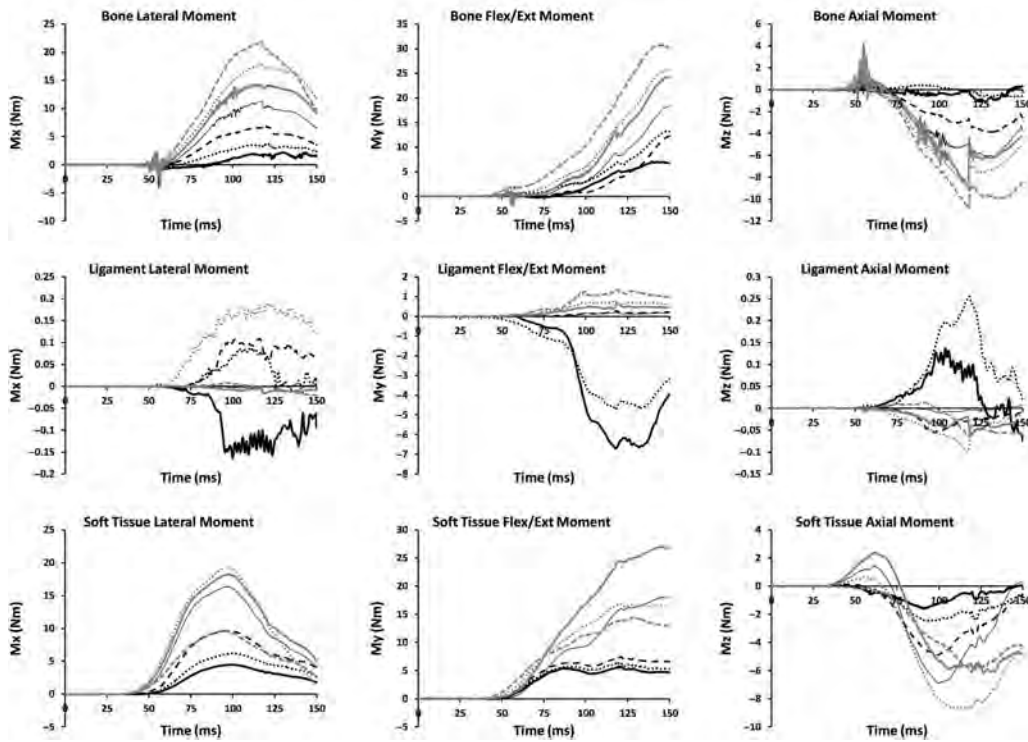reased tension in both CTDR simulations, established injury threshold levels were not reached. Overall, cervical arthroplasty at the C5-6 level did not appear to have a deleterious effect on the dynamic neck response during a simulated rotary-wing aircraft impact.

Introduction

While degeneration of the intervertebral discs (IVDs) is part of the normal ageing process, it typically remains asymptomatic in most individuals [9,42,46,66]. However, surgical intervention may be required should clinical symptoms manifest, such as axial neck pain, radiculopathy, or myelopathy. Several previous studies have investigated the epidemiology of degenerative disc disease (DDD) in active-duty military personnel. Between 2001 and 2010, DDD was diagnosed in 131,986 active-duty US military personnel with an overall incidence rate of 9.51 per 1000 person-years [53]. During this 10-year timespan, DDD-specific and DDD-related medical encounters resulted in a total of 90,855 lost duty days. Pilot and aircrew personnel composed 5505 of those individuals diagnosed with DDD, corresponding to a 9.87 per 1000 person-years incident rate [53]. An earlier study reported the incidence rate of herniated nucleus pulposus to be 1 per 1000 aviator-years in US Army aviators [45]. Flight status was permanently revoked in approximately 7.4% of the diagnosed aviators.

Between 2000 and 2009, cervical radiculopathy was diagnosed in 24,742 active-duty US military personnel, corresponding to an incidence rate of 1.79 per 1000

person-years [69]. Even though cervical radiculopathy may result from cervical spondylosis or spinal stenosis, it has been reported that 56% of surgeries to treat degenerative cervical spine disease involved DDD [81]. When non-operative treatment fails to adequately control the symptoms of DDD, fusion or arthroplasty may be required. Anterior cervical discectomy and fusion (ACDF) has remained the primary surgical treatment for symptomatic cervical degenerative disc disease (CDDD) for more than half a century [4,14,54,70]. While ACDF is an effective treatment for CDDD, the procedure does alter the biomechanics of the cervical spine, potentially increasing the occurrence of adjacent segment degeneration (ASD) [47,78]. In an effort to maintain same-level and adjacent-level physiologic motion and loading, cervical arthroplasty has become more common as an alternative to ACDF [1,3,54,75]. Even though experimental and computational studies have supported the functional equivalence between a cervical total disc replacement (CTDR) and an IVD [19,28,43,63,86], there is still much debate on the efficacy of cervical arthroplasty in preventing ASD [10,13,21,25,49,51,52, 55,67,73,77,88,89]. Irrespective of the ASD mitigation abilities of CTDRs, several studies have reported greater improvement in neurological

---

CONTACT Nicholas A. White ✉ whiten@vt.edu

symptoms and a shorter post-operative recovery time for cervical arthroplasty as compared to fusion [34,52,59].

Military spine surgeons have shown an increased interest in cervical arthroplasty as a means to safely expedite recovery time in members of the armed forces afflicted with CDDD [37,76]. While some medical waiver guidelines have been established to determine the physical readiness of a service member after CDDD surgery [15–17], final discretion lies with the surgeon. Unlike the general population, military personnel are subjected to many physically demanding tasks, potentially increasing their risk of spinal injury [6,35,38,62]. It is important to ensure that surgical treatment for CDDD does not place these individuals at a greater risk of injury. Preliminary studies have indicated that military recipients of cervical arthroplasty were able to return to full unrestricted duty with little to no complications [37,76]. However, more research is required to evaluate dynamic neck response post-arthroplasty, particularly for military helicopter pilots [64,65].

Experimental sled tests have been previously conducted by the Naval Air Warfare Center Aircraft Division (NAWCAD, Patuxent River, MD) to evaluate the effects of varying helmet weight and centre of gravity (CG) on aviator neck response during rotary-wing aircraft crashes using Hybrid III 5th, 50th, and 95th percentile anthropomorphic test devices (ATDs) [60,61]. A rigid, crashworthy seat system was mounted to a horizontal accelerator, oriented to represent a 30° pitch-down impact scenario. White et al. previously developed and validated a finite element (FE) environment for one of these experimental sled tests (#530) [83]. This study reported the head acceleration, chest acceleration, and upper and lower neck loading response of the Global Human Body Models Consortium (GHBMC) 50th percentile seated, male model (v3.5). The accelerations and loading were comparable, in magnitude and phase, between the GHBMC simulation, ATD simulation, and ATD physical test. Additionally, the change in curvature of the GHBMC cervical spine was consistent with the change in curvature observed in cadavers subjected to similar loading conditions [5,7].

The purpose of the current study was to evaluate the effects of C5-6 CTDR on cross-sectional neck loading and cervical spine kinematics of the GHBMC model during a simulated rotary-wing aircraft ground impact. Cross-sectional neck loading was captured at each level of the cervical spine, along with the midsagittal kinematics of the C5-6 segments.

Methods

Three rotary-aircraft crash FE simulations were conducted in LS-DYNA (R4.2.1, LSTC, Livermore, CA)
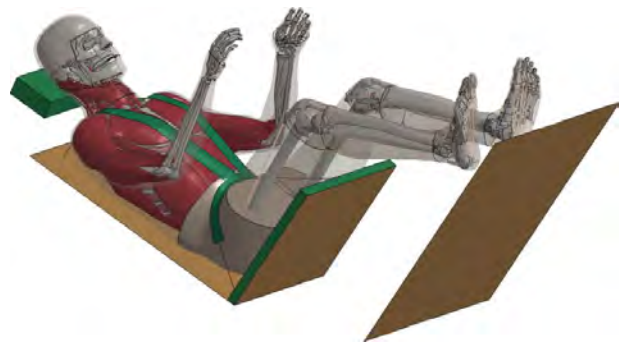
Figure 1. Initial position of the GHBMC model, including the five-point restraint system.

using the GHBMC model as a surrogate aviator (Figure 1). This model is a high-fidelity human body model developed to investigate human body response during dynamic impact events and validated in various impact scenarios [29,33,79,80]. The neck has been validated on a segmental level, as well as on the full cervical spine level [18,26,27,48,57,58,72]. On a segment level, the cervical spine has been validated in axial rotation, flexion, extension, lateral bending, and translation [57]. In the majority of the simulations, the predicted response fell within one standard deviation of the experimental response corridors. The biofidelity of the cervical spine has also been evaluated using a combined corridor and cross-correlation analysis which yields a score from 0 (no correlation) to 1 (perfect correlation) [87]. Model biofidelity is considered 'good' if the score falls between 0.65 and 0.86 [36]. The kinematic response of the cervical spine in quasi-static segment flexion and extension and quasi-static whole spine tension was assessed [58]. A total biofidelity assessment score of 0.89 was achieved for quasi-static loading, with a 0.83 score for bending and 0.96 score for tension. The kinematic response of the head from dynamic frontal impact scenarios was also assessed [58]. A total biofidelity assessment score of 0.68 was achieved for dynamic loading, with a 0.67 score for the 8 g case and 0.68 score for the 15 g case. The tissue-level failure response of the cervical spine has been validated in tension, compression, flexion, and extension [18]. The model proved capable of predicting the failure locations reported in the experimental testing and of predicting peak failure forces within the reported experimental corridors. The neck is composed of the seven cervical vertebrae with detailed facet joints and intervertebral discs. It also includes non-linear, rate dependent ligaments, 3D passive muscles and 1D active muscles.

The rotary-aircraft crash simulations were based on NAWCAD experimental test #530 [60,61]. In this test, a Hybrid III 50th percentile ATD was secured with a five-

point restraint to a rigid, crashworthy seat system mounted to a horizontal accelerator. The seat was oriented to represent a 30° pitch-down rotary-aircraft impact scenario. The prescribed crash pulse represented the seat pan acceleration of an energy absorbing seat structure during a survivable rotary-aircraft impact. This pulse consisted of a 7.62 m/s delta-V and 16.25 g peak acceleration. An additional 1.81 kg of mass, representing the weight of a helmet, was added to the ATD head. The distribution of this mass essentially maintained the original centre of mass of the head. This additional helmet mass was added to the GHBMC skull using the LS-Pre-Post (4.0, LSTC, Livermore, CA) mass trimming function. This built-in function allows the user to modify part mass properties to obtain a desired mass, centre of mass, and inertia. The additional 1.81 kg of helmet mass was automatically distributed as nodal masses about the skull in a manner that maintained the original head CG, consistent with the experimental set-up. Experimental preloading of the restraint system was simulated using a pretensioner system in the model. To allow for settling due to gravity and initial belt tensioning, the simulation was run for 70 ms prior to the start of the sled pulse.

Two of the three simulations included a C5-6 CTDR; either the Prestige ST (Medtronic, Minneapolis, MN) or the ProDisc-C (Synthes, West Chester, PA) [84]. The Prestige ST is a metal-on-metal implant capable of three-axis rotation and anteroposterior (AP) translation due to its ball-and-trough design (Figure 2(a)). Vertebral body (VB) screws are used to secure it to the adjacent VBs. The ProDisc-C is a metal-on-polymer implant with a ball-and-socket design, allowing for three-axis rotation (Figure 2(b)). It is press-fit between adjoining vertebrae, with central keels implanted into the adjacent VBs. The geometries of both these CTDRs were reverse engineered from a physical implant with material properties listed in Table 1 [20,22,32,86]. Prior to insertion of these CTDRs, several modifications consistent with the actual surgical procedure were made to the neck model. The IVD, end-plates, and anterior longitudinal ligaments associated
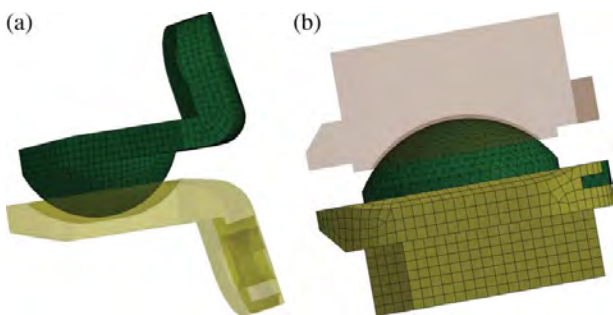
Table 1. Material properties assigned to the cervical implants.

Implant	Part	Material model	Element	ρ (kg/mm³)	E (GPa)	ν
Prestige ST	End plates	Rigid — 316L SST[a]	Shell	8.00E-06	190	0.3
ProDisc-C	End plates	Rigid — CoCrMo[b]	Shell	8.30E-06	210	0.3
	Insert	Elastic — UHMWPE[c]	Solid	9.36E-07	1.3	0.3

[a]SST: stainless steel.
[b]CoCrMo: cobalt-chromium-molybdenum.
[c]UHMWPE: ultra-high-molecular-weight-polyethylene.

with this level of the cervical spine were removed. The geometry of the C5 and C6 vertebral bodies were modified using select element deletion and advanced morphing techniques (Figure 3). The CTDRs were secured to the vertebrae using tied node contacts. The modelled CTDRs and C5-6 modifications were then reviewed and approved by board certified neurosurgeons.

Cross sections were defined at each cervical level to capture neck forces and moments using a method previously described by White et al. [85]. A local coordinate system (LCS) was defined for each cervical vertebrae with its origin located at the CG of the respective vertebrae. Positive-x was directed to the midpoint of the superior and inferior portion of the anterior vertebral body in the midsagittal plane. Positive-z was directed inferiorly to the vertebra along the midsagittal plane, orthogonal to the local x-axis. A cross section was then defined for each local xy-plane, with forces and moments reported in the LCS. Force and moment polarity, according to head–chest manipulation, is described in Table 2 [71]. Cross sections were also used to capture forces transmitted though the C5-6 IVD of the unmodified neck and C5-6 facets for all neck models. The IVD and facet cross-sectional forces, as well as the implant contact forces, were reported in the C6 LCS. The cross-sectional results were post-processed using Oasys T/HIS (v11, Arup, London, UK) and MATLAB (v7.12.0, R2011a, MathWorks,

Figure 2. Lateral view of the (a) Prestige ST and (b) ProDisc-C finite element models.
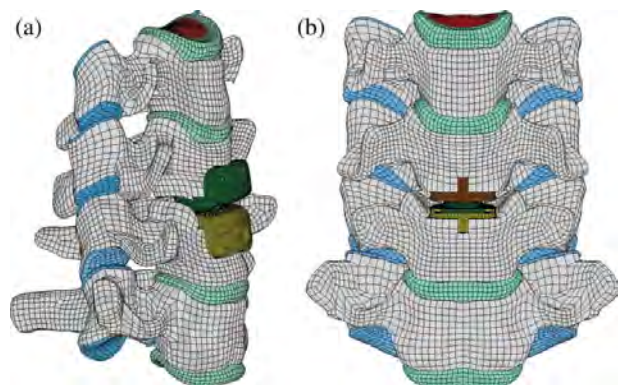
Figure 3. The intervertebral disc and anterior longitudinal ligament between C5 and C6 were removed from the GHBMC neck. The inferior vertebral body of C5 and superior vertebral body of C6 were modified to accept the (a) Prestige ST and (b) ProDisc-C implants.

Table 2. Polarity of the cross-sectional forces and moments according to the relative motion between the head and chest [71].

Load type	Transducer	Polarity	Head−chest manipulation	Load name
AP shear force	Fx	+	Head rearward, chest forward	Positive AP shear
		−	Head forward, chest rearward	Negative AP shear
Axial force	Fz	+	Head upward, chest downward	Tension
		−	Head downward, chest upward	Compression
Bending moment	My	+	Chin toward chest	Flexion
		−	Chin away from chest	Extension

Natick, MA). The forces and moments were filtered in accordance with SAE J211 [71].

The N_{ij} neck injury criterion was calculated for the upper neck using the C1 cross-sectional loading [23,24]. An N_{ij} value of 1.0 corresponds to a 22% risk of an AIS 3+ (Abbreviated Injury Scale) neck injury [2,23]. The beam criterion (BC) was calculated for the lower neck using the C7 cross-sectional loading [5,7]. A BC value of 1.0 corresponds to a 50% risk of AIS 2+ neck injury. Critical intercepts for the 50th percentile adult male were used for both the N_{ij} and BC calculations. The N_{ij} critical values were 6806 N, 6160 N, 310 Nm, and 135 Nm for tension, compression, flexion, and extension, respectively. The BC critical values were 5660 N, 5430 N, and 141 N m for tension, compression, and flexion, respectively.

The axial force and bending moment for each cervical level were used to calculate adjacent-level, cross-sectional ratios: C1/C2, C2/C3, C3/C4, C4/C5, C5/C6, and C6/C7 [85]. These ratios were calculated at the time of maximum tension, compression, extension, and flexion for the C7 level. Loading at the superior level was less than at the inferior level for ratios less than 1 and greater than at the inferior level for ratios greater than 1.

A quantitative analysis was conducted using CORA (v3.6.1, Partnership for Dummy Technology and Biomechanics, Germany) to compare the cross-sectional loading reported in the implant simulations with the loading in a baseline simulation previously reported by White et al., which did not included a C5-6 CTDR [30,31,74]. CORA rates the correlation of a signal with a baseline using two different methods: a corridor method and a cross-correlation method. An overall score is then calculated between 0 (no correlation) and 1 (perfect match) from the weighted sum of these two ratings.

The neck kinematics in the midsagittal plane were captured for both the entire cervical spine and for the C5 and C6 vertebrae. Changes in cervical spine curvature were depicted by plotting the CG coordinates of each vertebra with respect to C7 [82]. Linkages between these points created a visual interpretation of the spinal curvature at a given time. Interbody relative motion of C5-6 was captured using the points that defined the local x-axes for both vertebrae. The coordinates of these points were plotted with respect to the C6 CG and rotated so the C6 local x-axis always remained horizontal. Linkages between these points created a visual interpretation of the shear, axial, and rotational relative motion between these adjacent vertebrae at a given time.

Results

Neck loading

Cross-sectional (AP) shear force, axial force, and bending moment were captured at each cervical level of the neck with peak values reported in Table 3. None of these peak values approached established neck injury thresholds for the mid-sized male [50]. The calculated injury criterion values did not vary greatly between the three simulations (Table 4). The N_{ij} calculation predicated a 7.5% risk of AIS 3+ neck injury in the upper neck while the BC calculation predicted close to a 50% risk of AIS 2+ injury for the lower neck.

The C5 and C6 cross-sectional AP shear forces, axial force, and bending moment time histories are reported for each simulation (Figures 4 and 5). Adjacent-level, cross-sectional loading was adequately maintained in both implant simulations as evidenced by the total CORA ratings of 0.988 for the Prestige ST and 0.909 for the ProDisc-C (Table 5). AP shear force remained predominantly negative throughout each simulation. Both cervical levels initially experienced a period of compression and extension followed by a period of predominantly tension and flexion. A plateau in flexion moment occurred between $t = 195-234$ ms, ending at the approximate time of maximum head flexion.

Adjacent-level loading ratios were similar between simulations for each level (Figure 6, Table 6). Noticeable changes occurred in load ratios between the C3/C4 and C4/C5 adjacent-levels at maximum tension and extension, and C2/C3 and C3/C4 adjacent-levels at maximum compression. The lower level ratios approached or exceeded 1.0, while the upper level ratios remained less than 1.0. At the maximum flexion moment, adjacent-levels in the upper and lower neck approached a ratio of 1.0 while a noticeable dip in ratio occurred in the middle levels.

Table 3 . Peak cross-sectional forces and moments reported at each cervical level in the respective local coordinate system.
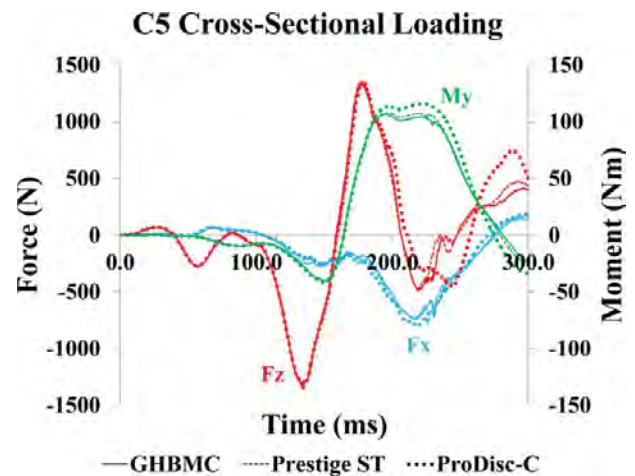
VB	Simulation	AP shear (+Fx)		AP shear (-Fx)		Tension (+Fz)		Compression (-Fz)		Flexion (+My)		Extension (-My)	
		Time (ms)	Force (N)	Time (ms)	Force (N)	Time (ms)	Force (N)	Time (ms)	Force (N)	Time (ms)	Moment (Nm)	Time (ms)	Moment (Nm)
C1	GHBMC	136	793.8	177	−694.5	183	751.4	134	−929.0	189	77.4	300	−5.6
	Prestige ST	135	794.4	177	−691.0	182	738.9	135	−928.2	189	77.4	300	−5.6
	ProDisc-C	138	786.8	177	−679.9	182	755.3	134	−907.5	192	78.2	300	−6.6
C2	GHBMC	135	542.8	174	−485.4	183	918.9	135	−1132.2	192	78.2	300	−5.4
	Prestige ST	135	545.7	174	−478.2	182	910.1	135	−1138.6	189	78.7	300	−5.5
	ProDisc-C	135	541.1	174	−478.6	184	933.4	134	−1113.7	193	79.0	300	−6.6
C3	GHBMC	284	124.3	217	−415.7	183	1050.3	135	−1404.6	192	84.7	148	−11.7
	Prestige ST	282	128.4	228	−432.1	181	1064.3	135	−1412.3	190	85.0	148	−11.5
	ProDisc-C	272	124.1	218	−460.0	183	1068.5	134	−1383.1	193	86.4	148	−12.5
C4	GHBMC	297	162.8	219	−740.1	178	1286.1	135	−1372.1	193	96.8	150	−35.1
	Prestige ST	300	192.8	227	−781.3	178	1275.3	135	−1395.1	193	97.4	150	−35.0
	ProDisc-C	300	225.2	219	−790.1	180	1276.7	135	−1359.0	195	101.5	150	−36.4
C5	GHBMC	300	149.3	217	−740.8	178	1348.7	134	−1345.9	195	106.7	150	−40.3
	Prestige ST	300	173.5	226	−782.2	178	1347.2	135	−1367.7	196	107.7	150	−40.4
	ProDisc-C	300	197.7	219	−797.5	178	1344.6	134	−1329.6	222	116.2	150	−41.9
C6	GHBMC	293	143.7	215	−636.9	178	1415.5	134	−1363.4	195	106.7	149	−33.7
	Prestige ST	300	158.7	226	−674.6	178	1409.8	135	−1373.7	195	108.3	149	−33.9
	ProDisc-C	300	210.9	217	−655.8	180	1403.6	134	−1329.9	218	114.5	149	−35.3
C7	GHBMC	179	204.7	138	−504.9	180	1426.0	134	−1344.7	196	110.7	149	−26.4
	Prestige ST	180	221.0	138	−535.0	180	1392.8	135	−1411.6	197	112.1	149	−26.2
	ProDisc-C	293	183.0	137	−540.8	181	1443.6	134	−1337.6	217	120.0	149	−27.5

AP shear and axial interbody loads between C5 and C6 are presented in Figure 7 with peak loads reported in Table 7. Negative AP shear force was the predominant shear loading in the implant simulations, while sustained periods of both positive and negative shear occurred in the non-modified simulation. The timing of peak negative AP shear was similar for all three simulations, but the implant simulations experienced a larger peak load. The interbody axial loading remained in compression for the duration of all simulations with the largest peak value occurring in the unmodified simulation.

AP shear and axial loading between the inferior C5 and superior C6 facets are presented in Figure 8 with peak loads and average maximum capsule ligament strains reported in Table 8. The facets experienced primarily negative AP shear and compression with peak values occurring within 4 ms of one another. Up to approximately 175 ms, the difference between left and right facet loading was negligible for a given simulation. A departure between left and right side loading occurred after this point. The right facet experienced noticeably larger negative AP shear and compressive loads than the left facet. Obvious axial tension occurred in the left facets toward the end of both implant simulations.

Figure 4. Cross-sectional AP shear forces, axial forces, and bending moments for the C5 level.

Table 4. Neck injury criteria calculated for the upper and lower cervical spine. The N_{ij} was calculated for the upper neck (C1) and the beam criterion was calculated for the lower neck (C7). An N_{ij} value of 1.0 corresponds to a 22% risk of an AIS 3+ neck injury [2,23]. A BC value of 1.0 corresponds to a 50% risk of AIS 2+ neck injury [5,7].

Simulation	C1 FMVSS 208	C7 BC
GHBMC	0.35	0.98
Prestige ST	0.35	0.98
ProDisc-C	0.36	1.05

Figure 5. Cross-sectional AP shear forces, axial forces, and bending moments for the C6 level.

Table 5. Quantitative analysis of the cross-sectional neck loading response of the Prestige ST and ProDisc-C models to the baseline GHBMC model. The CORA rating system ranges from 0 (no correlation) to 1 (perfect correlation).

Simulation	Total rating	VB level	Transducer	Corridor	Correlation	Overall
Prestige ST	0.988	C5	Fx	0.986	0.985	0.985
			Fz	0.984	0.992	0.988
			My	0.999	0.989	0.994
		C6	Fx	0.981	0.977	0.979
			Fz	0.988	0.992	0.990
			My	0.998	0.987	0.992
ProDisc-C	0.909	C5	Fx	0.940	0.953	0.946
			Fz	0.788	0.886	0.837
			My	0.897	0.948	0.922
		C6	Fx	0.963	0.965	0.964
			Fz	0.805	0.903	0.854
			My	0.906	0.949	0.928

Table 6. Adjacent-level, cross-sectional loading ratios calculated at the times of maximum C7 tension, compression, flexion, and extension.

Loading	Simulation	C1/C2	C2/C3	C3/C4	C4/C5	C5/C6	C6/C7
Tension	GHBMC	0.82	0.85	0.82	0.95	0.95	0.97
	Prestige ST	0.80	0.85	0.82	0.96	0.95	1.01
	ProDisc-C	0.79	0.86	0.86	0.96	0.94	0.95
Compression	GHBMC	0.82	0.81	1.02	1.02	0.99	1.01
	Prestige ST	0.81	0.81	1.02	1.02	1.00	0.97
	ProDisc-C	0.81	0.81	1.02	1.02	1.00	0.99
Flexion	GHBMC	0.98	0.92	0.86	0.90	1.00	0.96
	Prestige ST	0.97	0.92	0.85	0.90	1.00	0.96
	ProDisc-C	0.95	0.91	0.78	0.86	1.01	0.95
Extension	GHBMC	0.42	0.30	0.33	0.87	1.19	1.27
	Prestige ST	0.37	0.29	0.33	0.87	1.18	1.28
	ProDisc-C	0.49	0.34	0.34	0.87	1.18	1.28

Head and neck kinematics

Midsagittal head rotations were similar for the three simulations with an initial period of extension followed by a more pronounced period of flexion (Figure 9). Maximum head extension was almost identical for all simulations. Maximum head flexion was almost identical between the unmodified and Prestige ST simulations, while the flexion magnitude was approximately 4.5° greater in the ProDisc-C simulation (Table 9).

Comparison of cervical spine incremental kinematics between the unmodified and implant simulations is presented in Figure 10. The spine curvature was reported at specific points in time corresponding to major loading and kinematic events in the unmodified simulation (Table 10). Peak cross-sectional loading at the C7 level was used. The overall curvature did not vary greatly between the unmodified and implant simulations. For all simulations, an S-shaped curvature was produced during neck compression followed by a C-shaped curvature during neck tension. The most notable difference in curvature was seen at the time of maximum head flexion for the ProDisc-C simulation. There appeared to be an increase in rotation of C5 with respect to C6, increasing flexion of the entire neck.

Interbody relative motion of C5-6 with respect to C6 is presented for each simulation in Figure 11. The motion is described relative to the initial midsagittal
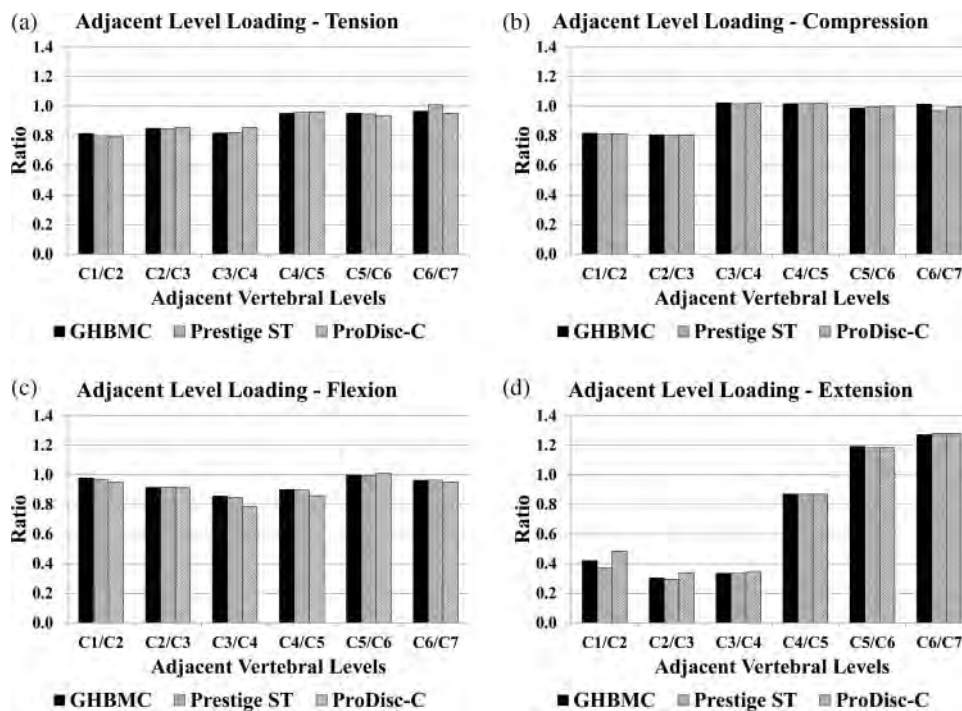
Figure 6. Adjacent-level loading ratios at the time of maximum C7 cross-sectional (a) tension, (b) compression, (c) flexion, and (d) extension.
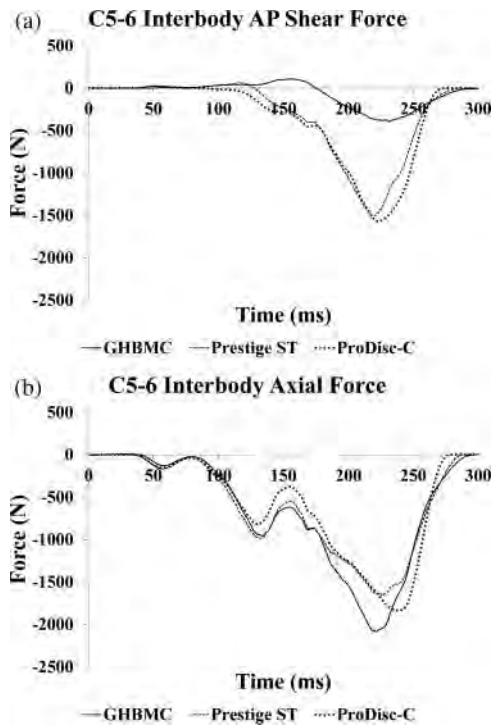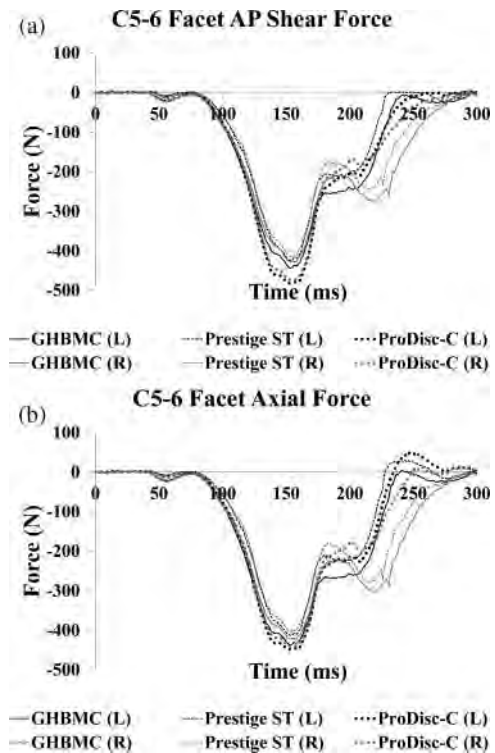
Figure 7. Interbody (a) AP shear force and (b) axial force reported in the C6 LCS. These forces were reported as cross-sectional forces from the IVD in the non-modified GHBMC simulation and as contact forces for both implant simulations.

Table 7. Peak C5-6 interbody loading reported in the C6 LCS.

	AP shear (+Fx)		AP shear (-Fx)		Compression (-Fz)	
Simulation	Time (ms)	Force (N)	Time (ms)	Force (N)	Time (ms)	Force (N)
GHBMC	156	107.2	232	−395.3	222	−2085.2
Prestige ST	116	70.9	220	−1507.7	227	−1658.4
ProDisc-C	49	24.1	223	−1570.0	238	−1836.3

orientation of C5 with respect to C6 at $t = 0$ ms. Minimal relative motion occurred in the simulations during the initial 70 ms settling phase. Extension of the C5-6 interbody space occurred for the first 180 ms in all simulations, with the greatest rotation occurring in the implant simulations. By the time of maximum flexion moment, $t = 196$ ms, the implant extension angles were minimal. The time of maximum flexion moment for the ProDisc-C simulation did not occur until $t = 217$ ms, $10-11$ ms later than the unmodified and Prestige ST simulations. Interbody flexion increased up to the time

Figure 8. Left and right C5-6 cervical facet (a) AP shear force and (b) axial force reported in the C6 LCS.

of maximum head flexion, $t = 231$ ms, most noticeably in the ProDisc-C simulation.

Discussion

Overall neck response

The introduction of a CTDR at the C5-6 level did not appear to greatly alter the global neck response during a simulated rotary-wing aircraft impact. Midsagittal head rotation in the implant simulations was maintained in both extension and flexion, though the peak flexion in the ProDisc-C simulation was slightly larger than for the other two simulations. The incremental, midsagittal cervical spine kinematics for the implant simulations were almost identical to the unmodified simulation up to the time of maximum head flexion. Both S-shaped and C-shaped bending were reported during the simulations,

Table 8. Peak cross-sectional C5-6 cervical facet loading reported in the C6 LCS and average maximum capsule ligament strain.

		AP shear (-Fx)		Tension (+Fz)		Compression (-Fz)		
Simulation	Facet	Time (ms)	Force (N)	Time (ms)	Force (N)	Time (ms)	Force (N)	Average maximum
GHBMC	Left	153	−443.4	242	4.4	153	−437.0	6.4 ± 2.9
	Right	157	−428.2	—	—	157	−422.6	3.9 ± 1.9
Prestige ST	Left	154	−424.4	246	29.9	154	−413.1	10.0 ± 2.5
	Right	154	−415.0	300	3.3	155	−403.9	5.6 ± 1.6
ProDisc-C	Left	153	−482.0	249	50.1	153	−448.3	14.1 ± 3.3
	Right	154	−475.1	258	12.5	154	−441.4	12.2 ± 2.7
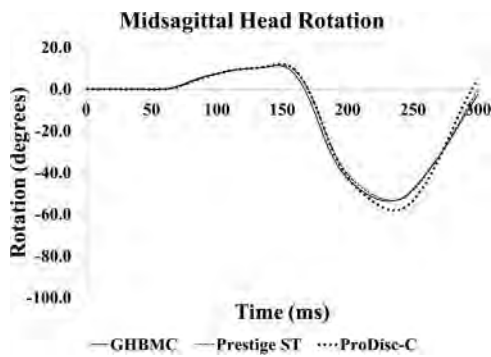
Figure 9. Rotation of the head centre of gravity in the midsagittal plane.

Table 9. Peak midsagittal head rotation for extension and flexion.

Simulation	Maximum head extension		Maximum head flexion	
	Time (ms)	Rotation (deg)	Time (ms)	Rotation (deg)
GHBMC	146	11.3	231	−53.8
Prestige ST	147	11.7	234	−53.4
ProDisc-C	147	11.9	234	−58.3
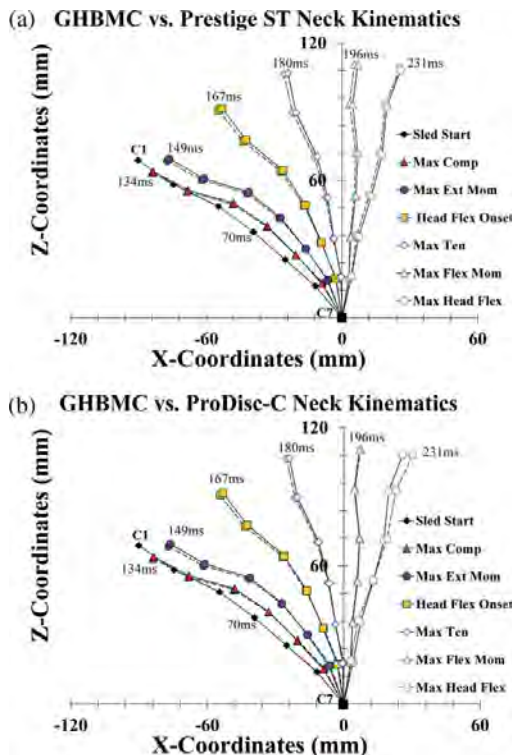
Figure 10. Incremental, midsagittal kinematics of the cervical spine for the (a) Prestige ST and (b) ProDisc-C simulations. The position of the local origin for each vertebra is plotted with respect to the C7 local origin, at different points in time. The solid lines represent the kinematics of the non-modified GHBMC simulation while the dashed lines represent the kinematics of the respective implant simulation.

Table 10. Timing of major loading and kinematic events for the non-modified GHBMC simulation.

| Event	Time (ms)
Sled pulse initiation	70
Max compression	134
Max extension moment	149
Onset of head flexion	167
Max tension	180
Max flexion moment	196
Max head flexion	231

similar to observations made in previous cadaver studies [5,7]. Minimal difference was noted in the simulation for adjacent-level loading ratios, indicating load transmission through the neck was maintained. Injury criteria calculations in the upper and lower neck were almost identical in all simulations, indicating the risk of injury did not appear to change due to the CTDRs. The calculated BC values in all simulations correspond to a probability of an AIS 2+ neck injury, indicating that this type of impact, while survivable, is not benign.

Adjacent-level response

The C5-6 adjacent-level, cross-sectional loading was maintained with the CTDRs, as was evident by the quantitative analysis comparison. The largest discrepancy occurred in the axial loading phase of the ProDisc-C simulation, most notably during the last 100 ms of the event. All simulations produced a similar flexion moment plateau period, however, the moment in the ProDisc-C simulation remained larger than the other simulations during this time. Additionally, the peak flexion moment occurred at the end of the plateau for the ProDisc-C simulation, unlike in the unmodified and Prestige ST simulations. Some of the differences in adjacent-level loading may be explained by the C5-6 relative motion. This difference in relative motion can be attributed to the difference in the degrees-of-freedom allowed by the CTDRs. The Prestige ST permitted both rotation and AP translation while the ProDisc-C permitted rotation only.

While the initial 70 ms of settling and belt pretensioning had a negligible effect on the unmodified C5-6 orientation, minimal extension occurred in both implant simulations. The C5-6 segment in both implant simulations remained more mobile than the unmodified simulation throughout time, with the ProDisc-C segment producing the greatest rotation and translation. This increase in mobility and subsequent change in segment kinematics is most likely responsible for any deviation in adjacent-level, cross-sectional loading from the unmodified simulation.

Even though the kinematics of the GHBMC cervical spine have been previously validated in numerous
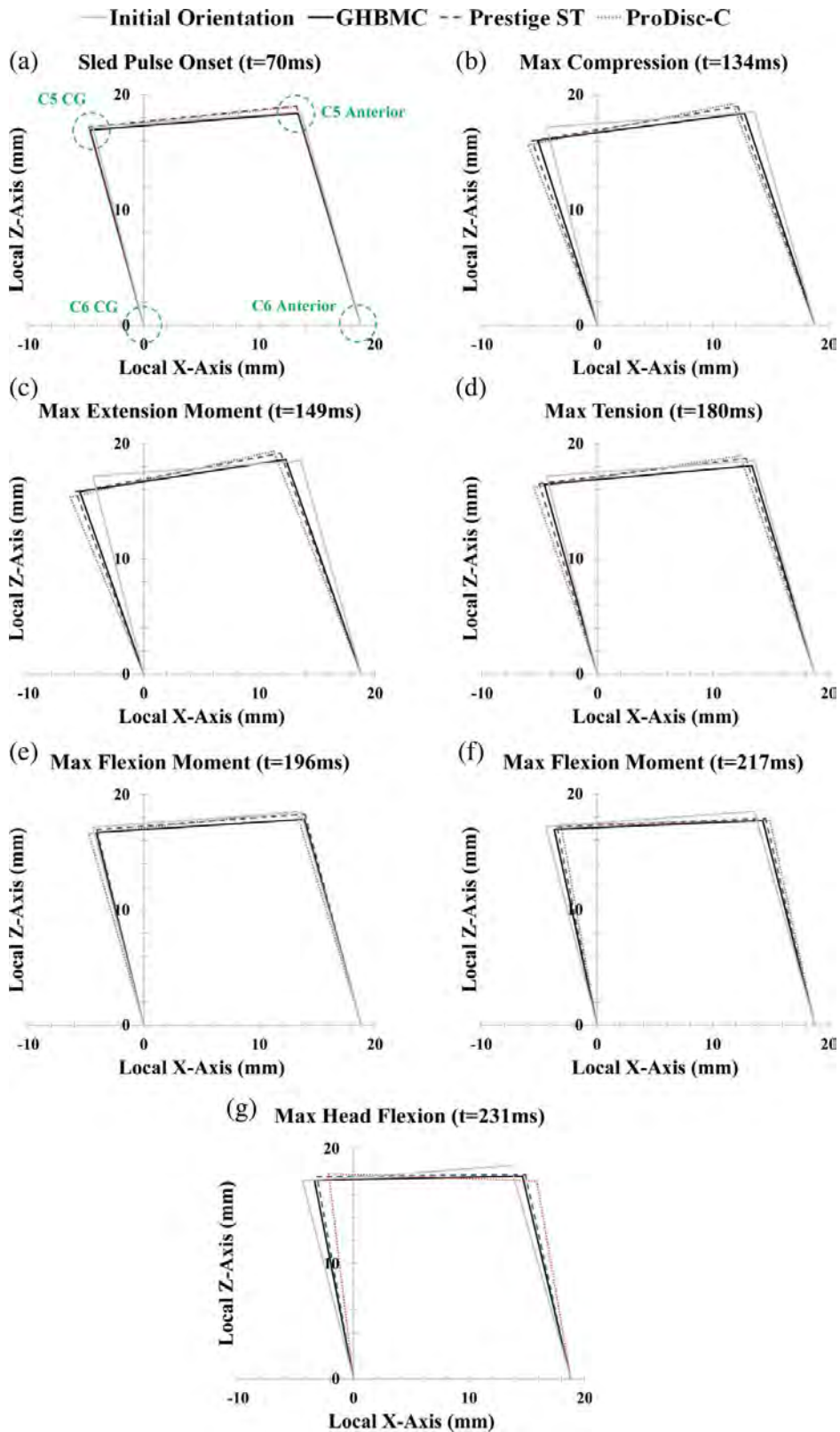
Figure 11. Relative C5-6 interbody midsagittal motion with respect to C6 at (a) sled pulse onset, (b) maximum compression, (c) maximum extension moment, (d) maximum tension, (e) maximum flexion moment (GHBMC and Prestige ST simulations), and (f) maximum head flexion. For reference purposes, the initial orientation of the non-modified GHBMC C5-6 interbody space ($t = 0$ ms) was included in all plots.

loading scenarios, a limitation of this study is that there is no direct validation of the cervical spine with CTDRs. However, the simulated kinematics of both the ball-and-trough Prestige ST and the ball-and-socket ProDisc-C appear physically appropriate. Additionally, the simulated range of motion (ROM) of the modified spinal segment can be indirectly validated against several cadaver, volunteer, and FE studies. Increased mobility at the implant level has been previously reported in cadaver, volunteer, and FE studies. Chang et al. [12] evaluated the ROM of cadaver cervical spines with a Prestige II and ProDisc-C implanted at the C6-7 level. The ROM increased at the surgically treated segment in both implant specimens as compared to the intact spine, with the ProDisc-C producing the greatest increase in flexion and extension. FE studies have also found that introduction of a CTDR increased the ROM in midsagittal bending [41,68]. A volunteer, *in vivo* study conducted by Kowalczyk et al. [39] investigated the effect of arthroplasty on spinal kinematics. The Prestige LP implant was found to preserve segmental ROM, while the ProDisc-C either maintained or increased the ROM. A similar finding was reported by Bertagnoli et al. [8] where flexion ROM was evaluated pre- and post-arthroplasty. Segmental rotation was found to increase from 4° to 12° with implantation of the ProDisc-C.

Interbody loading

Many of the peak interbody loads correspond to distinct events visualised in the simulation. In the Prestige ST simulation, positive AP shear force starts with the onset of the sled pulse at 70 ms and peaks at 116 ms when the implant ball reaches the posterior end of the trough. Unable to translate any farther, the ball rotates in place until approximately 128 ms. The AP shear force polarity reverses at this point as the ball translates anteriorly. The ball contacts the end of the trough at 220 ms, corresponding with the peak negative AP shear force. The implant continues to rotate in place, flexing the C5-6 segment. As this implant is unable to sustain any tension by design, compression was the sole mode of axial loading. Peak compression occurred 7 ms after the peak negative AP shear force, the apparent time of maximum implant rotation. Interbody loading decreases to zero at approximately 287 ms, at which point separation between the ball and trough was visualised. Tension in adjacent-level, cross sections, caused by the relative motion of the head with respect to the torso, was responsible for this separation. Separation did not occur earlier in the simulation due to flexion-induced compression experienced by the implant.

Unlike the Prestige ST simulation, the ProDisc-C simulation produced negligible AP shear force between $t = 70$ ms and $t = 100$ ms. During this 30 ms time period, rotation in the form of extension occurred, producing only axial compression. As the extension moment increases at both vertebral levels, the interbody AP shear force becomes negative, corresponding to the compression of the posterior aspect of the semi-spherical inlay. The negative AP shear force increased with onset of flexion in the neck, reaching its peak at 223 ms. Both the peak rotation and axial load occurred approximately 15 ms later. While the design of the ProDisc-C allows for rotation only, some AP translation occurred as a result of inlay deformation. Interbody loading decreased to zero at approximately 278 ms, at which point separation between the ball and socket was visualised. Tension in adjacent-level, cross sections, caused by relative head motion, was responsible for this separation. As with the Prestige ST simulation, separation did not occur earlier in the ProDisc-C simulation due to flexion-induced compression experienced by the implant.

Interbody loading though the IVD in the unmodified simulation differed from the loading in the implant simulations. The IVD allowed for simultaneous points of attachment to the adjacent vertebrae as opposed to the single point of contact for the CTDRs. A positive AP shear force was produced for the first 175 ms followed by a negative AP shear force lower in magnitude than for the implant simulations. The peak compression was noticeably larger in the unmodified simulation, aligning closer in time with the Prestige ST peak than the ProDisc-C peak. The larger compressive force helped to limit the overall rotation of the vertebral segment, potentially protecting the facets from increased loading. Unlike the CTDRs, the IVD was capable of supporting tension, though only approximately 5 N of tension occurred at the end of the simulation.

Facet loading

Due to geometrical symmetry, purely midsagittal motion of the head and neck should produce equal loading of the left and right facets for any given cervical level. However, a divergence in loading between the left and right facets at C5-6 was noted for all simulations. Midsagittal head and neck flexion was the dominant form of motion in the simulations; however, a small amount of lateral rotation occurred at the C5-6 segment. This lateral rotation accounted for the difference in facet loading, most notably in the unmodified and Prestige ST simulations. All three simulations experienced tension in the facet capsules; however, this load was much more prominent in the implant simulations, particularly for the left facets. The increased midsagittal rotation of the C5-6 segment with either implant appears to have increased the facet tension.

Failure from quasi-static retraction of the human cervical facet capsule ligament has been previously reported [40]. The average load for gross failure, partial failure, and ligament yielding was 61.81 ± 26.40, 45.81 ± 22.99, and 30.65 ± 25.54 N, respectively. While both the Prestige ST and ProDisc-C left facet tension reached these potentially injurious levels in the simulations, it should be noted that this loading only lasted for approximately 40 ms. Due to this dynamic loading environment, it may not be best to compare the loads with those of a quasi-static experiment run at 0.5 mm/s. Dynamic tests conducted at $150-250$ s^{-1}, comparable to the actual strain rate experienced in the cervical facet during a 20 g frontal automobile impact, have yielded a failure force of 286 ± 73 N [48]. These simulated facet loads fell well below the dynamic failure range.

Ligament failure is built into the cervical facet capsule material model such that sequential beam deletion occurs at predefined average failure distraction levels [72]. Failure of the C5-6 facet capsule did not occur in any of the simulations. Cervical facet strain is also a common metric used to predict both ligament failure and potential for persistent neck pain. In the simulations, the distraction of each C5-6 cervical capsule beam element was extracted and divided by the neutral ligament length to calculate the strain [56,72]. The results of dynamic experimental tests found the average failure strain of the cervical facet capsule to be 111.0 ± 46%, well above the average maximum strains calculated in the simulations [48]. Facet capsule strain of 45.0 ± 15.1% has been shown to correlate with persistent nerve after discharge in the caprine surrogate model, leading to persisting pain [11,44]. Again, the maximum tensile strain in the simulations did not approach this injurious range. While any tension in the cervical facet capsule has potential to cause injury, the increased loads in the CTDR simulations did not appear to reach injurious levels.

Conclusions

The effects of cervical arthroplasty on neck response during a simulated rotary-wing aircraft impact have been examined. Upper and lower neck loading and head kinematics were only minimally affected with the introduction of a CTDR at the C5-6 cervical level. Neck injury criteria calculations were almost identical between the unmodified and implant simulation. Quantitative analysis of the adjacent-level, cross-sectional neck loading above and below the site of the CTDRs showed very little difference with the adjacent-level loading of the IVD in the unmodified simulation. The AP shear C5-6 interbody force was greater for the CTDRs than IVD,

though the axial compression was greatest for the IVD. The C5-6 interbody kinematics were slightly altered with the CTDRs, with an increase in ROM in both flexion and extension. Additionally, the CTDRs were incapable of supporting tension, allowing for interbody separation to occur. This increased mobility created tension in the C5-6 facets not seen in the unmodified simulation. While tension in the facet capsules may lead to injury, the reported loads and strains did not appear to reach any established injury thresholds. Overall, cervical arthroplasty at the C5-6 level did not appear to have a deleterious effect on the dynamic neck response during a simulated rotary-wing aircraft impact.

Disclosure statement

No potential conflict of interest was reported by the authors.

ORCID

Nicholas A. White http://orcid.org/0000-0001-6914-0691

References

[1] T.J. Albert and M.D. Eichenbaum, *Goals of cervical disc replacement*, Spine J. 4 (2004), pp. 292S−293S. Available at http://www.ncbi.nlm.nih.gov/pubmed/15541679.

[2] Association for the Advancement of Automotive Medicine (AAAM), *Abbreviated Injury Scale © 2005 Update 2008*, T.A. Gennarelli and E. Wodzin, eds., AAAM, Barrington, IL, 2008.

[3] A.A. Baaj, J.S. Uribe, F.L. Vale, M.C. Preul, and N.R. Crawford, *History of cervical disc arthroplasty*, Neurosurg. Focus 27 (2009), pp. E10. Available at http://www.ncbi.nlm.nih.gov/pubmed/19722812.

[4] R.W. Bailey and C.E. Badgley, *Stabilization of the cervical spine by anterior fusion*, J. Bone Joint Surg. Am. 42-A

(1960), pp. 565−594. Available at http://www.ncbi.nlm.nih.gov/pubmed/13848906.

[5] C.R. Bass, L. Donnellan, R. Salzar, S. Lucas, B. Folk, M. Davis, K. Rafaels, C. Planchak, K. Meyerhoff, A. Ziemba, and N.M. Alem, *A new neck injury criterion in combined vertical/frontal crashes with head supported mass*, in *International Research Council on Biomechanics of Injury*, Madrid, Spain, 2006.

[6] C.R. Bass et al., *Dynamic models for the assessment of spinal injury from repeated impact in high speed planing boats*, International Research Council on Biomechanics of Injury, The Netherlands, 2007.

[7] C.R. Bass, R. Salzar, L. Donnellan, and H. Lucas, *Injury risk from HSM loading (HM 2,3,4,5 series)*, Rep. HEADMASS2, University of Virginia Center for Applied Biomechanics, Charlottesville, VA, 2004.

[8] R. Bertagnoli, J.J. Yue, F. Pfeiffer, A. Fenk-Mayer, J.P. Lawrence, T. Kershaw, and R. Nanieva, *Early results after ProDisc-C cervical disc replacement*, J. Neurosurg. Spine 2 (2005), pp. 403−410. Available at http://www.ncbi.nlm.nih.gov/pubmed/15871478.

[9] S.D. Boden, P.R. McCowin, D.O. Davis, T.S. Dina, A.S. Mark, and S. Wiesel, *Abnormal magnetic-resonance scans of the cervical spine in asymptomatic subjects. A prospective investigation*, J. Bone Joint Surg. Am. 72 (1990), pp. 1178−1184. Available at http://www.ncbi.nlm.nih.gov/pubmed/2398088.

[10] T.F. Boselie, P.C. Willems, H. van Mameren, R. de Bie, E.C. Benzel, and H. van Santbrink, *Arthroplasty versus fusion in single-level cervical degenerative disc disease*, Cochrane Database Syst. Rev. 9 (2012), CD009173. Available at http://www.ncbi.nlm.nih.gov/pubmed/22972137.

[11] J.M. Cavanaugh, Y. Lu, C. Chen, and S. Kallakuri, *Pain generation in lumbar and cervical facet joints*, J. Bone Joint Surg. Am. 88 Suppl 2 (2006), pp. 63−67. Available at http://www.ncbi.nlm.nih.gov/pubmed/16595446.

[12] U.K. Chang, D.H. Kim, M.C. Lee, R. Willenberg, S.H. Kim, and J. Lim, *Range of motion change after cervical arthroplasty with ProDisc-C and prestige artificial discs compared with anterior cervical discectomy and fusion*, J. Neurosurg. Spine 7 (2007), pp. 40−46. Available at http://www.ncbi.nlm.nih.gov/pubmed/17633486.

[13] J. Chen, S.W. Fan, X.W. Wang, and W. Yuan, *Motion analysis of single-level cervical total disc arthroplasty: A meta-analysis*, Orthop. Surg. 4 (2012), pp. 94−100. Available at http://www.ncbi.nlm.nih.gov/pubmed/22615154.

[14] R.B. Cloward, *The anterior approach for removal of ruptured cervical disks*, J. Neurosurg. 15 (1958), pp. 602−617. Available at http://www.ncbi.nlm.nih.gov/pubmed/13599052.

[15] Department of the Air Force, *Air Force Waiver Guide*, 88ABW-2012-3597, Wright-Patterson Air Force Base, 2013.

[16] Department of the Army, *Standards of Medical Fitness*, Army Regulation 40-501, 2011.

[17] Department of the Navy, *U.S. navy aeromedical reference and waiver guide*, in *13.4 Orthopedic: Intervertebral Disc Disease*, US Navy, Naval Aerospace Medical Institute, Pensacola, FL, 2013.

[18] J.A. DeWit and D.S. Cronin, *Cervical spine segment finite element model for traumatic injury prediction*, J. Mech. Behav. Biomed. Mater. 10 (2012), pp. 138−150. Available at http://www.ncbi.nlm.nih.gov/pubmed/22520426.

[19] D.J. DiAngelo, K.T. Foley, B.R. Morrow, J.S. Schwab, J. Song, J.W. German, and E. Blair, *In vitro biomechanics of cervical disc arthroplasty with the ProDisc-C total disc implant*, Neurosurg. Focus 17 (2004), pp. E7. Available at http://www.ncbi.nlm.nih.gov/pubmed/15636563.

[20] DIN ISO 5834-2:2007-12, *Implants for Surgery: Ultra-High-Molecular-Weight-Polyethylene, Part 2: Moulded Forms (ISO 5834-2:2006)*, Berlin, Germany, 2007.

[21] C. Ding, Y. Hong, H. Liu, R. Shi, T. Hu, and T. Li, *Intermediate clinical outcome of Bryan cervical disc replacement for degenerative disk disease and its effect on adjacent segment disks*, Orthopedics 35 (2012), pp. e909−916. Available at http://www.ncbi.nlm.nih.gov/pubmed/22691666.

[22] eFunda, *AISI Type 316L*, Sunnyvale, CA, 2013.

[23] R. Eppinger, E. Sun, F. Bandak, M. Haffner, N. Khaewpong, M. Maltese, S. Kuppa, T. Nguyen, E. Takhounts, R. Tannous, A. Zhang, and R. Saul, *Development of Improved Injury Criteria for the Assessment of Advanced Automobile Restraint Systems - II. NHTSA Docket No. 1999-6407-5*, 1999.

[24] R. Eppinger, E. Sun, S. Kuppa, and R. Saul, *Supplement: Development of Improved Injury Criteria for the Assessment of Advanced Automobile Restraint Systems - II. NHTSA Docket No. 2010-03-19*, 2000.

[25] A. Fallah, E.A. Akl, S. Ebrahim, G.M. Ibrahim, A. Mansouri, C.J. Foote, Y. Zhang, and M.G. Fehlings, *Anterior cervical discectomy with arthroplasty versus arthrodesis for single-level cervical spondylosis: A systematic review and meta-analysis*, PLoS One 7 (2012), pp. e43407. Available at http://www.ncbi.nlm.nih.gov/pubmed/22912869.

[26] J.B. Fice and D.S. Cronin, *Investigation of whiplash injuries in the upper cervical spine using a detailed neck model*, J. Biomech. 45 (2012), pp. 1098−1102. Available at http://ac.els-cdn.com/S0021929012000371/1-s2.0-S0021929012000371-main.pdf?_tid=4a9be1a8-82b0-11e2-b045-00000aacb35d&acdnat=1362170625_d1eb88bf63b35fccc50e8be1b63024d6.

[27] J.B. Fice, D.S. Cronin, and M.B. Panzer, *Cervical spine model to predict capsular ligament response in rear impact*, Ann. Biomed. Eng. 39 (2011), pp. 2152−2162. Available at http://www.ncbi.nlm.nih.gov/pubmed/21533673.

[28] F. Galbusera, C.M. Bellini, M.T. Raimondi, M. Fornari, and R. Assietti, *Cervical spine biomechanics following implantation of a disc prosthesis*, Med. Eng. Phys. 30 (2008), pp. 1127−1133. Available at http://www.ncbi.nlm.nih.gov/pubmed/18359659.

[29] F.S. Gayzik, D.P. Moreno, C.P. Geer, S.D. Wuertzer, R.S. Martin, and J.D. Stitzel, *Development of a full body CAD dataset for computational modeling: A multi-modality approach*, Ann. Biomed. Eng. 39 (2011), pp. 2568−2583. Available at http://www.ncbi.nlm.nih.gov/pubmed/21785882.

[30] C. Gehre, H. Gades, and P. Wernicke, *Objective rating of signals using test and simulation responses*, 21st

International Technical Conference on the Enhanced Safety of Vehicles, Stuttgart, Germany, 2009.

[31] C. Gehre and S. Stahlschmidt, *Assessment of dummy models by using objective rating methods*, 22nd International Technical Conference on the Enhanced Safety of Vehicles, Washington, DC, 2011.

[32] N.J. Hallab, M. Wimmer, and J.J. Jacobs, *Material properties and wear analysi*s, in Motion Preservation Surgery of the Spine: Advanced Techniques and Controversies, J. J. Yue, R. Bertagnoli, P.C. McAfee, and H.S. An, eds., Saunders, Philadelphia, PA, 2008, pp. 52−62.

[33] A.R. Hayes, N.A. Vavalle, D.P. Moreno, J.D. Stitzel, and F.S. Gayzik, *Validation of simulated chestband data in frontal and lateral loading using a human body finite element model*. Traffic Inj Prev 15 (2)(2014), pp. 181−186.

[34] J.G. Heller, R.C. Sasso, S.M. Papadopoulos, P.A. Anderson, R.G. Fessler, R.J. Hacker, D. Coric, J.C. Cauthen, and D.K. Riew, *Comparison of BRYAN cervical disc arthroplasty with anterior cervical decompression and fusion: Clinical and radiographic results of a randomized, controlled, clinical trial*, Spine (Phila Pa 1976) 34 (2009), pp. 101−107. Available at http://www.ncbi.nlm.nih.gov/pubmed/19112337.

[35] I.J. Hendriksen and M. Holewijn, *Degenerative changes of the spine of fighter pilots of the Royal Netherlands Air Force (RNLAF)*, Aviat. Space Environ. Med. 70 (1999), pp. 1057−1063. Available at http://www.ncbi.nlm.nih.gov/pubmed/10608601.

[36] International Organization for Standardization, *Road vehicles − anthropomorphic side impact dummy − lateral impact response requirements to assess the biofidelity of the dummy*, 1999.

[37] D.G. Kang, R.A. Lehman, R.W. Tracey, J.P. Cody, M.K. Rosner, and A.J. Bevevino, *Outcomes following cervical disc arthroplasty in an active duty military population*, J. Surg. Orthop. Adv. 22 (2013), pp. 10−15. Available at http://www.ncbi.nlm.nih.gov/pubmed/23449049.

[38] S.C. Knapp, *Medical and physiological effects of ejection and parachuting: An overview*, USAARL Rep. No. 71-9, US Army Aeromedical Research Laboratory, Fort Rucker, AL, 1970.

[39] I. Kowalczyk, B.C. Lazaro, M. Fink, D. Rabin, and N. Duggal, *Analysis of in vivo kinematics of 3 different cervical devices: Bryan disc, ProDisc-C, and Prestige LP disc*, J. Neurosurg. Spine 15 (2011), pp. 630−635. Available at http://www.ncbi.nlm.nih.gov/pubmed/21905776.

[40] D.J. Lee and B.A. Winkelstein, *The failure response of the human cervical facet capsular ligament during facet joint retraction*, J. Biomech. 45 (2012), pp. 2325−2329. Available at http://www.ncbi.nlm.nih.gov/pubmed/22840489.

[41] S.H. Lee, Y.J. Im, K.T. Kim, Y.H. Kim, W.M. Park, and K. Kim, *Comparison of cervical spine biomechanics after fixed- and mobile-core artificial disc replacement: A finite element analysis*, Spine (Phila Pa 1976) 36 (2011), pp. 700−708. Available at http://www.ncbi.nlm.nih.gov/pubmed/21245792.

[42] I.J. Lehto, M.O. Tertti, M.E. Komu, H.E. Paajanen, J. Tuominen, and M.J. Kormano, *Age-related MRI changes at 0.1 T in cervical discs in asymptomatic subjects*, Neuroradiology 36 (1994), pp. 49−53. Available at http://www.ncbi.nlm.nih.gov/pubmed/8107998.

[43] F. Liu, J. Cheng, R.D. Komistek, M.R. Mahfouz, and A. Sharma, *In vivo evaluation of dynamic characteristics of the normal, fused, and disc replacement cervical spines*, Spine (Phila Pa 1976) 32 (2007), pp. 2578−2584. Available at http://www.ncbi.nlm.nih.gov/pubmed/17978657.

[44] Y. Lu, C. Chen, S. Kallakuri, A. Patwardhan, and J.M. Cavanaugh, *Neural response of cervical facet joint capsule to stretch: A study of whiplash pain mechanism*, Stapp Car Crash J. 49 (2005), pp. 49−65. Available at http://www.ncbi.nlm.nih.gov/pubmed/17096268.

[45] K.T. Mason, J.P. Harper, and S.G. Shannon, *U.S. Army Aviation Epidemiology Data Register: Incidence and Age-Specific Rates of Herniated Nucleus Among U.S. Army Aviators, 1987−1992, 95−33*, U.S. Army Aeromedical Research Laboratory, Fort Rucker, AL, 1995.

[46] M. Matsumoto, Y. Fujimura, N. Suzuki, Y. Nishi, M. Nakamura, Y. Yabe, and H. Shiga, *MRI of cervical intervertebral discs in asymptomatic subjects*, J. Bone Joint Surg. Br. 80 (1998), pp. 19−24. Available at http://www.ncbi.nlm.nih.gov/pubmed/9460946.

[47] S. Matsunaga, S. Kabayama, T. Yamamoto, K. Yone, T. Sakou, and K. Nakanishi, *Strain on intervertebral discs after anterior cervical decompression and fusion*, Spine (Phila Pa 1976) 24 (1999), pp. 670−675. Available at http://www.ncbi.nlm.nih.gov/pubmed/10209796.

[48] S.F. Mattucci, J.A. Moulton, N. Chandrashekar, and D.S. Cronin, *Strain rate dependent properties of younger human cervical spine ligaments*, J. Mech. Behav. Biomed. Mater. 10 (2012), pp. 216−226. Available at http://www.ncbi.nlm.nih.gov/pubmed/22520433.

[49] P.C. McAfee, C. Reah, K. Gilder, L. Eisermann, and B. Cunningham, *A meta-analysis of comparative outcomes following cervical arthroplasty or anterior cervical fusion: Results from 4 prospective multicenter randomized clinical trials and up to 1226 patients*, Spine (Phila Pa 1976) 37 (2012), pp. 943−952. Available at http://www.ncbi.nlm.nih.gov/pubmed/22037535.

[50] H.J. Mertz, A.L. Irwin, and P. Prasad, *Biomechanical and scaling bases for frontal and side impact injury assessment reference values*, Stapp Car Crash J. 47 (2003), pp. 155−188. Available at http://www.ncbi.nlm.nih.gov/pubmed/17096249.

[51] P.V. Mummaneni, B.Y. Amin, J.C. Wu, E.D. Brodt, J.R. Dettori, and R.C. Sasso, *Cervical artificial disc replacement versus fusion in the cervical spine: A systematic review comparing long-term follow-up results from two FDA trials*, Evid. Based Spine Care J. 3 (2012), pp. 59−66. Available at http://www.ncbi.nlm.nih.gov/pubmed/23236315.

[52] P.V. Mummaneni, J.K. Burkus, R.W. Haid, V.C. Traynelis, and T.A. Zdeblick, *Clinical and radiographic analysis of cervical disc arthroplasty compared with allograft fusion: A randomized controlled clinical trial*, J. Neurosurg. Spine 6 (2007), pp. 198−209. Available at http://www.ncbi.nlm.nih.gov/pubmed/17355018.

[53] D. Mydlarz, *Degenerative disc disease, active component, U.S. Armed Forces, 2001-2011*, MSMR 19 (2012), pp. 6−9. Available at http://www.ncbi.nlm.nih.gov/pubmed/22694587.

[54] S.O. Nesterenko, L.H. Riley, 3rd, and R.L. Skolasky, *Anterior cervical discectomy and fusion versus cervical disc arthroplasty: Current state and trends in treatment*

for cervical disc pathology, Spine (Phila Pa 1976) 37 (2012), pp. 1470−1474. Available at http://www.ncbi.nlm.nih.gov/pubmed/22343278.

[55] P.D. Nunley, A. Jawahar, E.J. Kerr, 3rd, C.J. Gordon, D. A. Cavanaugh, E.M. Birdsong, M. Stocks, and G. Danielson, *Factors affecting the incidence of symptomatic adjacent-level disease in cervical spine after total disc arthroplasty: 2- to 4-year follow-up of 3 prospective randomized trials*, Spine (Phila Pa 1976) 37 (2012), pp. 445−451. Available at http://www.ncbi.nlm.nih.gov/pubmed/21587111.

[56] M.M. Panjabi, A.M. Pearson, S. Ito, P.C. Ivancic, S.E. Gimenez, and Y. Tominaga, *Cervical spine ligament injury during simulated frontal impact*, Spine (Phila Pa 1976) 29 (2004), pp. 2395−2403. Available at http://www.ncbi.nlm.nih.gov/pubmed/15507801.

[57] M.B. Panzer and D.S. Cronin, *C4-C5 segment finite element model development, validation, and load-sharing investigation*, J. Biomech. 42 (2009), pp. 480−490. Available at http://www.ncbi.nlm.nih.gov/pubmed/19200548.

[58] M.B. Panzer, J.B. Fice, and D.S. Cronin, *Cervical spine response in frontal crash*, Med. Eng. Phys. 33 (2011), pp. 1147−1159. Available at http://www.ncbi.nlm.nih.gov/pubmed/21665513.

[59] J.H. Park, K.H. Roh, J.Y. Cho, Y.S. Ra, S.C. Rhim, and S. W. Noh, *Comparative analysis of cervical arthroplasty using mobi-c(r) and anterior cervical discectomy and fusion using the solis(r) -cage*, J. Korean Neurosurg. Soc. 44 (2008), pp. 217−221. Available at http://www.ncbi.nlm.nih.gov/pubmed/19096680.

[60] G.R. Paskoff, *Cervical Injury Risk Resulting from Rotary Wing Impact: Assessment of Injury Based Upon Aviator Size, Helmet Mass Properties and Impact Severity*, NAW-CADPAX/RTR-2004/86, Patuxent River, MD, 2004.

[61] G.R. Paskoff and E. Sieveka, *Influence of Added Head Mass Properties on Head/Neck Loads During Standard Helicopter Impact Conditions*, Forty Second Annual SAFE Association Symposium, SAFE Association, Salt Lake City, UT, 2004, pp. 20−40.

[62] M. Petren-Mallmin and J. Linder, *Cervical spine degeneration in fighter pilots and controls: A 5-yr follow-up study*, Aviat. Space Environ. Med. 72 (2001), pp. 443−446. Available at http://www.ncbi.nlm.nih.gov/pubmed/11346010.

[63] C.M. Puttlitz, M.A. Rousseau, Z. Xu, S. Hu, B.K. Tay, and J.C. Lotz, *Intervertebral disc replacement maintains cervical spine kinetics*, Spine (Phila Pa 1976) 29 (2004), pp. 2809−2814. Available at http://www.ncbi.nlm.nih.gov/pubmed/15599283.

[64] J. Reaume, *Cervical total disc replacement in a military helicopter and general aviation pilot*, The Federal Air Surgeon's Med. Bull. 50 (2012), pp. 11−12.

[65] J. Reaume, *You're the flight surgeon: cervical degenerative joint disease and total disc arthroplasty*, Aviat. Space Environ. Med. 84 (2013), pp. 169−171. Available at http://www.ncbi.nlm.nih.gov/pubmed/23447858.

[66] J.S. Roh, A.L. Teng, J.U. Yoo, J. Davis, C. Furey, and H.H. Bohlman, *Degenerative disorders of the lumbar and cervical spine*, Orthop. Clin. North Am. 36 (2005), pp. 255−262. Available at http://www.ncbi.nlm.nih.gov/pubmed/15950685.

[67] M. Rollinghoff, K. Zarghooni, L. Hackenberg, A. Zeh, F. Radetzki, and K.S. Delank, *Quality of life and radiological outcome after cervical cage fusion and cervical disc arthroplasty*, Acta Orthop. Belg. 78 (2012), pp. 369−375. Available at http://www.ncbi.nlm.nih.gov/pubmed/22822579.

[68] M.A. Rousseau, X. Bonnet, and W. Skalli, *Influence of the geometry of a ball-and-socket intervertebral prosthesis at the cervical spine: A finite element study*, Spine (Phila Pa 1976) 33 (2008), pp. E10−4. Available at http://www.ncbi.nlm.nih.gov/pubmed/18165735.

[69] A.J. Schoenfeld, A.A. George, J.O. Bader, and P.M. Caram, *Incidence and epidemiology of cervical radiculopathy in the United States military: 2000 to 2009*, J. Spinal Disord. Tech. 25 (2012), pp. 17−22. Available at http://www.ncbi.nlm.nih.gov/pubmed/21430568.

[70] G.W. Smith and R.A. Robinson, *The treatment of certain cervical-spine disorders by anterior removal of the intervertebral disc and interbody fusion*, J. Bone Joint Surg. Am. 40-A (1958), pp. 607−624. Available at http://www.ncbi.nlm.nih.gov/pubmed/13539086.

[71] Society of Automotive Engineers, *SAE J211/1 - Instrumentation for Impact Test-Part 1-Electronic Instrumentation*, 2007.

[72] J.D. Stitzel, *Global Human Body Models Consortium (GHBMC) Male 50th Percentile (M50) Occupant Model Manual*, Virginia Tech − Wake Forest University Center for Injury Biomechanics, Winston-Salem, NC, 2011.

[73] S. Tharin and E.C. Benzel, *Cervical spine arthroplasty: fact or fiction: The absence of need for arthroplasty*, Clin. Neurosurg. 59 (2012), pp. 82−90. Available at http://www.ncbi.nlm.nih.gov/pubmed/22960518.

[74] C. Thunert, *CORA Release 3.6 User's Manual*, GNS mbH, Germany, 2012.

[75] V.C. Traynelis, *Cervical arthroplasty*, Clin. Neurosurg. 53 (2006), pp. 203−207. Available at http://www.ncbi.nlm.nih.gov/pubmed/17380753.

[76] L.M. Tumialan, R.P. Ponton, A. Garvin, and W.M. Gluf, *Arthroplasty in the military: A preliminary experience with ProDisc-C and ProDisc-L*, Neurosurg. Focus 28 (2010), pp. E18. Available at http://www.ncbi.nlm.nih.gov/pubmed/20568934.

[77] C.D. Upadhyaya, J.C. Wu, G. Trost, R.W. Haid, V.C. Traynelis, B. Tay, D. Coric, and P.V. Mummaneni, *Analysis of the three United States Food and Drug Administration investigational device exemption cervical arthroplasty trials*, J. Neurosurg. Spine 16 (2012), pp. 216−228. Available at http://www.ncbi.nlm.nih.gov/pubmed/22195608.

[78] T.D. Uschold, D. Fusco, R. Germain, L.M. Tumialan, and S.W. Chang, *Cervical and lumbar spinal arthroplasty: Clinical review*, AJNR Am. J. Neuroradiol. 33 (2012), pp. 1631−1641. Available at http://www.ncbi.nlm.nih.gov/pubmed/22033716.

[79] N.A. Vavalle, B.C. Jelen, D.P. Moreno, J.D. Stitzel, and F. S. Gayzik, *An evaluation of objective rating methods for full-body finite element model comparison to PMHS tests*, Traffic Inj. Prev. 14 Suppl (2013), pp. S87−94. Available at http://www.ncbi.nlm.nih.gov/pubmed/23905846.

[80] N.A. Vavalle, D.P. Moreno, A.C. Rhyne, J.D. Stitzel, and F.S. Gayzik, *Lateral impact validation of a geometrically accurate full body finite element model for blunt injury prediction*, Ann. Biomed. Eng. 41 (2013), pp. 497−512.

Available at http://www.ncbi.nlm.nih.gov/pubmed/23135331.

[81] M.C. Wang, L. Chan, D.J. Maiman, W. Kreuter, and R.A. Deyo, *Complications and mortality associated with cervical spine surgery for degenerative disease in the United States*, Spine (Phila Pa 1976) 32 (2007), pp. 342−347. Available at http://www.ncbi.nlm.nih.gov/pubmed/17268266.

[82] N.A. White, P. Begeman, W. Hardy, K.H. Yang, K. Ono, F. Sato, K. Kamiji, T. Yasuki, and M. Bey, *Investigation of Upper Body and Cervical Spine Kinematics of Post Mortem Human Subjects (PMHS) During Low-Speed, Rear-End Impacts*, SAE Technical Paper 2009-01-0387, Society of Automotive Engineers, Warrendale, PA, 2009.

[83] N.A. White, K.A. Danelson, F.S. Gayzik, and J.D. Stitzel, *Head and neck response of a finite element anthropomorphic test device and human body model during a simulated rotary-wing aircraft impact*, J. Biomech. Eng. 136 (2014). Available at http://www.ncbi.nlm.nih.gov/pubmed/25085863.

[84] N.A. White, D.P. Moreno, P.J. Brown, F.S. Gayzik, W. Hsu, A.K. Powers, and J.D. Stitzel, *Effects of cervical arthrodesis and arthroplasty on neck response during a simulated frontal automobile collision*, Spine J. 14 (2014), pp. 2195−2207. Available at http://www.ncbi.nlm.nih.gov/pubmed/24614252.

[85] N.A. White, D.P. Moreno, F.S. Gayzik, and J.D. Stitzel, 2015. *Cross-sectional neck response of a total human body fe model during simulated frontal and side automobile impacts*. Comput Methods Biomech Biomed Engin 18 (3)(2015), pp. 293−315.

[86] W. Womack, P.D. Leahy, V.V. Patel, and C.M. Puttlitz, *Finite element modeling of kinematic and load transmission alterations due to cervical intervertebral disc replacement*, Spine (Phila Pa 1976) 36 (2011), pp. E1126−1133. Available at http://www.ncbi.nlm.nih.gov/pubmed/21785298.

[87] L. Xu, V. Agaram, S. Rouhana, R.W. Hultman, G.W. Kostyniuk, J. Mccleary, H. Mertz, G.S. Nusholtz, and R. Scherer, *Repeatability evaluation of the pre-prototype NHTSA advanced dummy compared to the hybrid III*, SAE Technical Paper 0148-7191, Society of Automotive Engineers, Warrendale, PA, 2000.

[88] B. Yang, H. Li, T. Zhang, X. He, and S. Xu, *The incidence of adjacent segment degeneration after cervical disc arthroplasty (CDA): A meta analysis of randomized controlled trials*, PLoS One 7 (2012), pp. e35032. Available at http://www.ncbi.nlm.nih.gov/pubmed/22558112.

[89] S. Yin, X. Yu, S. Zhou, Z. Yin, and Y. Qiu, *Is cervical disc arthroplasty superior to fusion for treatment of symptomatic cervical disc disease? A meta-analysis*, Clin. Orthop. Relat. Res. 471 (2013), pp. 1904−1919. Available at http://www.ncbi.nlm.nih.gov/pubmed/23389804.